SYNTHESIS AND CHARACTERIZATION OF BIOACTIVE GLASS-CERAMIC PARTICLES WITH ADVANCED ANTIBACTERIAL PROPERTIES FOR APPLICATIONS IN BONE REGENERATION

By

Natalia Pajares Chamorro

A DISSERTATION

Submitted to
Michigan State University
in partial fulfillment of the requirements
for the degree of

Materials Science and Engineering − Doctor of Philosophy

2021

ABSTRACT

SYNTHESIS AND CHARACTERIZATION OF BIOACTIVE GLASS-CERAMIC PARTICLES WITH ADVANCED ANTIBACTERIAL PROPERTIES FOR APPLICATIONS IN BONE REGENERATION

By

Natalia Pajares Chamorro

Bacterial infections are major surgical complications, which have worsened due to the continued evolution of drug-resistance. In coping with the decay of the antibiotic era, scientists eagerly search for alternative treatments. Multi-functional biomaterials capable of combating infections while triggering tissue regeneration are of great interest. For example, bioactive glasses have been regularly used to deliver drugs and regenerate tissue owed to their unique bone-bonding ability. Doping the bioactive glass structure with broad-spectrum biocide ions such as Ag^+ confers advanced antibacterial properties. The release of Ag^+ is controlled by the degradation process of the glass network, maintaining the dose within a therapeutic window that is not cytotoxic to eukaryotic cells. Despite the extensive research performed on Ag-doped bioactive glasses, their regenerative properties in bone tissues have been rarely investigated.

This thesis presents promising interactions between Ag-doped bioactive glass (Ag-BG) microparticles and osteoprogenitor cells, providing evidence of the ability to support bone regeneration. Ag-BG's degradation provoked cell proliferation and cell differentiation *in vitro* and demonstrated healing of critical calvaria defects in mice after one month of implantation, thanks to the release of Si and Ca ions. Additionally, Ag-BG was antibacterial against *Staphylococcus aureus* (*S. aureus*), the most common cause of bone-degenerative diseases like osteomyelitis, and demonstrated low proclivity to induce resistance. The antibacterial potential originated from the degradation by-products of the structure. The mechanism of inhibition was built upon four main

sources from higher to lower contribution: Ag^+ release, oxidative stress, mechanical damage by nano-sized debris, and osmotic effect. In addition, Ag-BG was capable of restoring ineffective antibiotics with cell-wall-related inhibitory mechanisms by simple combinatorial therapies, rendering them effective in clearing infections. This unprecedented functionality of Ag-BG was expanded with antibiotic depots, where Ag-BG served as a carrier for an ineffective drug.

Bioactive glass nanoparticles (BGNs) have been proposed to advance biological and antibacterial properties compared to their micro-sized counterparts. However, the challenges of producing BGNs with multifold metallic ions in a reproducible manner have limited their use. Here, the Stöber method was comprehensively studied to understand the effect of process variables on BGNs' composition, structure, and morphology. The use of methanol as solvent and the early addition of metallic ion reagents before catalysis helped improved their cation incorporation within the glass network. Extended stirring was key to achieving the targeted composition and controlling the particle size. Monodispersed 10 nm Ag-doped BGNs (Ag-BGNs) were achieved. These Ag-BGNs were stronger antimicrobial weapons, providing bacterial inhibition within hours of treatment. The biological properties were not significantly advanced in the Ag-BGNs compared to Ag-BG; however, cell proliferation, differentiation, and bone re-growth were still provoked.

These Ag-BGNs were used as fillers in hydrogel nanocomposites with natural matrices consisting of collagen type I or extracellular matrix. Ag-BGNs distributed homogeneously along the polymer fibrils and allowed polymerization within hours at physiological conditions. These materials hold potential for injectable devices, designing minimally invasive single-step treatment for debilitating bone infections while promoting tissue recovery.

“No importa lo que haga, cada persona en la Tierra está siempre representando el papel principal de la historia del mundo y normalmente no lo sabe” – Paulo Coelho, El Alquimista.

Este trabajo es mi granito de arena a la Ciencia y está enteramente dedicado a mi familia, por su apoyo constante y amor incondicional. Os llevo conmigo a donde vaya.

ACKNOWLEDGMENTS

Many people say starting a Ph.D. is a combination of bravery and insanity. I am still not sure which of them drove me the most to take this path in my career. What I can say without a doubt is it has been a great adventure, and now that it is concluding, I can finally relate to the famous quote "Veni, Vidi, Vici". Before I close this period, I wanted to take the opportunity to thank everyone who has inspired, guided, and supported me throughout the process.

This dissertation would not have been possible without Dr. Xanthippi Chatzistavrou, my advisor and mentor. Thank you, Xanthippi, for allowing me to take part in this fantastic research and work side by side with such an incredible person and scientist. You have taught me how to become a better engineer by example, nurturing and supporting both my personal and professional growth with patience, enthusiasm and immense knowledge. Thank you for giving me the confidence I needed to believe in my capabilities. I cannot imagine having a better advisor. First times are something that you never forget, and I am grateful that you chose me as your first graduate student. I do not doubt that the future generation will benefit immensely from having you as mentor. I would also like to express my deepest appreciation to my fantastic committee members: Dr. Kurt Hankenson, Dr. Neal Hammer, Dr. Martin Crimp, and Dr. Shiwang Cheng, whose experience and contributions have been invaluable for my work. I want to acknowledge the time and effort each of you have placed on achieving my research goals and for showing me the best practices in Education. Thank you, Kurt and Neal, for welcoming me in your labs and guiding me to become an independent user in your field. Special thanks to Dr. Jonathan Hardy, who has also contributed to this project.

I would like to extend my sincere thanks to the Biomaterials group, especially Mr. Adam Marsh, Mr. Logan Soule, and Ms. Kayla Chuong, for contributing to my development as a lab partner and mentor. I also wish to thank the contribution and support of Dr. Yadav Wagley, Dr. Daniel Youngstrom and Ms. Parker Acevedo from the Hankenson Lab; Mr. John Shook, and Mr. Joshua Lensmire from the Hammer Lab; and, Dr. Per Askeland and Dr. Alicia Withrow. I am grateful to Dr. Katy Colbry for allowing me to play a leadership role in the College of Engineering.

I'm deeply indebted to Dr. Carl Boehlert, who encouraged me to pursue my Ph.D. and the Boehlert-Somohano family, who included me in their tribe. Thank you for giving me a sense of belonging in the U.S. I cannot leave Michigan State University without acknowledging all the friends I made along the way. A sound support system is essential for thriving and staying sane in Grad School. I am lucky to meet Mr. Alex Mirabal, Ms. Geeta Kumari, Ms. Lexi Rogien, Dr. Kanchan Chavan, Dr. Sabyasachi Das, Dr. Aritra Chakraborty, Dr. Mary Ensch, Mr. Chauncey Splichal, Dr. Maddie Shelgren and Dr. Makena Neal. Thanks to my friends at home and around the globe, who still don't understand why I do what I do but support me nonetheless.

My deepest gratitude goes to my family. Mom, Dad, you are a relenting source of inspiration that challenges me to become my best self. Thank you Rafa, Marilines, Inma, Antonio, Raquel, Dani, Tesla and my other relatives, whose advice and encouragement have helped me push forward; and my grandfather, who always was my role model and unfortunately, is no longer here to see this our dream come true. The best outcome of my university studies has been, without a doubt, finding David Hernández, who makes both the journey and the destination worthwhile. Thank you for sticking by my side, for your commitment and determination to live our lives to the fullest. Finally, thank you, reader, for choosing this dissertation and joining my journey. Now, let's see how the magic begins!

TABLE OF CONTENTS

LIST OF TABLES

LIST OF FIGURES

KEY TO SYMBOLS AND ABBREVIATIONS

A	Atomic mass of an atom.
ACAN	Aggrecan. Gene.
ACP	Amorphous calcium-phosphate.
ADU	Arbitrary density units.
Ag-BG	Silver-doped bioactive glass microparticles (< 20 μm) derived from sol-gel.
Ag-BG/antibiotic	Combination of Ag-BG microparticles and the specified antibiotic.
Ag-BG@vanc	0.5 mg of Ag-BG microparticles loaded with vancomycin during 6 h of immersion.
Ag-BGNs	Silver-doped bioactive glass nanoparticles (< 10 nm).
AgNT	Silver nitrate. Reagent in bioactive glass synthesis.
AlNT	Aluminum nitrate nonahydrate. Reagent in bioactive glass synthesis.
ARS	Alizarin red staining. Method used for cell mineralization analysis.
ATR	Attenuated total reflectance.
BET	Brunauer-Emmet-Teller.
BG	Silver-free bioactive glass microparticles (< 20 μm) derived from sol-gel.
BGNs	Bioactive glass nanoparticles.
BMP	Bone morphogenetic protein.
BO	Bridging oxygen. Bond formed between network formers (i.e., -Si-O-Si-).
BSP	Bone sialoprotein. Gene.
CaNT	Calcium nitrate tetrahydrate. Reagent in bioactive glass synthesis.

CFU	Colony forming units. Measuring unit to quantify bacteria.
cip	Ciprofloxacin. Antibiotic.
Col	Collagen.
Col/Ag-BGNx	Nanocomposite of collagen matrix and Ag-BGNs fillers. X indicates the wt.% of Ag-BGNs.
Col10A1	Collagen alpha-1(x). Gene.
cpl	Chloramphenicol. Antibiotic.
CS	Chitosan.
d	Interplanat spacing between crystal planes.
DLS	Dynamic light scattering.
DMEM	Dulbecco's modified- Eagle's medium.
E	Young's modulus.
E_0	Accelerating voltage used in SEM.
E_c	Minimum emission voltage to detect an element in EDS.
ECM	Extracellular matrix.
ECM/Ag-BGNx	Nanocomposite of ECM matrix and Ag-BGNs fillers. X indicates the wt.% of Ag-BGNs.
EDS	Energy dispersive spectroscopy.
ery	Erythromycin. Antibiotic.
fosfo	Fosfomycin. Antibiotic.
FT-IR	Fourier transform infrared.
GAPDH	Glyceraldehyde 3-phosphate dehydrogenase. Gene.
gent	Gentamicin. Antibiotic.

G_x	Generation of MRSA after subsequent Ag-BG treatments. X indicates the number of Ag-BG treatments.
H&E	Hematoxylin and eosin. Staining used in immunohistology.
HA	Hydroxy apatite.
hBMSC	bone-marrow-derived human marrow stromal cells.
hBMSCs	Human bone-marrow-derived stromal cells
HCA	Hydroxycarbonate apatite.
HNO_3	Nitric acid.
I_c	Initial concentration of a solution.
ICSD	Inorganic Crystal Structure Database.
IUPAC	International Union of Pure and Applied Chemistry.
IVIS	In vivo Imaging System.
KNT	Potassium nitrate. Reagent in bioactive glass synthesis.
L	Camera lenght in TEM-SAD.
LB	Luria Bertani. Nutrient-rich medium used in bacteria growth.
M1	Method 1 followed for BGNs synthesis. The different processes applied are indicated as P1 and P2.
M2	Method 2 followed for BGNs synthesis. The different processes applied are indicated as P1 and P2.
MAS-NMR	Magic angle spinning nuclear magnetic resonance.
MIC	Minimum inhibitory concentration. Lowest dose of an antimicrobrial that decreases bacterial concentration.
micro-CT	Micro-computed-tomography. Imaging method.
M-OR	Metal (M) alkoxide (OR). For example, $Si-(OC_2H_5)_4$.

MRSA	Methicillin-resistant *S. aureus*. Mutant of S. aureus resistant to several antibiotics.
MSU	Michigan State University.
NaNT	Sodium nitrate. Reagent in bioactive glass synthesis.
NBO	Non-bridging oxygen. Bond formed between network former and modifier (i.e., -Si-O-Na-).
NC	Network connectivity. Abbreviation used for calculation purposes only.
NH_3OH	Ammonium hydroxide.
OCN	Osteocalcin. Gene.
OD	Optical density.
OMD	Osteomodulin. Gene.
OSX	Osterix. Gene.
oxa	Oxacillin. Antibiotic.
PBS	Phosphate buffer saline.
PCL	Poly(ε-caprolactone).
Penicillin-binding protein	PBP
Q^n	Nomenclature to identigy the tetrahedra units in silica-based material, where n is the number of BO.
qRT-PCR	Quantitative reverse transcription polymerase chain reaction. Method used for gene analysis.
R_c	Resicudal concentration of a solution.
RLMCA	Reaction-limited monomer-cluster aggregation. Model to describe particle growth.
ROS	Reactive oxygen species.

RunX2	Runt-related transcription factor 2. Gene.
R-value	Ration between H_2O/TEOS in sol-gel processes.
S. aureus	*Staphylococcus aureus*. Gram-positive bacterium.
SAD	Selected area diffraction.
SBF	Simulated body fluid.
SEM	Scanning electron microscope.
SNPs	Single nucleotide polymorphism (used in genome sequence analysis).
sol-gel	Solution - gelation.
T_a	Annealing temperature.
TEM	Transmission electron microscope.
TEOS	Tetraethyl orthosilicate. Reagent in bioactive glass synthesis.
TEP	Triethyl phosphate. Reagent in bioactive glass synthesis.
T_g	Glass transition temperature.
TMBA	Too Many Bloody Acronyms
T_m	Melting point.
tobra	Tobramycin. Antibiotic.
TSA	Tryptic soy agar. Nutrient-rich gel used to grow colonies on a plate.
TSB	Tryptic soy broth. Nutrient-rich medium for bacteria growth.
UV-Vis	Ultraviolet and visible.
vanc	Vancomycin. Antibiotic.
WT	Wild type. Used to designate MRSA before subsequent Ag-BG treatments.
X_1	Stirring time at the first step of BGNs synthesis (i.e., mixing TEOS and TEP)

X_2	Stirring time at the second step of BGNs synthesis (i.e., after addition of CaNT in M2 approach)
X_3	Stirring time at the third step of BGNs synthesis (i.e., after addition of catalyst in M2 approach)
XRD	X-ray diffraction.
Z	Atomic number of an atom.
λ	Wavelength of the energy source.
ρ	Density.

1. INTRODUCTION

1.1. Bioactive materials in restorative medicine: clinical problem

In the vast majority of the cases, bone fractures can heal without surgical intervention [1,2]. The inherent regenerative properties of bone tissue are often activated by external stimulation and, unfortunately, are insufficient to remodel large defects [3]. Autograft techniques and transplantation are widespread for treating highly damaged bone tissue [4]. With over 2 million procedures annually, bone tissue transplants are only surpassed by blood transfusions in the list of most common transplants [5]. Tissue engineering, which combines engineering principles and life sciences, stands out in developing biomaterials that provoke stimuli to trigger tissue regeneration [2]. Silicate-based bioactive glass-ceramics are attractive in this regard, because of their bone-bonding ability and their potential for osteogenesis and angiogenesis [6,7]. The physicochemical and biological response of bioactive glasses are associated with the sub-products they release during degradation, and thus, they can be tailored through the composition, structure, and morphology of the bioactive glasses [8–10]. These three variables have significant impacts on the rate of ion diffusion and ion release. Therefore, it is fundamental to control the composition, structure, and morphology of the bioactive glasses to fulfill the requirements for the intended medical application.

The capability of the bioactive glasses to be used as delivery platforms makes them desirable for therapeutic purposes. For example, the demand for delivery of heavy metal ions (i.e., Ag, Cu, Zn) or organic molecules (i.e., antibiotics) to fight infections has increased diametrically. Simultaneous delivery of both agents offers synergistic possibilities and enables dose reduction, minimizing toxicity [11–13]. Silver-doped bioactive glass-ceramic (Ag-BG) microparticles have been recently

highlighted as dual agents for antibacterial and tissue regeneration [14–16]. The Ag^{+} release is controlled through the degradation of the glass structure, causing bacterial inhibition. However, the current knowledge of the mechanism of inhibition of this system is vague and does not guide the optimization of the response by tunning particle composition, structure, or morphology. The combination of Ag-BG microparticles with encoded antibiotics revealed a potential for restoring the antimicrobial ability of the drug [17]. This unique synergism becomes particularly attractive for treating infections that conventional antibiotics are no longer effective in eradicating, due to bacterial resistance.

Even though bioactive glasses provide enhanced regeneration, their delivery needs to be optimized for the specific size and shapes of defects [7,18]. In these cases, composites materials arise as alternative candidates to fill complex shape defects while allowing localized therapy [19–21]. Bioactive glass particles can act as fillers in biopolymers or hydrogel matrices, providing bone-bonding, biodegradability, and therapeutic delivery capabilities. The polymer matrix allows the particles to remain in the defect and is responsible for flexibility that adjusts the composite to the defect shape and size [19,22]. The homogenous distribution of the filler within the matrix is key to accomplishing synergism between both phases, and it is facilitated by nano-sized bioactive glass particles [23,24]. Due to their small size and large surface area to volume ratio, the properties of bioactive glass nanoparticles (BGNs), defined as those < 100 nm in diameter, differ from the properties of the bulk materials. Specifically, BGNs offer advanced surface reactivity, which accelerates their bone-bonding ability and improves their potential as antimicrobial agents [25–27]. Similar to microparticles, BGNs may be doped with therapeutic ions or molecules to tailor the material for specific medical applications.

The fabrication of BGNs has been attempted by different solution-gelation (sol-gel) approaches [28]. While most processes showed means to control particle size, up to date none of them have been able to produce adequate control over the composition of the BGNs [29,30]. For example, most processes targeting compositions, such as 70 SiO2 - 30 CaO (mol.%) resulted in particles with a composition of 90 SiO2- 10 CaO (mol.%). Consequently, the application of BGNs as a regenerative tool is currently very limited, and thus, new strategies must be developed to gain control of the synthesis process.

1.2. Objective and dissertation roadmap

This project aims to address the problem of diseased bone tissue regeneration from a materials science approach. A single-step technology with multi-functional properties is proposed to target infectious diseases, while providing support for tissue re-growth. This strategy consists of delivering heavy metals and antibiotics simultaneously in a bioactive glass nano-platform.

In Chapter 2, the fundamentals and current literature related to this thesis are reviewed, presenting at the end a detailed explanation of the aims and hypotheses of this work. The instrumentation and experimental methods are described in Chapter 3. This dissertation is structured in four fundamental pillars, as represented in **Figure 1**, that were used to organize the results and discussion in Chapters 4 and 5, respectively. First, Ag-doped bioactive glass-ceramic (Ag-BG) microparticles were characterized in terms of degradability and biocompatibility when interacting with cells and tissues of bone lineage. Second, the antibacterial capabilities and the Ag-BG inhibition mechanisms were evaluated alone and in combination with antibiotics. Third, the synthesis of highly dispersed Ag-doped bioactive glass nanoparticles (Ag-BGNs) was addressed by optimizing a Stöber-derived method. Finally, a single-step delivery method of Ag-BGNs was

explored by the development of injectable nanocomposites. This thesis concludes by presenting the highlights (Chapter 6) and the research gaps and recommendations for future investigations (Chapter 7).

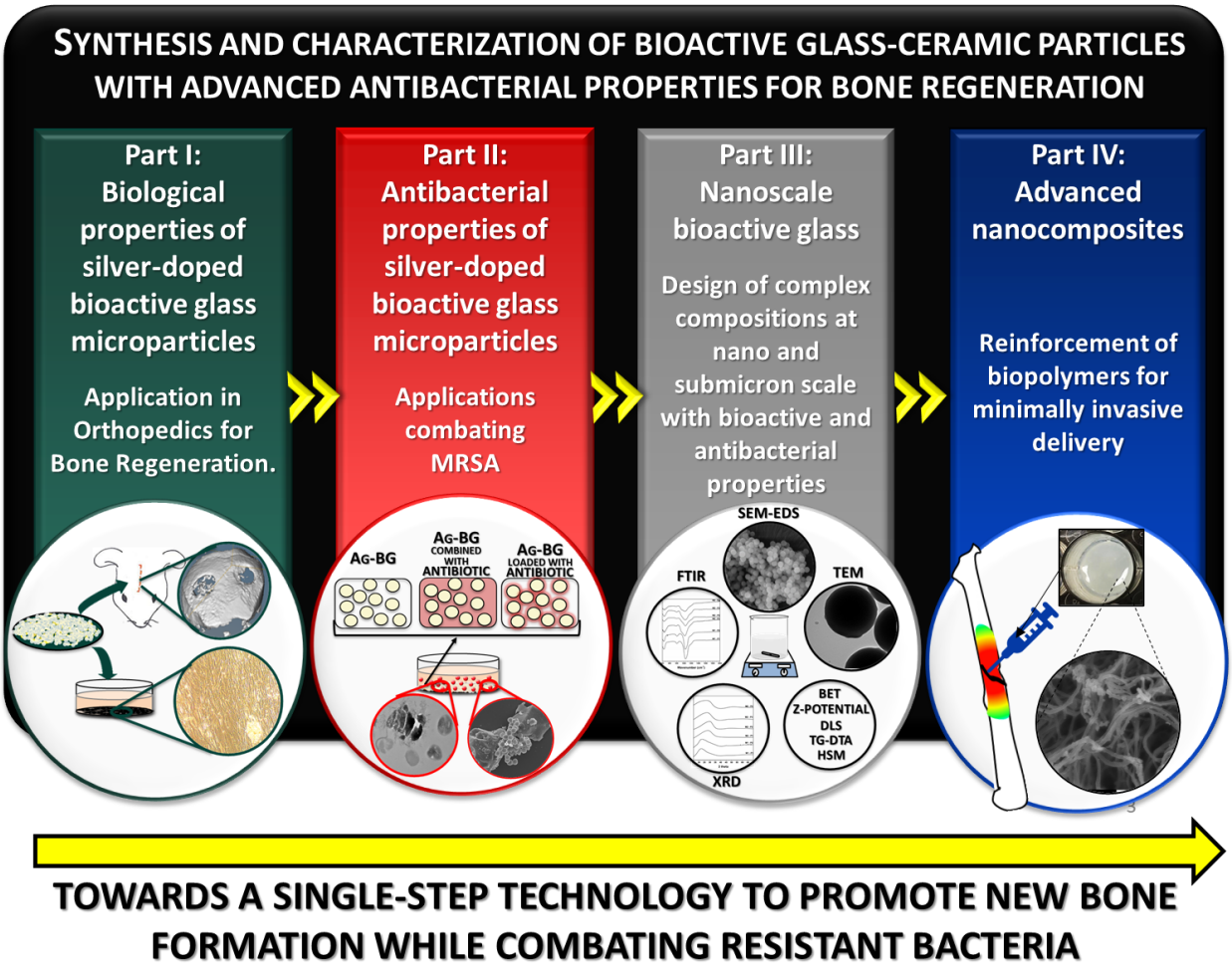

Figure 1: Schematic overview of the research approach followed in this dissertation organized in 4 main pillars.

2. FUNDAMENTALS AND LITERATURE REVIEW

2.1. Bioactive glasses and glass-ceramics

Bioactive materials are defined as those that elicit a bond at the tissue-material interface [31]. Bioactive glasses are a type of inorganic bioactive material that incorporate various cations (i.e., Ca, Na, P, K, Sr, and Zn) and chemically bond to the bone by forming a hydroxycarbonate apatite phase (HCA) at the interface [32]. Bioactive glasses release those ionic species during their degradation and trigger specific cellular responses, such as forming new bone [32]. The regeneration process may continue until the biomaterial is entirely absorbed by the body [33]. The degradation behavior, which leads to the biological properties, can be tailored by tuning glass composition, morphology, and processing parameters [7,34].

Since their discovery in the late 1960s by L. Hench [7], bioactive glasses have yielded several FDA-approved products such as NovaBone and Novamin [7]. In this project, the next generation of bioactive glasses is targeted to regenerate tissue and prevent and fight bacterial infections. Among the various shapes and morphologies in which bioactive glasses may be produced, particles, in micro and nano sizes, attract attention due to their easy processing adaptability and high versatility for different clinical applications. In this chapter, the background, and state of the art of bioactive glass particle science are presented to identify the research gaps and present the framework that fundaments this research work.

2.1.1. The structure of bioactive glasses

Glasses are amorphous solids primarily formed by oxide species divided into network formers and network modifiers [35,36]. Network former oxides, including SiO_2, P_2O_5, and B_2O_3, are

characterized by the formation of bridging oxygens (BO), which connect units to develop a network. For example, silicate glasses consist of silica tetrahedra units (one silicon atom bonded to four oxygens) connected by BO bonds (-Si-O-Si- shown in **Figure 2** a). Different elements may be incorporated, and depending on their concentrations, they play a different role in the network. For example, network modifier oxides, such as CaO and Na_2O, disrupt the network by breaking the BO bonds into non-bridging oxygens (NBO). The ratio of BO to NBO in the structure defines the network connectivity, which is critical for properties such as degradability. The network connectivity is usually evaluated in terms of the Q^n speciation as represented in **Figure 2** b. Highly connected networks present primarily Q^4 species. The Q speciation decreases (Q^3, Q^2, Q^1, or even Q^0) as network modifiers are introduced in the structure, decreasing the number of BO. For example, Q^3 species are formed when out of the four oxygens, three present (-Si-O-Si-) bonds and one present (-Si-O-NBO). Some elements are also referred to as network intermediate oxides (i.e., aluminum and phosphorous), as they can act as both network former and modifier by varying their coordination number depending on their concentration. For instance, phosphorous appears in orthophosphate (PO_4) units when acting as network former [37] and as Si-O-P bridges when modifying the network [38]. Understanding the role of each cation is the basis for the material design as it is correlated to the final structure of the bioactive glasses and, thus, to its final properties.

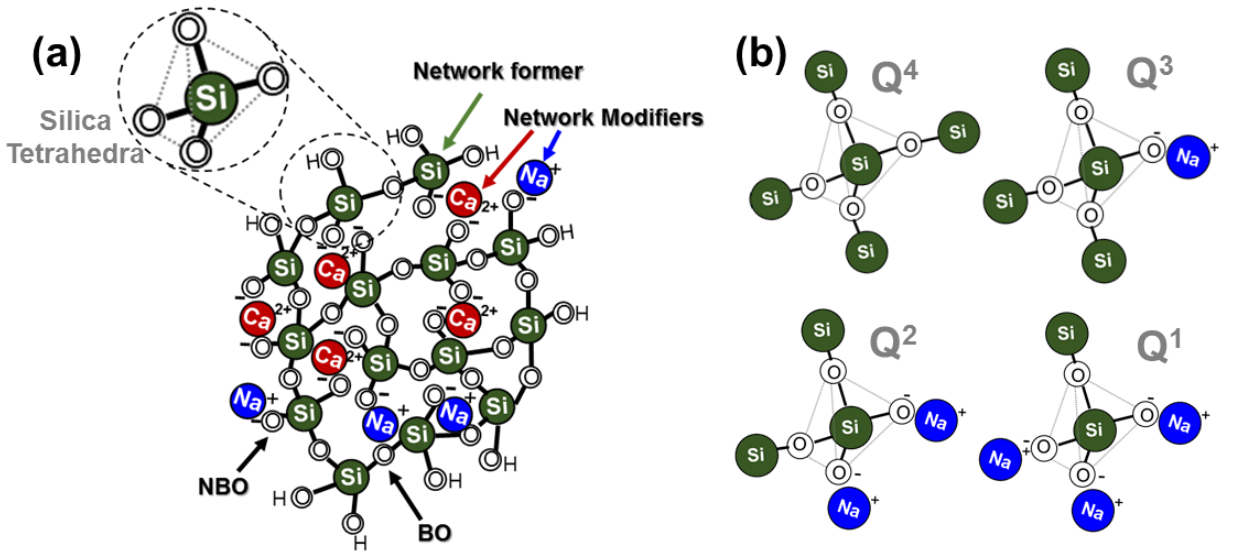

Figure 2: 2D Structure of bioactive glass (a). The different atoms forming the glass network are represented with color circles: silicon (Si) in green, oxygen (O) in white, sodium (Na) in blue, and calcium (Ca) in red. Hydrogen protons (H^+) balance the negative charge of external oxygens, forming silanol groups (Si-OH). The interaction between atoms occurs by bridging oxygen (BO) bonds or non-bridging oxygen (NBO) bonds. The elements distribute within the glass, forming Q^n units (b), where n indicates the number of -Si-O-Si- BO bonds in the tetrahedron.

2.1.2. The role of composition in bioactive glasses

The bulk composition of the glass plays a crucial role in the chemical response of the material. Hench [39] discovered that only some specific compositions of glass in the system SiO_2, CaO, Na_2O, and P_2O_5 could form a bond with bone and soft tissue, and described a compositional diagram [40] to anticipate the material-tissue interaction (**Figure 3**). For example, bioactive glasses of composition within region A and region S (of $SiO_2 < 60$ wt.%) are bioactive and capable of bonding to hard and soft tissue, respectively. Bioactive glasses in region B are bioinert, present very low reactivity, and get encapsulated by non-adherent fibrous tissue when implanted. In contrast, bioactive glasses in the region C are highly reactive and get resorbed within a month before the material can bond to the tissue. Region D bioactive glasses have not been implemented; however, based on the effect of other compositions, bioactive glasses in this region are predicted

to not bond with tissues. Finally, the diagram highlights region E, where the bioactive glass presents a composition of SiO_2 45 – Na_2O 24.5 – CaO 24.5 – P_2O_5 6 (wt.%), possibly the most exploited glass system in Industry, registered with the trademark Bioglass® 45S5. In multi-component systems with more than 4 different oxides, it is not possible to find a simple relationship between compositions and tissue response to express in a 2D diagram.

Nonetheless, Andersson *et al*. [41] developed a model for compositional optimization to predict the glass-tissue interaction without animal testing. This model allows selecting compositions for specific applications since most glass properties are additive within certain composition limits. The influence of several critical ions in the structure and properties of bioactive glass has been presented in other works [9,42–44] and is summarized in **Table 1**.

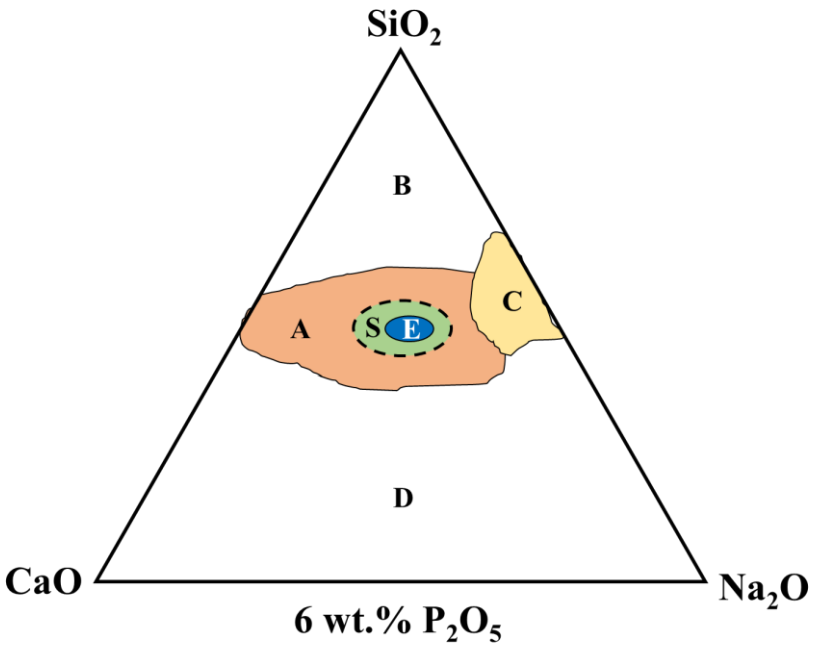

Figure 3: 2D ternary diagram of bioactive glass composition (in wt.%) dependence on the material-tissue interaction. Region A, B, and C depicts bioactive, bioinert, and resorbable glasses. Region D indicates non-glass forming. In region S, bioactive glasses bond to soft tissue. Region E marks the composition of Bioglass ® 45S5, registered trademark. Modified from [40].

Table 1: Effect of ions on bioactive glasses' structure and biological response [9,42–44].

Ion	Effect on the structure	Effect on the biological response
Si	Formation of the network backbone.	Calcification of bone and increase of bone mineral density. Essential in metabolic processes. Component of connective tissue, assists on collagen type I formation and contributes to its resilience
Ca	Decrease connectivity of the network. Increase degradability.	Main component in hard tissue. Favors cell mineralization and upregulation of growth factors in osteoblasts cells.
P	Reduce the tendency to crystallization. Decrease elastic modulus and T_m.	Increase bioactivity of glass Involved in the synthesis of lipids and proteins. Stimulates the expression of matrix proteins for bone formation.
Na	Decrease connectivity of the network. Decrease T_g and T_m.	Maintains osmotic pressure. Regulates the absorption of salts and amino acids. No effect on bone bonding.
K	Decrease connectivity of the network. Reduce the tendency to crystallization Decrease elastic modulus and T_m.	Regulates osmotic pressure. Affects glycogenesis. No effect on bone bonding.
Al	Stabilize glass structure. Decrease thermal expansion coefficient.	Decrease bioactivity of glass. May inhibit bone bonding.
Ag*	Increase BO. Reduce dissolution of the glass.	Provides antibacterial activity. May increase toxicity of the glass.

* The role of Ag in the bioactive glass is detailed in section 2.4.1.

2.1.3. The vitrification process of materials

Glasses are usually obtained by progressive solidification of a liquid that does not crystallize during cooling. The vitrification of a material can be controlled by the cooling rate, attending to the variations of properties, like enthalpy or free volume, as the temperature decreases (**Figure 4**) [45,46].

The specific volume of a crystal increases as the temperature approaches the melting point (T_m), at which the material undergoes a sudden phase transition from solid to liquid (path F-B in **Figure 4**). The temperature rise above T_m continues the volume expansion of the melt as its viscosity decreases (path B-A in **Figure 4**). The rate at which this melt is cooled controls the crystallization or vitrification of the material.

Crystallization occurs when the cooling rate is slow enough to allow atomic diffusion and organization into the lowest energy configuration. This way, the cooling/free volume path will be coincident, but opposite, to the heating path (path A-B-F-G in **Figure 4**), and a stable crystal lattice will form.

Vitrification occurs at high cooling rates when the molecular mobility of the liquid decreases rapidly as a function of the temperature. The viscosity of the liquid increases until the molecular mobility is insufficient to allow the system to find equilibrium, suppressing crystallization. The atomic spatial distribution in the liquid is retained in the solid, and therefore, the structure is characterized by its disorder. As the temperature decreases, the supercooled liquid achieves the consistency of a solid without suffering abrupt changes in its specific volume (path A-C-D in **Figure 4**), forming a metastable glass structure. Note that the volume of a glass is usually higher than that of its crystal counterpart.

The temperature that delimits the transition between glassy behavior and liquid is defined as the glass transition temperature (T_g), which is obtained by the intersection of the supercooled liquid line (path C-B) and the glass line (path D-C). The glass transition is not a true thermodynamic phase transition, and therefore, there is not a single glassy state. Since the glass is in a non-equilibrium state, its structure may relax towards lower energy configurations during annealing (path C-E in **Figure 4**). The gentle temperature transition between the annealing point (T_a) and just above T_g (by cooling or reheating) allows slow molecular re-arrangement that can result in the formation of crystal domains, yielding glass-ceramic materials.

The non-equilibrium state of glasses results in high reactivity, especially at the surface, making them ideal materials for fast tissue bonding. In contrast, glasses usually present mechanical weakness and low fracture toughness due to the amorphous network. Partial crystallization of the amorphous network (i.e., bioactive glass-ceramics) enhances the mechanical and flexural strength of the glass; however, the improvements of these properties are achieved at the expense of bioactivity [47–49]. The inherent low strength of bioactive glasses does not lessen their value in clinical applications. For example, the low strength has no influence when the bioactive glass is used as buried or low-load bearing implants or used in the form of powders and composites, which are the main applications targeted in this project.

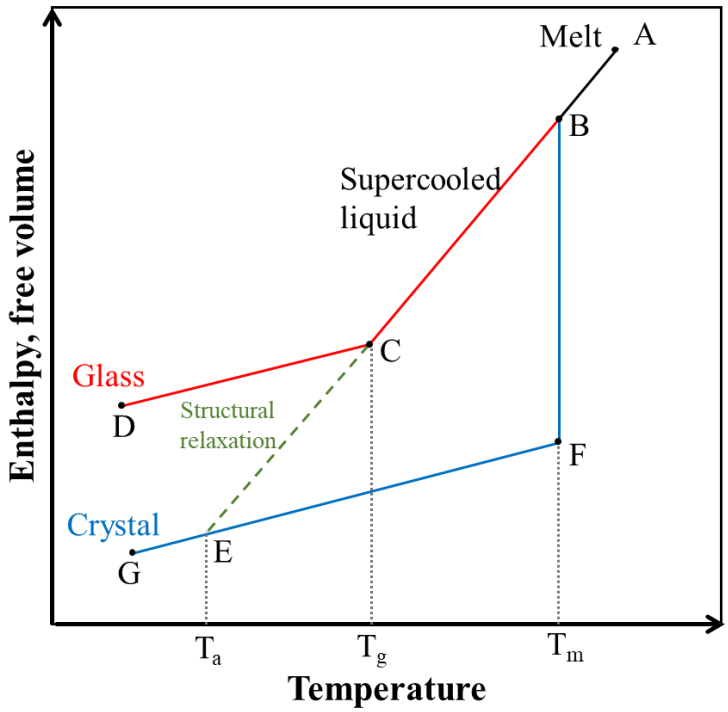

Figure 4: Schematic diagram of the enthalpy/free volume change in liquid, crystalline, and glassy state as a function of temperature during processing. A crystal increases its specific free volume during heating (path G-F) and suffers solid-liquid transition (path F-B) when the melting temperature (T_m) is reached. If the liquid is cooled at a slow rate, following the same curve of heating (path A-B-F-G), the melt returns to its crystalline solid state. If the cooling rate is fast, the liquid passes through point B without abrupt changes in volume, avoiding crystallization (path A-C-D). The glass transition temperature (T_g) identifies the transition points where the supercooled liquid reaches the consistency of solid, based on its viscosity. Structural relaxation occurs between the annealing temperature (T_a) and T_g when the cooling rate slows down during glass processing. Modified from [45].

2.2. Processing of bioactive glasses

Bioactive glass particles can be synthesized by two main routes: melt-quench and sol-gel chemistry. The different processing between these two methods can affect the material characteristics significantly. Briefly, the melt-quench route consists of the proportional mixture of solid precursors in a flame reactor for their melting (T > 1300 ºC) [50,51]. Quenching is then performed so that the cooling rate is higher than the crystallization rate and an amorphous material is formed. In contrast, in the sol-gel methods, the precursors are dissolved in solution, where the pH controls the network's formation before heat-treatment at low temperatures (T < 700 ºC). On this basis, the sol-gel method is convenient and versatile since it does not require complex equipment, and the morphology and composition of the glass can be tailored in a straightforward manner [52,53]. The sol-gel method is a time-consuming approach, due to the waiting time between reagents dissolution and the several heat-treatment steps. However, a broader spectrum of bioactive compositions than those presented in **Figure 3** can be obtained. Therefore, in this project, the bioactive glass particle synthesis was performed by sol-gel approaches.

2.2.1. The sol-gel method

The sol-gel process is a chemical synthesis approach in which highly pure precursors are dissolved in a water/acid or water/base bath to generate a colloid that later forms an oxide network [30]. During the process, the colloids are converted to viscous gel and then to a solid material. The colloid is usually obtained from the transformation of metal alkoxide precursors (M-(OR)). For example, tetraethyl orthosilicate (TEOS), which consists of one Si atom surrounded by four ethyl groups (Si-$(OC_2H_5)_4$), is the most common precursors of silicate-based sol-gel glasses. The metal alkoxide transformation into an oxide gel progresses through a series of interdependent chemical

reactions, namely hydrolysis, and condensation. In the case of TEOS, hydrolysis occurs by substitution of the alkoxide chain (-(C_2H_5O)) with hydroxyls (-OH), producing a hydrated chain of silicon ($Si(OH)_4$) and ethanol (C_2H_5OH) (**Equation 1**). The condensation reaction, also known as polymerization, produces siloxane bonds (-Si-O-Si-) to form the colloids. Two condensation reactions have been identified in the formation of the silicate colloid: water and alcohol condensation. For instance, the siloxane bond may form between two hydrated silicon chains (water condensation, **Equation 2**) or between a hydrated chain of silicon and a silicon alkoxide (alcohol condensation, **Equation 3**). Other metallic precursors, usually nitrates, can be added during or after completing these reactions to achieve the composition of the glass system.

Hydrolysis: $$\equiv Si - OC_2H_5 + H_2O \rightarrow \equiv Si - OH + C_2H_5 - OH$$ **Equation 1**

Condensation:

Water: $$\equiv Si - OH + OH - Si \equiv \rightarrow \equiv Si - O - Si \equiv + H_2O$$ **Equation 2**

Alcohol: $$\equiv Si - OH + H_5C_2O - Si \equiv \rightarrow \equiv Si - O - Si \equiv + C_2H_5 - OH$$ **Equation 3**

The silica network formation is greatly influenced by the relative rates of hydrolysis and condensation reactions and the pH of the solution. In an acid-catalyzed system, particles aggregate as condensation continues leading to a 3D gelled structure, while in basic conditions, repulsive forces may prevent this aggregation.

The gel obtained after the condensation reactions is submitted to heat-treatment to produce the final glass. The gel is first aged (~ 60-90 ºC) and dried (~ 120-200 ºC) to eliminate water and alcohol residues and then stabilized (~ 400 – 600 ºC), reducing the concentration of silanols at the surface and calcinated (> 600 ºC) to burn-off nitrate by-products. The heating rate in-between

steps and dwell time plays a key role in the generation or relief of internal stresses in the network that can cause cracking of the 3D gel or maintained its macro-architecture.

Sol-gel bioactive glasses are elementally homogeneous and show less network connectivity than melt-derived glasses due to retained H^+ acting as network modifiers. The high surface area and elevated silanol concentration at the surface make sol-gel glasses highly reactive, and therefore, their interaction with tissues is usually faster.

While bioactive glass particles, in micro and nano sizes, can be derived from both acid and basic catalysis, each approach yields different products. In acid-catalysis, the particles are usually obtained by mechanical separation, pulverizing the 3D glass in a mill. This process leads to highly irregular particles and broad distribution of sizes that must be sorted by sieving. The acid-catalysis approach may be considered unsuitable for nanoparticle fabrication because of the milling limitations to achieve nano-sized powders. In contrast, monodispersed uniformed nanoparticles are easily obtained in basic-catalysis. Although this approach has shown a more precise control of particle size and distribution, several concerns have been raised regarding nanoparticle composition, which shows discrepancies with the targeted system during synthesis. Other sol-gel-like strategies have been developed to gain control of size, morphology, dispersity, and composition, such as microemulsion, polymeric templates, and two-step catalysis, among others, complicating the synthesis process without providing a clear benefit. Nonetheless, the most adapted sol-gel strategy for bioactive glass nanoparticle production is still the Stöber method, a one-step polymer-free basic catalyzed strategy. To maintain maximum simplicity in the synthesis process, the Stöber method was followed in this project for nanoparticle fabrication, and therefore, other approaches are not discussed in this dissertation.

2.2.2. The Stöber method

In the late 1960s, Stöber *et al*. reported a pioneering synthesis method for uniform silica nanoparticles, where alterations in the pH, temperature, and reagent concentration can lead to silica particles with sub-micrometer (100−1000 nm) or nano (< 100 nm) sizes, with the simultaneous formation of aggregates for the latter [52,54,55]. The Stöber method has been adapted to synthesize BGNs, as these can be considered ion-doped silica nanoparticles [56–58].

The original Stöber method is a sol-gel strategy performed under highly basic conditions [52,59]. During synthesis, TEOS is added to a solution of water, alcohol, and ammonium hydroxide under agitation. Excess OH^- ions catalyze the hydrolysis and condensation reactions, promoting the nucleation of highly positively charged particles. The formation of the gel by particle aggregation is suppressed due to electrostatic repulsion between particles when the pH is above the isoelectric point of soluble silica.

2.2.2.1. Mechanism of particle growth

Like the traditional sol-gel process, the rates of hydrolysis and condensation control the nucleation and growth of Stöber-derived particles. Two models have been proposed to explain particle formation under elevated pH: the Lamer model [60] and the nucleation-aggregation model [61,62].

The Lamer model describes the burst nucleation of primary nanoparticles (~10 nm) as the alkoxide concentration reaches supersaturation [60]. The decrease in soluble alkoxide stops the formation of new nuclei and triggers particle growth by adding hydrolyzed monomer species onto the surface of primary nanoparticles. Monomer attachments are governed by the local structure described by

the reaction-limited monomer-cluster aggregation (RLMCA) model [52]. Briefly, the monomers (i.e., silica tetrahedra) collide with the clusters (i.e., primary nanoparticles) to sample potential bond sites at the surface to achieve particle growth. All clusters' sites are occupied with equal probability, giving rise to spherical particles [52].

Alternatively, the nucleation-aggregation model [61,62] predicts particle growth by aggregating small particles yielding larger ones that are more uniform [63]. Briefly, the primary particles are unstable due to their size, and the surface charge is insufficient to overcome the agglomeration of particles due to Brownian motion. The reagents concentration will rule the competition between the formation of new nuclei and their agglomeration in < 50 nm. The presence of multimodal size nanoparticles favors their re-structure by Oswald ripening, which describes the dissolution and re-precipitation of the unstable primary particles to be consumed by the larger, more stable ones, forming secondary particles (~ 50 – 250 nm) [64]. The growth of these secondary particles is explained again by RLMCA, although in this case, the primary or small secondary particles act as monomers [52]. This theory is supported by experimental observations where the surface of silica nanoparticles presented significant spherical-like topography features [52,62,65,66] instead of a smooth colloid surface [67–69]. Due to the limitations of each model to give a viable explanation of particle nucleation and growth at different stages of the process, the general scientific consensus states a combination of both mechanisms. The nucleation-aggregation model dominates the early stages of the process, while the Lamer theory is more accurate to describe the later stages of particle growth.

The critical factor for obtaining spherical, dispersed, and uniform nanoparticles is the surface charge [59]. Under elevated pH, particles develop a negative charge above the isoelectric point of silica, which causes repulsion between particles and, thus, monodispersity [52]. The introduction

of metallic ions to develop bioactive glasses can alter this surface charge and disturb the growing mechanism [55]. Therefore, the traditional Stöber method needs to be modified to address the need for metallic ion incorporation while finding alternatives to control particle size and dispersity.

2.2.2.2. Composition limitations in bioactive glass nanoparticles

The composition of bioactive glasses determines their structure and properties, and therefore, there is much attention on controlling the synthesis process to tailor the composition of the material for specific applications. The addition of network modifying metallic ion precursors in the synthesis process of silicate-based nanoparticles may impair the control over particle size, shape, and dispersity, even at low concentrations [70,71]. However, the main unsolved issue is the persisting discrepancy between the nominal composition and the actual one obtained after the fabrication process [56,72,73]. Specifically, the concentration of P and Ca^{2+} ions in BGNs, which are both key elements for osteoconductivity and bone-bonding, is consistently lower than that aimed [74].

The most frequently used precursors for incorporating calcium and phosphorous ions during sol-gel synthesis are triethyl phosphate (TEP) and calcium nitrate, respectively. The incorporation of P ions depends on the hydrolysis of TEP, usually performed in a solution already containing TEOS as the leading reagent for SiO_2. The low amount of P_2O_5 (mol %) in the final BGNs system has been attributed to the different hydrolysis rates between these two precursors, TEOS and TEP, under elevated pH, which causes the rapid condensation of SiO_2 nanoparticles lacking P ions [71]. In the case of Ca^{2+} ions incorporation, calcium nitrate's addition occurs after the hydrolysis and condensation of nanoparticles. In this process, Ca^{2+} ions cover the particles' surface by bonding to hydroxyl species and get diffused during calcination above 400 °C, thus modifying the network [75]. This mechanism results in deficient amounts of CaO (mol %) in the final BGNs system

resulting in a composition significantly different in the nominal one. Different reasons explain this outcome: the lack of sufficient hydroxyl groups at the nanoparticles' surface to bond with elevated concentrations of Ca^{2+} ions in solution or the low strength of these bonds, which cannot withstand the washing steps before the calcination [76]. Additionally, Ca^{2+} ions are likely to form other species, such as carbonate groups or calcium-rich components, without being adequately incorporated into the amorphous structure [70,72].

Different approaches have been explored to overcome these challenges. For example, the addition of calcium nitrate during the early stages of particle condensation allowed higher calcium detection by EDS, resulting in a drop in particle dispersity [71]. Additionally, it was unclear if the observed calcium was modifying the silica network of the BGNs as modifier ions or calcium was trapped as CaO molecules in BGNs, or forming calcium carbonate or calcium hydroxide molecules. Another approach reported the increase of the actual calcium concentration into the BGN network by increasing the Ca: Si ratio in the synthesis protocol beyond the expected ratio of the nominal composition [70]. The Ca^{2+} ion-supersaturated solution, along with the absence of the washes before calcination, resulted in the detection of higher calcium content as well as the formation of calcium-rich areas in the delivered BGNs [70,72]. Once these calcium-rich areas were removed, the measured amount of the CaO in the BGNs was only around 10 mol.%. Lately, Kesse *et al*. [77] have shown the effect of different concentrations of CaO content in BGN, adjusting their protocol to achieve 15.4 mol%, the maximum amount reached up to date in monodispersed submicron bioactive glass particles by a one-step basic catalyzed synthesis. Alternative calcium sources such as calcium chloride and calcium methoxy ethoxide have also been explored to improve the concentration of CaO in the BGNs; however, the secondary reactions with other reagents or their temperature sensitivity have made them unsuitable for the synthesis process [78,79]. The

compositional discrepancies in BGNs will be rectified in this thesis by optimizing a Stöber-like method to synthesize BGNs in the system SiO_2 –CaO–P_2O_5.

In addition to P and Ca, other functional ions may also be incorporated in BGNs; although, intermediate oxides have been barely observed in BGNs formulations. One strategy is to add all metallic precursors in the formation and growth of silica nanoparticles [50,51], while another is to incorporate the ions in silica nanoparticles through post-modification [80,81]. Despite the successful synthesis of multifold metallic ion BGNs, both methods still suffer from the limitations of high content incorporation and precise control of the composition. Therefore, more efficient methods are still demanded. In this work, the optimized Stöber method for ternary BGNs was adapted to incorporate intermediate oxides in monodispersed nanoparticles.

2.2.2.3. Properties of bioactive glass nanoparticles: morphology, size, and dispersity

The morphology and size of BGNs hold a significant effect on the final properties of the systems, as they are directly related to the exposed surface-area and, thereby, the surface reactivity of the material [30]. BGNs synthesized by an acid-catalyzed sol-gel process are usually irregular in shape and sizes as they are obtained by extensive milling. In contrast, Stöber-derived BGNs exhibit uniform sphere-like shapes as determined by particle growth mechanism [52,59]. Spherical shapes present advantages such as enhanced flow properties and more efficient drug delivery. The uniformity of the shape also facilitates the use of BGNs in medical applications by their integration in nanocomposites [28]. Therefore, the Stöber method is usually preferred for BGN synthesis. In terms of morphology, the mesoporosity of BGNs is also an interesting property for therapeutic delivery, as different factors, ions or molecules can be loaded within the core of the nanoparticle for specialized and localized delivery systems [82–84]. However, and in agreement with the

particle growth model, conventional Stöber-like BGNs are often non-porous. The use of polymeric templates like CTAB has been proposed as an alternative to tailor mesoporosity [83].

The size of BGNs is essential for their distribution in tissues and their integration as building blocks in nanocomposites [23,24,85,86]. In the Stöber method, the particle size is easily controlled with the processing parameters such as the concentration of TEOS, the ratio of H_2O/TEOS (known as the R-value), the concentration of the catalyst (i.e., ammonium hydroxide), or the temperature [72]. The effect of each variable is not completely clear, as most papers used different parameters, challenging the comparison of literature information. The most comprehensive reports providing information on processing parameters effects are Stöber *et al*. [66], Bogush *et al*. [87], Rao *et al*. [88], and Greasley *et al*. [72], who demonstrated the complex interdependency among all reaction parameters. As a general observation, particle size follows an inverse curve trend as a function of the water or ammonium concentrations. The particle size increases with the concentration of either solvent until it reaches an inflection point where a further increase of solvent concentration causes the slow decrease in particle size. The effect of temperature has not been systematically studied. Bogus *et al*. [87] and Park *et al*. [89] showed an unexpected monotonical decrease of particle size as temperature increases and reported that at low temperatures (T< 20ºC), monodispersity was not achieved. Rao *et al*. [88] correlated the effect of temperature with the role of the R-value. Particle size increase with temperature at high R values, whereas the opposite effects were observed for low R-values.

The dispersity of the nanoparticles is related to many parameters, especially particle size and composition. Larger BGNs (> 200 nm) usually exhibit better dispersity than smaller BGNs (< 100 nm), which tend to self-aggregate to reduce their surface energy [52,74,90]. The composition of BGNs also influences their dispersity. As previously mentioned, the incorporation of metallic

precursors changes the surface charge of primary nanoparticles during nucleation and growth, causing their aggregation [76,91]. Polymeric species may be introduced during synthesis to coat the surface of BGNs and exert a steric effect reducing their aggregation [92]. Nonetheless, polymers at the particle surface reduce their exposed surface-area and consequently influence BGNs reactivity. Therefore, the synthesis of highly disperse multifold ion BGNs, smaller than 100 nm remains a challenge. In this work, there is an emphasis on distinguishing agglomeration and aggregation of nanoparticles. In the former, BGNs form solid bonds and partial densification between their surfaces, while in the latter, the interaction is merely electrostatic. On this basis, the aggregation of BGNs is less concerning for medical applications as they can be easily detached in suspension before their use.

2.3. Physicochemical and biological properties of bioactive glasses particles

The immersion of bioactive glasses in fluids triggers their degradation, as the structure is not in equilibrium. Degradation occurs by the controlled release of ionic dissolution products, which may interact with cells, tissues, and bacteria. One of the most important reactions in bioactive glasses is the so-called mechanism of bioactivity, responsible for the tissue-material bonding, which will be reviewed in this section. The study of bioactive glasses *in vitro* and *in vivo* has demonstrated their ability for osteogenesis and angiogenesis as well as anti-microbial properties [31,93–95], all of which are presented here.

2.3.1. Mechanism of bioactivity: apatite formation

Bioactive glasses are well-known for their bone-bonding ability, result of forming a hydroxy-carbonate apatite (HCA) layer at the tissue-material interface [59]. HCA is a naturally occurring mineral that makes 60% of bone mineral content [96], with Ca and P as main components in a

atomic ratio close to Ca/P=1.67 [97]. HCA formation is a multi-step process that starts when the bioactive glass interacts with an aqueous solution, and stems from an ion exchange process induced by the instability of the highly energetic bioactive glass structure [7,8,39,98].

The mechanism of HCA formation is schematically presented in **Figure 5** [7]. First, network modifying cations (i.e., Na^+, Ca^{2+}) are exchanged with protons (H^+) from the solution, elevating the local pH. Second, as the degradation progresses, soluble silica from the cleavage of -Si-O-Si- bonds is released to the solution, forming a silanol (Si-OH) rich layer at the surface. Third, the silanol groups re-polymerize, creating an SiO_2 rich layer depleted in Na^+ and Ca^{2+}. Next, Ca^{2+} and PO_4^{3-} groups diffuse through the SiO_2 layer towards the surface, where they bond with soluble ions from the supersaturated solution to develop an amorphous Ca-P (ACP) layer. The ACP nucleation is a homogeneous and heterogeneous process due to the ionic interaction from different sources. Finally, the ACP layer crystallizes by incorporating OH^- and CO_3^{2-} groups from the solution, yielding the HCA layer. The apatite formation in BGNs follows a similar process to that in other macro-architectures. However, bioactive glasses of the same composition will exhibit faster HCA deposition in nanoparticle form due to the high surface reactivity. The small size of BGNs only allows the formation of needle-like apatite that cluster around individual nanoparticles.

The bone-bonding between bioactive glasses and tissue occurs due to the similarities of this HCA layer with a natural bone. Attachment and differentiation occur at the tissue-material interface as the HCA layer adsorbs growth factors that favor cell seeding.

The HCA layer formation depends mainly on three factors: bioactive glass composition, its structure, and the type of medium. The concentration of ionic species released to the solution is critical to induce the bioactive response [8,9,99]. Thus, the bioactive glass composition will

determine whether this critical concentration is achieved, whereas the structure (i.e., Q^n speciation) will determine the rate at which the response is triggered. The nature of the medium also influences the rate of deposition and the density of the layer. HCA formation has been observed in various mediums, such as phosphate buffer saline (PBS), TRIS-buffer, simulated body fluid (SBF), and cell culture medium. The concentration of the medium is key to achieving the supersaturation that leads to phase deposition.

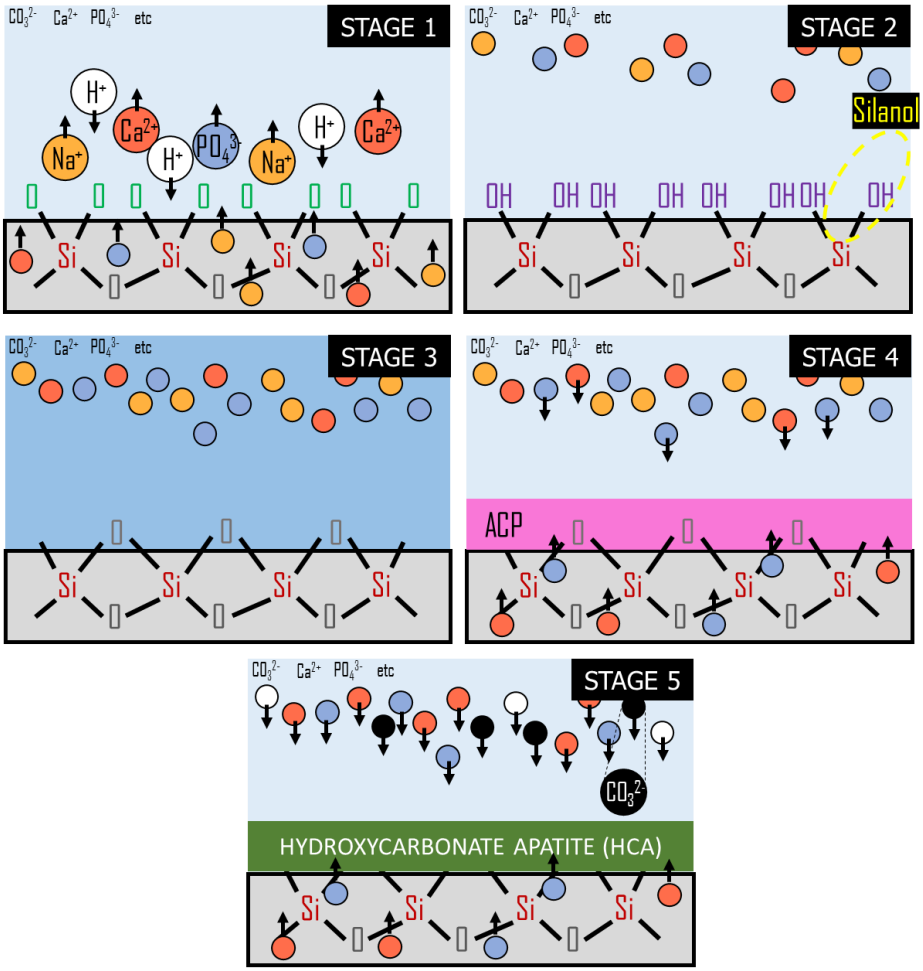

Figure 5: Schematic representation of the mechanism of bioactive in bioactive glasses as described by Hench [40]. Upon immersion in medium, bioactive glasses start to degrade by ion exchange (stage 1). The adsorption of protons leads to a silanol layer at the surface (stage 2) which re-polymerizes, forming a SiO_2-rich layer (stage 3). An amorphous Ca-P (ACP) layer nucleates at the interface from diffused Ca^{2+} and PO_4^{3-} from the core and the deposition of supersaturated (stage 4). The absorption of protons and carbonates causes the crystallization of ACP into hydroxycarbonate apatite (HCA), which is used as evidence of bioactivity expression (stage 5).

It should be mentioned that the formation of the HCA layer, while helpful, is not critical for bone regeneration. Instead, the fundamental mechanisms are related to the controlled release of ionic dissolution products from the degrading bioactive glass [31,40,100–102]. The ion release starts as soon as bioactive glasses are exposed to a fluid. At the early stages, a burst release of ions is commonly observed [103], which then progresses in a sustained manner, accompanying the glass's degradation. The initial burst release could cause a sudden rise of local pH value that may be lethal to either cells or bacteria [104], which should be looked for, especially in BGNs, due to their faster reactivity. The therapeutic effect is only achieved when the release period matches the time for specific cellular responses, and the ion is delivered within a specific concentration window.

2.3.2. Cytotoxicity and particle uptake

The cytotoxicity of bioactive glasses particles is directly related to the glass composition, the particle size, and dose delivered [73,93]. Understanding the effect of each of these parameters in the interaction between material and cells or tissues is critical towards their successful implementation in clinical applications [103,105]. The first step towards the characterization of the biological properties of bioactive glasses is performed at a cellular level by *in vitro* studies to understand the effect of degradation products on cell behavior. Then, the material can be tested *in vivo* at tissue or organ levels.

As previously mentioned, the key mechanism of bioactive glasses is related to the release of ionic dissolution products [8,9,31,40,100–102]. In this regard, the bioactive glass composition will determine its network connectivity and, consequently, its degradation rate. Bioactive glasses formed by multifold metallic ions are usually more reactive and degrade faster because of their low network connectivity.

The particle size also affects the degradation rate. For example, smaller particles, such as BGNs, degrade significantly faster than larger ones of the same composition owed to the higher surface area exposed [106,107]. The fast degradation may lead to rapid changes in the pH or saturation of ion concentration, both of which can be toxic to mammalian cells [108]. Particle size also influences their intracellular uptake, tissue distribution, and elimination [109,110]. For example, BGNs can diffuse through the cell membrane if their size is < 30 nm or internalized by phagocytosis if they are < 250 nm. Micro-sized particles (5 μm – 10 μm) can be engulfed by macrophages for their transport. In the current literature, there are many contradictions about the effect of particle size on cells. While the general public believes in their overall positive effect, some reports have shown that particles in the 10-30 nm range inhibited cell differentiation [111].

The concentration of particle treatment is probably the most significant parameter [112], as the dose administrated can lead to therapeutic or toxic effects similar to any other treatment in Medicine. For example, Tsigkou *et al*. [70] showed that increasing the BGNs concentration from 50 to 200 μg/mL caused a decrease in metabolic activity of bone marrow stem cells. The time of exposure also affects cytotoxicity. The continued degradation of the particles causes the accumulation of ions over culture time, beyond the concentration tolerated by cells [113,114].

2.3.3. Osteogenesis by bioactive glasses

Numerous animal studies have established the scientific basis for using bioactive glasses to repair orthopedic defects [7,115–117]. The bioactivity has been associated with the formation of the HCA layer [118] and the dissolution products [119], which exert control over the osteoblast cell cycle to regulate osteogenesis. This discovery revolutionized the approach of bone repair, shifting the focus from implants to replace bone to those that stimulate bone regeneration [120].

Osteogenesis occurs when osteoprogenitor cells receive the chemical stimuli to activate segments of their cell cycle like mitosis and differentiation [121,122]. The release of ion products [123], especially soluble Si and Ca, from bioactive glass degradation boosts the activation of genes without additional supplements like dexamethasone or bone morphogenetic protein (BMP) [124]. Therefore, to control the molecular biology of osteoprogenitor cells, the degradation profile of the bioactive glass must provide the critical ion concentration for osteogenesis. It is feasible to design bioactive glass particles with desired dissolution rates since they are influenced by the particles' composition, size, and morphology.

The capacity of bioactive glasses for osteostimulation has reached clinal practice in various bone graft applications such as in craniofacial and periodontal osseous defects [7,116,125]. Different bioactive glass compositions have been developed over the years, doping the structure with various ions to improve the bone-seeking properties (i.e., Cu, Zn, Sr) with promising osseointegration and angiogenesis, among other cellular pathways [126,127]. These treatments provide the additional benefit of a single-stage procedure, reducing patient discomfort and hospital costs. The structure of bioactive glasses has been doped with heavy metals like Ag and Au too for enhanced antibacterial properties [128,129]. Therefore, developing glass formulations to trigger significant bone remodeling while eradicating a bacterial infection. Despite their positive *in vitro* results, bioactive glasses doped with heavy metals have not been extensively studied *in vivo* [130,131]. The evaluation of the spectrum of action of Ag-doped bioactive glasses for antibacterial and regenerative applications is the ultimate goal of this dissertation.

2.3.4. Antibacterial properties

Inorganic materials have been introduced as a new strategy for preventing and treating infections as a direct result of the antimicrobial crisis. The inadequate use of antibiotics to treat all sorts of health conditions has encouraged the emergence and dissemination of drug-resistant bacteria [2,3]. Such antibiotic resistance is concerning to almost every region of the world, dismissing the effectiveness of currently licensed therapies [4]. Bioactive glasses are proposed as a superior alternative for long bone infection treatment [132] to mitigate the risk of antibiotic resistance. Although the antibacterial capabilities of bioactive glasses have been extensively demonstrated, there is not much information regarding the mechanism of action.

Allan *et al*.[133] and Zhang *et al*.[134] first reported the antibacterial activity of commercially available bioactive glasses, namely 45S5 and S53P4, which contain SiO_2, CaO, P_2O_5, and Na_2O. Since then, several works have joined their hypothesis on the intrinsic antibacterial activity of bioactive glasses consisting of two simultaneous actions: increase of pH and osmotic effect [135–137]. These traits have been attributed to BG's degradation process, which starts with the exchange of ions to form a HCA interface layer. During this ion release process, the media becomes supersaturated with alkali components, and therefore, it is not uncommon to observe an increase in pH above 9, which is toxic to microbiota [138]. The faster the ionic release, the more pronounced the pH increase, and consequently, a more substantial antibacterial effect will occur. This is one of the reasons why nanoparticles, which degradation is faster due to their high surface reactivity, are anticipated to show stronger antibacterial activity than their micrometer counterparts [104]. The Ca content in bioactive glasses may play a role in the inhibition mechanism. Bioactive glasses of higher Ca content present a higher antibacterial action [139,140] (i.e., 58S with 33 mol.% of CaO was more antibacterial than 63S with a 28 mol.% CaO). Mortazavi *et al*.[141] attributed this

antibacterial effect to a synergy between calcium and the hostile alkaline pH level. Although the pH value has been the main suspect for the antibacterial behavior of bioactive glasses, Gubler *et al*. [142] demonstrated that a mere pH raise was insufficient for proper antibacterial behavior and instead suggested an osmotic effect caused by the surrounding alkaline environment, as the leading antibacterial source. Regardless of which of these two was the dominant antibacterial mechanism, such remarkable changes in the media osmolarity and pH values may challenge eukaryotic cell survival [143]. Therefore, recent research has prioritized bioactive glasses formulations that maintain a neutral pH, even at the expense of losing antibacterial action.

Surprisingly, although a vast number of antibacterial mechanisms have been reported for other inorganic materials like heavy metal ions (e.g., cell-wall damage, disruption of protein synthesis, DNA condensation, inhibition of respiratory enzymes, or the production of reactive oxygen species (ROS)) [144,145], only the increase of pH and osmotic effect have been associated to bioactive glasses to date. This dissertation aims to provide new insights on the mechanisms that lead to bacterial destruction and elucidate the interactions between bioactive glass-ceramic particles and pathogens under different conditions.

2.4. Silver-doped bioactive glass particles

One of the major risks in using implants is the adherence and colonization of the surface by bacteria compromising the interaction between material and tissue, causing implant failure due to sepsis [146]. The use of heavy metal ions (e.g., silver, copper, zinc) against drug-resistant bacteria is a promising approach for efficacious treatment of infections since they have been demonstrated as a potent antibacterial agent [147–153]. However, the release of heavy metal ions in the body raises a general toxicity concern that prevents systematic use. It is well known that silver ions (Ag^+) act as broad-spectrum biocides against different Gram-negative and Gram-positive bacteria, including resistant strains. Over the past decades, research has been performed to understand various mechanisms by which Ag^+ causes bacteria death [147,153]. Due to this effect on bacteria, concerns about cytotoxic behavior frequently arise, and release in the human body raises a general toxicity concern that prevents systematic use [154]. The addition of Ag in bioactive glass structures confers long-lasting antibacterial properties while maintaining the intrinsic bioactive characteristics.

A wide range of Ag-doped silica glasses have been developed by sol-gel methods leading to multi-functional materials suitable for tissue engineering [129,141,155–162]. The incorporation of Ag may occur at the solution stage of the sol-gel or via ion-exchange in post-modification processes [130]. The synthesis approach determines the status of Ag within the structure. For example, the incorporation of Ag^+ during the sol-gel may cause its rapid oxidation and, consequently, reduce its antibacterial properties. While Ag^+ ions may be trapped within the bioactive glass by ion-exchange processes, their interaction with the structure may be weaker, leading to its uncontrollable release. In this dissertation, the Ag-doped bioactive glass formulation presented by Chatzistavrou *et al*. [163] (referred to as Ag-BG) was investigated in terms of bioactive and antibacterial properties. Chatzistavrou *et al*. [163] reported an optimized method for doping

bioactive glass microparticles in which Ag^+ ions were trapped by electrostatic attraction with $[Al_2O_4]^-$ tetrahedra. The incorporation of Ag^+ did not affect the material's degradation, which showed a similar profile for the release of ionic species in the bioactive glasses devoid of Ag (**Figure 6**). The release of Si and Ca increased with soaking time while P was delivered at a steady dose for up to a month. The released concentration of Ag^+ remained stable at 0.7 ppm after 8 days of immersion, which is within the therapeutic window of 0.1 ppm – 1.6 ppm that delimit the minimum concentration for antibacterial effect and the maximum tolerated by mammalian cells, respectively. Therefore, this system is predicted to hold potential antibacterial action while preserving the bioactive properties of the structure. Based on the results obtained in dental tissues [15,163], this Ag-doped bioactive glass system is predicted to behave similarly in bone tissue. However, the capability to support *in vivo* bone regeneration is yet to be demonstrated and will be addressed in this dissertation. Such study would also fill an important gap in the literature since very few works on bioactive glasses doped with heavy metals have studied their properties *in vivo* [130,131].

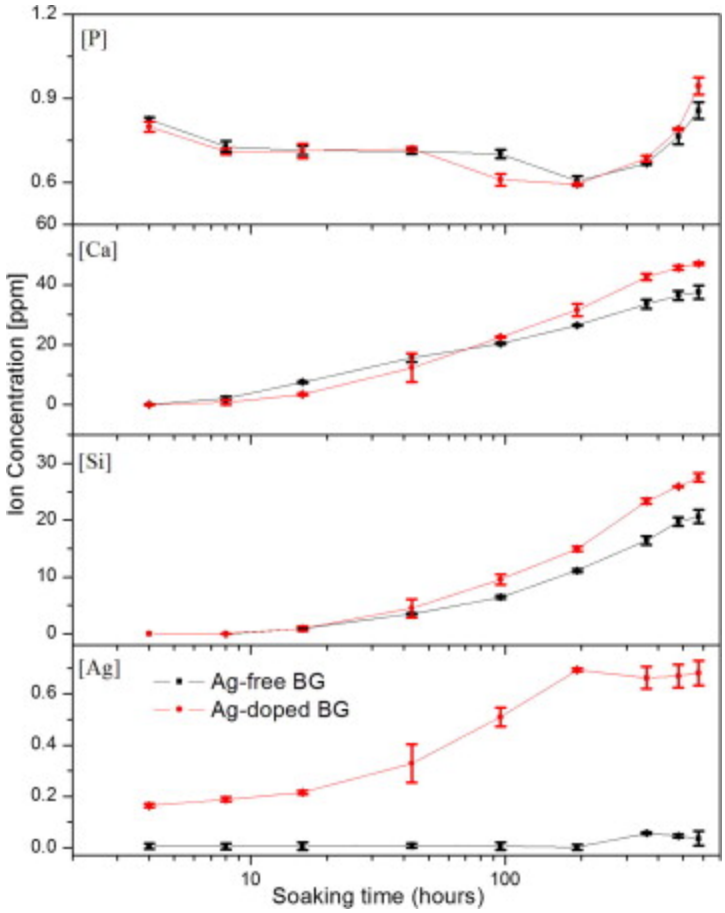

Figure 6: Ion release profile of the Ag-BG microparticles developed by Chatzistavrou *et al*., reproduced from [163].

2.4.1. Effect of silver incorporation on the structure and properties of bioactive glasses

The structure of the bioactive glass is determined by the role of each cation within the network. Ag is a known network modifier; however, its effect on the structure would depend on the overall composition of the glass [164]. For instance, when Ag is introduced at the expense of a network former, the network connectivity will increase, whereas introducing Ag at the expense of another network modified of higher valency will increase the network connectivity.

The incorporation of high amounts of Ag may lead to the precipitation of metallic silver and tricalcium phosphate crystals within the glass [165–167]. The presence of these precipitates

decreases network connectivity by disturbing the continuity of the network. The presence of silver has also been associated with a viscosity reduction, decreasing the total pore volume while broadening the pore size distribution [168].

Several studies have shown that silver doping does not affect the *in vitro* bioactivity of the glass nor the formation of the HCA layer. However, the interaction of Ag^+ ions with the salts from the medium may cause the additional deposition of AgCl crystals [156]. There would be a competition between the deposition of AgCl and HCA, where higher Ag content will tend to favor the former [160,169]. Additionally, Ag^+ ions may bind to the PO_4^- ionic species in solution, forming silver phosphate nanoclusters that act as nucleation sites for ACP. Interestingly, the release of Ag^+ ion can also facilitate the early supersaturation of the medium, decreasing the critical concentration of other ionic species for HCA deposition [156].

2.4.2. Synergistic combination with antibiotics

As indicated by their name, combinatorial therapies consist of treating an infection with two or more antibacterial agents. The purpose of applying multiple components is to increase the effectiveness of the treatment by reaching multiple bacterial targets. Synergy occurs when the combination of multiple components amplifies the effect each of them has independently and allows the reduction of each agent's dose to achieve an equivalent antibacterial effect. One of the most potent effects of synergistic combinations is the potential to restore the effectiveness of old antibiotics against bacteria that have previously developed resistance against them [170]. This approach allows the recycling of antibiotics that had been discarded due to antibiotic resistance. In the last 20 years, there has been increased attention to this approach, especially when the

antibiotics are combined with inorganic materials (**Figure 7**), where material science has been key for the engineering of metallic and ceramic structures with antibacterial properties.

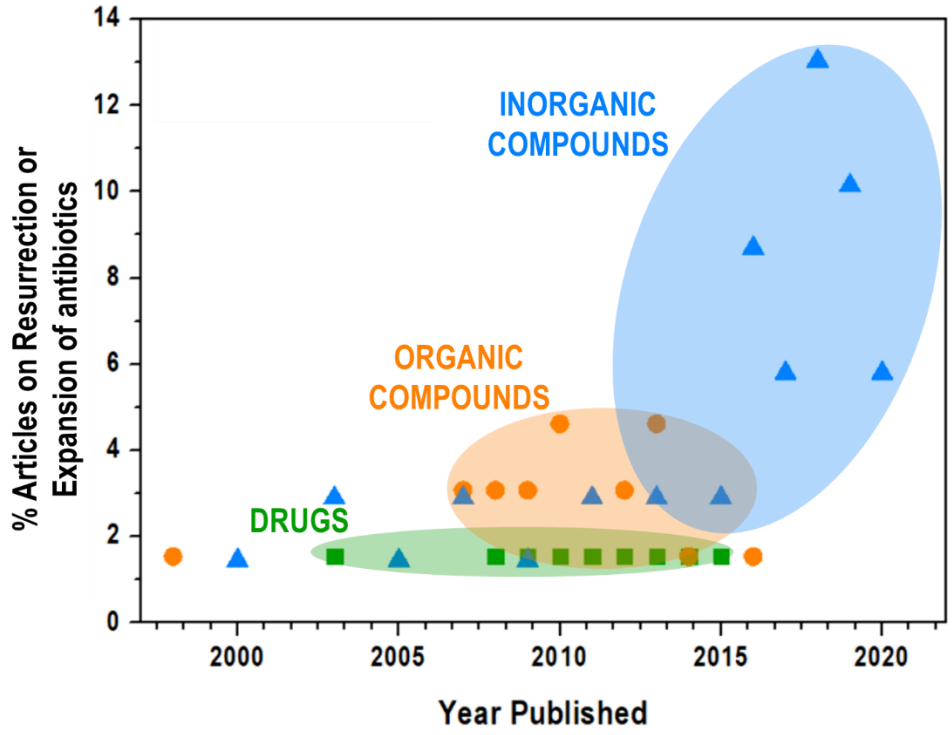

Figure 7: 20-year evolution of research work in the resurrection of antibiotics by combinatorial therapies with drugs, organic compounds, and inorganic compounds.

Although most of the research has been performed in combinatorial therapies with heavy metals [171–174] or metal oxides [175–180] owed to their broad antimicrobial effect, the restorative effect has also been observed in some ceramic structures such mesoporous silica nanoparticles [181] and calcium-phosphates [182,183]. This restorative property has not been reported for bioactive glasses. Therefore, this dissertation will prioritize investigating the antibacterial properties of bioactive glass particles combined with ineffective antibiotics to target multi-resistant pathogens.

2.5. Fabrication of bioactive glass/polymer nanocomposites: injectable devices

Bioactive glass/polymer composites have been presented as a new family of materials for tissue engineering [184,185]. The combination of bioactive glass particles and biodegradable polymers can eliminate their individual disadvantages and exhibit properties that are more than the sum of their parts [184,186,187].

The size of the filler particles is a critical parameter that affects the homogeneity and stability of the composite, due to molecular interactions [188]. Monodispersed BGNs are usually preferable since their small size facilitates a better integration in the matrix [23,184]. Additionally, nanoparticles induce nanostructure features on the final scaffold that mimic the structure of natural bone. For instance, the hierarchical architecture of bone presents nano-scaled HA crystallites in a collagen-based matrix [23]. The polymer matrix selection must also attend to biocompatibility requirements and ideally present composition and structure that is attractive for cellular responses. For example, natural-based materials such as chitosan or silk have been successfully used as matrices to prepare nanocomposites [189,190]. Natural-based hydrogels (i.e., collagen and extracellular matrix) are polymeric materials characterized by their high water-uptake capacity [191,192]. Their structure can resemble a 3D extracellular matrix network found in tissues [10], enabling cell attachment and nurture through species' transport across the pores [193–195]. Hydrogels can be conveniently shaped or structure into various geometries, making them ideal candidates for injectable applications. However, they lack mechanical stability and consistency across different batches [191,196,197]. The clinical use of injectable composites lies in the minimal invasive administration that eliminates the need for an operation [198,199]. The composite is injected into the area of interest, filling the damaged site rapidly where it polymerizes, providing a 3D network to support tissue regeneration [200]. On this basis, natural-based hydrogels

were selected as dispersing matrices for the developed Ag-BGNs to design a straight-forward injectable device for infected bone defects.

The development of bioactive glass/polymer nanocomposites must consider the size and amount of filler, as it certainly influences the rheological properties of the system. The addition of BGNs to the hydrogel solution can lead to two scenarios: nanoparticles are dispersed but do not interact with the matrix or chemically bond to the polymeric chains. The nanocomposite's structural properties are influenced by these interactions, affecting the degree of crosslinking of the polymer [201].

The amount of filler may also alter the polymer's hydrophilicity, increasing its degradability [202]. For instance, it is possible to observe nanoparticle aggregation within the matrix, resulting in mechanical stability deterioration [23]. The poor cross-linking of the matrices due to excessive filler may cause liquid-solid phase-separation and, consequently, the unintentional distribution of the implant outside the defect [200,203]. Wang *et al*. [204] showed that when the BGNs concentration is optimum, the polymeric network became more ordered and channel pores preferentially aligned, and several other studies are congruent with the stiffening effect of particle incorporation in polymers [205]. Therefore, it is imperative to address the nanoparticles' monodispersity to ensure it is maintained during the nanocomposite processing. The degradation profiles of the organic and inorganic phases are probably the most important consideration in injectable nanocomposites for medical applications. The degradation of both materials should coincide at comparable rates to maintain the structural and mechanical integrities [23,201]. The release of ions from the BGN degradation can have a significant influence on the polymeric material. Nguyen *et al*. [206] reported that the released Ca^{2+} ions could be incorporated into the polymeric network reinforcing its structure and resistance to degradation. Other work described

the decelerated acidic degradation of the polymer due to local pH rise [207]. These observations suggest the degradation rate of the nanocomposite may be modulated by varying the glass/polymer ratio. Understanding the interaction between BGNs and hydrogel is key for an optimized design. In this thesis, the design and synthesis of nanocomposites were addressed to provide a proof-of-concept in the capabilities of the system. The in-depth characterization of the polymer-glass interaction was beyond the scope of this work.

2.6. Conclusions and research objectives

The capabilities of bioactive glasses in tissue regeneration have been extensively demonstrated in the literature. There is an increasing interest in multi-functional systems that sum new properties to biological behavior. Bioactive glasses have been studied for antimicrobial applications focusing on the outcomes without supplying information about the inhibition mechanism. Doping the bioactive glass with Ag^{+} can boost the antibacterial properties. Ag-doped bioactive glasses have also shown encouraging *in vitro* results. However, the current research lacks evidence regarding its ability to support *in vivo* regeneration. The presence of Ag can also be exploited for the restoration of antibiotics. Nonetheless, this functionality in bioactive glasses is yet to be explored. Finally, nanotechnology has attracted attention to advance the biological and antibacterial behavior of bioactive glasses. The Stöber method, routinely applied for silica nanoparticle synthesis, has been adapted for BGNs synthesis, complicating the fabrication process without providing any clear improvement. The major challenge in Stöber-like methods is, without a doubt, the incorporation of metallic ions in monodispersed < 100 nm size BGNs. Acknowledging these research gaps, this project is founded on the following research objectives:

Aim 1: Evaluate the functionalities of Ag-BG microparticles in osteoprogenitor cells.

- Challenge: Control the Ag-BG degradation to support cell behaviors without adverse effects due to Ag^{+} ions release.
- Approach: Study the degradation profile and Ag-BG interaction with fibroblasts *in vitro* to understand the effect of Ag-BG treatment on cell viability, proliferation, and differentiation. The regenerative potential will be investigated by filling critical calvaria defects in small animals.
- Expected outcome: Based on previous studies for odontology, Ag-BG is not expected to cause cytotoxicity but instead promote tissue re-growth to heal the defect.

Aim 2: Investigate the potential of Ag-BG to combat resistant pathogens like Methicillin-Resistant *Staphylococcus aureus* (MRSA).

- Challenge: Develop a system able to debilitate or even eradicate an infection while reducing the risk of resistance development. Such a system must also maintain a robust bioactive behavior.
- Approach: Identify the minimum dosage required for inhibition and explore the bacteria-material interaction under different conditions to elucidate the inhibition mechanisms.
- Expected outcome: Based on the antibacterial activity against oral bacteria, Ag-BG is expected to cause inhibition of MRSA. The mechanisms of inhibition are anticipated from the degradation products of the bioactive structure, as they have been key for all the other functionalities.

Aim 3: Study the capability of Ag-BG to restore the action of antibiotics against antibiotic-resistant bacteria.

- Challenge: Determine the type of ineffective antibiotics that can be recycled, recovering their effectiveness, by combination with Ag-BG and optimize the Ag-BG: antibiotic ratio.

- Approach: The Ag-BG microparticles will be combined with antibiotics that MRSA resists or tolerates at high concentrations to evaluate how their different inhibition mechanisms can synergize. Additionally, Ag-BG will be used as an antibiotic depot, loading one of the previously characterized antibiotics to expand the synergistic capability to single-unit treatment.
- Expected outcome: Previous works have suggested the synergism between bioactive glasses and antibiotics. However, this would be the first time a bioactive glass system is used to restore antibiotics. The use of Ag-BG as an antibiotic carrier is anticipated to provide controlled delivery of substances for long-term antibacterial action.

Aim 4: Advance the biological and antibacterial capabilities of Ag-BG microparticles by down-scaling the system to nano-sized (i.e., Ag-BGNs).

- Challenge: Incorporate multi-fold metallic ions at the desired concentration in BGNs through simplified Stöber-like methodologies.
- Approach: Ternary system BGNs will be developed, optimizing the incorporation of P and Ca within the structure by performing a comprehensive study of the synthesis parameters. Then, the method will be modified to develop Ag-BGNs, which biological and antibacterial properties will be addressed and compared to the micrometer counterpart.
- Expected outcome: The incorporation of metallic ions is expected to challenge the control over particle size and dispersity as higher concentrations are attempted. The Ag-BGNs are anticipated to degrade faster due to the surface reactivity providing an earlier therapeutic response.

Aim 5: Explore a possible clinical delivery mechanism for Ag-BGNs employing injectable nanocomposites to develop a minimally invasive treatment for bone defects.

- Challenge: The homogeneous distribution of Ag-BGNs, which tend to aggregate to reduce their surface energy without disturbing the polymerization of the matrix.
- Approach: Nanocomposites will be synthesized using natural-hydrogel matrices. The effect of Ag-BGNs in the polymerization will be addressed by incorporating different concentrations, and the biological and antibacterial properties will be evaluated to understand the changes in the release of degradation products.
- Expected outcome: Ag-BGNs are anticipated to monodisperse in the matrix as it limits nanoparticle mobility. Considering the high-water capacity of the hydrogels, a densified solid nanocomposite is not expected even at low Ag-BGNs concentrations. The presence of the polymer is hypothesized to delay the biological and antibacterial action of the system.

3. EXPERIMENTAL METHODS AND TECHNIQUES

3.1. Development of Ag-doped bioactive glasses

3.1.1. Materials for bioactive glass synthesis

The synthesis of the various bioactive glasses was performed with a combination of the following reagents, as specified in their respective synthesis protocols (section 3.1.2 and 3.1.3): analytical grade tetraethyl orthosilicate (TEOS), triethyl phosphate (TEP), calcium nitrate tetrahydrate (CaNT), aluminum nitrate nonahydrate (AlNT), silver nitrate (AgNT), potassium nitrate (KNT) and sodium nitrate (NaNT). The solvents used were distilled water, 2N nitric acid (HNO_3), ethanol 200 proof, methanol, and 28% ammonium hydroxide (NH_3OH). All reagents were purchased from Millipore Sigma in the United States and used as received without further purification. The reagent dissolution process was carried out under a fume hood using Teflon beakers and magnetic stirring. The beaker mouth was covered with two layers of aluminum foil and parafilm to prevent solvent evaporation, contamination, and cross-reactions with the environment.

3.1.2. Sol-gel synthesis of bioactive glass microparticles

Ag-free bioactive glass (BG) with a composition of SiO_2 58.6–CaO 24.9–P_2O_5 7.2–Al_2O_3 4.2–Na_2O 2.1–K_2O 3 (wt.%) and Ag-BG with a concentration of SiO_2 58.6-CaO 24.9-P_2O_5 7.2-Al_2O_3 4.2-Na_2O 1.5-K_2O 1.5-Ag_2O 2.1 (wt.%) were synthesized in the form of microparticles. The sol-gel technique was acid-catalyzed utilizing 2N HNO_3 and distilled water as solvents. The fabrication protocol consisted of the combination of the solution stage of a 70 (vol.%) of a 58S bioactive glass (SiO_2 58 –CaO 33–P_2O_5 9 (wt.%)) with 30 (vol.%) of another sol-gel glass-ceramic with a composition of SiO_2 60 –CaO 6–P_2O_5 3–Al_2O_3 14–Na_2O 7–K_2O 10 (wt.%) or SiO_2 60 –

CaO 6–P_2O_5 3–Al_2O_3 14–Na_2O 5–K_2O 5 Ag_2O 7 (wt.%), for BG and Ag-BG, respectively, as previously described elsewhere [16]. After combination, the solution was homogenized at 400 rpm before a heat treatment, which consisted of several stages. First, drying the solution at 60 °C for 65 h, and 90 °C for 10 h, and then, aging at 180 °C for 20 h increasing the temperature with a heating rate of 5 °C/min. Second, stabilization took place in three steps: (1) at 400 °C by increasing the temperature with a heating rate of 0.3 °C/min, (2) at 600 °C with a heating rate of 0.2 °C/min for 10 h, and (3) at 700 °C with a heating rate of 0.4 °C/min for 20h. Finally, the material was cooled down to 25 °C with a cooling rate of 5 °C/min. The resulting material was dried ball-milled in a jar using zirconia balls with a 3:1 mass ratio of zirconia balls: bioactive glass for 2 days, and sieved with a mesh size of 20 μm. Both Ag-BG and BG were collected in powder form with a particle size < 20 μm and stored in a desiccator to prevent oxidation. The structural and morphological characterization of these BG and Ag-BG microparticles has been previously reported by Chatzistavrou *et al*. [16,163]. The highlight of their findings can be found in section 2.4.

3.1.3. Modified Stöber methods for bioactive glass nanoparticles

BGNs with a nominal composition of SiO_2 62 -CaO 34.5 -P_2O_5 3.2 (mol. %) were prepared using one-step catalysis in basic pH. The synthesis protocols are illustrated in **Figure 8**. Two solutions were initially prepared. Solution A contained 41.6 mL of solvent, 5.55 mL of TEOS, and 0.5 mL of TEP and was stirred for X_1 amount of time. The optimization of the stirring time X_1, required for incorporating P ions in BGN, is presented in **Figure S1** (Appendix A). Solution B was used to catalyze the reaction and was prepared with differe nt concentrations of ethanol, NH_3OH, and distilled water to evaluate their effect on the final product. The ratios of the reagent concentrations

(in molarity, M) in Solution B are summarized in **Table 2**. All processes were performed at room temperature under vigorous agitation (~ 500 rpm).

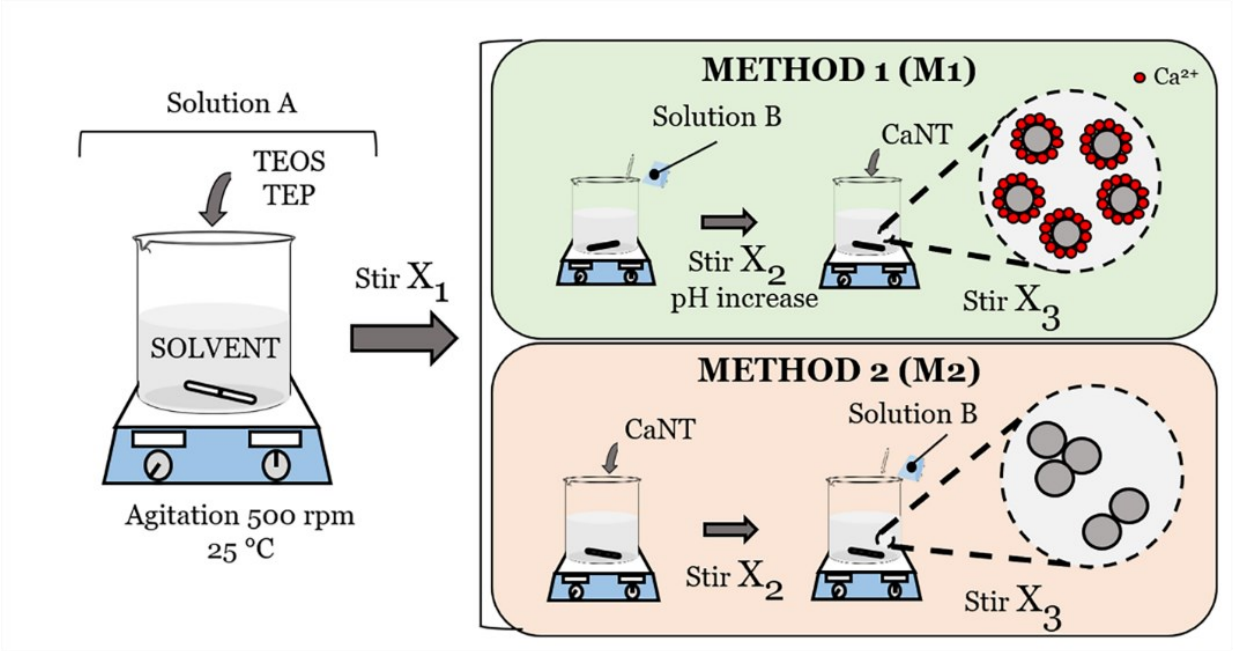

Figure 8: Layout of the modified Stöber methods for the synthesis of ternary system BGNs.

Method 1 (M1) has been previously reported by Zheng *et al*. [74] and is utilized here as a reference. Briefly, Solution B was poured into Solution A and stirred for 30 min to trigger particle nucleation before adding 3.14 g of CaNT. The solution was homogenized for 2 h before collecting the BGN. The effect of the solvent type was also investigated by using ethanol (M1-P1 as described by the Zheng *et al*. [74] protocol) or methanol (M1-P2) as an alternative solvent in Solution A. On the contrary, Method 2 (M2) studies the effect of changing the order in which CaNT is added to Solution A. In this case, methanol was used as the solvent because of the advances shown in M1-P2. The 3.14 g of CaNT was directly added to Solution A, which was then stirred for X_2. Particle collection occurred once Solution B was added and stirred for 24 h. The effect of the stirring time after catalysis (X_3) on particle composition and size for M1 protocols was not evaluated in this

project as other research groups have extendedly explored it. However, the effect of X_3 on particle size and composition was studied for the novel M2 protocols, and is reported in **Figure S2** (Appendix A), using M2-P1 as representative approach.

The fabrication of Ag-BGNs in the system SiO_2 59.6-CaO 25.5-P_2O_5 5.1-Al_2O_3 7.2 - Ag_2O 2.2 (wt.%) was carried out, modifying the M2-P1 approach detailed above since it allowed the most control in terms of particle size and size distribution. After the preparation of Solution A, AlNT was added to form $[Al_2O_4]^-$ tetrahedra. Then, AgNT was pulverized and introduced in solution to electrostatically bond Ag^+ ions with $[Al_2O_4]^-$ tetrahedra to trap Ag^+ within the nanoparticles. Lastly, CaNT was added to minimize the interaction of Ca^{2+} with $[Al_2O_4]^-$ tetrahedra, and therefore, ensure enough $[Al_2O_4]^-$ units were available to accommodate Ag^+. A stirring time of 24 h was allowed in between the addition of each of the three nitrates. Finally, and following M2-P1, Solution B was incorporated to trigger particle nucleation for 24 h.

Table 2: Synthesis parameter of M1 and M2 ternary-BGNs synthesis protocols, including the type of solvents and their concentrations and stirring times. Green shading with bold fonts indicates the key differences in the protocols.

Protocol	M1-P1	M1-P2	M2-P1 and Ag-BGNs	M2-P2 A	M2-P2 B	M2-P2 C
Solvent Type *(in Solution A)*	**Ethanol**	Methanol	Methanol	Methanol	Methanol	Methanol
H_2O (M) *(in Solution B)*	12.7	12.7	12.7	**7.3**	**7.3**	**7.3**
Ratio of H_2O *(in Solution B)* / TEOS *(in Solution A)*	55.9	55.9	55.9	**32.2**	**32.2**	**32.2**
Ratio of NH_4OH *(in Solution B)* / TEOS *(in Solution A)*	5.3	5.3	5.3	5.3	5.3	5.3
Ratio of H_2O/Ethanol *(in Solution B)*	1.1	1.1	1.1	**0.56**	**0.56**	**0.56**
Stirring X_1 (h)	24	24	24	24	**48**	24
Stirring X_2 (h)	**0.5**	**0.5**	24	24	24	**48**
Stirring X_3 (h)	**2**	**2**	24	24	24	24

After stirring time X_3, all particles were collected by centrifuging at 3000 rpm for 3 min and then, dried at 60 °C for 6 h, calcinated at 700 °C for 2 h with a heating rate of 2 °C/min, and cooled down to room temperature at a cooling rate of 5 °C/min. The powder obtained was pulverized and washed with ethanol twice to remove calcium-rich areas [72] and air-dried before characterization. The resulting powder was stored in a desiccator.

3.2. Characterization of particle structure and surface features

3.2.1. Scanning electron microscopy and energy dispersive spectroscopy

A scanning electron microscope (SEM) produces an image by focusing an electron beam with voltages in the range of 5 – 30 keV at the surface of a solid specimen with spatial resolution ~ 4

nm [208]. This beam passes through a series of electromagnetic lenses that allow the user to focus on the desired area of study. The inelastic interaction between the beam and the surface of the specimen causes the emission of various signals like the secondary electron, backscattered electrons, and x-rays, among others, that reveal information of morphology, topography, crystalline structure, and chemical composition. The specimen's morphology and topography can be examined with the secondary electrons that escape from the top 5-50 nm thickness of the sample. To obtain the most information on the surface, SEMs are operated at voltages in the range of 3-10 keV. The elemental distribution and chemical composition are obtained from the emitted x-rays, which can come from up to microns in depth from the specimen surface. The energy of these x-rays is specific for each atom, allowing their identification. SEMs can come equipped with energy-dispersive spectroscopy (EDS) detectors capable of collecting these x-rays energy. The sensitivity of EDS (~ 130 eV) is its more significant limitation compared to other elemental analysis techniques since it challenges the identification of some elements due to overlapping of their energy spectra and their detection for concentrations below 0.1 (wt. %) [209]. The beam is set-up with higher voltage (15-30 keV) and lower beam currents (bigger spot sizes) to maximize the EDS signal. Castaing´s formula (**Equation 4**) can be used to calculate the analytical area (z_m) in EDS [210]:

$$z_m = 0.033\ (E_0^{1.7} - E_c^{1.7})\frac{A}{\rho Z} \qquad \textbf{Equation 4}$$

where E_0 is the accelerating voltage (kV), E_c is the minimum emission voltage (keV), A is the atomic mass, ρ is the density (kg/m^3), and Z is the atomic number.

The morphological, topographical, and elemental analysis of the bioactive glass particles was performed in a JEOL 7500 SEM equipped with an Oxford EDS system. The specimens were

prepared by spreading the pulverized powder in carbon tape mounted on aluminum-based stubs. A metallization process with either Pt or Os (30 s or 5 s, respectively) was performed on all SEM samples to avoid electron changing due to the glass's insulating nature. The SEM was operated at 5 keV for imaging. EDS was used as a semi-quantitative tool to assess the composition of the particles, and therefore, verify the incorporation of metallic cations. The elemental analysis was performed at 15 keV and 10 kX magnification, in agreement with the Scientific Working Group for Materials Analysis guidelines for the elemental analysis of glass. Additionally, the selected voltage for EDS provides an analytical area, based on **Equation 4**, of around 4 μm (considering ρ ~ 2.7 kg/m$^{3)}$, which is enough to obtain a representative spectrum of the particles' bulk composition.

3.2.2. Transmission electron microscopy

The transmission electron microscope (TEM) forms a projected image of the sample by collecting the electrons that passed through it. In TEM, the electron beam is operated at higher voltages than SEM, usually in the range of 100-300 keV, which yields a spatial resolution of ~ 0.2 nm [211]. The electron beam must be able to penetrate the specimen to produce an image, and therefore, only ultra-thin samples (< 100 nm) can be observed. After penetrating the specimen, part of the beam is transmitted (following its original path) or scattered. Both transmitted and scattered signals travel through electromagnetic lenses to provide different information from the specimen.

On one hand, bright field images are formed with the transmitted beam, showing a dark specimen in a bright background. The contrast observed arises mainly from mass-thickness variations. On the other hand, the dark field image uses diffracted beams, resulting in the specimen appearing bright, where the different contrast indicates changes in the diffraction angle. Scattered electrons

are collected on a single point when they travel through the lenses (i.e., back focal plane of the objective lens), which can be utilized to form the image of the selected area diffraction (SAD) pattern. If the specimen area is crystalline, the pattern shows sharp spots or defined rings, whereas if the area is amorphous, the pattern is formed by diffuse rings. The interplanar spacings can be determined from the distance between the transmitted beam and diffracted spot/ring in the SAD pattern by following the mathematical approximation of Bragg's Law (**Equation 5**) for TEM-SAD (**Equation 6**)[212]. Phase identification is possible by comparing the calculated interplanar spacings with those recorded in the Inorganic Crystal Structure Database (ICSD).

$$n\lambda = 2d \sin\theta \qquad \textbf{Equation 5}$$

$$d = \frac{\lambda L}{R} \qquad \textbf{Equation 6}$$

where d is the interplanar spacing between crystal planes, λ is the wavelength of the energy source used, n is the order of the spectrum, L is the camera length, θ is the angle of incidence, and R is the distance between the diffraction spot and the transmitted beam.

Particle size, shape, and dispersity were investigated in a JEOL 1400 Flash TEM operated at 100-120 keV. The structure was also characterized by the SAD patterns collected. The specimens were prepared by either of the following routes:

- Dispersion in medium: 10 µL of 1 mg/mL particles in ethanol dispersion were pipetted on the surface of carbon-coated copper grids 200 mesh.
- Dispersion in resin: ~ 0.5 mg of particles were dispersed in 200 µL of Spurr resin (EM0300, Electron Microscopy Sciences) and then solidified in a block-mold at 60 °C overnight. The block was trimmed and sectioned using an RMC MYX

ultramicrotome (Leica), collecting sections of 70 - 100 nm thickness in copper grids 200 mesh.

3.2.2.1. Imaging analysis of particle size

Particle size and size distribution were determined using ImageJ (NIH, USA). The images were processed to binary conversion (**Figure 9**) and then analyzed with the software. TEM images of magnifications between 10-20 kX were processed to collect the nanoparticles' representative measurement. The sizes reported resulted from measuring at least 300 particles per sample.

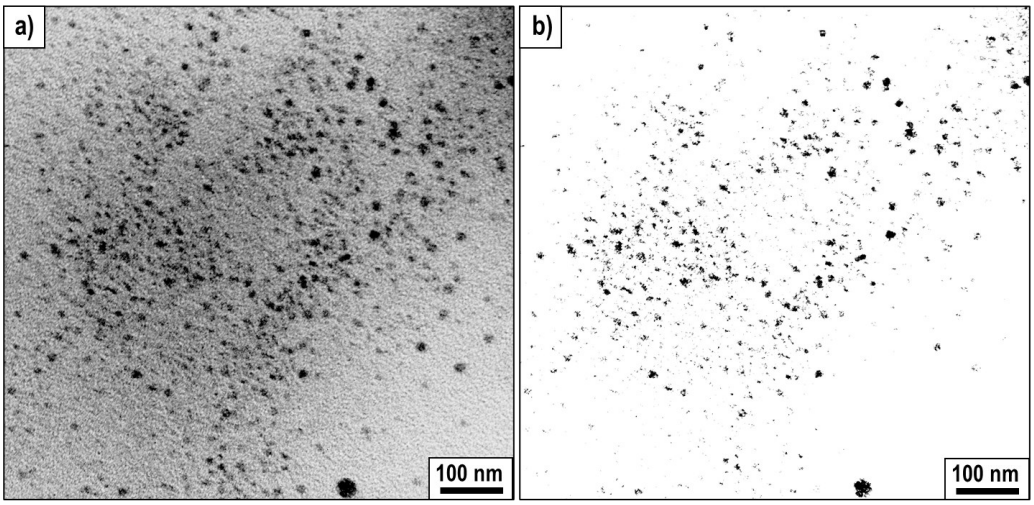

Figure 9: TEM image transformation from original (a) to binary (b) for particle size measurement

3.2.3. Dynamic light scattering and zeta-potential

Dynamic light scattering (DLS) is a well-established technique for measuring the size and size distribution of particles dispersed in a liquid. A monochromatic laser beam (argon laser source, λ= 6330 Å) incidences a suspension and gets scattered when it reaches a particle due to the Brownian motion, defined as the random movement of particles in a solvent [213]. The angle of scattering varies with particle size according to the Stokes-Einstein relationship [214], which enables the

system to categorize particles based on their dimensions and provide a distribution of their sizes. Highly diluted particle solutions are required to minimize particle aggregation and, therefore, obtain reliable data. The temperature also needs to remain stable during the measurement since it will affect the Brownian motion.

The zeta-potential is used to estimate the surface charge of nanoparticles and determine the stability of the nanoparticle suspension using an electrophoresis method. Particles in suspension attract ions forming a charged Stern layer around their surface [215]. The zeta-potential takes the charge difference between the dispersion medium and this Stern layer by applying an electric field through the suspension to induce particles' movement. The zeta potential values above +25 mV or below -25 mV usually present higher colloidal stability, whereas values between -25 and +25 mV typically lead to aggregation due to van der Walls interparticle attraction [216]. The most critical factors for zeta-potential measurement are the pH and temperature of the medium.

Dispersions of particles with a concentration of 1 mg/mL in milli-Q water (pH 7.0 at 25 °C) were ultrasonicated for 10 min before their analysis in a DLS system equipped with a lased Doppler (Zetasizer- nano series, Malvern Instruments Ltd). These measurements, performed in collaboration with Dr. Xuefei Huang's group from the Department of Chemistry at MSU, were carried out at an angle perpendicular to the incident laser. The data were collected with 3 min scans.

3.2.4. Fourier transform infrared spectroscopy

Fourier transforms infrared (FT-IR) spectroscopy is used to identify organic and inorganic compounds in the sample. In this technique, infrared radiation (10000 – 100 cm^{-1}) is used to excite the covalent bonds with a dipole moment within the material. The radiation absorbed by the

specimen is converted to vibrational energy (in wavenumber units), the fingerprint of every molecule. The resultant spectrum is usually recorded from 4000 – 400 cm^{-1}.

In this project, a Jasco FT-IR–4600 was used to evaluate the chemical bonds forming the particles' glass structure at different stages. The specimens were prepared by fine pulverization of powder before evaluation in attenuated total reflectance (ATR) mode in the range of 2000 – 400 cm^{-1} with a resolution of 1 cm^{-1}.

3.2.5. X-ray diffraction

X-ray diffraction (XRD) is a non-destructive technique used to characterize the structure of a material providing information of its nature (crystalline or amorphous), phases, texture, and grain size [217]. A monochromatic x-ray beam (usually from Cu Kα source, λ= 1.5406 Å) hits the specimen, creating constructive interferences when the x-rays scatter at specific angles according to Bragg's Law (**Equation 5**) [212]. The XRD pattern is characteristic of the periodic atomic arrangement in each material, and therefore, can be used for phase identification by comparison with tabulated standards in the ICSD.

The particles' crystalline-amorphous structure was characterized using a Rigaku Smartlab XRD System in Bragg-Brentano mode, operated at 40 kV and 44 mA. The diffraction patterns were collected from $15 < 2\theta < 90$ ° with a resolution of 0.1 °2θ. The background was fitted using an exponential function, and the peak positions were re-defined using shift axial displacement to correct errors. The specimens were prepared by spreading an even layer of fine pulverized particles in a glass holder.

3.2.6. Solid-state nuclear magnetic resonance

Solid-state magic-angle spinning nuclear magnetic resonance (MAS-NMR) holds value in studying the environments of specific nuclei and is used in Materials Science to determine the chemical structure of certain materials. NMR operates under the principle of nuclei's magnetic properties. When an external magnetic field is applied in specific pulses of radiofrequency to the sample, the nuclei get excited, and their spins shift away from equilibrium, therefore varying their magnetic orientation [218]. When the spins return to equilibrium, the excess energy released induces currents at specific resonant frequencies. The precise frequency is correlated to the nucleus electron shielding and can give information about its local environment. For example, in the case of silica-based glasses, NMR enables identifying the coordination number of the tetrahedra (i.e., Q^4, Q^3, etc. units).

In this project, the coordination of silicon and aluminum was evaluated with a Varian Infinity-Plus 400 MAS-NMR. Samples were spun in a 5-6 mm probe at 4-5 kHz for a spectrometer frequency set to 79.49 MHz for ^{29}Si and 104.16 MHz for ^{27}Al. All spectra were collected by the Max T. Rogers NMR facility staff at MSU, using a proton enhanced cross-polarization (CP) method with a pulse length of 1 ms and 4 ms for ^{29}Si and ^{27}Al, respectively. Recycle delay between successive accumulations was 0.2 s – 100 s, and the total number of scans was 17,000 for all spectra.

The network connectivity (NC) was estimated from the Q^n speciation (%) obtained by peak Gaussian peak deconvolution of the NMS spectrum. The experimental NC was obtained from the Q^n ratio (**Equation 7**). The NC was also calculated from theoretical models (**Equation 8**) based on the composition of BGN in (mol.%) detected by SEM-EDS and considering the role of each ion in the network. As mentioned before, ions can form BO acting as network formers or create

NBO modifying the network. For example, Si and Ca act as a network former and a network modifier, respectively. Phosphorous can appear as orthophosphate (Q^0) and forming Si-O-P bridges (Q^1). Orthophosphates are associated with an increase in silicate polymerization and, therefore, act as network formers [37], whereas Si−O−P bridges decrease the network connectivity of the glass modifying the network [38]. Because of the low level of P in the synthesized BGNs (62 Si/3 P) and its preferable chemical bonding to form orthophosphate units, the overall effect of Si−O−P bridges in the presented BGN system would be minimum. Thus, the theoretical model based on **Equation 8** assumed that P was present only as orthophosphate, neglecting the small percentage of phosphorous in Si−O−P bridges [219–225]. Although it is beyond the scope of this project, note that a more exact approximation of the theoretical model would require ^{31}P MAS-NMR studies to determine the distribution of P in orthophosphate and Si-O-P bridges.

$$Experimental\ NC = \frac{Q^2}{Q^3} = \frac{Q_H^2 + Q_{Ca}^2}{Q^3} \qquad \textbf{Equation 7}$$

$$Theoretical\ NC = \frac{BO - NBO}{bridges} = \frac{4[SiO_2] - 2[CaO] + 6[P_2O_5]}{[SiO_2]} \qquad \textbf{Equation 8}$$

The coordination of aluminum in Al^{IV}, $Al^{V,}$ or Al^{VI} species was used to determine the status of Ag in Ag-BGNs.

3.2.7. Nitrogen adsorption/desorption

N_2 adsorption-desorption is a routine method to obtain information about surface area, porosity, and pore size distributions in samples using the Brunauer-Emmet-Teller (BET) method [226]. Briefly, the process consists of filling the pores of the sample with liquid N_2. When the pressure is increased, N_2 condenses, changing the overall total volume. The volume of gas adsorbed to the

surface is calculated at various pressures, giving an isotherm curve characteristic of specific porosity, pore size, shape, etc. These different isotherms have been classified in the International Union of Pure and Applied Chemistry (IUPAC) database, a tabulated reference for data analysis.

The isotherms of the M2-P1 BGNs were collected by Dr. Calabrese-Barton's group at MSU, operating an ASAP 2020 Micrometrics machine at 77 K. The fine powder was outgassed for 16 h at 200 °C under high vacuum. The total pore volume was estimated from the adsorbed amount of N_2 at a relative pressure of 0.995.

3.2.8. Ultraviolet and visible light spectroscopy

UV-Vis light spectroscopy measures the light absorption at different wavelengths in the spectrum to determine the relationship of conjugation to color. The appearance of several absorption peaks or shoulders at different wavelengths gives information of highly conjugated systems (i.e., single, double, etc. bonds). Therefore, it can be used to identify the status of specific elements.

In addition, when the light beam passes through a liquid sample, its intensity gets attenuated. This attenuation can be related to the solution's concentration as described by Beer-Lambert's law [227]. Thereby, the solution's concentration can be calculated by measuring its absorbance or optical density (OD).

The solid-state UV-Vis spectrum of Ag-BGNs was collected with a Lambda900 spectrometer from 350-600 nm with a resolution of 1 nm to determine the chemical status of Ag in the structure.

3.3. Degradation of bioactive glass particles *in vitro*: bioactive response

3.3.1. Reagents for *in vitro* degradation analysis

The degradation of the particles was evaluated by their immersion in PBS, Dulbecco's modified-Eagle's medium (DMEM), or SBF. PBS and DMEM pH 7.4 at 37 °C were purchased from Life Sciences and preserved at 2 °C while SBF was prepared following Kokubo's recipe [228].

The SBF preparation required sodium chloride (NaCl), sodium hydrogen carbonate ($NaHCO_3$), potassium chloride (KCl), dipotassium hydrogen phosphate trihydrate ($K_2HPO_4 \cdot 3H_2O$), magnesium chloride hexahydrate ($MgCl_2 \cdot 6H_2O$), calcium chloride ($CaCl_2$), sodium sulfate (Na_2SO_4), Tris-hydroxymethyl aminomethane: ($(HOCH_2)_3CNH_2$) (Tris), 0.93 M Hydrochloric Acid (HCl) and distilled water. The composition of SBF as described by Kokubo *et al*. [228] is presented in **Table S1** (Appendix D). All reagents were purchased from Millipore Sigma and used without further purification.

3.3.2. pH evolution

The immersion of particles in media triggers the ionic release. The resulting alkaline environment causes fluctuations in the pH that can be a potential hazard for biological applications. Therefore, particles were pulverized and dispersed in either PBS or DMEM at a 5 mg/mL concentration. The suspensions were maintained at 37 °C, and the pH was monitored with an Orion Star A210 pH-meter.

3.3.3. Apatite-forming ability

The *in vitro* bioactive behavior of the particles was assessed qualitatively in terms of the apatite-forming ability with an immersion test in SBF, which reproduces the composition of blood plasma. Particle suspension (3.33 mg/mL) was placed in an incubator at 37 °C under agitation (175 rpm). The solution was centrifuged after 3, 7, and 14 days to collect the particles. Ethanol washes were used to stop the ion-exchange reaction before drying the particles at 37 °C. The presence of the HCA layer was evaluated with a combination of the following techniques: SEM-EDS, TEM-SAD, FT-IR, or XRD.

3.4. Characterization of material-cell interaction *in vitro*.

3.4.1. Experimental conditions and set-up for biological studies

The cell-material interaction was studied with an indirect exposure test, utilizing polycarbonate transwells with a 0.4 µm porous membrane bottom (Millipore Sigma) to hold the particles in 24-well plates.

The two different cell culture media recipes used in these experiments are listed below:

- Growth media: α-MEM supplemented with 16% fetal bovine serum, 1% Antibiotic-Antimycotic (Gibco 15,240,062), and 1% L-glutamine.
- Osteogenic media: α-MEM supplemented with 8% fetal bovine serum, 1% Antibiotic-Antimycotic, and 1% L-glutamine, supplemented with 25 µg/mL ascorbic-acid-2-phosphate, 5 mM beta-glycerophosphate, and 100 nM of dexamethasone.

All experimental data collected was analyzed in collaboration with Dr. Kurt Hankenson's group at the University of Michigan, and the analysis was conducted with the guidance of Dr. Yadav Wagley.

3.4.2. Sample preparation for biological studies: pre-conditioning of particles

As previously mentioned, the release of ionic species from glass structures can lead to sharp changes in the pH, hazardous for cells. The pH evolution assessment showed concerning pH values (i.e., above pH 8.5) in the first 3-4 days of immersion. Therefore, all particles were pre-conditioned by suspension in DMEM at a 5 mg/mL concentration for 4 days to prevent the cell's exposure towards the burst ionic release. After pre-conditioning, particles were centrifuged, were with ethanol, and dried at 60 °C. Then, the powder was disinfected with UV radiation for 2 h before the experiment.

3.4.3. Cell culture preparation

Primary human bone-marrow-derived stromal cells (hBMSC) were purchased from the Institute of Regenerative Medicine, Texas A&M University. Frozen vials of cells were thawed and propagated in growth media (3000 cells/cm^2), maintaining the cultures in a humidified 37 °C/5% CO_2 incubator. Cells were expanded to 80-90% confluence and were used in passage 4 or 5. The health and confluence of the cells were monitored with an optical microscope. At the time of seeding, cells were enzymatically lifted from culture dishes using trypsin and then centrifuged for 5 min at 1200 rpm. The pellet was resuspended in fresh media, and cells were plated at specific densities (**Table 3**) by pipetting 0.5 mL/well. Seeding was allowed for 24 h before exposure to different treatments. The pre-conditioned particles were suspended in 0.5 mL of culture media and transferred to the transwells (**Figure 10**).

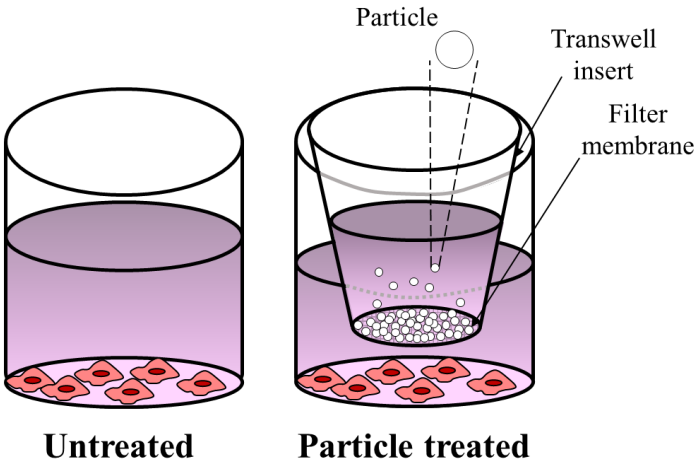

Figure 10: Experimental set-up for material-cell interaction assays. The sketch represents the wells at 0 h of treatment.

Table 3 summarizes the particle treatments studied in this project. The final volume per well was 1 mL of media, which was fully refreshed every other day. The effect of the treatment was compared to a positive control consisting of cells immersed in culture media (untreated).

Table 3: Experimental groups for the *in vitro* cellular bioactivity of particles.

Sample	**Cell proliferation**				**Cell differentiation**		
	Mass (mg)	Cell density (cell/well)	Time point (days)	Assay	Mass (mg)	Cell density (cell/well)	Time point (days)
Ag-BG	2.5, 5, 7.5, 12.5	$30 \cdot 10^3$	2, 4, 6	MTT	5, 7.5, 12.5	$30 \cdot 10^3$	10
Ag-BGNs	5, 10, 20	$15 \cdot 10^3$	2, 4, 6	CCK-8	5, 10	$15 \cdot 10^3$	14

3.4.4. Cell proliferation

Cell metabolic activity and, consequently, cell viability and proliferation were assessed following colorimetric methods (Millipore Sigma) upon availability (**Table 3**).

- MTT assay is a destructive approach to measure cell metabolic activity. At each time point, 500 µL of MTT solution was added to each well and allowed 4 h at 37 °C for its cleavage to formazan crystal. Then, 500 µL of the solubilizing solution, containing dimethyl sulfoxide, was added and incubated for 24 h to dissolve the crystal, staining the solution. The OD_{570} of the formazan dye for each tested group was measured using a UV-Vis spectrometer (section 3.2.8), as it provides a direct correlation to the concentration of cells.
- WST-8 assay, also known as CCK-8 assay, is a non-destructive approach to measure cell metabolic activity. At each time point, 100 µL of CCK-8 solution was added to each well and allowed 3 h at 37 °C for its bioreduction by cellular dehydrogenases to formazan. Similar to the MTT assay, the OD_{460} of the formazan is correlated to the number of living cells.

3.4.5. Cell differentiation

Cell differentiation to osteoblasts was evaluated in terms of gene expression and cell mineralization. **Table 3** summarizes the studied groups and the experimental parameters.

3.4.5.1. Gene expression

Gene expression is a dynamic process occurring during the lifespan of a cell to control its function, which also affects cell morphology. It is controlled by a series of transcription factors encoded in the DNA that serve as activators or repressors when bound to regulatory elements on genes. The

expression of osteoblastic genes like bone sialoprotein (*BSP*), osteocalcin (*OCN*), Runt-related transcription factor 2 (*RunX2*), osterix (*OSX*), osteomodulin (*OMD*), aggrecan (*ACAN*), collagen alpha-1(x) (*COL10A1*) was evaluated using quantitative reverse transcription-polymerase chain reaction (qRT-PCR). Cells were maintained in the osteogenic medium as specified in **Table 3**, fully refreshed every other day. A high-capacity cDNA Reverse Transcription Kit (Applied Biosystems) was used to reverse transcribe 300 ng of RNA extracted from cells after exposure to cDNA in a 20 µL reaction. The cDNA (1 µL) was amplified using Power SYBR® Green PCR Master Mix and gene-specific primers (**Table 4**) in a 7500 Fast Real-Time PCR System (Applied Biosystems) following manufacturer's instructions. Relative expression ratios were normalized to the geometric mean of glyceraldehyde 3-phosphate dehydrogenase (*GAPDH*). Then, the gene expression of the untreated cells was normalized to a value of 1 to compare with the expression in particle-treated cells.

Table 4: List of primers used in qRT-PCR for human genes.

Primer Name	Direction	Sequence (5'-3')
GAPDH	Sense	TGGTATCGTGGAAGGACTCATGAC
	Antisense	ATGCCAGTGAGCTTCCCGTTCAGC
BSP	Sense	ACAACACTGGGCTATGGAGA
	Antisense	CCTTGTTCGTTTTCATCCAC
OCN	Sense	CACCGAGACACCATGAGAGC
	Antisense	CGGATTGAGCTCACACACCT
OSX	Sense	GCTTGAGGAGGAAGTTCACTAT
	Antisense	GCTTCTTTGTGCCTGCTTTG
OMD	Sense	TCCAAGAAATTTGGAACACC
	Antisense	TGACCATTAGTGCTTCGTTG
ACAN	Sense	ACTCTGGGTTTTCGTGACTCT
	Antisense	ACACTCAGCGAGTTGTCATGG
Col10A1	Sense	ATGCTGCCACAAATACCCTTT
	Antisense	GGTAGTGGGCCTTTTATGCCT

3.4.5.2. Alizarin red staining

Cell mineralization is a commonly occurring process in osteoblast differentiation, where the cells produce vast extracellular calcium deposits. Alizarin red staining (ARS) is a destructive technique used to identify calcium-containing osteocytes since their combined reaction has a bright red stain. The intensity of this stain is directly proportional to the concentration of calcium minerals in the cell culture.

The capability of particles to induce cell mineralization was studied under two growth conditions (growth medium and osteogenic medium) for Ag-BG microparticles and only with osteogenic medium for Ag-BGNs (**Figure 11**). The immersion of these types of particles in a medium triggers

the deposition of calcium-rich phases (i.e., HCA) at their surface, which could interfere with the reading of calcium from osteocytes. Wells containing only Ag-BG without hBMSC (acellular) served as a control in the ARS assay to verify cell mineralization. After the desired exposure time, the transwells were removed, and 500 µL of ARS solution in water (Millipore Sigma) was added for 30 min to the wells. The monolayers were dissolved using 500 µL of 10 % acetic acid, and the OD_{405} of the dyed solution was measured with a UV-Vis spectrometer. The OD_{405} corresponding to untreated cells was normalized to 100 % to analyze and compare the cell mineralization induced by particle-treated cells.

Additionally, particles used for cell treatment were collected at the end of the experiment to analyze the apatite-like phase formation. All particles were washed with ethanol and dried at 60 °C for 2 h before analysis. The morphology and elemental composition, and structural differences were characterized by SEM-EDS and FT-IR according to the procedures explained in sections 3.2.1 and 3.2.4, respectively.

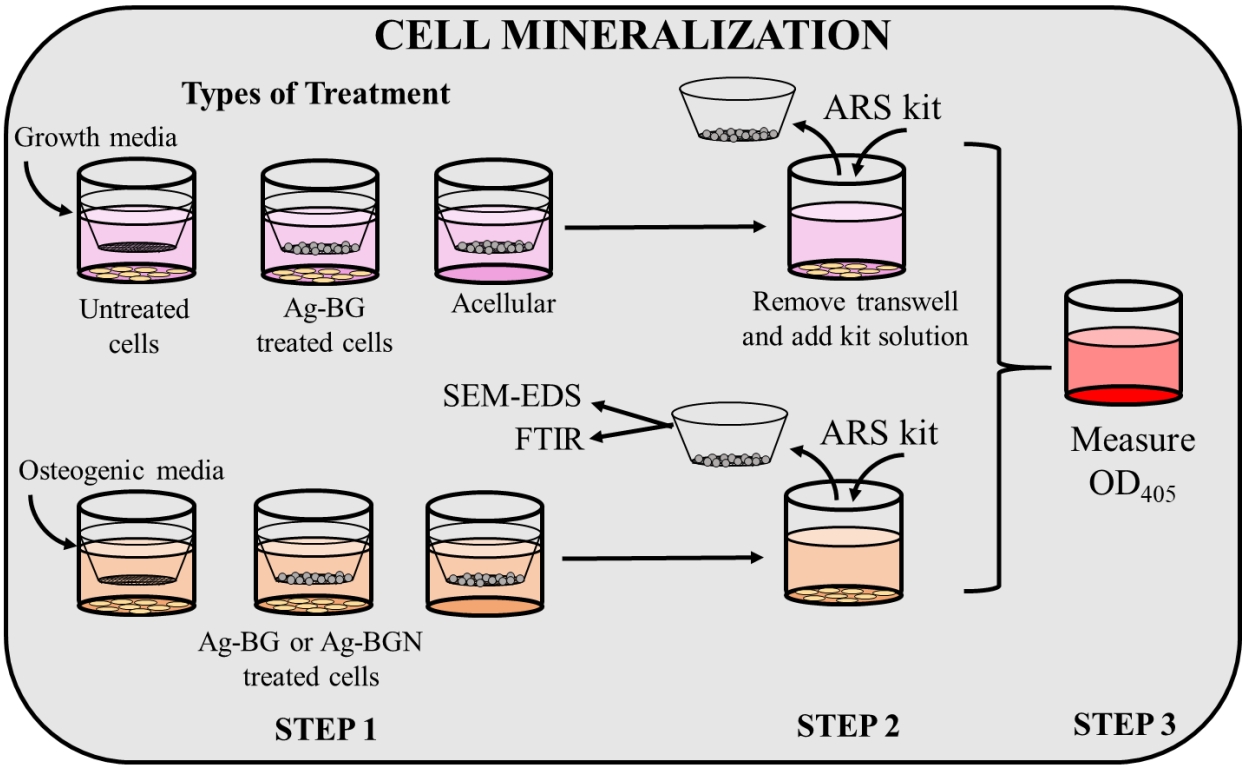

Figure 11: Experimental procedure layout for the evaluation of cell mineralization.

3.4.6. Transmission electron microscopy for cell-containing samples

The internalization of Ag-BGNs after the cell mineralization test for 14 days in the osteogenic medium was evaluated using TEM and compared to untreated cells. The transwells were removed, and the cell monolayers were washed twice with water to remove the nanoparticles not engulfed by the cells. Then, the monolayers were fixed inside the 24-well plate with 4 % paraformaldehyde in PBS overnight at 2 °C. After fixative removal, the monolayers were washed three times with PBS for 10 min each. Post-fixation was performed with 1 % of osmium tetroxide in PBS for 30 min following three washes in PBS for 10 min each. Dehydration was performed in series of ethanol (35, 50, 75, and 100 %) for 5 min each. After dehydration, ethanol was substituted for propylene oxide, which served as an intermediator between alcohol and resin. The monolayers were covered with propylene oxide for 15 min, refreshing the solution twice. Then, infiltration was

performed with a dilution of Poly/Bed®812 resin and propylene oxide (1:1 and 2:1) for 30 min at room temperature. Embedding in 100% resin was allowed overnight in the fridge keeping the plate lid opened. The resin was substituted before polymerization at 60 °c overnight. The resin layers were collected by mechanical separation of the wells from the plate using a hammer and chisel (**Figure 12** a). The walls of the wells were removed with flat pliers. The resulting disks were immersed in liquid N_2 for 1 min to separate the resin sample from the culture plate's plastic bottom (**Figure 12** b). The samples were cut with razor blades and glued with epoxy to blank blocks (**Figure 12** c). The fragment was oriented so that the face of the piece previously attached to the well's bottom is upwards. Finally, sectioning of the blocks across the length (z-direction) was performed in agreement with section 3.2.2. The 100 nm sections were collected in a 200 mesh Cu-grid (**Figure 12** d) and then positive stained in 2 % uranyl acetate for 5 min and lead citrate for 3 min before observation at 100 kV.

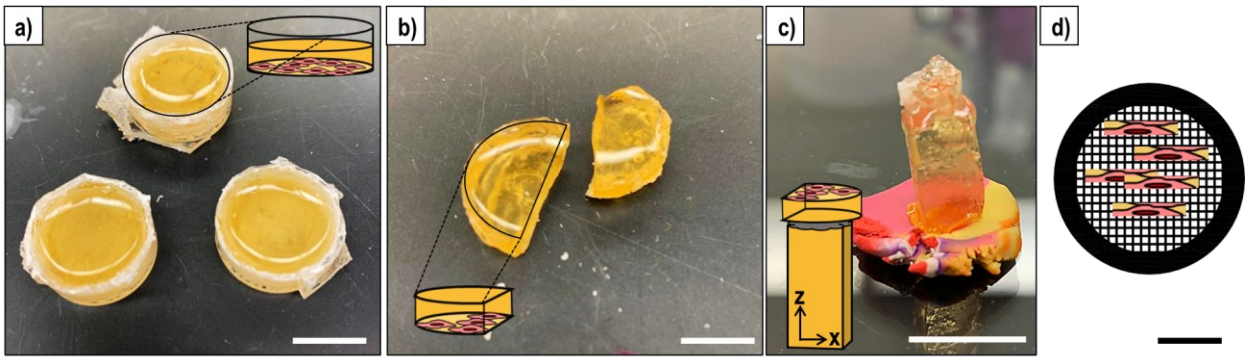

Figure 12: Schematic preparation of resin block for TEM eukaryotic cell sample observation. (a) Mechanically separated wells. (b) Fragmented resin layers were collected from the wells by immersion in liquid N2. (c) Final resin block for ultra-thin sectioning sitting on modeling clay. The drawings are used to identify the location of the cells during the sample preparation. The ultra-thin sections cut in the z-direction were collected in a 200 mesh Cu grid. Scale bars represent 10 mm (a-c) and 1 mm (d).

3.5. Characterization of particle-tissue interaction for *in vivo* bone regeneration

3.5.1. Implant sample preparation

The implant samples consisted of collagen sponges (Pfizer Gelfoam), sectioned to a 3 mm diameter size, loaded with a slurry of particles suspended in 40 µL PBS or natural extracellular matrix (ECM) hydrogel (from urinary bladder matrix) [229]. Particles were precondition as described in 3.4.2 and loaded into the sectioned sponges by pipetting the slurry solution before clinical implantation. As negative controls, the sponges were humidified with the corresponding solvent (i.e., PBS or ECM). The experimental conditions for each studied group, including final particle mass implanted and sample size, are summarized in **Table 5**. All the experimental data collected were analyzed in collaboration with Dr. Kurt Hankenson's group at the University of Michigan.

Table 5: Experimental group evaluated for *in vivo* bone regeneration. Shading indicates different materials tested, with a darker color for particle-containing samples

Samples	Mass (mg)	Number of mice	Harvest time
Ag-BG/PBS	10.5	5	30
PBS	0	5	30
Ag-BG/ECM	10.5	5	30
ECM	0	5	30
Ag-BGN/PBS	10	8	40
PBS	10	7	40

3.5.2. Surgical procedure and sample harvest

6-month-old mice on a C57B/L6 background were randomly assigned an experimental treatment. The number of mice per group is presented in **Table 5**. Mice were anesthetized in isoflurane, and

defect sites were aseptically prepared. Bilateral 3 mm defects on each mouse's parietal bones were created using a Mectron Piezosurgery drill with an OT11 osteotomy bit under saline irrigation [230]. The implants were transferred to each defect (**Figure 13**) using tweezers and spatula, and the skin was closed using 3M™ Vetbond™ surgical adhesive (3M Science Applied to Life.™). After surgery, the mice were injected subcutaneously with a narcotic analgesic consisting of 0.1 mg/kg of buprenorphine hydrochloride every 12 h for the following 48 h.

At the time of harvest, mice were euthanized by CO_2 asphyxiation followed by cervical dislocation for the calvaria biopsies. Then, the bone samples were fixed in 4 % paraformaldehyde for 24 h and rinsed with water before analysis.

All experiments were conducted under the University of Michigan animal care and use committee's oversight and following the National Institute of Health guide for the care and use of laboratory animals (NIH Publications No. 8023, revised 1978).

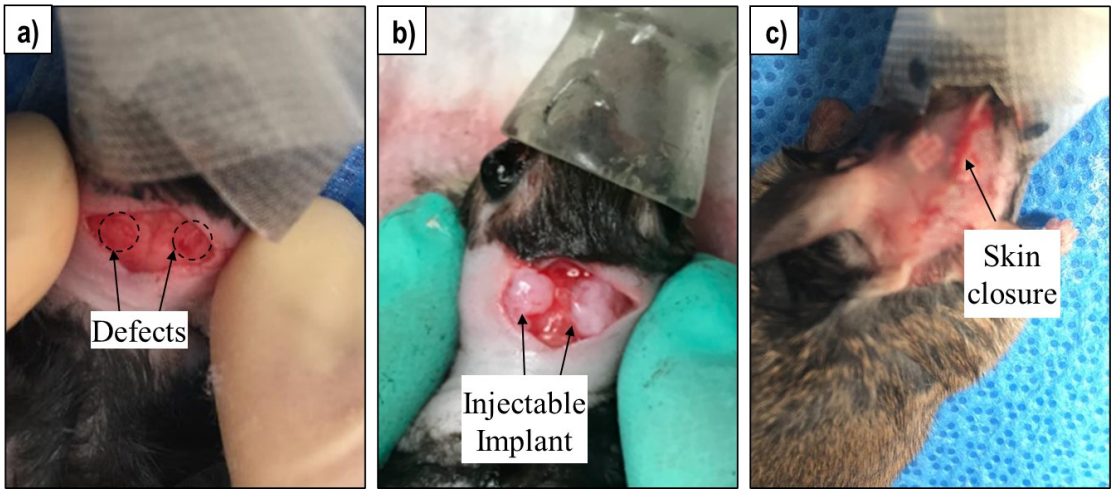

Figure 13: Surgical schematic procedure on calvaria defect model: (a) drilled defects, (b) defects filled with an injectable collagen implant, and (c) skin would closure with liquid stitches.

3.5.3. Assessment of post-surgical bone tissue

The presence of new bone in the harvested calvaria was evaluated with two techniques for complementary data validation. First, samples were imaged with micro-computed tomography (micro-CT) and then histologically assessed.

3.5.3.1. Micro computed-tomography

Micro-CT is a non-destructive x-ray imaging technique that can provide accurate and precise volume measures since it reconstructs a sequence of individual images to produce a 3D model of the sample. Image resolution varies from 1-20 μm/voxel since they are usually collected at accelerating voltages of 70-225 kV [231]. Micro-CT has been adapted for routine evaluation of skeletal specimens in small-animal imaging. Specifically, for quantifying bone growth in the volume of interest, given the density differences made by thresholding. Therefore, the thresholds and density unit values applied during the analysis play a key role in the outcome and must be carefully selected to account for the bone voxels of various densities.

In this project, the calvaria was scanned in an eXplore Locus Micro-CT (GE Healthcare) or Scanco μCT50, at 55kV and 145 μA. Images were collected with a resolution of 8 μm^3, and an integration time of 800 ms and then analyzed in Parallax Microview software. The formation of new bone in the cranial defect was assessed using a 2.9 mm diameter x 2 mm high cylindrical region of interest center on each defect. The threshold value was selected based on the intensity histogram of a region of interest containing the entire calvaria (**Figure 14** a). Voxels for very low density were excluded from the analysis. Bone and water arbitrary density units (ADU) were selected from the intensity of a line profile scanned through the undamaged bone (**Figure 14** b), where bone intensity is the maximum peak detected and water is the baseline.

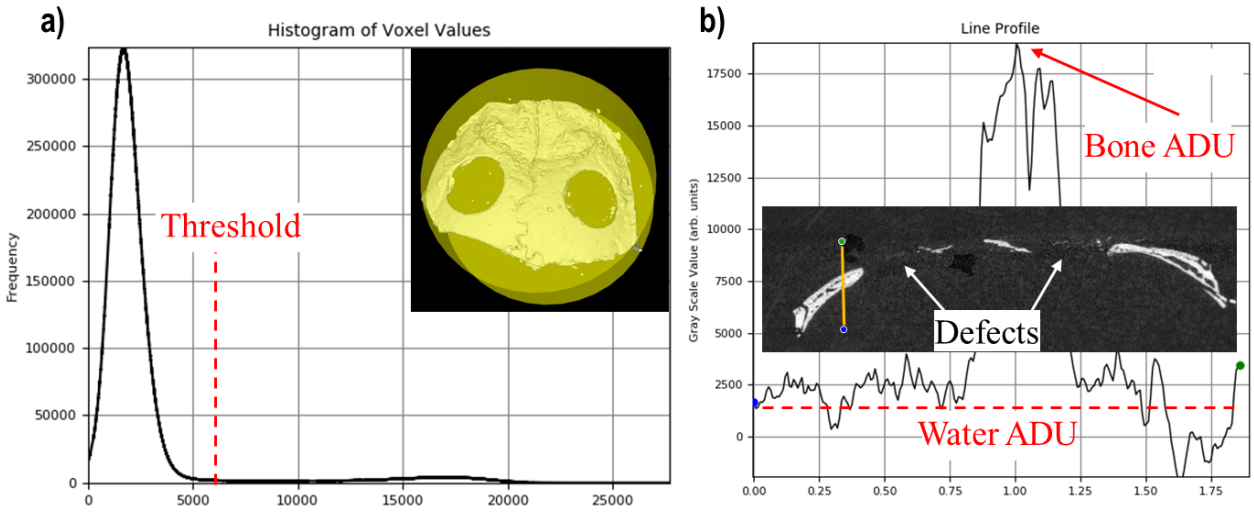

Figure 14: Identification of micro-CT analysis values for (a) threshold, where the inset shows the entire calvaria and the region of interest (yellow cylinder), and for (b) bone and water ADUs, where the inset shows the cross-sectional view of the calvaria with the selected line profile.

3.5.3.2. Histology

Histological analysis studies the microscopy features of tissues recognizing the cells' structure as a prerequisite for correlation with their function. After micro-CT imaging, the calvaria was demineralized in 5 mL of 14 % ethylenediaminetetraacetic acid, refreshed every 48 h for a total of 6 days. Samples were rinsed with water four times, and x-ray scanned to demonstrate the decalcification, and then immersed in 70 % ethanol. All samples were submitted to the Research Histology and Immunohistochemistry core lab at the University of Michigan for paraffin embedding and coronal cross-sectioning across the sagittal crest. The sections were stained with hematoxylin and eosin (most commonly known as H&E staining), showing a pink cytoplasm and a purple nucleus before imaging.

3.6. Characterization of particle-bacteria interaction

3.6.1. Antibacterial behavior against planktonic MRSA

All experimental data collected in this section were analyzed in collaboration with Dr. Neal Hammer's group from the Department of Microbiology and Molecular genetics at MSU.

3.6.1.1. Bacteria culture preparation

All experiments presented in this section 3.6.1 were conducted using the laboratory-derived MRSA USA300 JE2 [232]. Bacteria were streaked in tryptic soy agar (TSA) and grown at 37 °C overnight. Then, an isolated colony was collected and propagated in 5 mL of tryptic soy broth (TSB) under agitation (~ 225 rpm) at 37 °C overnight to stationary phase. The culture was centrifuged, and the pellet washed in PBS twice before use. Next, 1 mL of the MRSA solutions was prepared in the desired medium (i.e., PBS or TSB, as specified in **Table 7** and **Table 8**) with OD_{600} equal to 1 (equivalent to 10^8 colony forming units (CFU)/mL), applying **Equation 9**.

$$C_1 \cdot V_1 = C_2 \cdot V_2 \qquad \textbf{Equation 9}$$

where C_1 is the OD_{600} of the desired bacterial suspension, V_1 is the desired final volume, C_2 is the OD_{600} of the overnight bacterial suspension, and V_2 is the volume required from the overnight culture to prepare the desired suspension for the experiment. In this case, $C_1=V_1=1$.

3.6.1.2. Materials and antibiotics for the evaluation of bacteria-particle interaction

The particle-bacteria interaction was studied for Ag-BG microparticles, BG particles, 58 S microparticles, BGN, and Ag-BGNs synthesized as described in section 3.1.2 and 3.1.3, and preconditioned according to section 3.4.2 unless otherwise specified.

The ability of particles to synergize with antibiotics was also evaluated for specific combinations. **Table 6** summarizes the list of antibiotics used in this project along with their primary functions. The minimum inhibitory concentration (MIC) of the antibiotics against MRSA in PBS and TSB was studied before combinatorial studies (**Figure S3** and **Figure S4**, Appendix B). All antibiotics were purchased from Sigma Aldrich in powder USP Reference Standard and were used without further purification.

Table 6: List of antibiotics used in this project and their function against MRSA.

Antibiotic name	**Abbreviation**	**Class**	**Principal target**	**MIC(µg/mL)** PBS	TSB
Oxacillin	oxa	β − lactam	Peptidoglycan synthesis	RS**	RS**
Fosfomycin	fosfo	N/A*	Peptidoglycan synthesis	RS**	RS**
Vancomycin	vanc	Glycopeptide	Peptidoglycan synthesis	RS**	0.5
Gentamicin	gent	Aminoglycoside	Ribosome Synthesis	0.05	-
Tobramycin	tobra	Aminoglycoside	Protein Synthesis	1	-
Ciprofloxacin	cip	Fluoroquinolone	DNA gyrase	0.5	0.25
Erythromycin	ery	Macrolide	Ribosome Synthesis	RS**	RS**
Chloramphenicol	cpl	N/A*	Ribosome Synthesis	RS**	8

*N/A: unclassified antibiotics.
**RS: resistant. MRSA presents high tolerance to the antibiotic; the MIC was not found.

3.6.1.3. Viability of planktonic bacteria

The term “planktonic bacteria” refers to free-living bacteria dispersed in a solution, where they do not adhere to a surface. The viability of these planktonic bacteria was evaluated in either PBS or TSB. Growth-arrested conditions were induced by suspending the bacteria in PBS, a medium that lacks elements required for growth such as a carbon source for example. In this condition, bacteria enter a dormant state due to starvation and are less virulent, simulating a biofilm-like metabolic state. On the contrary, TSB was used to support bacteria growth and correlate Ag-BG and BG antibacterial capabilities with a bacteriostatic or bactericidal behavior.

The bacterial suspensions were mixed at 1:1 volume ratio with 2-fold concentrated solutions of each treatment in microcentrifuge tubes, as presented in **Table 7**. An untreated control was also prepared by mixing 1:1 the bacterial suspension with fresh medium.

Table 7: List of particles (Ag-BG, BG, 58 S, BGNs, and Ag-BGNs) and experimental conditions used against planktonic MRSA. Yellow shading indicates tests performed on TSB.

Particles studied Type	(mg/mL)**	**Medium**	**Condition**	**Analysis**	**Exposure time**
Ag-BG	1.25 – 5	PBS	Aerobic	CFU, SEM and TEM	12, 24 and 48 h
	1.25 – 5	PBS	Anaerobic	CFU	24 h
	5 – 100	TSB	Aerobic	CFU and TEM	24 h
BG	1.25 – 5	PBS	Aerobic	CFU and TEM	24 h
	1.25 – 5	PBS	Anaerobic	CFU	24 h
	5 – 100	TSB	Aerobic	CFU	24 h
58S micro	1	PBS	Aerobic	CFU	24 h
BGNs*	1	PBS	Aerobic	CFU	24 h
Ag-BGNs	0.05 – 1	PBS	Aerobic	CFU	0.5 - 24 h
	2.5 – 40	TSB	Aerobic	CFU	12 and 24 h

(*) Antibacterial properties of BGNs were evaluated for M1-P1, M2-P1, and M2-P2C. (**) Final concentration.

The experiments performed using TSB required a higher concentration of particles to counteract the bacteria proliferation. The use of microcentrifuge tubes with these higher concentrations of particles usually hinders their ionic release since those particles at the bottom are barely exposed to media. Therefore, to maximize the particles' exposed area, the experiments with TSB were performed in culture plates with a non-adherent surface coating (Nunclon™ Sphera™ 24-well plate, ThermoFisher Scientific) instead of microcentrifuge tubes.

The role of oxygen in particles' inhibitory capability was evaluated by comparing bacteria treated under aerobic and anaerobic conditions. Anaerobiosis was achieved by exposing bacteria to treatment in a growth receptacle containing an AnaeroGen compact anaerobic atmosphere-

generating pouch (Oxoid Ltd., England). Bacteria were transferred to the chamber as a pellet without any medium, and then bacterial suspensions were prepared with PBS degassed for 48 h inside the chamber before treatment.

The concentration of bacteria after the experimental treatments was obtained by enumeration of CFU on TSA, with a limit of detection of 100 CFU, and reported as $\log_{10}$ of CFU/mL, calculated with **Equation 10**. For example, in **Figure 15**, 10 µL of 10-fold serial dilutions were plated, revealing a total of 5 CFU at a dilution of 10^3. Therefore, **Equation 10** shows that the original bacterial suspension had about $5 \cdot 10^5$ CFU/mL. Additionally, selected samples were evaluated in the SEM or TEM to identify morphological and structural differences caused by the treatments (**Table 7**).

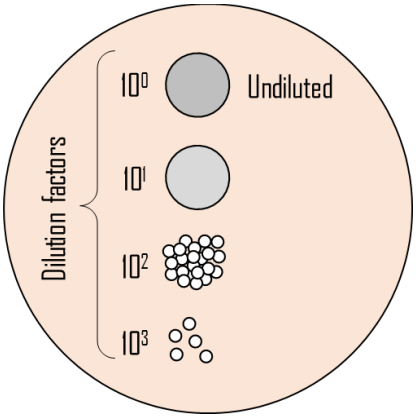

Figure 15: Example of a TSA plate with 10 µL spots of 10-fold bacterial suspensions for CFU enumeration.

$$CFU/mL = \frac{CFU \cdot dilution\ factor}{Volume\ plated\ (mL)} \qquad \textbf{Equation 10}$$

where CFU is the number of colonies counted in the plate for a specific dilution and, the dilution factor refers to the % of volume from the original solution.

3.6.1.4. Tolerance to Ag-BG microparticle treatment

The development of resistance towards any type of antibacterial treatment is one of the most significant concerns in microbiology. In this section, we evaluate the ability of MRSA to resist Ag-BG microparticles after being exposed to the same treatment repeatedly. **Figure 16** schematically represents the experimental procedure followed to obtain clones of a different generation. Briefly, the wild-type (WT) MRSA, which is the original strain, was exposed to 2.5 mg/mL of Ag-BG in PBS for 24 h. Then, bacteria were platted for CFU enumeration, and selective colonies were isolated from the TSA plate and propagated in TSB overnight to obtain the first generation (G1) of surviving bacteria. These G1 bacteria were exposed again to 2.5 mg/mL of Ag-BG in PBS for 24 h, and after platting, new colonies were isolated to obtain the second generation (G2) of bacteria. This process was repeated until the surviving colonies were below the limit of detection of our experiment. Colony selection was performed attending to their phenotype to collect bacteria of different characteristics. Two main colony sizes were identified: type I (regular, WT size) and type II (a small colony variant). All the treatments were performed in triplicate, isolating 3 colonies from each. Therefore, each generation yielded 9 new clones, which followed the serial treatment. The results are reported for each phenotype type, averaging the data from similar clones.

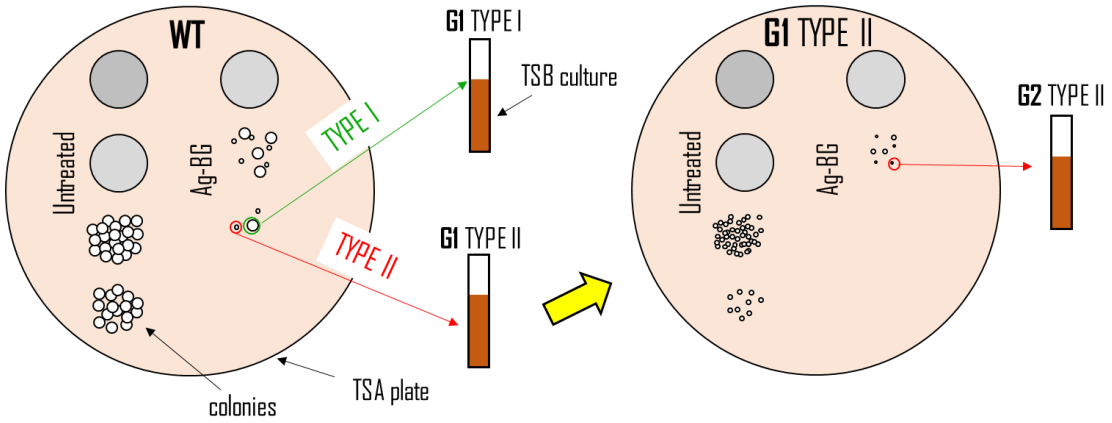

Figure 16: Schematic process for the collection of new generation clones. After treating wild-type (WT), MRSA with 2.5 mg/mL of Ag-BG, colonies of the different phenotype (i.e., regular size (type I) or small-colony variants (type II)) were isolated and treated again with the same concentration of Ag-BG. This process was repeated through several generations to evaluate the ability of MRSA to develop resistance to Ag-BG.

The effect of the serial Ag-BG microparticle treatment on the generation was discerned in terms of CFU after 24 h exposure. The limit of detection was 100 CFU for G1 and G2 and 10 CFU for G3. The morphological and structural features of each clone type were assessed with SEM and TEM.

All of these structural changes may also affect bacterial reactions like antibiotic resistance. WT-MRSA was strongly resistant to oxacillin and fosfomycin (**Table 6**). To evaluate if this resistance was carried through generations, G3-type II MRSA, which was the most different from the WT, was exposed to increasing concentration oxacillin and fosfomycin in TSB. Additionally, phenotypic alterations may be correlated to genomic mutations. Therefore, the genome sequence of G3-type II MRSA was obtained next.

3.6.1.4.1. Bacteria genome sequence

The phenotype change was also correlated to the genome sequence. Genomic DNA was isolated from an overnight culture of G3-type II MRSA JE2 grown in TSB. The overnight culture was

centrifuged, resuspended in a buffer containing lysostaphin (ABMI, Lawrence, NY), and incubated for 30 minutes at 37°C. The protoplasts were pelleted, and genomic DNA was isolated using the Wizard genomic DNA purification kit (Promega, Madison, WI) following the manufacturer's directions. Genomic DNA sequence was performed by Microbial Genome Sequencing (Pittsburg, PA). Files were imported in Geneious Prime and paired. Trimming was performed using BBDuk, and samples were mapped to the USA300_FRP3757 reference using the Geneious assembler to identify the single nucleotide polymorphism (SNPs). Genetic changes were determined in Geneious Prime. Cluster of orthologous groups categories were determined using EggNOG-mapper [233,234]. The genome sequencing was performed at the Microbial Genome Sequencing Center (MiGS) at the University of Pittsburgh. The analysis was conducted by Mr. Josh Lensmire, a Ph.D. Candidate at Dr. Hammer's group in MSU.

3.6.1.5. Combinatorial therapies of particles and antibiotics

The ability of particles to synergize with antibiotics is presented as a useful tool against resistant bacteria. In this set of experiments, both particles and antibiotics were mixed at concentrations near or below their respective MICs. Antibiotics were selected based on their target, and their MICs were identified as listed in **Table 6**. The particle-antibiotic combinations, their concentrations, and the experimental conditions for each test are presented in **Table 8**.

The first set of experiments was performed mixing Ag-BG microparticles and antibiotics (Ag-BG/antibiotic) in PBS to identify which combinations were synergistic. Ag-BG was used at a concentration near its MIC (2.5 mg/mL), while the antibiotic concentration remained at sub-inhibitory levels to reproduce an antibiotic-resistant condition. Since bacteria recover at a slower pace in growth-arrested conditions (i.e., in PBS), the structural damage is easier to identify.

Therefore, the bacteria that survived after treatment with a synergistic combination of Ag-BG/antibiotic were analyzed in TEM to help determine the mechanism of synergism. MRSA was also treated with BG/fosfo as a representative sample to test the role of Ag^+ ions in the synergistic process. Additionally, this synergistic concentration dependency was evaluated by exposing MRSA to different combinations of Ag-BG/vanc in 2 different set-ups. First, 0.5 mg/mL of vancomycin were delivered with increasing concentrations of Ag-BG (1.25 − 6.25 mg/mL); and second, 2.5 mg/mL of Ag-BG were combined with increasing concentrations of vancomycin (100 – 1000 μg/mL).

In the second set of experiments, MRSA was treated with Ag-BG/antibiotic in TSB to determine if the synergistic combinations identified in PBS were also successful in a more virulent environment. Ag-BG was used at its MIC (20 mg/mL). The antibiotic concentration was adjusted to maintain the same Ag-BG: antibiotic ratio in those combinations, where the antibiotic by itself was ineffective against MRSA. For example, Ag-BG/oxa in PBS consisted of 2.5 mg/mL Ag-BG and 0.1 μg/mL of oxacillin, and to keep the same ratio, Ag-BG/oxa in TSB was used at 20 mg/mL Ag-BG and 0.8 μg/mL of oxacillin. Nevertheless, since MRSA was not resistant to ciprofloxacin, the combination of Ag-BG/cipro in TSB maintained the same ciprofloxacin concentration used in PBS (i.e., 0.1 μg/mL), so that an antibiotic-resistant environment was still reproduced. As mentioned before, all experiments conducted with TSB were performed in non-adherent surface coated culture plates (Nunclon™ Sphera™ 24-well plate, ThermoFisher Scientific) to maximize particles' surface exposure.

The last set of experiments was performed using Ag-BGNs to investigate if the synergistic capability was preserved when down-scaling the particle size. Therefore, Ag-BGN/antibiotic was mixed using a concentration near the MIC of Ag-BGNs (0.5 mg/mL), maintaining the particle:

antibiotic ratios used before with microparticles (i.e., combinations of Ag-BG/antibiotic). Since Ag-BGNs presented stronger and faster antibacterial action alone than its microparticle counterpart, MRSA was exposed for 12 h instead of 24 h. Additionally, the role of particle size in the synergistic inhibition rate was evaluated by exposing MRSA to a combination of 2.5 mg/mL of Ag-BGNs with 0.1 µg/mL of oxacillin or 0.05 µg/mL of fosfomycin, which were the same concentrations used of microparticles (i.e., Ag-BG/antibiotic).

Table 8: List of combinations of particles with antibiotics for synergism evaluation. Yellow shading indicates tests performed on a different medium (TSB).

Particles studied		**Antibiotics studied**		**Medium**	**Analysis**	**Exposure time (h)**
Type	(mg/mL)	Type	(µg/mL)			
Ag-BG	2.5	Oxacillin	0.1	PBS	CFU and TEM	12 and 24
	2.5	Fosfomycin	0.05	PBS	CFU and TEM	12 and 24
	2.5	Vancomycin	100 – 1000	PBS	CFU	24
	1.25 – 6.25	Vancomycin	500	PBS	CFU and TEM	12 and 24
	2.5	Gentamicin	0.01	PBS	CFU and TEM	12 and 24
	2.5	Tobramycin	0.01	PBS	CFU	24
	2.5	Ciprofloxacin	0.05 and 0.1	PBS	CFU	12 and 24
	2.5	Erythromycin	5	PBS	CFU	24
	2.5	Chloramphenicol	1 and 5	PBS	CFU	24
	20	Oxacillin	0.8	TSB	CFU	24
	20	Fosfomycin	0.4	TSB	CFU	24
	20	Ciprofloxacin	0.1	TSB	CFU	24
BG	2.5	Fosfomycin	0.05	PBS	CFU and TEM	12 and 24
Ag-BGNs	0.5	Fosfomycin	0.01	PBS	CFU	12
	2.5	Oxacillin	0.1	PBS	CFU	0.5, 1, 2, 6 and 12
	2.5	Fosfomycin	0.05	PBS	CFU	0.5, 1, 2, 6 and 12

3.6.2. Antibacterial behavior against *S. aureus* biofilm.

The antibacterial capability of treatments against planktonic bacteria is valid during the first stages of bacteria colonization in an infection. However, implant-related infections usually appear in the form of biofilms, which consist of bacteria stuck to a surface embedded by a slimy extracellular matrix that acts as a protective cage. The presence of biofilm may render treatments, otherwise successful under planktonic conditions, ineffective.

In this section, Ag-BG and BG's ability to clear a biofilm was studied against *S. aureus* XEN36 (Perkin Elmer), a light-producing microorganism. The use of these types of bioluminescent pathogenic strain is at the forefront of antimicrobial treatment discovery since it is rapid, providing real-time efficacy data, and relatively inexpensive. Fireflies initially inspired the laboratory development of bioluminescent microorganisms. The emission of light energy occurs due to a chemical reaction between the enzyme luciferase and its substrate luciferin in the presence of ATP. Light-emitting lab-derived microorganisms, such as XEN36, have been modified to carry a stable copy of the gene encoding luciferase so that when bacteria are metabolically active, they emit light. This light's intensity can be recorded with an In vivo Imaging System (IVIS) and then correlated to the concentration of live bacteria.

All experimental data collected in this section were analyzed in collaboration with Dr. Jonathan Hardy’s group from the Institute of Quantitative Health Science and Engineering at MSU.

3.6.2.1. Development of bacteria biofilm

XEN36 was streaked for isolation in Luria Bertani (LB) plates overnight and then routinely grown in 5 mL of LB at 37 °C under agitation (~ 200 rpm) for 4 h to achieve bacterial logarithmic phase

at a concentration equivalent to OD_{600} = 0.5. A 1:100 bacterial was prepared in LB and incubated in regular 24-well culture plates (1 mL/well) to grow the biofilm. After 48 h, the LB medium was carefully removed, avoiding touching the edges of the well. The biofilm, produced as a ring around the wells, was washed twice for 5 min with PBS and imaged in IVIS before treatment (**Figure 17** (a)).

3.6.2.2. Treatment of bacteria biofilm

The XEN36 biofilm was exposed to 5, 10, and 20 mg/mL of Ag-BG and BG to evaluate particles' ability to clear bacteria. The particles were suspended in 1 mL of LB and then transferred to the biofilm after its preliminary imaging. A negative control, consisting of an untreated biofilm, was prepared by adding 1 mL of LB to the biofilm. The particle suspensions were gently pipetted into the wells avoiding its edges. The plate was imaged right after the addition of the treatment to prove that the particles did not provide any background signal interfering with that of the biofilm (**Figure 17** (b)). The biofilm was exposed to particles for 24 h maintaining the plates at 37 °C. Finally, the medium was removed, and the wells were washed twice with PBS before imaging.

3.6.2.2.1. Analysis of IVIS images

All IVIS images were collected with an exposure time of 2-3 min and medium binning. The photon emission from each well was extracted from the images using a region of interest grid and then converted to $\log_{10}$ for simplicity to quantify the particles' antibacterial action against the XEN36 biofilm (**Figure 17** (b)). The intensity from empty wells was subtracted from those containing a biofilm. The biofilms before treatment showed clear differences in photon emission from well to well, probably due to bacteria growth rate disparities (**Figure 17** (a)). Each well was evaluated independently, considering its photon emission before and after treatment to obtain the actual

percentage of viable bacteria after co-culture. The percentage before treatment on each well was normalized to 100 % of viable bacteria (**Figure 17** (b)). The results obtained for wells with the same treatment were averaged for statistical analysis.

a)

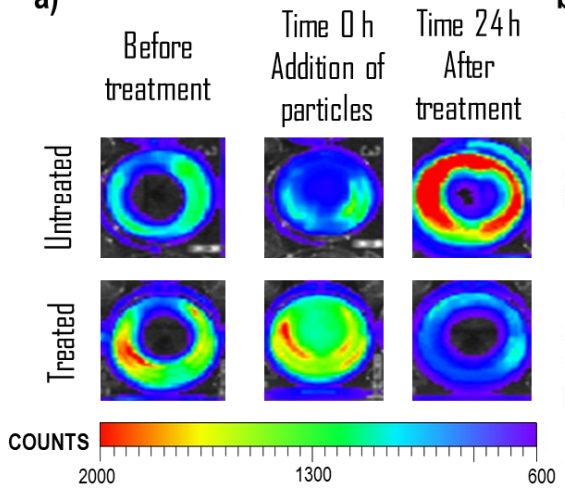

b)

	Photon Intensity	Before Treatment	Time 0 h	Time 24 h
Untreated	Original	$1.43 \cdot 10^6$	$1.43 \cdot 10^6$	$5.77 \cdot 10^6$
	Log 10	6.16	-	6.76
	Background subtraction	0.6	-	1.2
	Viable bacteria (%)	100	-	200
Treated	Original	$4.01 \cdot 10^6$	$4.01 \cdot 10^6$	$1.88 \cdot 10^6$
	Log 10	6.60	-	6.27
	Background subtraction	1.04	-	0.71
	Viable bacteria (%)	100	-	68.3

Figure 17: IVIS imaging analysis for bacteria viability. (a) Snapshots of representative wells during the three steps of the biofilm experiment (before treatment, after particle addition, and after 24 h exposure to particles), and (b) example of bacteria viability calculations based on photon emitted intensity, where orange and blue shading is used to highlight the normalized initial bacteria viability and the final one after treatment, respectively.

3.6.3. Morphology and structure of bacteria

The morphology, topography, and structure of bacteria were evaluated using electron microscopy to identify the characteristic features caused by each of the different treatments.

3.6.3.1. Scanning electron microscopy for bacteria-containing samples

The bacteria morphology and distribution were studied after exposure to Ag-BG microparticles for 12 h and compared to that of untreated bacteria. The samples were centrifuged and fixed for 2 h in Karnovsky fixative (2.5 % glutaraldehyde, 2.5 % formaldehyde, and 0.1 M cacodylate buffer in water). The fixed culture suspension was placed on a 1% poly-L-lysine cover-slips for 5 min

and then washed with water. Subsequently, the samples were dehydrated with a dilution series of ethanol (25 %, 50 %, 75 %, and 95 %) followed by three washes in 100 % ethanol, allowing 5 min between steps. Ethanol was substituted for liquid carbon dioxide in a critical point dryer (Leica Microsystem model EM CPD300) before mounting the cover-slip in aluminum stubs using epoxy glue (System Three Quick Cure 5 purchased from Systems Three Resins, Inc.) [235]. Finally, the samples were coated with 10 nm of osmium gas and examined at 5 kV using the SEM microscope (JEOL JSM-7500F).

3.6.3.2. Transmission electron microscopy for bacteria-containing samples

After different treatments (as specified in **Table 7** and **Table 8**), the bacteria structure was studied using TEM and compared to untreated cells or antibiotic-treated cells. In Ag-BG treated samples, the particles were allowed to settle. The solution (containing suspended bacteria and partial concentration of particles) was separated, centrifuged, and fixed in Karnovsky fixative for 2 h. After removing the fixative, a 2 % agarose solution in water solution was added to capture the bacteria pellets in a solid matrix and facilitate handling. Samples were washed three times with 0.1 M cacodylate buffer for 15 min each step before post-fixation in 2 % osmium tetroxide for 1 h following additional three washes. The agarose cubes were dehydrated in a series of acetone (25 %, 50 %, 75 %, and 100 %) and then infiltrated with Spurr resin dilutions in acetone (1:3, 1:1, and 3:1) for 3 h each and 100 % resin for 2 days. Embedding was performed in silicone molds using 100 % resin hardened at 60 °C overnight. Sectioning of the block was performed in agreement with section 3.2.2. Positive staining was done with 2 % uranyl acetate for 7 min and lead citrate for 3 min before observation at 100 kV.

3.7. Development of antibiotic depots using Ag-BG microparticles as carriers

3.7.1. Conjugation of Ag-BG and vancomycin

Ag-BG microparticles synthesized according to section 3.1.2 were utilized as carriers for vancomycin hydrochloride (USP Standard). The incorporation of vancomycin was performed by immersion of 0.5 mg of Ag-BG in 1.5 mL of uptake solution with an antibiotic concentration of 0.8 mg/mL of vancomycin in 1X PBS. The uptake was carried out under agitation (175 rpm) at 37 °C for 2, 6, and 24 h. At the end of each immersion time, samples were centrifuged at 500 rpm for 2 min. Particles and medium were separated and stored at 2 °C until use. Sterile conditions were maintained during the process.

After antibiotic uptake, the particles' surface loaded for 6 h (Ag-BG@vanc) was characterized using SEM and FT-IR techniques. The parameters for SEM-EDS and FT-IR analysis are presented in sections 3.2.1 and 3.2.4, respectively. To identify characteristic features of the drug loading process, Ag-BG's surface after uptake was compared to Ag-BG immersed only in PBS for 6 h and Ag-BG as synthesized.

The medium collected after uptake was analyzed with a UV-Vis spectrometer (section 3.2.8) at an absorbance length of 280 nm, maximum absorbance peak vancomycin in PBS (**Figure 18**). The Beer-Lambert relation [227] of OD and concentration was used to obtain a calibration curve of vancomycin in PBS (**Equation 11**). Since the absorbance is affected by temperature, all solutions were kept in ice during their evaluation.

$$Concentration\ of\ vancomycin\ (\frac{mg}{mL}) = \frac{OD_{280} - 0.04716}{0.59654} \qquad \textbf{Equation 11}$$

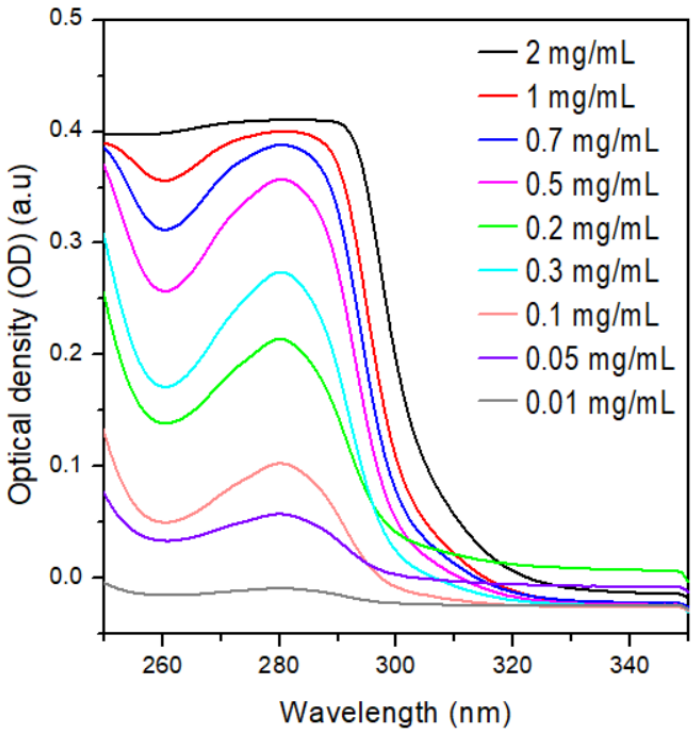

Figure 18: Characterization of vancomycin's light absorbance in PBS where higher vancomycin concentrations show higher optical density following Beer-Lambert's law.

The concentration of vancomycin loaded in the particles was then determined based on the residual vancomycin concentration of the medium collected from the uptake (**Equation 12**).

$$Drug\ loaded\ \left(\frac{mg}{mL}\right) = I_c - R_c \qquad \textbf{Equation 12}$$

where I_c is the initial concentration of uptake solution (0.8 mg/mL), and R_c is the residual concentration in the uptake solution after immersion.

3.7.2. The antibiotic release profile of Ag-BG@vanc

The release kinetics of vancomycin from Ag-BG@vanc was evaluated by immersing the loaded particles in 1 mL of PBS. The short-term release (up to 3 days) was assessed at 37 °C and agitation (175 rpm) to reproduce biological conditions. In comparison, long-term (up to 10 days) release

was assessed at 2 °C to prevent antibiotic degradation. At each collection time, particles were centrifuged, and half the volume was refreshed. The concentration of vancomycin in the substituted media was calculated according to the procedures in section 3.7.1.

3.7.3. Interaction between Ag-BG@vanc conjugate and bacteria or fibroblasts *in vitro.*

The *in vitro* capabilities of Ag-BG@vanc were evaluated in terms of antibacterial behavior and cell proliferation. **Table 9** summarized the experimental groups evaluated in both tests.

The antibacterial assays were performed on planktonic MRSA following the experimental description presented in section 3.6.1.3 for 24 h of exposure time. The capability of the Ag-BG@vanc conjugated was compared to two controls consisting of 0.5 mg of Ag-BG and 0.68 mg of vancomycin. Additionally, the interaction of bacteria with the carriers was evaluated in SEM (sample preparation detailed in section 3.6.3.1.). In this experimental condition, vancomycin is mostly ineffective against MRSA. The ability to resist vancomycin in metabolically active *S. aureus* has been observed in some mutations, namely vancomycin-resistant S. aureus (VRSA) due to modifications in their cell-wall hinder antibiotic infiltration. Under this consideration, this set-up may also provide insights on how to target VRSA, performing experiments in a controlled environment with a less-lethal strain.

Cell viability and proliferation were assessed in hBMSCs, as described in section 0, for 1, 3, and 7 days using the CCK-8 assay. As negative controls, cells were also exposed to either 0.5 mg of Ag-BG or 0.06 mg/mL of vancomycin, which was refreshed with media at each time point.

Table 9: Experimental groups of vancomycin depots evaluated for cell proliferation and antibacterial properties.

	Sample	Cell proliferation				Antibacterial	
		Mass (mg)	Cell density (cell/well)	Time point (days)	Assay	Mass (mg)	Time point (days)
Vehicles	Ag-BG	0.5				0.5	
	Ag-BG@vanc	0.5@0.64	$15 \cdot 10^3$	1, 3, 7	CCK-8	0.5@0.64	24 h
	vanc	0.06				0.68	

3.8. Development of Ag-BGN/hydrogel nanocomposites

The combination of Ag-BGNs with polymers is a unique approach to create a new class of material that is easy to store and allows minimally invasive medical delivery. In this project, Ag-BGNs were used as fillers for 2 different types of injectable nanocomposites using naturally derived hydrogels.

3.8.1. Fabrication approach for Ag-BGN/hydrogel nanocomposites

Previously synthesized Ag-BGNs (section 3.1.3) were preconditioned according to the section before their incorporation into a polymer matrix since the goal is to use these composites directly in medical applications.

3.8.1.1. Development of injectable hydrogels

Hydrogels are defined as polymeric materials of hydrophilic nature capable of holding large amounts of water in their structure. Hydrogels can be designed with controllable responses based on changes in the external environment. In this project, two natural-based hydrogels were selected: ECM and type I collagen. The polymerization of these hydrogels occurs under human body

conditions like neutral pH and 37 °C. Therefore, these composites are ideal for liquid injection in liquid by a syringe for medical treatment.

The ECM hydrogel was provided by Dr. Badylak and prepared from decellularized porcine urinary bladder matrix [229]. The ECM digest was thawed from - 20 °C to 4 °C overnight before neutralization, which was accomplished by the addition of one-tenth of 0.1 N NaOH, to achieve pH 7.4 and one-ninth of 10X PBS from the digest volume. In this case, the digest was diluted in 1X PBS to the desired final ECM concentration, in this case, 8 mg/mL. The process was performed by maintaining the solution in ice to prevent gelation.

Type I collagen hydrogel (PureCol®, Advanced Biomatrix) was derived from bovine hides and stored at 4 °C. The collagen (col) was neutralized by mixing with one-tenth of 10X PBS and one-tenth of 0.1M NaOH to achieve neutral pH. The volume of collagen was adjusted with distilled water for a final concentration of 2.4 mg/mL. The process was performed by maintaining the solution in ice to prevent gelation.

The Ag-BGN/hydrogel nanocomposites were fabricated with different concentrations of Ag-BGNs, as specified in **Table 10** as X (wt.%). The hydrogel solutions after neutralization were gently mixed with the Ag-BGNs powder using a wide-mouth pipet. The nanocomposites solutions were placed at 37 °C for 1 h to allow polymerization. The resulting nanocomposites were named ECM/Ag-BGN and Col/Ag-BGN. Although the samples transitioned to a more viscous state, they still retained a significant amount of water. Hydrogel solutions without Ag-BGNs were also polymerized and used as a control.

3.8.2. Characterization of Ag-BGN/hydrogel nanocomposites

The morphology and nanoparticle distribution of ECM/Ag-BGN and Col/Ag-BGN samples were studied with SEM, following the sample preparation described in sections 3.6.3.1. The presence of the particles in the hydrogel was confirmed with EDS and FT-IR. Samples of ECM and Col without particles were also evaluated for comparison.

3.8.3. *In vitro* properties of Ag- BGN/hydrogel nanocomposites

The *in vitro* properties of the Ag-BGN/polymer nanocomposites were characterized in terms of cell proliferation and antibacterial behavior. **Table 10** summarizes the experimental conditions and nanocomposite groups evaluated in each experiment.

Cell viability and proliferation of hBMSCs (**Figure 19** a) were evaluated after 2, 4, and 6 days in hBMSCs at 5 $\cdot 10^3$ cell/well, using a CCK-8 assay (as described in section 0). The injectable nanocomposites right after neutralization were pipetted into the transwells to achieve a total volume 0.1 mL. Therefore, each hydrogel nanocomposite delivered a different concentration of Ag-BGNs to the cells.

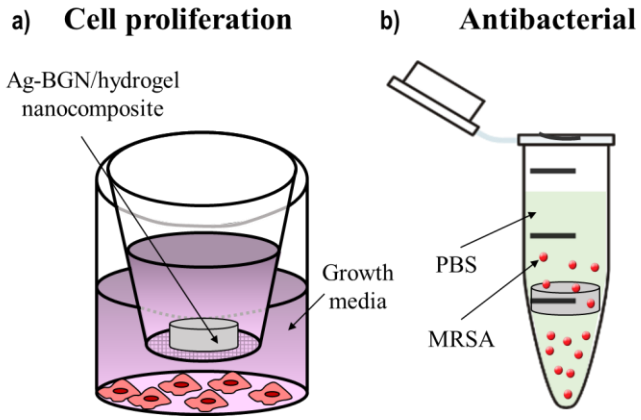

Figure 19: Experimental set-up of cell proliferation test (a) and antibacterial test against MRSA (b) performed with Ag-BGN/hydrogel nanocomposites.

Finally, the interaction between nanocomposites and bacteria was evaluated against planktonic MRSA (as described in section 3.6) for 24 h in PBS. The nanocomposites (with and without Ag-BGNs) were mixed with bacteria in microcentrifuge tubes (**Figure 19** b). In this case, the volume of nanocomposite was chosen so that all groups delivered the same mass of Ag-BGNs, therefore allowing a comparison of the Ag-BGNs degradation in different hydrogel materials. MRSA was also exposed to the concentration of Ag-BGNs alone for reference. The results were collected by CFU enumeration.

Table 10: Experimental groups for the *in vitro* assay of Ag-BGN/hydrogel nanocomposites. The wt.% of Ag-BGNs in each nanocomposite is represented by X.

Injectable sample	**Cell proliferation**			**Antibacterial**		
	x (wt.%)	Transferred volume	Transferred Ag-BGNs	x (wt.%)	Transferred volume	Transferred Ag-BGNs
Col	N/A	N/A	N/A	0	0.4 mL	0 mg
Col/Ag-BGNx				5	0.4 mL	0.05 mg
				10	0.4 mL	0.1 mg
ECM	0	0.1 mL	0 mg	0	0.1 mL	0 mg
ECM/Ag-BGNx	25	0.1 mL	0.4 mg	5	0.1 mL	0.05 mg
	50	0.1 mL	0.8 mg	10	0.1 mL	0.1 mg

*N/A: non-applicable. The test was not performed.

3.9. Statistical analysis

All data were expressed as the arithmetic mean and standard deviation. The experiments were repeated three times using triplicates. The statistical analysis was performed in GraphPad Prism Software using the Student's t-test, two-tailed, n=9, and results were considered significant when $p < 0.05$.

4. RESULTS

4.1. The degradation of Ag-BG microparticles *in vitro*

The degradation of microparticles was evaluated in terms of pH evolution and apatite-forming ability. The in-depth structural characterization of these Ag-BG microparticles was previously reported [163,236]. The evaluation of the acellular behavior presented in this section was used to verify that the developed Ag-BG had the same response as the one in the literature.

4.1.1. pH evolution of Ag-BG microparticles

The degradation of Ag-BG microparticles was evaluated by immersion in PBS and monitored through the pH of the solution, which remained around neutral values during the experiment (**Figure 20**). In the first 12 – 24 h of immersion, the pH increased from 7.4 to 7.5, probably due to the release of Si and Ca species. Nevertheless, increasing the soaking time for up to 4 days did not result in significant pH variations since it remained ~ 7.5. Therefore, Ag-BG's release of ionic species did not create a toxic pH environment for biological entities.

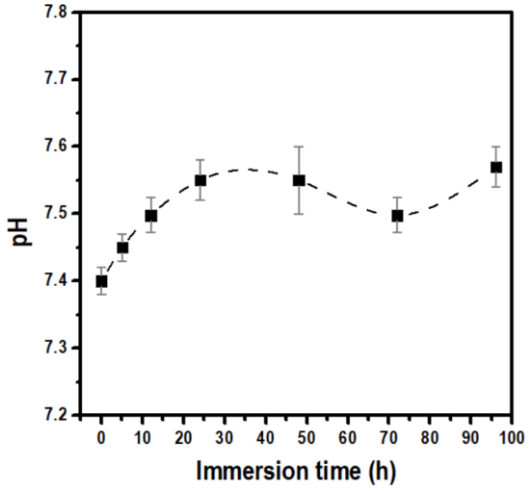

Figure 20: The degradation of Ag-BG immersed in PBS caused fluctuation in the pH value within a biologically neutral range. Modified from [237].

4.1.2. Apatite-forming ability of Ag-BG microparticles

The apatite-forming ability of bioactive glasses serves as an expression of their *in vitro* bioactivity. In this case, Ag-BG at a concentration of 3.33 mg/mL was immersed in SBF at 37 ºC and constant agitation to monitor the deposition of minerals. FT-IR spectra (**Figure 21** a) showed changes in the surface structure before and after soaking in SBF for 3, 7, and 14 days. Before immersion, bending and stretching modes of the Si-O-Si bonds were observed at 450, 805, and 1200 cm^{-1}. Additionally, before immersion, the central peak around 1000-1050 cm^{-1} broadens because of the overlapping between the P-O bending and the Si-O-Si stretching mode. Here, the shoulder at 900 cm^{-1} is attributed to Si-O-NBO resulted from the incorporation of network modifying atoms in the glass structure. Phosphate absorption double bands at 575-600 cm^{-1} were also observed. After immersion in SBF, the intensity of the P-O dual bands increased significantly, and carbonate bands at 1400 cm^{-1} develop as the soaking time increases. These absorption bands were similar to those observed in synthetic HCA.

The changes in surface emerging in Ag-BG before and after soaking were evaluated with SEM. The material before SBF consisted of aggregates of random-sized particles (< 20 μm) with a smooth surface and roughness due to densification of nanoparticles during sol-gel synthesis (**Figure 21** b). After soaking for 14 days, a layer of flakes covered entirely the Ag-BG surface (**Figure 21** c). Flakes are one of the characteristic structures in which an apatite layer can deposit in bioactive glasses.

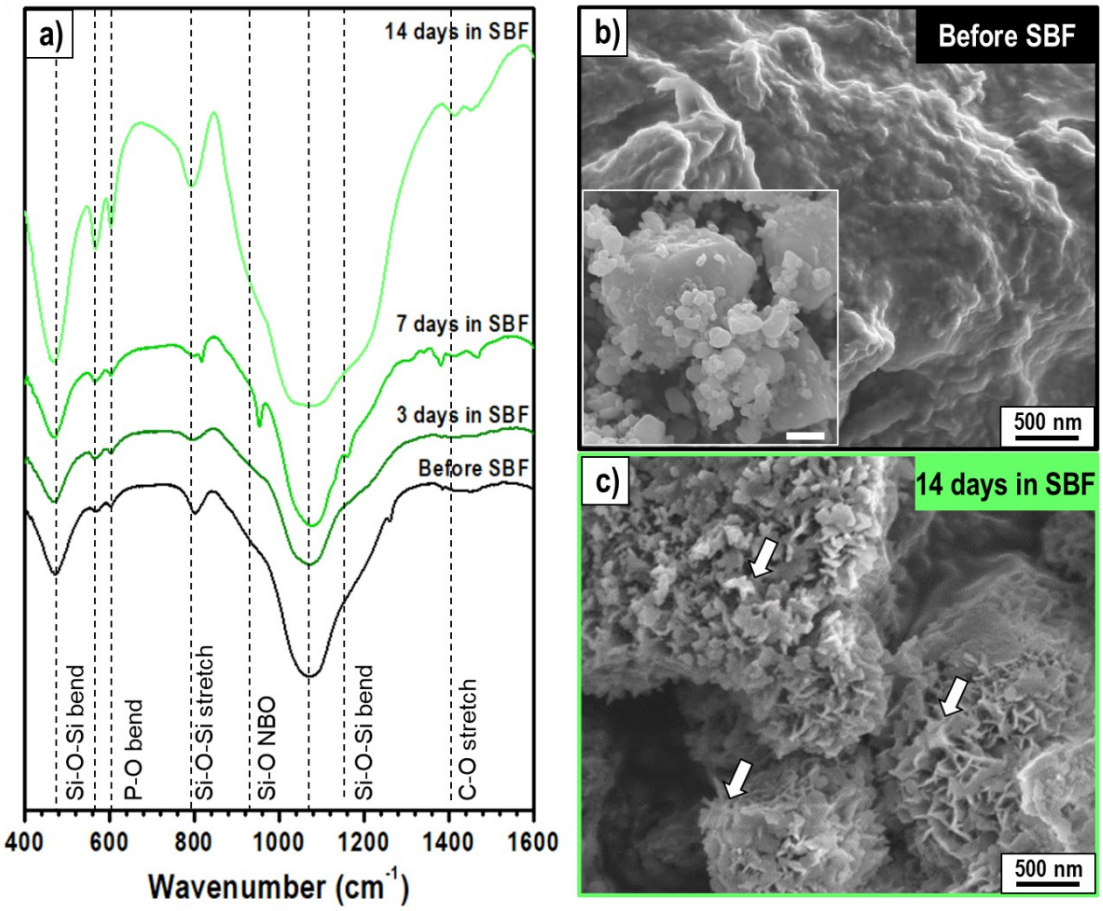

Figure 21: Capability of Ag-BG to stimulate the formation of apatite layer when immersed in SBF. (a) Structural vibration in FT-IR shows an increase of the intensity for P-O bending and C-O stretching after immersion. (b) The surface of Ag-BG microparticles is smooth before immersion and lacks the presence of deposits. Inset shows a lower magnification image of particles with a scale bar representing 2 µm. (c) Apatite flakes (marked as white arrows) are deposited at Ag-BG's surface after 14 days immersed in SBF.

4.2. The interaction of Ag-BG microparticles with cells and tissue: biocompatibility

This section includes the main characterization of the interaction between Ag-BG microparticles and eukaryotic cells (i.e., hBMSCs *in vitro* and bone tissue *in vivo*). The groups studied in this section were reported in **Table 3** and **Table 5** for *in vitro* and *in vivo* experiments, respectively. The results presented here have been previously published as "Pajares-Chamorro, Natalia, *et al*. "Silver-doped bioactive glass particles for in vivo bone tissue regeneration and enhanced

methicillin-resistant Staphylococcus aureus (MRSA) inhibition" Materials Science and Engineering: C (2020): 111693."

4.2.1. *In vitro* cell proliferation

The response of cells towards treatments with Ag-BG microparticles was evaluated in terms of cell viability and proliferation in growth media with the MTT assay. The OD_{570} values serve as a direct correlation to cell concentration. **Figure 22** a shows a similar concentration of cells, and therefore, no difference in cell viability, for untreated and Ag-BG treated cells at each time point. However, after 2 days of exposure, a slight decrease in cells' viability correlates with increasing Ag-BG concentration. This effect is transitory and disappears at later time points where no statistical difference was found. Next, **Figure 22** b compares the growth or proliferation rates of the different groups. The OD_{570} data over time were linearly fit for $R^2 > 0.9$ to report the slopes, which serve as an indication of the proliferation rate. Despite the slight drop in cell viability at the beginning of the treatment, Ag-BG-treated cells proliferated at double the speed of untreated cells. Interestingly, increasing the Ag-BG concentration did not alter the proliferation rate, suggesting that at higher concentrations of Ag-BG, cell proliferation is not the main biological process affected.

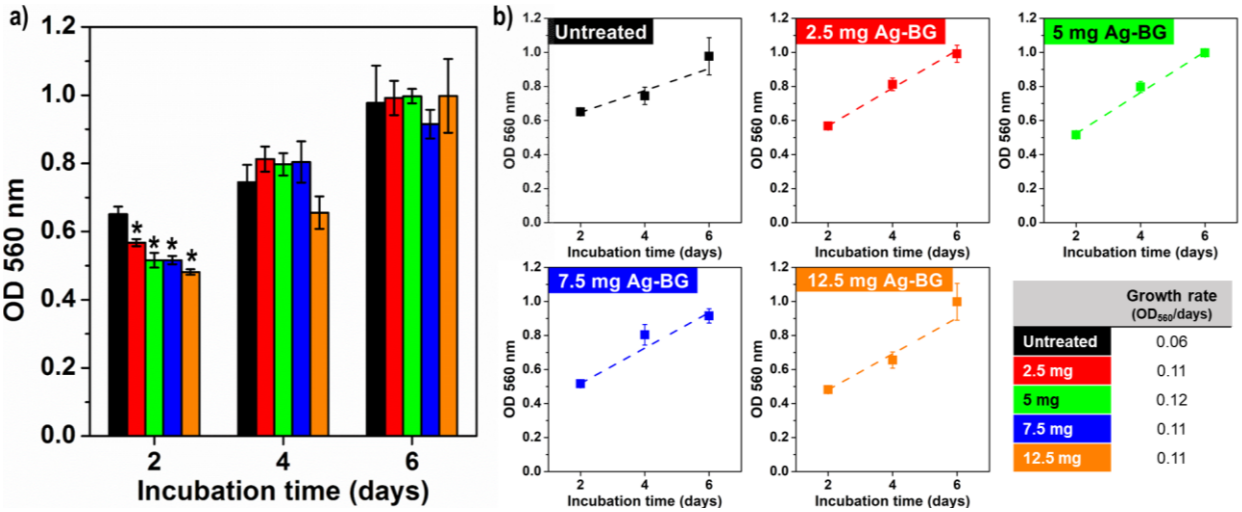

Figure 22: Cell viability (a) and proliferation rate (b) of hBMSCs after exposure to different concentrations of Ag-BG (2.5 mg in red, 5 mg in green, 7.5 mg in navy blue, and 12.5 mg in orange) in the growth medium. Note that Ag-BG treated cells proliferate faster than the untreated cell. Statistical significance ($p < 0.05$) between untreated and Ag-BG treated cells is indicated with (*) [238].

4.2.2. *In vitro* cell differentiation

Gene expression of *BSP*, *OCN*, and *RunX2* was measured using qRT-PCR and normalized to the GAPDH housekeeping gene for the printed bone constructs. *BSP*, *OCN*, and *RunX2* were selected as representative genes due to their roles in osteoblasts differentiation. For instance, *BSP* is a significant component of the bone extracellular matrix [239], *OCN* is correlated with bone mineral density [240], and *RunX2* is a crucial transcription factor during differentiation [241]. The relative gene expression of the target genes in untreated hBMSCs was normalized to a value of 1 to determine the Ag-BG treatment's effect. **Figure 23** shows significant differences in transcription levels of osteogenic genes with *BSP* expression significantly upregulated after all treatments, while that of *OCN* only increased at the higher Ag-BG concentration used. In contrast, *RunX2* expression level was downregulated for all the Ag-BG treatments. Unlike the effect observed in the growth rate (**Figure 22** b), the Ag-BG concentration from 5 mg to 12.5 mg significantly upregulated the expression of all three genes.

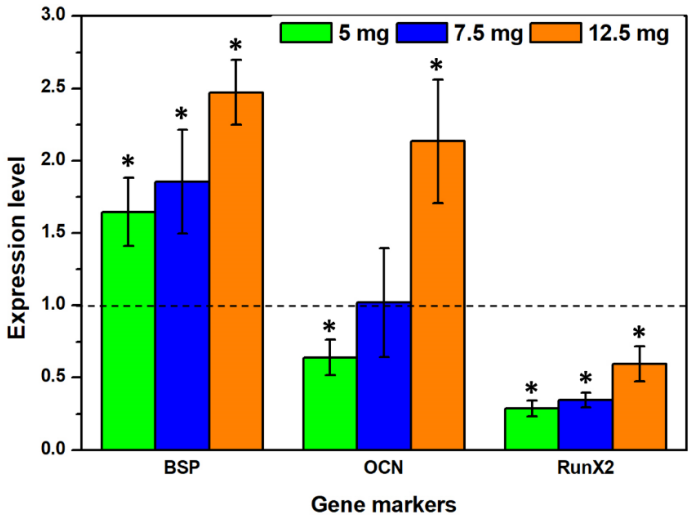

Figure 23: Expression level for *BSP*, *OCN*, and *RunX2* gene markers after 10 days in osteogenic medium with increasing Ag-BG concentrations (5 mg in green, 7.5 mg in navy blue, and 12.5 mg in orange). Normalized gene expression of untreated hBMSCs is represented with a dashed line. Statistical significance ($p < 0.05$) between untreated and Ag-BG treated cells is indicated with (*). Modified from [238].

Bone tissue is characterized by its high mineral phase content, and thus, cell differentiation can also be correlated to the minerals secreted by cells. In this case, the mineralization of cells was evaluated in terms of secretion of Ca with ARS when co-cultured with Ag-BG in growth or osteogenic medium. The mineral secretion in untreated hBMSCs was normalized to a value of 1 to determine the Ag-BG treatment's effect. In general, Ag-BG microparticles caused higher secretion of mineral compared to untreated cells (**Figure 24**). Although in growth medium cell mineralization was only slightly higher in Ag-BG treated cells, the mineral content formation significantly increased with the concentration of the Ag-BG treatments (**Figure 24** a-b). In contrast, the mineral phase content in the osteogenic medium reached 400 % higher after co-culture with Ag-BG microparticles (**Figure 24** c-d). In this case, diverse Ag-BG amounts did not lead to any difference among sets, probably due to a color supersaturation. Additionally, optical images showed that fibroblasts presented a spindle-like shape and almost reached confluence after 10 days of culture (**Figure 24** b and d). The acellular wells containing only Ag-BG and media lacked any

red stain after the ARS assay and, therefore proving that the measured mineral phase belonged solely to hBMSC differentiation.

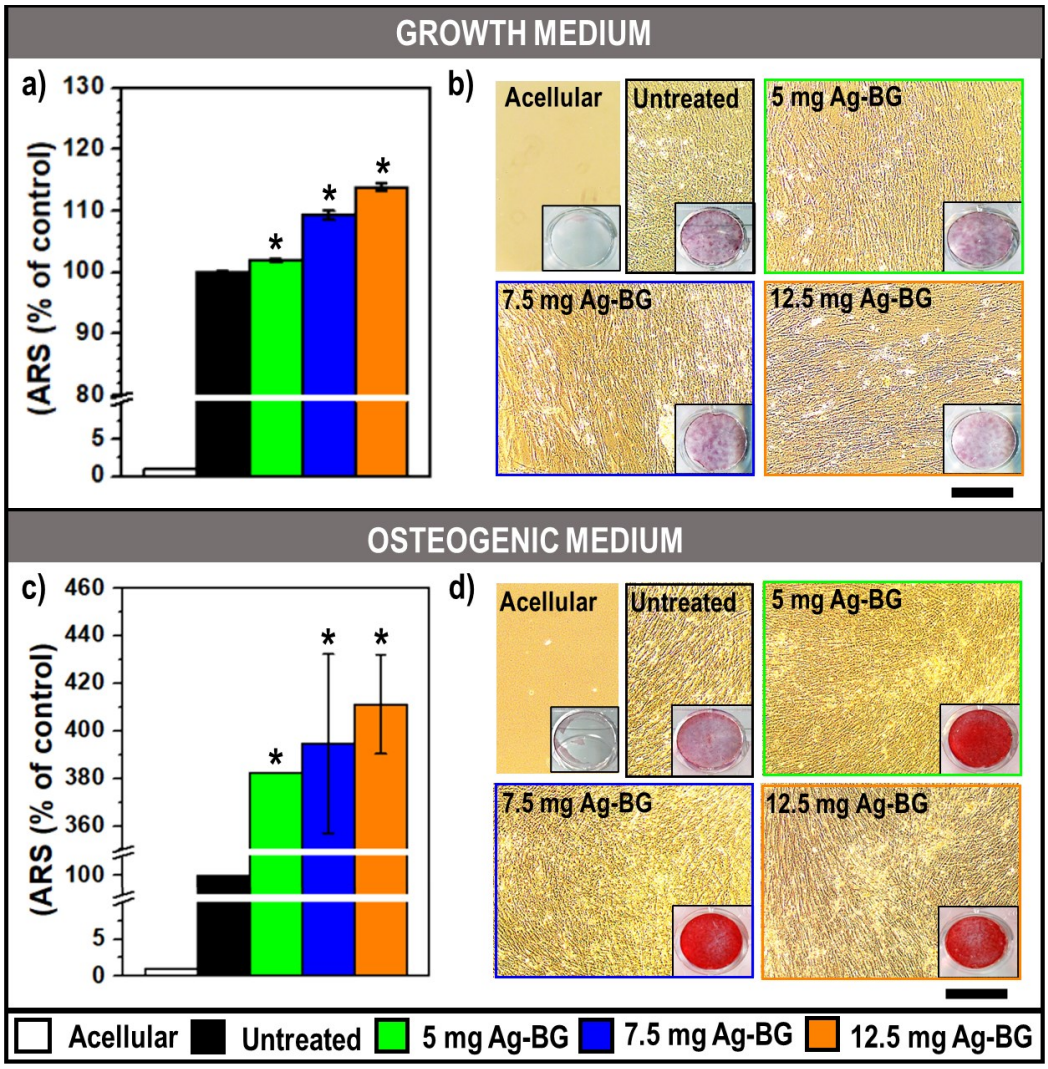

Figure 24: Secretion of Ca minerals in hBMSC differentiation in growth (a-b) and osteogenic media (c-d) after treatment with Ag-BG (5 mg in green, 7.5 mg in navy blue, and 12.5 mg in orange). Optical density (a and c) was normalized using untreated cells (in black) as 100%. Fibroblast presented a spindle-like shape and reached confluence after 10 days (b and d, where the scale bar represents 500 µm). The insets of the 16 mm diameter wells show the stained cell monolayers after ARS. Acellular wells that contained only Ag-BG and medium did not yield to a red-stained monolayer. Statistical difference between untreated and Ag-BG treated cells for $p < 0.05$ is indicated with (*) [238].

4.2.3. Ag-BG microparticle surface evolution after cell exposure

The bioactive response by Ca-P deposition on Ag-BG in an acellular body simulated environment (i.e., in SBF) was demonstrated previously (**Figure 21**). The simultaneous exposure of Ag-BG to medium and cells is expected to lead to a similar surface reaction. Ag-BG's apatite-forming ability after the *in vitro* cell culture can serve to better understand the mineralization behavior of particles with a more accurate simulation of the human body reaction. As has been previously mentioned, as-synthesized Ag-BG presents a smooth surface (**Figure 25** a and c). However, cauliflower deposits can be observed after 10 days of co-culture with hBMSC in the osteogenic medium (**Figure 25** b and d). The EDS showed a significant increase in Ca after co-culture (insets in **Figure 25** c and d). The elemental analysis of these deposits revealed a composition rich in Ca and P with a Ca/P ratio close to 1.8, characteristic of the non-stoichiometric HA phase.

The formation of mineral apatite also modified the intensity of the vibrational modes in IR spectra (**Figure 25** e). Similar to the effect of SBF immersion, after cell exposure, the intensity of P-O vibrational modes at 575-620 cm^{-1} increased, and the bands become sharper, indicating a crystallization process. The nature of the deposits was also analyzed with XRD (**Figure 25** f). In agreement with the FT-IR observations, XRD shows an increase in the crystalline contributions. The main peaks appeared at 26 º, 32 º and 46 º, confirming the nature of the deposits as carbonated hydroxyapatite (ICCD, PDF No. 9003552).

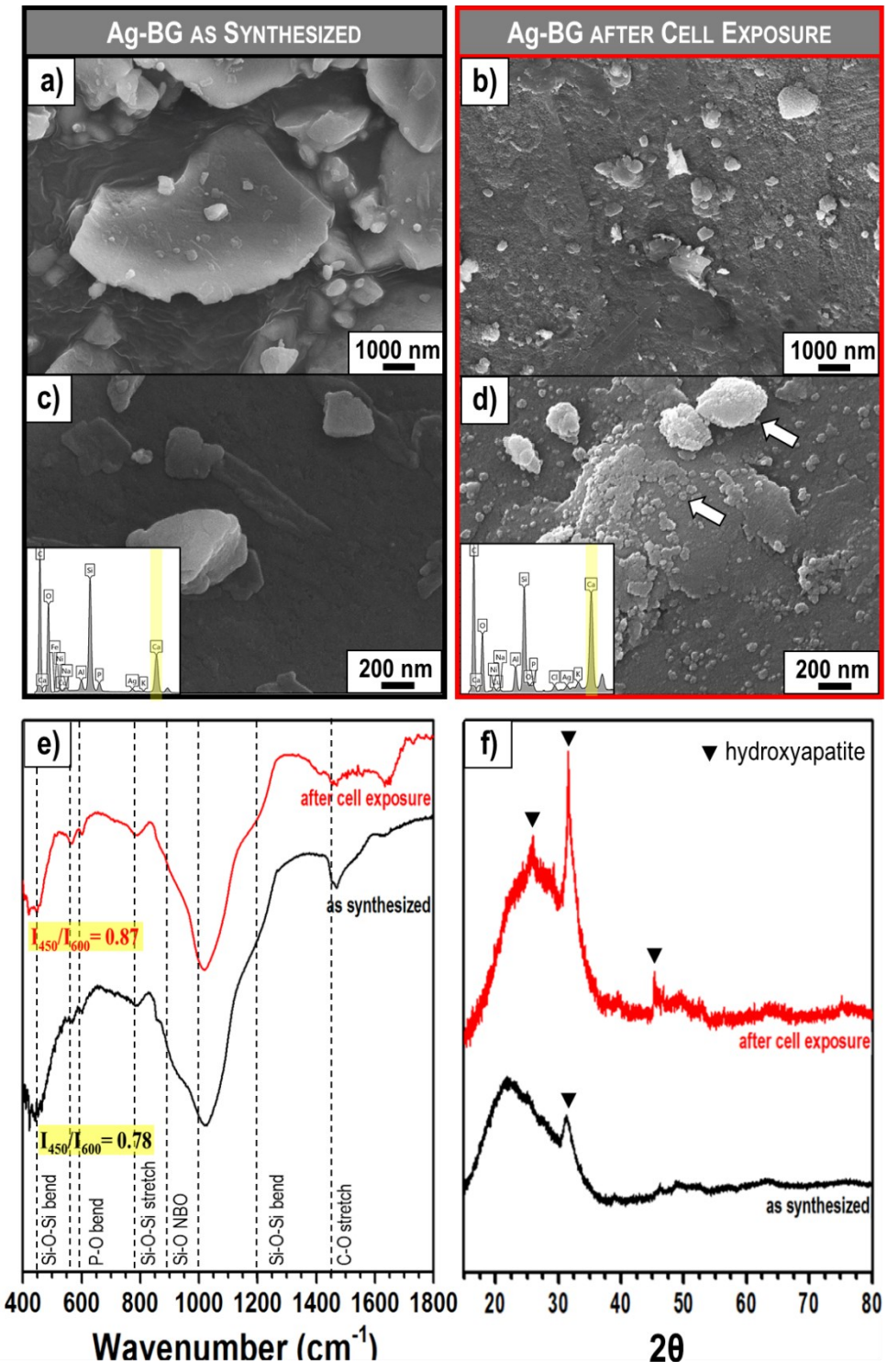

Figure 25: Evolution of Ag-BG surface topography (a-d) and structure (e-f) after 10 days in cell culture with the osteogenic medium. As synthesized particles (a-b) present a smooth surface, while after co-culture (c-d), a Ca-P rich phase (white arrows) is deposited at the surface. EDS spectra (insets in b and d) showed an increase in Ca content intensity (highlighted in yellow). FT-IR (e) and XRD (f) of Ag-BG microparticles as-synthesized (black line) and after exposure to cells (red line) confirmed the presence of biomineralized hydroxyapatite. Modified from [238].

4.2.4. *In vivo* bone regeneration

Collagen-sponge-based implants were prepared by soaking with a slurry solution of Ag-BG in PBS or ECM. **Figure 26** a shows the homogeneous distribution of the infiltrated microparticles throughout the implant maintaining the strut structure and pore dispersion of the collagen scaffold. The growth of bone tissue in the calvaria defects after treatment was evaluated with micro-CT and histology analysis. On the one hand, micro-CT images showed defects partially filled with the new bone after treatment with Ag-BG while the defects remained critically opened in the Ag-BG free groups (**Figure 26** b). The differences in the volume occupied by new bone among sample sets were quantified in micro-CT images proving numerically the development of new bone in Ag-BG treated samples (**Figure 26** c). This result was validated with the 2D histological analysis. In this case, only Ag-BG/PBS showed significantly greater bone area, with a 3-fold increase compared to its Ag-BG free counterpart (**Figure 26** d). ECM containing groups presented similar bone areas. The histology images (**Figure 26** e) revealed this new bone formation for Ag-BG/PBS treated calvaria was taking place across the entire 3 mm defect. Only moderate new bone formation was observed in PBS-treated groups.

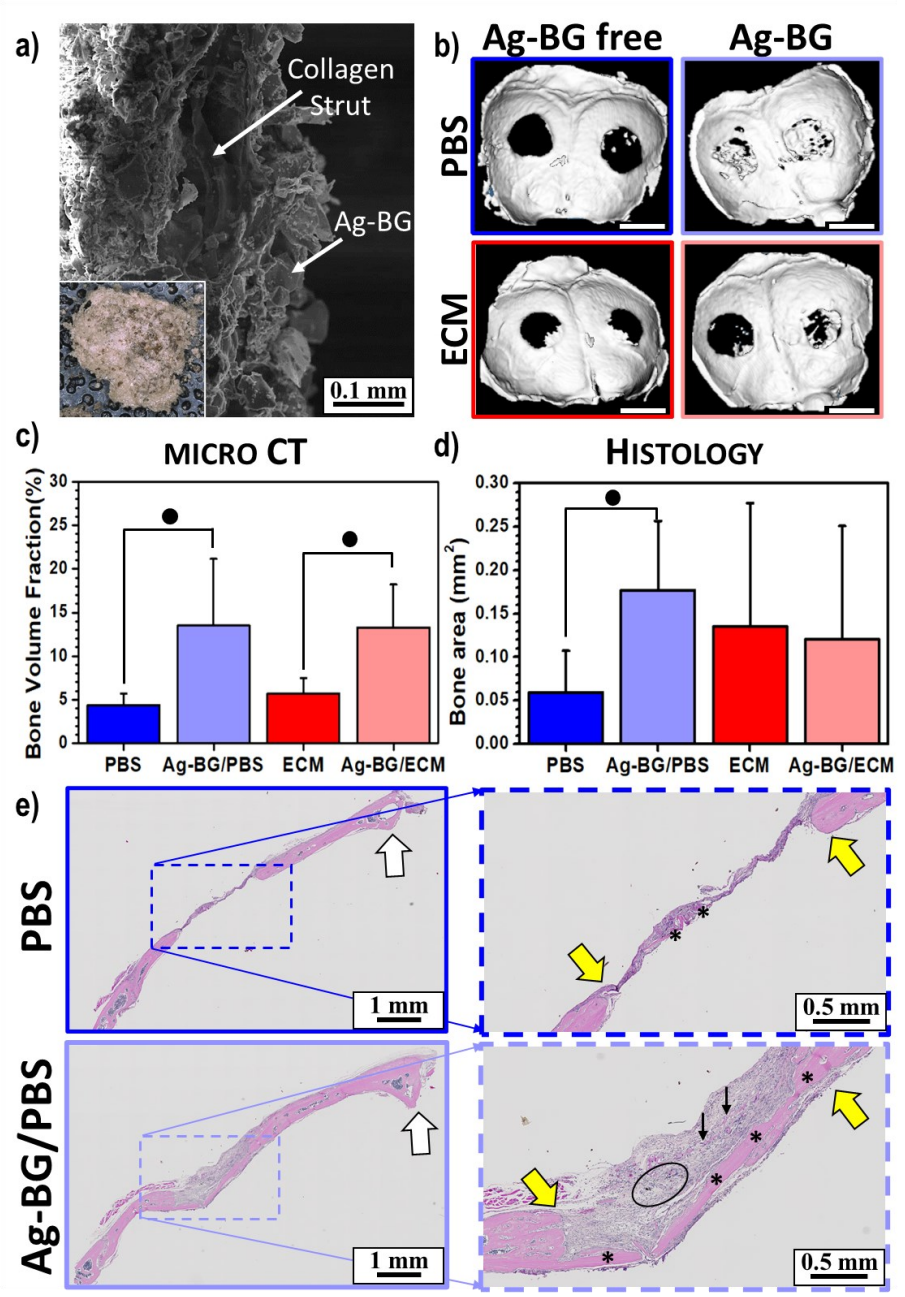

Figure 26: The cross-sectional view of the implant (a) shows a homogeneous distribution of the Ag-BG microparticles loaded on the collagen sponge. The inset is the top optical view of the implant. Micro-CT images of the calvaria after 30 days of treatment, where the white scale bar represents 3 mm, are displayed in (b). Bone volume fraction formed (c) and 2D assessment of bone area (d) were calculated from micro-CT and histology, respectively, for n=5 animals and 2 defects/animal. Statistical significance ($p < 0.05$) between groups is marked with (●). Histology images of the coronal cross-sections of calvaria are divided in half along the sagittal crest (e), where the presence of new soft tissue and bone is indicated with (*). Yellow arrows represent the edges of the defect, black circumference for retained Ag-BG microparticles, and black arrows for collagen sponge. Note that mice treated with PBS present little overall regeneration of calvaria defect. [238]

4.3. The interaction between Ag-BG microparticles and bacteria: antibacterial behavior, mechanisms, and therapeutic framework.

This section includes the thorough characterization of the interaction between Ag-BG microparticles and bacteria (i.e., MRSA and XEN36 *S. aureus*). Different groups and conditions were studied for Ag-BG microparticles (as reported in **Table 7**) and particle/antibiotic combination (as reported in **Table 8**). Part of the results presented here has been previously published as Pajares-Chamorro, N., Shook, J., Hammer, N. D., & Chatzistavrou, X. (2019), "Resurrection of antibiotics that methicillin-resistant Staphylococcus aureus resists by silver-doped bioactive glass-ceramic microparticles", Acta Biomaterialia, 96, 537-546".

4.3.1. Minimum inhibitory concentration against MRSA.

Increasing concentrations of microparticles were incubated with bacteria under different environmental conditions to determine the basal level of Ag-BG and BG antibacterial activity (**Figure 27**). The microparticles were mixed with growth-arrested bacteria, using PBS as dispersing medium, to simulate the inactive metabolic state of bacteria in a biofilm (**Figure 27** a-b). The minimum inhibitory concentration (MIC) of Ag-BG was estimated around 2.5 mg/mL after 24 h treatment (**Figure 27** a), where the concentration of bacteria was below the 10^5 CFU/mL required to define an infection [242,243]. Exposure to 5 mg/mL Ag-BG brought the CFU number below the detection limit (**Figure 27** a). BG microparticles exhibited lower inhibition capacity on MRSA at similar concentrations, reducing viability at 2.5 mg/mL and bacterial concentration to around 105 CFU/mL at 5 mg/mL (**Figure 27** b). In general, BG was 20 % less toxic to MRSA than Ag-BG.

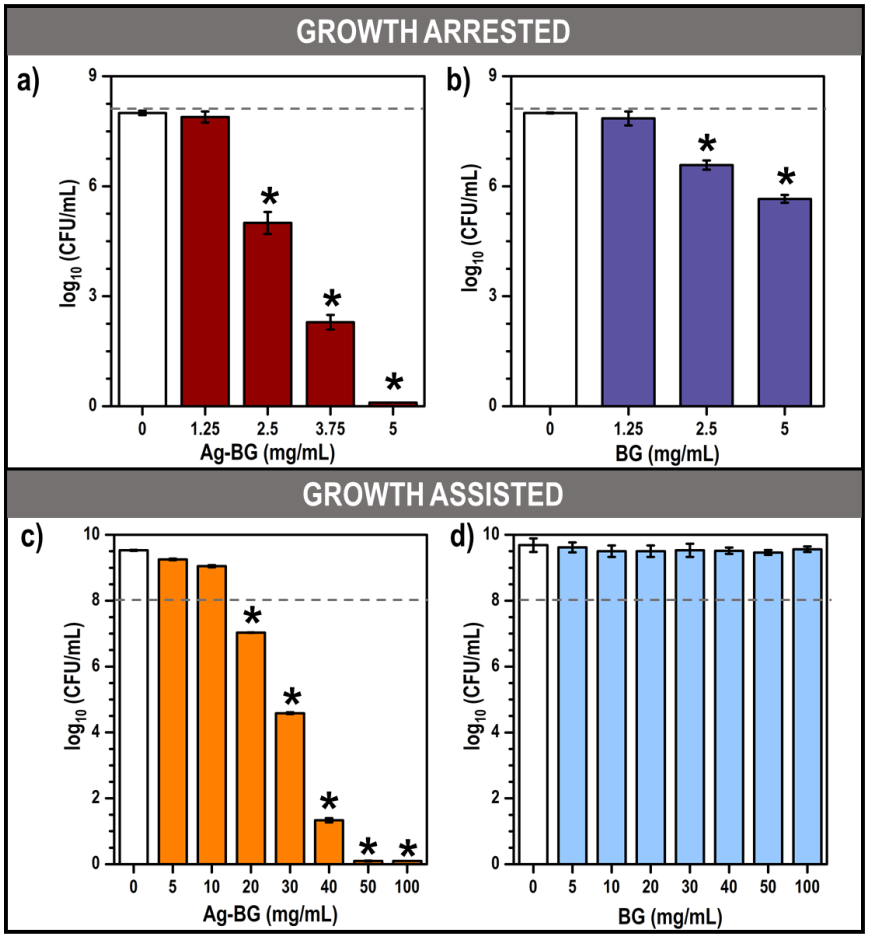

Figure 27: Ag-BG and BG microparticles exhibit strong antibacterial action against growth-arrested MRSA (a and b). Bacteria growth was inhibited after exposure to Ag-BG (c), but bacteria remained viable when treated with BG (d). Suspensions of MRSA (OD_{600} = 1 equivalent to ~ 10^8 CFU/mL, represented by a dashed line) were mixed with fresh PBS (a-b) or TSB (c-d) medium (0 mg/mL, untreated control represented by white bars) and increasing concentrations of Ag-BG (a and c) or BG (b and d). The CFUs were enumerated after 24 h with a limit of detection of 10-100 CFU. (*) Indicates the significant difference between the untreated versus the particle-treated groups ($p < 0.05$). Modified from [237].

The microparticles' antibacterial ability was also monitored in growth-assisted conditions using TSB as dispersing medium (**Figure 27** c-d). This set-up reproduces the first stages of bacteria colonization, where they are more virulent to develop an infection. Note that in this case, untreated MRSA grew from the 10^8 CFU/mL set at 0 h to $10^{9.5}$ CFU/mL after 24 h. Ag-BG was still toxic to metabolically active MRSA but required higher microparticle concentration to cause significant damage (**Figure 27** c). Exposure to 20 mg/mL of Ag-BG decreased bacterial concentration that

reached 10^5 CFU/mL after exposure to 30 mg/mL of Ag-BG. Note that a 10-fold higher Ag-BG concentration was required to reduce the CFUs below the detection limit in growth-assisted (~ 50 mg/mL) vs. growth-arrested conditions (~5 mg/mL). In contrast, BG was unable to inhibit bacterial growth up to 100 mg/mL (**Figure 27** d).

4.3.2. Time-dependent inhibition of MRSA

The antibacterial of 2.5 mg/mL Ag-BG in PBS was also time-dependent, the bacterial viability being significantly decreased from 12 to 48 h (**Figure 28** a). Notably, the CFUs were reduced below the detection limit after 48 h of incubation, indicating that Ag-BG is bactericidal to MRSA. This inhibitory trend is correlated to the degradation rate of particles in the solution, which increases over time as more antibacterial species are released from the glass structure.

The morphology of bacteria cultured alone (**Figure 28** b I-II) and upon exposure to Ag-BG microparticles (**Figure 28** b III-IV) was observed using SEM to analyze the bacteria-microparticle interaction. Untreated bacteria aggregated without signs of damage, and extracellular matrix formation (pink arrow in **Figure 28** b II) could be observed surrounding some bacteria. However, the bacterial morphology was altered by Ag-BG, and the microparticles were colonized by a significant number of bacteria attached to the surface (**Figure 28** b III-IV). Bacterial damage was evidenced by the presence of cellular remnants such as cytoplasmic contents between cells (yellow arrows in **Figure 28** b III) or cell-wall fragments (red arrow in **Figure 28** b IV) found on the surface of the microparticles.

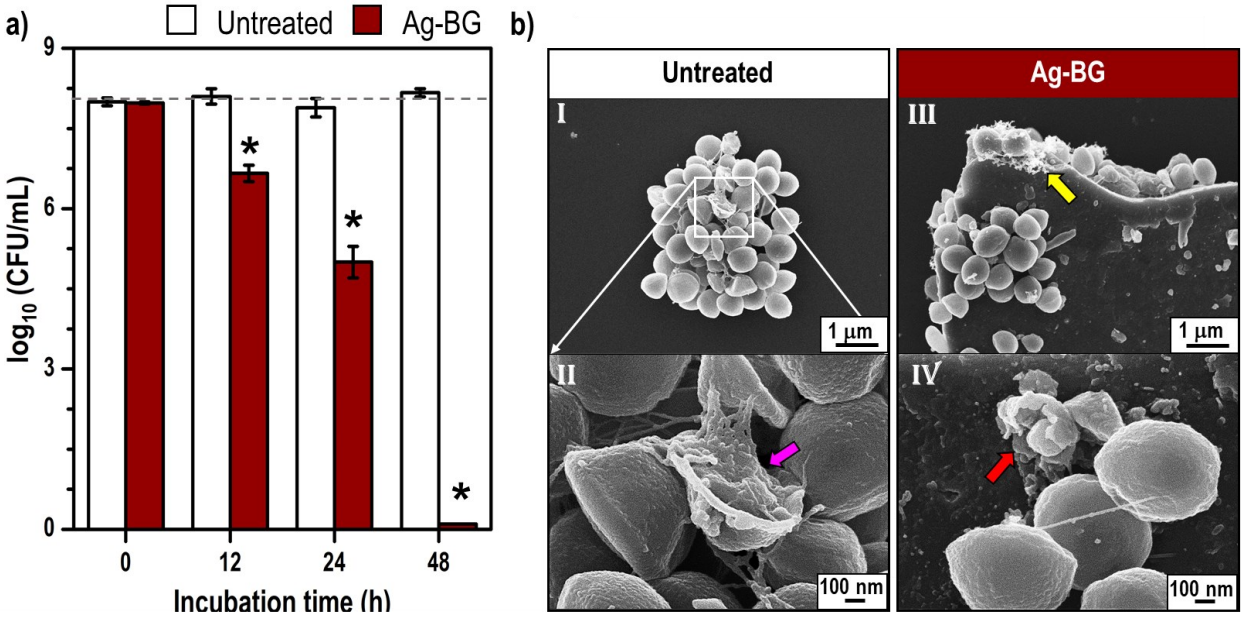

Figure 28: The bactericidal activity of Ag-BG increased over time (a). Suspensions of MRSA (OD_{600} = 1 equivalent to ~ 10^8 CFU/mL, represented by a dash line) were mixed with fresh PBS medium (0 mg/mL, untreated control represented by white bars) and 2.5 mg/mL of Ag-BG (red bars). The CFUs were enumerated for up to 2 days with a limit of detection of 100 CFU. Note that the concentration of untreated bacteria did not decrease over time. (*) Indicates the significant difference between the untreated versus the particle-treated groups ($p < 0.05$). The morphology of untreated (b, I-II) and Ag-BG-treated (b III-IV) MRSA was evaluated in SEM after 12 h in PBS. Extracellular matrix, cytoplasmic content, and cell-wall fragments are indicated with pink, yellow and red arrows, respectively. Modified from [237]

4.3.3. Contribution of oxygen species

To determine the contribution of oxygen to antibacterial activity, growth-arrested MRSA were incubated with Ag-BG and BG microparticles under aerobic and anaerobic conditions (**Figure 29**). Ag-BG exposure led to a decrease in the number of CFUs compared to the control groups in both aerobic and anaerobic conditions. At 2.5 mg/mL of Ag-BG, the aerobic inhibition induced was at least 40% higher than that obtained under anaerobiosis (**Figure 29** a). The inhibition discrepancies between aerobic and anaerobic conditions could be attributed to ROS created by the released Ag^+ ions. The antibacterial activity of BG microparticles also became 15 % more toxic aerobically than anaerobically (**Figure 29** b). Nevertheless, 2.5 mg/mL BG was insufficient to decrease bacterial

viability anaerobically, a task that was achieved at 5 mg/mL. The differences between aerobic and anaerobic conditions in BG suggest the generation of toxic ROS from the material structure.

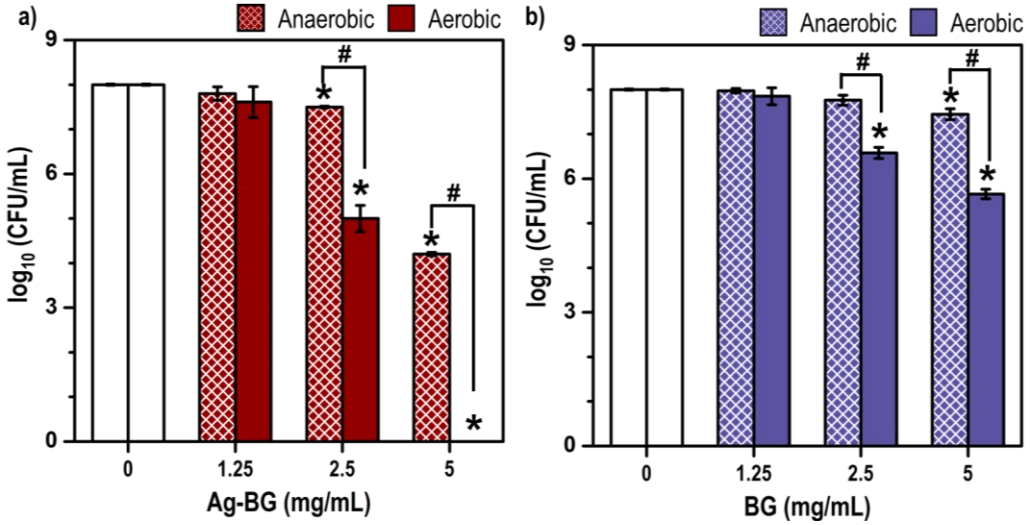

Figure 29: Reactive oxygen species (ROS) play a significant role in the antibacterial activity of Ag-BG (a) and BG (b) microparticles against MRSA. Suspensions of bacteria (OD_{600} = 1 equivalent to ~ 10^8 CFU/mL) were mixed with fresh PBS medium (0 mg/mL, untreated control represented by white bars) and increasing concentrations of Ag-BG or BG under aerobic (plain bars) and anaerobic (patterned bars) conditions. The CFUs were enumerated after 24 h with a limit of detection of 100 CFU. (*) Indicates the significant difference between the untreated versus the particle-treated MRSA, and (#) indicates the significant difference between aerobic and anaerobic conditions ($p < 0.05$).

4.3.4. Inhibition of bacteria biofilm

The Ag-BG and BG microparticles presented strong antibacterial action against bacteria simulating the metabolic state in a biofilm. Here, the ability of Ag-BG to eradicate an *in vitro* biofilm was evaluated against the bioluminescent XEN36 *S. aureus*. Biofilms were grown for 2 days in 24-well plates before exposure to increasing concentrations of microparticles. In **Figure 30** the photon emission was translated to bacterial viability since non-viable bacteria do not emit a light signal. The highest concentration of bacteria is represented in red. Note that no photon emission was detected for Ag-BG and BG dispersed in the medium, thus providing no interference

between the treatment and the bacteria. After 24h, untreated XEN36 grew 20-30 % from its initial concentration, whereas Ag-BG treatment cleared the biofilm as shown by lack of bioluminescence signal (**Figure 30** insets). The gray background observed belong to Ag-BG microparticles attached to the well plate. In agreement with effects detected in planktonic growth-arrested MRSA, 5 mg/mL Ag-BG was utterly toxic to XEN36 biofilm (**Figure 27** a). Similarly, BG significantly reduced bacterial viability while being unable to clear the biofilm.

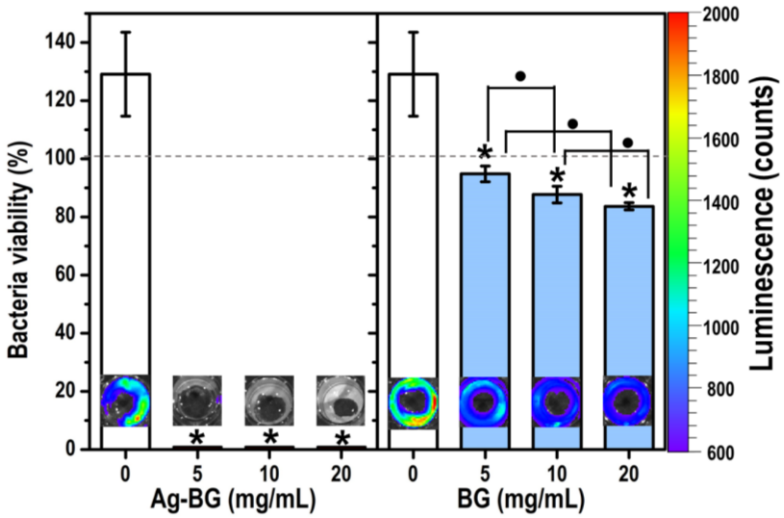

Figure 30: Ag-BG eradicated the XEN36 biofilm after 24 h treatment *in vitro*. BG significantly decreased bacteria viability but did not clear the biofilm. Untreated biofilms (0 mg/mL, represented by white bars) were used as controls. Bacteria viability is reported as % compared to the biofilm before treatment (100 % viability represented by a dashed line). (*) Indicates the significant difference between the untreated versus the particle-treated biofilm, and (●) indicates the significant difference between BG-treatments ($p < 0.05$). Insets show the biofilm luminescence emission from 16 mm diameter wells after treatment.

4.3.5. Development of resistance against Ag-BG

The ability of pathogenic strains to develop resistance to antibacterial treatment is one of the biggest concerns in microbiology and medicine. Therefore, the development of resistance towards 2.5 mg/mL Ag-BG microparticles was evaluated by exposing MRSA to repeated treatments with this dose. Briefly, the original MRSA strain, referred to as WT, was exposed to Ag-BG for 24 h

in growth-arrested conditions (**Figure 31** a). The survivor bacteria presented 2 different colony phenotypes on account of the Ag-BG treatment. Colonies showing a similar size as the WT were identified as “clone type I” whereas those with significantly smaller size were labeled as “clone type II” (**Figure 31** b). Both of these clones were treated again with 2.5 mg/mL of Ag-BG for 24 h and resulted in two phenotypes: colonies with similar size to their untreated control and smaller colonies. The next generations were collected, maintaining the same categorization criteria: colony type I had the same size as the untreated control, and colonies type II were smaller than their untreated control. Therefore, the bacteria analyzed from colony type I had a comparable size to WT, while clone type II became consistently smaller as the generations progressed.

Ag-BG had a similar inhibitory effect on clone type I than WT (**Figure 31** c) over 3 consecutive generations. Conversely, a different behavior was observed for colony type II, which grew less CFU than WT and kept decreasing with the next generations (**Figure 31** d), despite the fixation of the MRSA concentration to OD_{600} = 1. The inhibitory capability of Ag-BG increased with the generations in clone type II. In the last generation evaluated (G3), Ag-BG was lethal to bacteria, decreasing the CFUs below a limit of detection of 10 CFU.

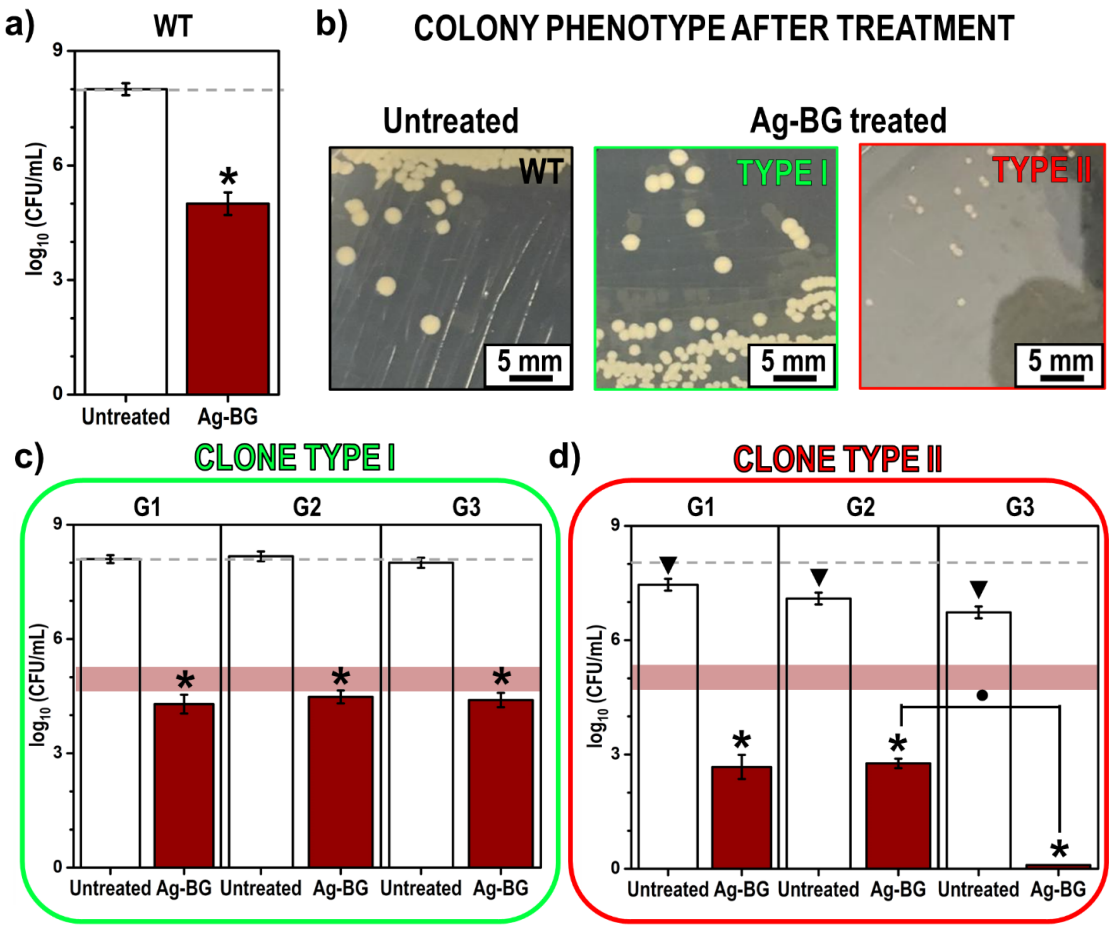

Figure 31: The antibacterial activity of Ag-BG (a) induced phenotypic changes in wild-type (WT) MRSA after treatment in grow-arrested conditions (b). Colonies were classified depending on their size. Clone type I identifies colonies that maintained the same size as the WT, while clone type II identifies the ones that became smaller. A surviving colony after Ag-BG treatment was collected to produce the different generations (G_x). Ag-BG had a similar effect on clone type I than in the WT (c) regardless of the generation. Clone type II developed higher sensitivity towards Ag-BG treatment, which increased with the generation (d). The red shaded line (c and d) indicates the CFU resulted from Ag-BG-treated WT as illustrated in (a) for reference. Each clone and generation's bacterial suspension was always prepared with $OD_{600} = 1$ and mixed with fresh PBS to serve as a control (white bars). The untreated WT and clone type I groups grew up to 10^8 CFU/mL (indicated as a dashed line), while clone type II yielded consistently lower CFU as the generations progressed. The CFUs were enumerated after 24 h with a limit of detection of 10-100 CFUs. The statistical significance for $p < 0.05$ is indicated with (▼) between the untreated group in WT and clone type II, (*) between untreated and Ag-BG-treated at each generation, and (●) between Ag-BG-treated bacteria of a different generation.

The colony phenotypes observed in **Figure 31** were correlated with structural changes by electron microscopy (**Figure 32** a). WT bacteria presented the characteristic cocci-shape (i.e., spherical) with 500 nm diameter and 40 nm cell-wall thickness (**Figure 32** b). Clone type I maintained the same cell size and spherical shape as WT through generations, but its cell-wall thinned to 20 nm (**Figure 32** c-d). Note that the surface of WT and clone type I was plain and smooth. In contrast, clone type II bacteria appeared in multi-cellular clusters, swollen and undivided (**Figure 32** a). These features are correlated to an impaired and uncompleted mother-daughter cell division, which is characteristic of small colony phenotypes in *Staphylococcus* strains. Because of the irregularities in cell shape and dispersity, the cell size could not be accurately measured. The location of the septa favored one side of the bacteria, leading to asymmetrical cell division. Additional information and images of structural features in MRSA clones at each generation are presented in **Figure S5**, Appendix C. Additionally, the surface of clone type II bacteria developed two apparent features. Fibrils (marked with pink arrows in **Figure 32** a) grew around the bacteria as strings and were also found between several bacterial units. Crumbs (marked with purple arrows in **Figure 32**) looked like small spheres and may result from the condensation of fibrils. These features were organic as identified by SEM-EDS (**Figure S6**, Appendix C), and their development is hypothesized to increase surface adherence and, therefore, be responsible for forming multi-cellular clusters. The cell-wall of colony type II was initially thinner than WT's, but then, it thickened after the 3 consecutive treatments, almost doubling the cell-wall of WT (**Figure 32** d).

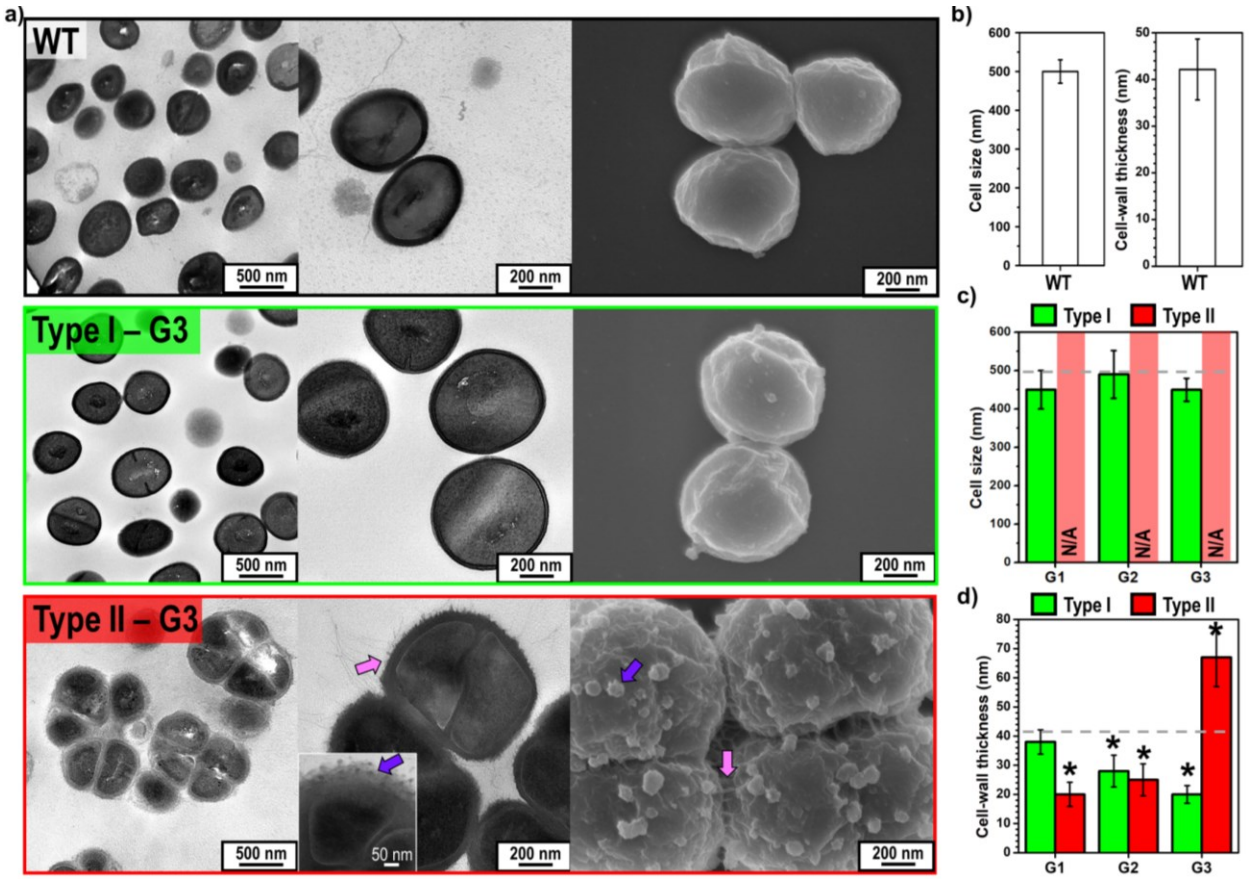

Figure 32: The produced colony phenotypes present different morphological and structural features than WT (a). Clone type II at the G3 developed hair-like extensions (pink arrows) and spherical elements (purple arrow) around the surface. Cell size and cell-wall thickness measurements of WT (b) are represented as a dashed line for comparison. The cell size in clone type I was similar to WT (c) and could not be accurately measured in clone type II due to cell aggregation (indicated as N/A). The cell-wall thickness presents a decreasing trend as generations progressed from the G1 to the G3 in clone type I and from the G1 to the G2 clone type II (d). Note that the cell-wall thickness increased in the G3 of clone type II above that of WT. Measurements were collected from at least 100 bacteria. The statistical difference $p < 0.05$ between WT and the clones is indicated with (*).

The material-bacteria interaction after exposing G3 clone type II to Ag-BGNs was also evaluated in TEM (**Figure 33**). Similar to the SEM observations (**Figure 28** b), the cells of this small colony variant surrounded microparticles, probably attempting to colonize the surface. The envelope was thinner than in G3 clone type II untreated (**Figure 32** a) and hard to identify after treatment, although it still presented surface fibrils. Additionally, nano-size debris was found to accumulate in the cytoplasm.

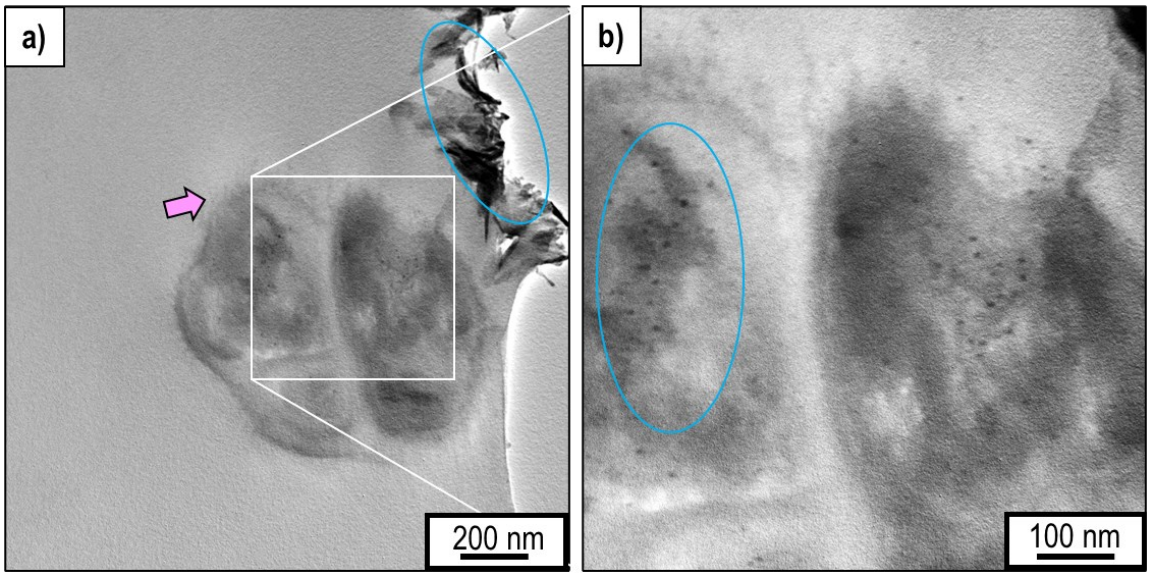

Figure 33: Structure of a G3-clone type II multi-cellular cluster after 24 h of Ag-BG treatment in PBS. (a) The cells presented surface appendices (pink arrow) and surrounded Ag-BG microparticles (blue circle). (b) Intracellular accumulation of nano-size debris (white circle).

4.3.5.1. Genome mutations after Ag-BG treatment

The genome of G3-clone type II was sequenced to correlate genetic and phenotypic changes. The cluster of orthologous group functional prediction was investigated for each SNP. Interestingly, most SNPs displayed non-synonymous changes leading to single amino acid changes, and one insertion leading to a frameshift was detected (**Table 11**). A hypothetical lipoprotein, SAUSA300_0100, with a K to Q amino acid change is predicted to be involved in cell wall/membrane/envelope biogenesis (Table 1). Other SNPs are predicted to be involved in amino acid metabolism (SAUSA300_0315, SAUSA300_1753), inorganic ion transport (SAUSA300_0611), or post-translational modification (SAUSA300_1539).

Table 11: Single nucleotide polymorphism (SNPs) from the genome sequence of G3-clone Type II MRSA.

loci	description	nucleotide change	coverage	frequency	p-value	protein change	COG*
SAUSA300_0050	hypothetical	G61025A	65	100	1.00E-208	L->F	S
SAUSA300_0100	tandem lipoprotein	A110752C	168	45.20	1.30E-111	K->Q	M
SAUSA300_0315	N-acetylneuraminate lyase	C376057T	82	100	2.50E-271	D->N	EM
SAUSA300_0611	hypothetical	T684887C T684884G Insertion 684889-68488 1bp	31 26 32	35.50 65.40 62.50	7.00E-15 5.00E-10 1.80E-7	L->S I->S frameshift	P
SAUSA300_1169 (ftsK)	DNA translocase	A1286986G	46	100	1.62E-152	K->R	D
SAUSA300_1444	segregation and condensation protein B	A1599008C	36	41.70	5.40E-33	L->R	D
SAUSA300_1539	chaperone protein DnaJ	C1688528T	55	92.70	2.10E-158	A->T	O
SAUSA300_1753	serine protease SpiF	C1939443G	88	100	1.60E-185	A->V	E
SAUSA300_2231 (fdhD)	formate dehydrogenase accessory protein	C2549677T	69	37.70	2.70E-57	E->G	C
SAUSA300_2372	adenosylmethionine-8-amino-7-oxononanoate aminotransferase	C2549677T	58	98.30	2.30E-181	R->H	H

* Cluster of Orthologous Groups (COG) abbreviation key. RNA processing and modification (A); chromatin structure and dynamics (B); energy production and conversion (C); cell cycle control and mitosis (D); amino acid metabolism and transport (E); nucleotide metabolism and transport (F); carbohydrate metabolism and transport (G); coenzyme metabolism (H); lipid metabolism (I); translation (J); transcription (K); replication and repair (L); cell wall/membrane/ envelope biogenesis (M); cell motility (N); post-translational modification, protein turnover, chaperone function (O); inorganic ion transport and metabolism (P); secondary structure (Q); general functional prediction only (R); function unknown (S); signal transduction (T); intracellular trafficking and secretion (U); nuclear structure (Y); cytoskeleton (Z).

4.3.5.2. Antibiotic sensitivity restoration after the mutation

The ability of MRSA to develop antibiotic resistance has rendered most common treatments ineffective, as is the case of high concentrations of oxacillin and fosfomycin that are well tolerated by these bacteria (**Figure 34** a-b). After Ag-BG treatment, MRSA underwent significant structural modifications. In this section, the antibiotic-resistance of clone type II is briefly explored. As previously mentioned, clone type II presented impaired cell division, which led to fewer CFUs than WT. For example, a suspension concentration of OD_{600} =1 in WT and clone type II is equivalent to 10^8 and 10^7 CFU/mL (marked with dashed lines in (**Figure 34**), respectively. After 24 h propagating in TSB, both strains grew almost 2-ten folds (i.e., from 10^8 to 10^{10}).

In contrast to WT, clone type II growth was significantly inhibited upon exposure to oxacillin and fosfomycin for 24 h (**Figure 34** c-d). Sterile conditions were not achieved even at concentrations of 100 μg/mL. Nevertheless, these results suggest that the administration of ineffective antibiotics after several Ag-BG treatments restores their antibacterial capability.

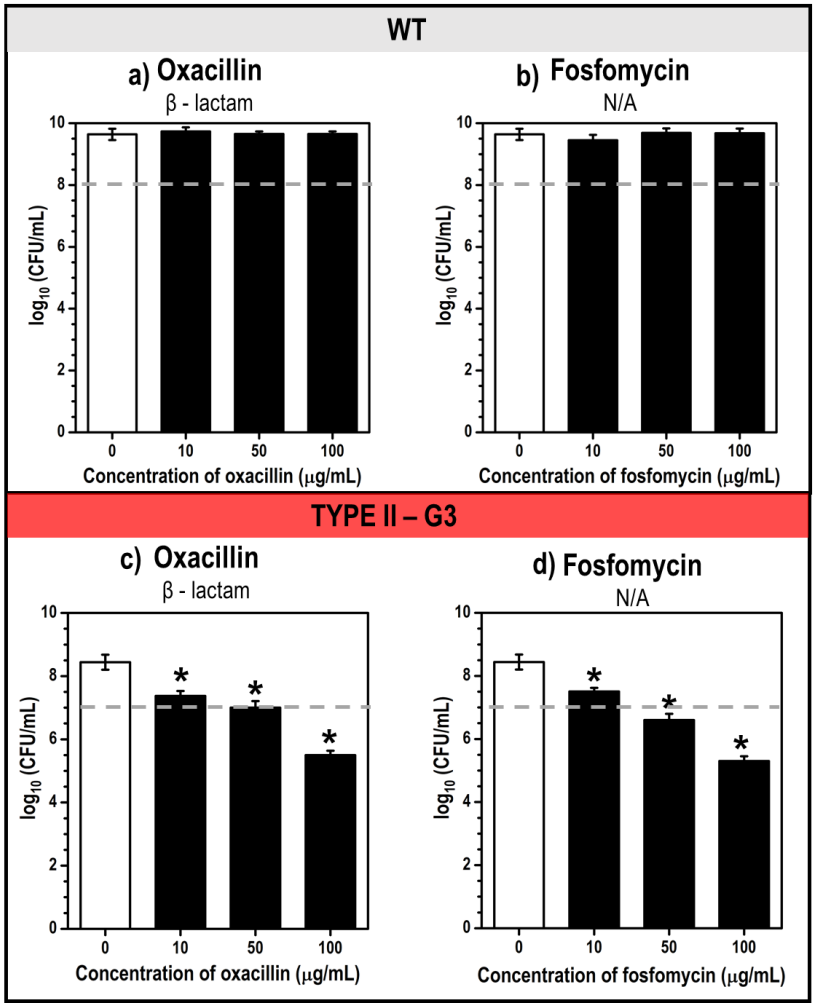

Figure 34: Consecutive Ag-BG-treatments generate a MRSA mutant responsive to antibiotics. MRSA WT is resistant to oxacillin (a) and fosfomycin (b) after 24 h exposure under growth-assisted conditions. Clone type II at the G3 acquired higher sensitivity to both oxacillin (c) and fosfomycin (d) after 24 h. The bacterial suspensions were prepared with OD_{600} = 1 in fresh TSB (white bars). Note that the untreated WT and clone type II presented 10^8 and 10^7 CFU/mL at 0 h (represented with dashed lines), respectively. The CFUs were enumerated with a limit of detection of 100 CFU. The statistical significance $p<0.05$ between untreated and antibiotic-treated MRSA is indicated with (*).

4.3.6. The resurrection of antibiotics by combination with Ag-BG

The combination of heavy-metals like Ag and antibiotics has been reported synergistic in the literature [11,12,172,244], and it is a common phenomenon in Ag-containing materials like Ag-BG microparticles. In this section, the ability of Ag-BG to synergize with antimicrobials was

expanded towards antibiotic-resistance scenarios. As previously presented, concomitant Ag-BG treatments induced phenotypic mutations and genome alterations that reduced antibiotic tolerance (**Figure 34**). It was hypothesized that treating MRSA directly with a combination of Ag-BG and highly-tolerated antibiotics would trigger the restoration of their antibacterial activity similarly and accelerate the inhibitory process.

4.3.6.1. Effect of the antibiotic type on the synergism

Antibiotics were selected based on their bacterial target (i.e., cell-wall, ribosomes, and DNA) and combined with Ag-BG at concentrations below their MIC, at which antibiotics alone were ineffective against MRSA (black bars in **Figure 35** and **Figure 36**). These combinations were labeled as Ag-BG/antibiotic. The antibacterial capability of Ag-BG/antibiotics was first evaluated under growth-arrested conditions to simulate the metabolic state of a biofilm (**Figure 35**), using a 2.5 mg/mL Ag-BG concentration according to its basal activity in PBS (**Figure 27** a and **Figure 28** a).

Oxacillin and fosfomycin are two cell-wall targeting antibiotics to which MRSA is resistant. The β-lactam oxacillin blocks the action of the penicillin-binding proteins (PBPs) that assemble the cell-wall [245], whereas fosfomycin inhibits the UDP-N-acetylglucosamine-3-enolpyruvyltransferase, MurA an essential enzyme required for peptidoglycan and cell-wall synthesis [246]. Exposure to 0.1 µg/mL of oxacillin and 2.5 mg/mL of Ag-BG (Ag-BG/oxa) enhanced bactericidal activity over time (**Figure 35** a) beyond that of either agent alone. Additionally, 12h after administering 0.05 µg/mL fosfomycin with Ag-BG (Ag-BG/fosfo), inhibition was also achieved (**Figure 35** b). The antibacterial activity was also time-dependent. Moreover, Ag-BG enhanced the bactericidal activity of other cell-wall targeting antibiotics like

vancomycin, a glycopeptide that blocks cell-wall synthesis by binding and occluding access to the D-Ala-D-Ala termini of Lipid II [247]. Thus, the transport of new cell-wall precursors from the cytoplasm to the peptidoglycan is precluded. Although MRSA is not resistant to vancomycin, it can tolerate up to 10 mg/mL of the antibiotic under growth-arrested conditions. Exposure to 0.5 mg/mL vancomycin with Ag-BG (Ag-BG/vanc) significantly decreased MRSA viability after 12 h (**Figure 35** c). Similar to other antibiotics, Ag-BG/vanc was more toxic over time. Therefore, Ag-BG was able to restore the inhibition potential of cell-wall targeting antibiotics.

The synergism between Ag-BG and antibiotics inhibiting protein synthesis was more variable depending on the antibiotic type. In this work, three groups of protein inhibitors were tested. Aminoglycosides, like gentamycin and tobramycin, provide inhibition owed to their cationic nature[248]. The antibiotic molecule's positive charge presents a high electrostatic affinity to bond with negatively charged biomolecules like membrane lipids and RNA [249,250]. Once inside the bacteria, aminoglycosides bind to the A site of the 30S ribosomal subunit, causing mistranslation of mRNA and premature termination of the peptide chain [251–254]. MRSA is not resistant to gentamycin and tobramycin. Exposing bacteria to a combination of Ag-BG and gentamycin (Ag-BG/gent) (**Figure 35** d) or tobramycin (Ag-BG/tobra) (**Figure 35** e) did not improve the overall inhibition. Similarly, Ag-BG did not synergize with erythromycin (Ag-BG/ery) (**Figure 35** f), which binds to the 50S ribosomal subunit for irreversibly inhibiting protein synthesis at two stages: impairing tRNA translocation and inducing abortion of peptide elongation by blocking the exit tunnel [255]. MRSA presents erythromycin-resistance [256] and, when exposed to sub-inhibitory concentrations of the drug, did not synergize with Ag-BG. Chloramphenicol is a broad-spectrum bacteriostatic antibiotic that blocks protein synthesis by reversible inhibition of the peptidyl transferase reaction at the 50S ribosomal subunit, and hence preventing peptide bond formation

between amino acids [257]. Although no intrinsic resistance to chloramphenicol has been observed for MRSA [258], high tolerance was found under growth-arrested conditions, as expected from its bacteriostatic nature. Ag-BG strongly synergizes with chloramphenicol (Ag-BG/cpl) under growth-arrested conditions (**Figure 35** g).

Ciprofloxacin is a benchmark fluoroquinolone agent whose primary mechanism is the inhibition of DNA gyrase [259]. This enzyme is responsible for the compaction of the DNA strands to fit in the spatial constrain inside the bacteria, and its inhibition puts a hold on bacterial replication. MRSA is not resistant to ciprofloxacin. Exposing MRSA to 0.05 μg/mL of ciprofloxacin with Ag-BG (Ag-BG/cip) significantly decreased bacteria viability after 12 h (**Figure 35** h). Similar to other antibiotics, Ag-BG/cip was more toxic over time.

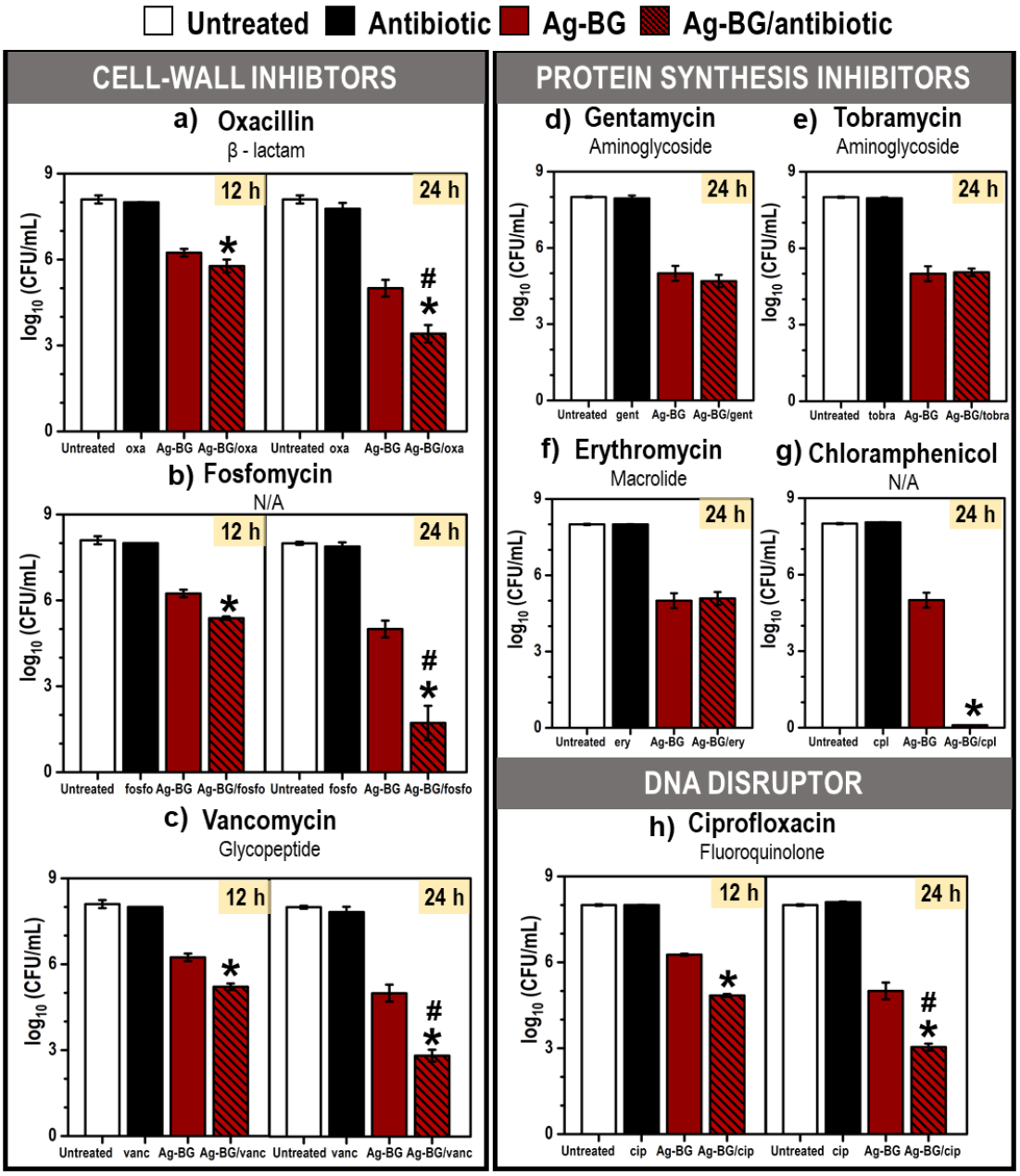

Figure 35: Ag-BG resurrects selected antibiotics against MRSA under growth-arrested conditions. Ag-BG synergizes with cell-wall targeting antibiotics: oxacillin (a - 0.1 µg/mL), fosfomycin (b - 0.05 µg/mL) and vancomycin (c - 500 µg/mL). Ag-BG's combination with protein synthesis inhibitors showed no synergism for aminoglycosides gentamycin and tobramycin (d and e - 0.01 µg/mL) nor erythromycin (f, 5 µg/mL). Chloramphenicol (g - 1 µg/mL) and ciprofloxacin (h - 0.05 µg/mL) became more toxic to MRSA when delivered with Ag-BG. Suspensions of MRSA (OD_{600} = 1 equivalent to ~ 10^8 CFU/mL) were mixed with fresh PBS medium (untreated control - white bars), antibiotic (black bar), 2.5 mg/mL of Ag-BG (red bars) or a combination of substances (red pattern bars). Note that antibiotics alone were ineffective against MRSA. The CFUs were enumerated after 12 h and 24 h, as specified, with a limit of detection of 100 CFU. (*) Indicates the significant difference between Ag-BG and Ag-BG/antibiotic and (#) the significant difference for the combination at the two different time points ($p < 0.05$). Modified from [237].

Previous results have shown that Ag-BG was bactericidal against metabolically active MRSA (**Figure 27** c), and thus, it could be used to prevent bacterial colonization and infection development. On this basis, the antibacterial potential of the Ag-BG/antibiotic combinations was also evaluated under growth-assisted conditions. A higher concentration of Ag-BG (~ 20 mg/mL) was required to achieve a basal inhibition level against active MRSA. Oxacillin and fosfomycin were selected owed to the unique capability of Ag-BG to resurrect their activity in PBS. The combination of Ag-BG with 0.8 µg/mL of oxacillin (Ag-BG/oxa) (**Figure 36** a) and 0.4 µg/mL of fosfomycin (Ag-BG/fosfo) (**Figure 36** b) was also synergistic against active MRSA. Similarly, the combination of Ag-BG with ciprofloxacin (Ag-BG/cip) significantly enhanced the antibiotic's action at sub-inhibitory levels (**Figure 36** c). These results prove Ag-BG retained its antibiotic re-sensitization capability under virulent conditions.

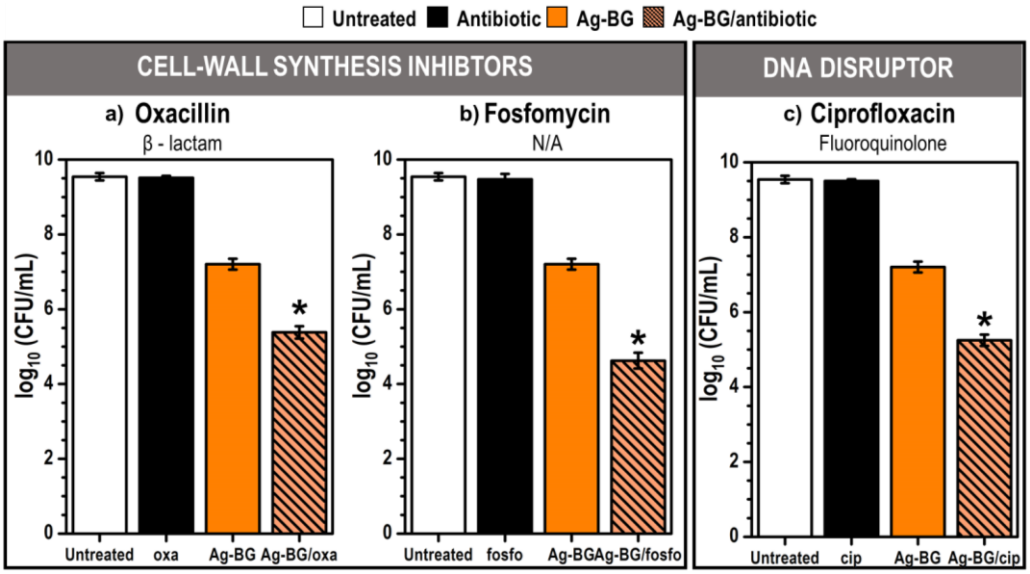

Figure 36: Ag-BG resurrects the inhibitory action of oxacillin and fosfomycin and decreases the MIC of ciprofloxacin against MRSA under growth-assisted conditions. MRSA was exposed to antibiotics (black bars): oxacillin (0.8 µg/mL) (a), fosfomycin (0.4 µg/mL) (b), ciprofloxacin (0.1 µg/mL) (c); Ag-BG (20 mg/mL – orange bars) and a combination of substances (orange pattern bars). Suspensions of MRSA (OD_{600} = 1 equivalent to ~ 10^8 CFU/mL) were mixed with fresh TSB medium (untreated control - white bars). Note that antibiotics alone were ineffective against MRSA. The CFUs were enumerated after 24 h with a limit of detection of 100 CFU. (*) Indicates the significant difference $p < 0.05$ between Ag-BG and Ag-BG/antibiotic treatments.

4.3.6.2. Bacteria structure after combinatorial treatment

The antibacterial activity of the different antibiotic and/or Ag-BG combinations was also evaluated in terms of structural modifications in bacteria (**Figure 37**). As mentioned before, MRSA is a cocci-shaped bacterium with a 500 nm diameter approximately. Bacteria presented a uniformly thick cell-wall well attached to the cytoplasm (**Figure 37** A–C). The homogeneity of the electron-density of the cell-wall and the smooth transition from the wall to the cytoplasm are characteristic of healthy bacteria. These features were also representative of MRSA exposed to oxacillin (**Figure 37** D–F), fosfomycin (**Figure 37** G–I), and vancomycin alone (**Figure 37** J–L), confirming MRSA resistance to these antibiotics. However, the bacteria exposed to Ag-BG concentrated in the areas near the microparticles (marked with blue lines, **Figure 37** M–O) and harbored a damaged cell-wall that allows the release of cytoplasmic content (marked with yellow arrow).

The damaged cell-wall areas are underscored by a loss of electron-density contrast and irregular thickness. Released cytoplasmic contents can also be found near some of the cells. Additionally, MRSA developed a clear void (red arrows) between the cell envelope and cytoplasm after exposure to Ag-BG. The difference in the size of gaps and the status of the damaged cells suggest the void space increased over time, creating a localized separation before the cell-wall breakdown and the release of the cellular content. These features were exacerbated after 24 h with the Ag-BG/oxa combination (**Figure 37** P–R). MRSA presented an apparent cytoplasmic membrane disruption (**Figure 37** Q) and a void space between the cell envelope and cytoplasm (**Figure 37** R, red arrows).

Moreover, many bacteria contained a damaged cell-wall separated from the cytoplasm (yellow arrows). In the case of MRSA exposed to the Ag-BG/fosfo combination (**Figure 37** S-U), intact

bacteria were rarely observed. Instead, nano-sized Ag-BG pieces, originating from microparticle degradation in the medium, accumulated within the cellular material (areas highlighted with blue lines). Fragmented cell-walls and cytoplasmic content are also observed detached from bacteria (**Figure 37** U). Finally, bacteria exposed to Ag-BG/vanc (**Figure 37** V–X) showed similarities with those treated with the Ag-BG/fosfo combination, such as accumulations of Ag-BG pieces within cellular structures were observed (**Figure 37** W and X, marked with blue lines). Interestingly, nano-tunnel/channels were created in the dark gray areas (**Figure 37** V, marked with black arrow), showing the penetration of nano-sized particles through the cell-wall. Substantial ultrastructural changes were apparent in the more prominent diameter of the silhouettes of treated vs. untreated bacteria.

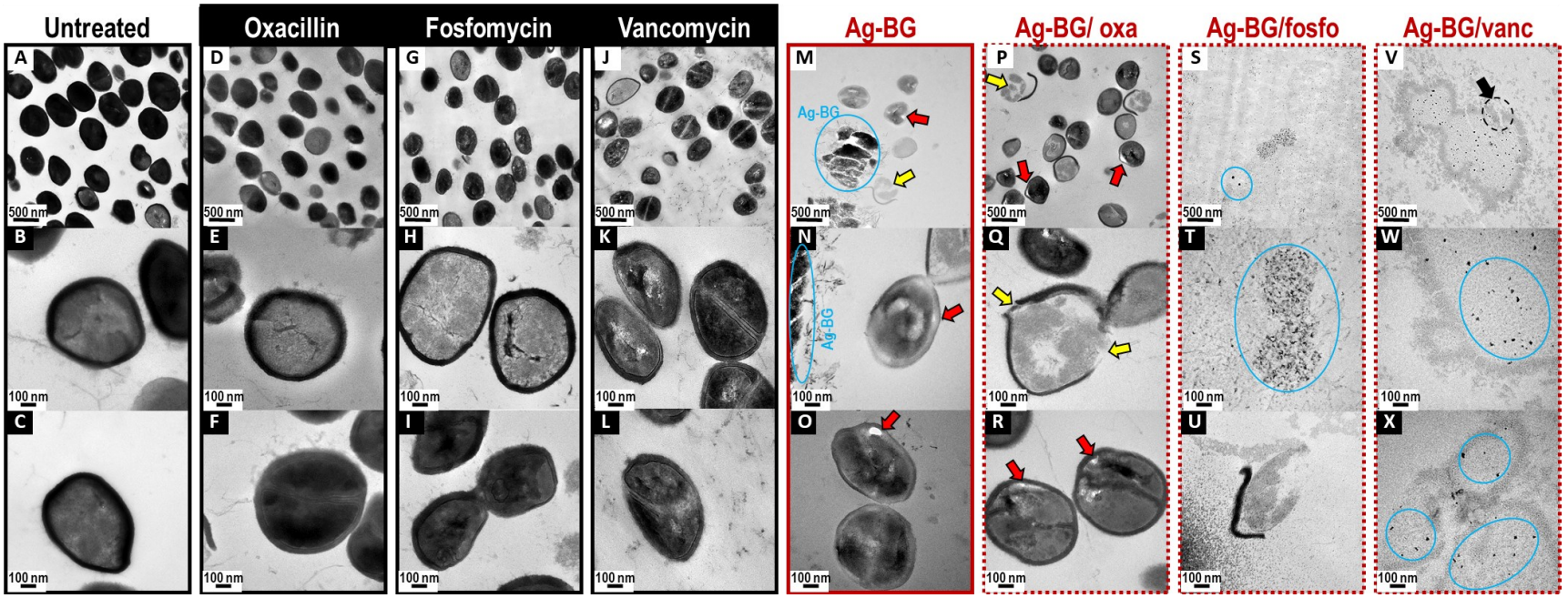

Figure 37: TEM images of bacteria untreated (A–C), after being exposed for 24 h to oxacillin alone (D–F), fosfomycin alone (G–I), vancomycin alone (J–L), Ag-BG microparticles alone (M–O), or to the combinations: Ag-BG/oxa (P–R), Ag-BG/fosfo (S–U), and Ag-BG/vanc (V–X). Ag-BG micro-sized and nano-sized particles were marked with blue lines. Yellow arrows point to damaged cells. Red arrows indicate the void formation between the cell envelope and cytoplasm, and the black arrow marks a nano-tunnel/channel. Modified from [237].

4.3.6.3. Concentration-dependent inhibition of the antibacterial agent

The capability of Ag-BG to synergize with antibiotic previously explored for a single combination of Ag-BG/antibiotic (**Figure 35** and **Figure 36**) is here expanded to understand how to tailor the concentration of antibacterial agents for maximum inhibition. Increasing the Ag-BG concentration (1.25-5 mg/mL) leads to higher inhibition of MRSA growth when exposed to a single concentration of vancomycin (0.5 mg/mL) (**Figure 38**). Combination 1.25 mg/mL/0.5 mg/mL Ag-BG/vanc did not induce a statistically significant reduction in bacterial viability. However, 2.5 mg/mL Ag-BG in the Ag-BG/vanc combination provided a similar inhibition level to 3.75 mg/mL of Ag-BG alone. This trend indicates that synergy with the antibiotic requires concentrations of AG-BG that are able to cause significant damage alone. Next, increasing concentrations of antibiotics were combined with 2.5 mg/mL Ag-BG to identify the minimum concentration required for synergism. Three antibiotics with different bacterial targets were selected for this study based on their previous synergism with Ag-BG. Note that the concentration of antibiotics in all combinations was below their reported MIC to reproduce antibiotic-resistance.

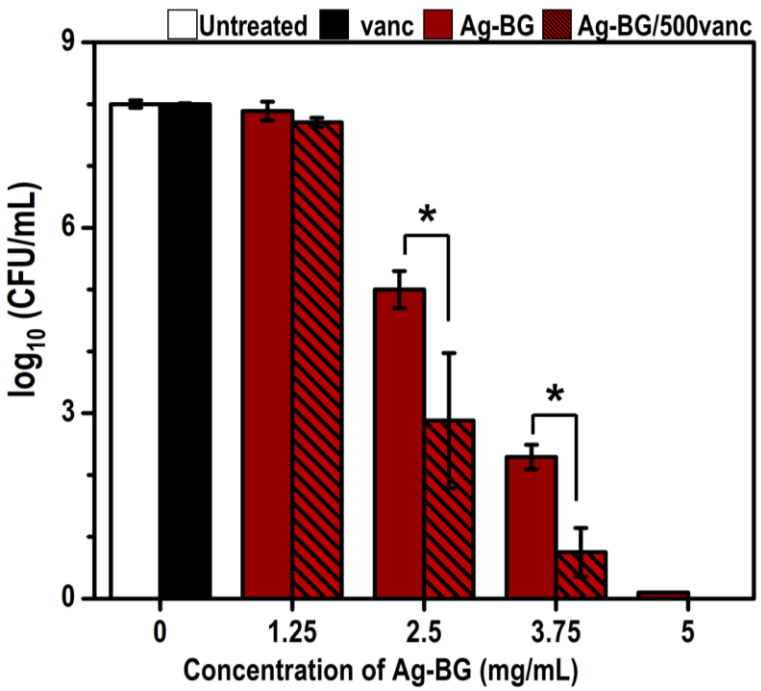

Figure 38: Ag-BG synergizes with vancomycin for concentrations above the MIC of Ag-BG (2.5 mg/mL). Suspensions of bacteria (OD_{600} = 1 equivalent to ~ 10^8 CFU/mL) were mixed with fresh PBS medium (0 mg/mL, untreated control, white bars), 500 µg/mL of vancomycin (antibiotic control, black bars) and increasing concentration of Ag-BG (red bars) and their combination with 500 µg/mL of vancomycin (Ag-BG/vanc, patterned bars). The grey shaded line indicates the CFU resulted from vancomycin treatment alone for reference. The CFUs were enumerated after 24 h with a limit of detection of 100 CFU. (*) Indicates the significant difference between Ag-BG and Ag-BG/500vanc ($p < 0.05$). Modified from [238].

Inhibition of MRSA increased with antibiotic concentration (**Figure 39**). Synergism with vancomycin was observed at a minimum concentration of 300 µg/mL since Ag-BG/vanc combinations, including lower antibiotic concentrations, provided higher inhibition than Ag-BG alone (**Figure 39**a). Chloramphenicol was synergistic with Ag-BG at 1 µg/mL, and based on the inhibition level (**Figure 39** b), a decrease in its concentration would not lead to synergism. The Ag-BG/cipro combination (**Figure 39** c) showed potent inhibition already at ~0.05 µg/mL, and synergism may be maintained for an even slightly lower antibiotic concentration. Sterile conditions could be achieved by tailoring the concentration of antibiotics in the Ag-BG/antibiotic system. Specifically, the combination of 2.5 mg/mL Ag-BG with either 1000 µg/mL vancomycin, 5 µg/mL

chloramphenicol, or 0.1 µg/mL ciprofloxacin inhibited bacterial growth below a detection limit of 10 CFU.

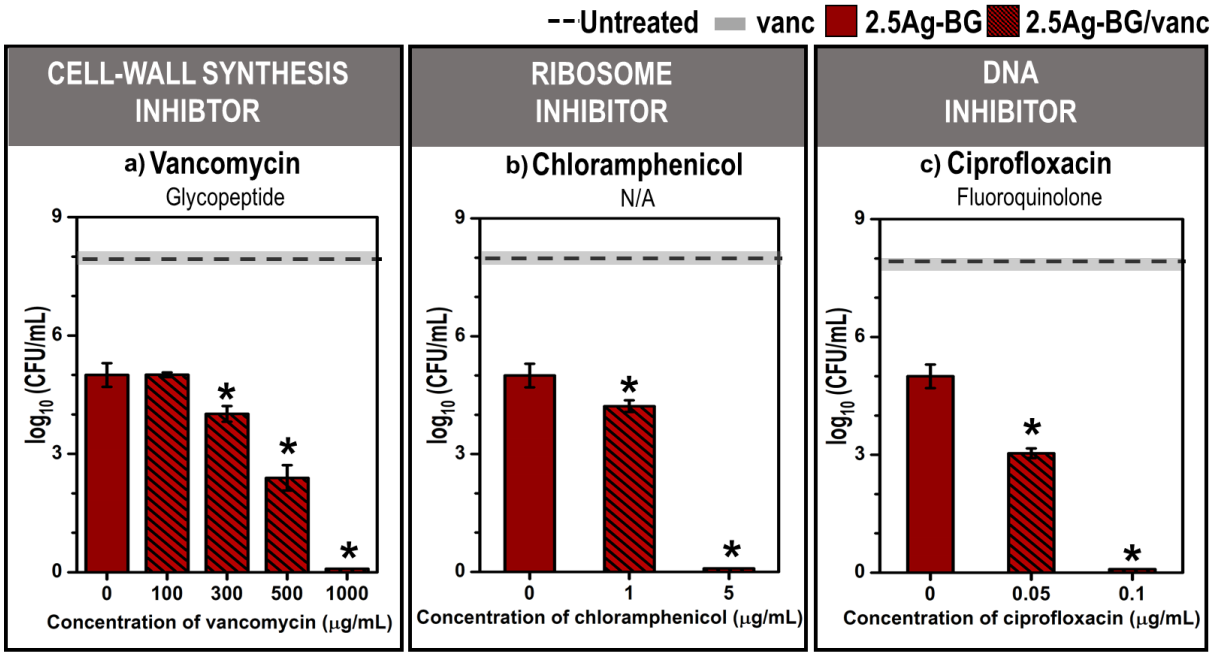

Figure 39: The concentration of vancomycin (a), chloramphenicol (b), and ciprofloxacin (c) combined with Ag-BG tailor the inhibition power of the Ag-BG/antibiotic system against growth-arrested MRSA. Suspensions of bacteria (OD_{600} = 1 equivalent to ~ 10^8 CFU/mL) were mixed with fresh PBS medium (untreated control represented by dashed line), 2.5 mg/mL of Ag-BG (red bar) and a combination of 2.5 mg/mL Ag-BG with increasing concentrations antibiotics (patterned bars). The grey shaded line indicates the CFU resulted from antibiotic treatment alone for reference. Note that antibiotics alone were ineffective against MRSA since the concentration used was below their MIC, as reported in **Table 6**. The CFUs were enumerated after 24 h with a limit of detection of 10 CFU. (*) Indicates the significant difference between 2.5Ag-BG and 2.5Ag-BG/antibiotic ($p < 0.05$). Modified from [238].

4.3.6.4. Role of Ag^+ ion in the synergistic effect

The role of Ag^+ ions in the restorative capability of Ag-BG was evaluated by comparing the inhibiting potential of Ag-BG/fosfo to that of BG/fosfo. MRSA were exposed to 2.5 mg/mL microparticles/0.05 µg/mL fosfomycin combinations (**Figure 40**). After 24 h, Ag-BG was considerably more lethal to bacteria than BG alone. The synergy of Ag-BG with fosfomycin against MRSA is in agreement with previous results. Interestingly, BG was also able to restore

fosfomycin's antibacterial capability, although it provided lower inhibition than its Ag-containing counterpart. These findings demonstrate that the synergism of microparticles with antibiotics is not limited to the presence of Ag^{+} ions, although they hold an influential role in the bactericidal action.

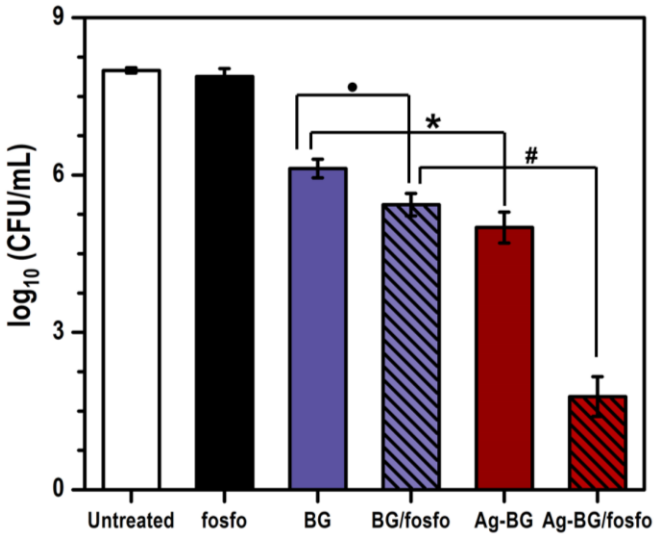

Figure 40: BG shows antibacterial properties and synergizes with fosfomycin (fosfo) to reduce MRSA viability under growth-arrested conditions (i.e., PBS medium). MRSA was exposed to fosfomycin (fosfo, 0.05 µg/mL – black bar), Ag-BG (2.5 mg/mL – red bar), or a combination of the substances (Ag-BG/fosfo – red pattern bar) but also to BG (2.5 mg/mL – purple bar) and a combination of the substances (BG/fosfo – purple pattern) for 24 h before the enumeration of CFU. The white bar indicates the CFU for the untreated control (0 mg/ml). (d) Indicates the significant difference between BG and the combination BG/fosfo, (*) the significant difference between BG and Ag-BG, and (#) the significant difference between the combinations BG/fosfo and Ag-BG/fosfo ($p < 0.05$). Modified from [237].

4.4. Ag-BG as therapeutic carrier against resistant infections

The unique capability of Ag-BG microparticles to resurrect antibiotics while simultaneously promoting new bone formation, as presented in sections 4.2 and 4.3, offering new hope to fight antibiotic-resistance in bone degenerative diseases.

4.4.1. Antibiotic immobilization on Ag-BG microparticles

The conjugate was developed following a co-precipitation method by incubating Ag-BG in a PBS bath containing vancomycin [260–262]. As previously stated, exposing Ag-BG to a medium triggers the release of ions from its structure. In this case, the release will lead to the supersaturation of the bath and, consequently, the precipitation of vancomycin.

The antibiotic uptake efficiency was evaluated by immersion in the bath after 2, 6, and 24 h. The mass of vancomycin loaded was indirectly measured as described in section 3.7.2. After 2 h of immersion, Ag-BG incorporated almost 50 % of the vancomycin it was initially exposed to (**Figure 41** a). Although extending the immersion period increased vancomycin uptake, no significant improvement was observed between 6 h and 24 h. Considering the trend of antibiotic deposition in Ag-BG, and considering that excessive antibiotic deposition can cause a considerable delay in drug release [263,264], 6 h was selected as the optimum uptake time, and the resulting loaded microparticles are hereafter referred to as Ag-BG@vanc conjugate.

The structure of Ag-BG before and after antibiotic uptake was evaluated to confirm the presence of antibiotics (**Figure 41** b). The FT-IR spectrum of Ag-BG has been presented previously and is used here as a reference. Briefly, Ag-BG presents the characteristic peaks of a semi-crystalline silicate network with vibration for Si-O (450, 800, 900-1200 cm^{-1}) and P-O bonds (575-605 and

900-1200 cm^{-1}). Vancomycin (analyzed in powder form) showed the typical vibrations of any organic compound; specifically, O-H groups at 630 and 1600 cm^{-1} and C-O groups at 1400 cm^{-1} and a characteristic peak at 700-800 cm^{-1}. After immersion in the antibiotic bath, the resulting Ag-BG@vanc conjugate presented a combination of the vibrations mentioned above, demonstrating vancomycin loading. Interestingly, the double P-O vibration at 575-605 cm^{-1} appeared sharper after antibiotic uptake, suggesting the precipitation of phosphate-rich minerals was taking along with vancomycin.

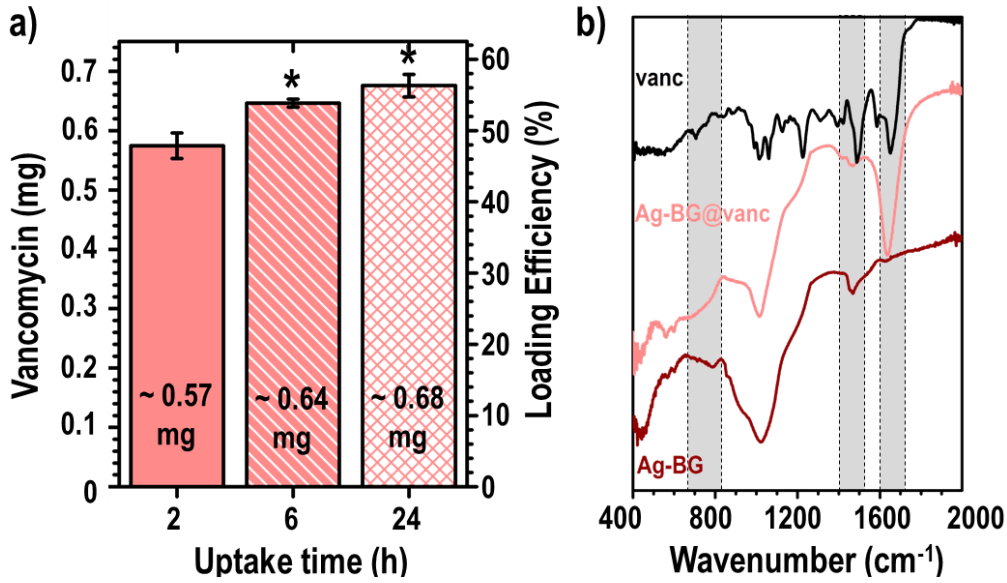

Figure 41: Mass of vancomycin (vanc) loaded on Ag-BG particles after 2, 6, and 24 h uptake time (a). The loading efficiency represents the % of vancomycin loaded from the initial uptake solution. Statistical significance $p < 0.05$ between 2 h uptake time the other groups is indicated as (*). No statistical difference was obtained between 6 and 24 h uptake. (b) FT-IR of Ag-BG (red), Ag-BG@vanc after 6 h uptake (pink), and vanc (black) revealed the development of new vibration modes in the conjugate (grey shading) that further proved vancomycin incorporation.

The presence of vancomycin and minerals at the Ag-BG surface is also evidenced in the morphology, topography, and composition of the microparticles. For example, the presence of the antibiotic may be evidenced by a significant increase in the intensity of Cl since vancomycin is a Cl-containing organic molecule. The surface features and their composition were analyzed using

SEM-EDS and compared under three conditions: as-synthesized Ag-BG, Ag-BG immersed in fresh PBS, and Ag-BG@vanc. As previously shown, as-synthesized Ag-BG has a smooth surface with a homogeneous distribution of Si, P, Ca, Na, and Ag (**Figure 42** a). Immersing Ag-BG in fresh PBS (Ag-BG/PBS) simulated the surface reaction during the antibiotic uptake process. Ag-BG/PBS (**Figure 42** b) presented a heterogeneous composition with local deposition of salts like NaCl and AgCl and Ca-P minerals. SEM-EDS also showed an enrichment of Ca and P species at the surface of the Ag-BG@vanc conjugate (**Figure 42** c) is in agreement with the FT-IR vibration (**Figure 41** b). Ag-BG@vanc also presented a consistent Na and Cl distribution across the surface, although their intensity was significantly higher than in Ag-BG/PBS and as-synthesized Ag-BG. The homogenous distribution of Cl in Ag-BG@vanc serves to justify the presence of trapped vancomycin. The EDS spectra also show consistent contributions of Al, Ni, Cu, and Fe due to the metallic stub that held the SEM samples. UV-Vis, FT-IR, and SEM-EDS together prove the development of a vancomycin depot using Ag-BG microparticles.

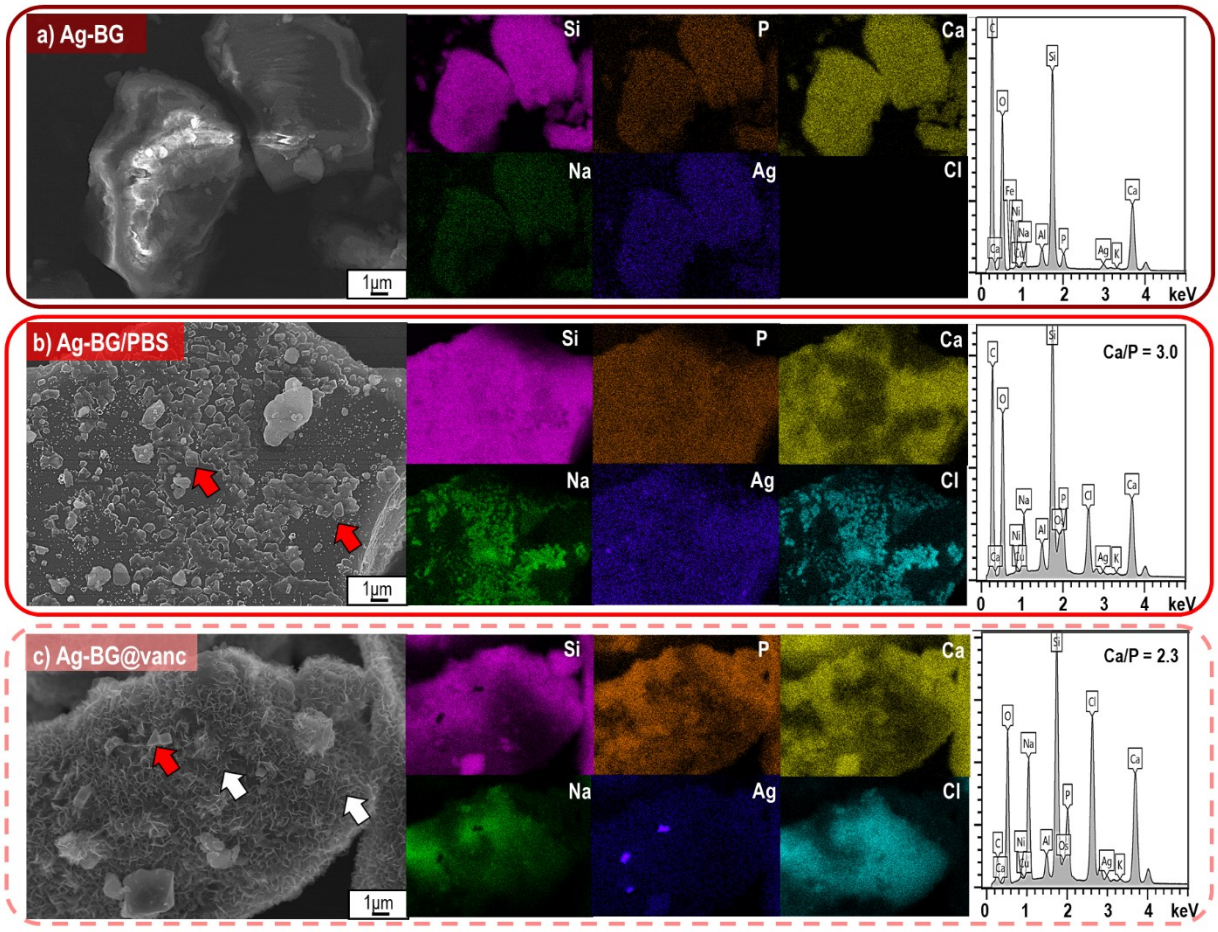

Figure 42: Surface morphology and chemistry of the Ag-BG particles as-synthesized (a), after immersion in PBS for 6 h (b), and after vancomycin uptake in PBS for 6 h (c). Elemental distribution presented with color maps for silicon (Si, fuchsia), phosphorous (P, orange), calcium (Ca, yellow), sodium (Na, green), silver (Ag, navy blue), and chlorine (Cl, cyan) and elemental spectrum. The homogeneous distribution of Cl in (c) is correlated to the precipitation of vancomycin. Salts and Ca-P deposits are indicated with red and white arrows, respectively.

4.4.2. Drug delivery *in vitro*.

The release profile of vancomycin from Ag-BG@vanc conjugate was evaluated under different environmental conditions. The short-term release (for up to 3 days) was monitored at 37 ºC (**Figure 43** a and c), simulating the human body, while the long-term release (for up to 10 days) was performed at 2 ºC (**Figure 43** b and d) due to concerns of antibiotic degradation. The dose delivered at each time point showed a Gaussian profile regardless of the conditions. As expected, the release

rate at 37 ºC (**Figure 43** a) was faster than at 2 ºC (**Figure 43** b) due to an accelerated surface reaction, as evidenced by the time point at which the release peak occurred. Specifically, after 12 h at 37 ºC (~0.08 mg/mL) and 48 h at 2 ºC (~0.12 mg/mL), the maximum drug release occurred. The conjugate sustained the delivery of vancomycin over time, although 100 % was never achieved. The cumulative release at 37 ºC did not reach a plateau but instead decreased the release rate after 12 h (**Figure 43** c). On the contrary, Ag-BG@vanc reached its full delivery capability after 4 days at 2 ºC with a total release of vancomycin of 0.5 mg from the 0.68 mg loaded and presented a plateau release after that (**Figure 43** d).

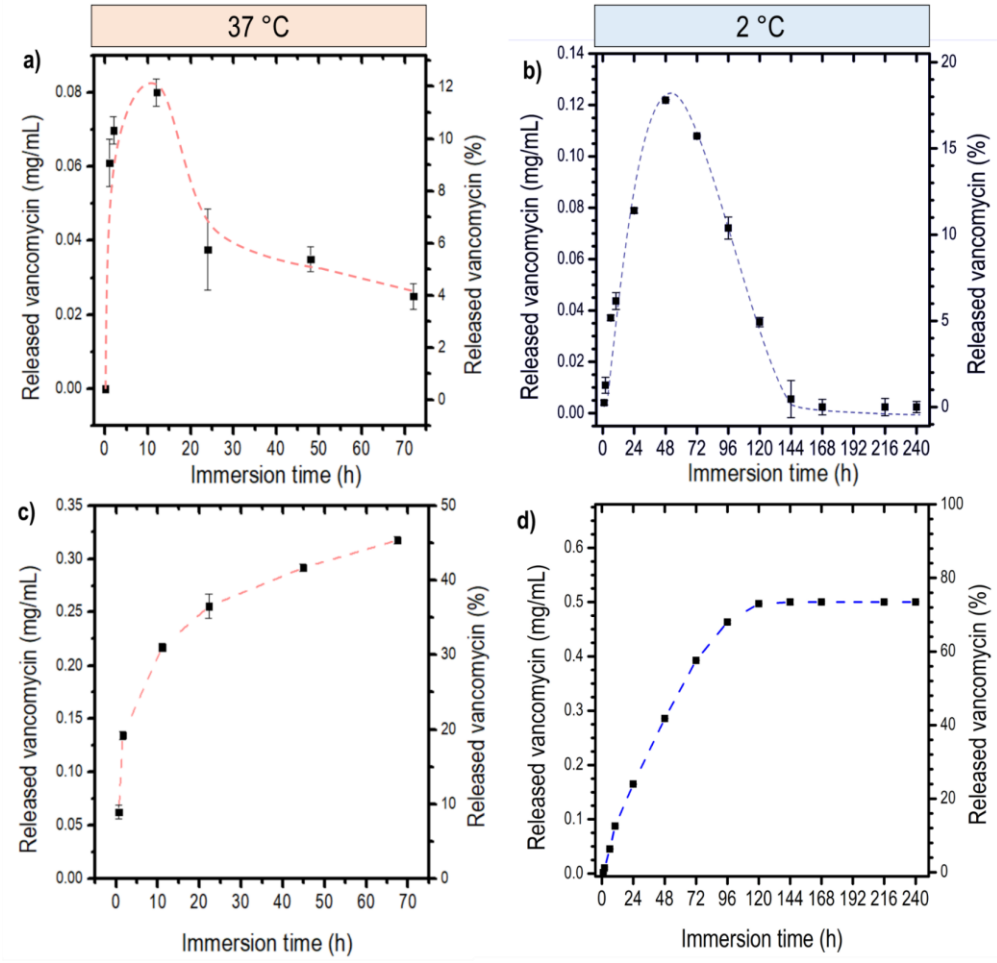

Figure 43: Daily release dose (a-b) and cumulative release profile (c-d) of vancomycin from Ag-BG@vanc in 1 mL of PBS at 37 ºC (a and c, pink dashed line) and 2 ºC (b and d, blue dashed line). The dashed lines are a guide to the eye.

4.4.3. Interaction of Ag-BG@vanc conjugate and bacteria

The capability of the Ag-BG@vanc conjugate to inhibit MRSA was compared to that of vancomycin, and Ag-BG delivered alone (**Figure 44** a). After 24 h, vancomycin was unable to decrease the viability of MRSA since, under our growth-arrested-like conditions, the antibiotic mechanism of action is bypassed. Therefore, simulating a vancomycin-resistant environment. On the contrary, exposure to Ag-BG particles caused significant damage, in agreement with previous results (**Figure 27**) [17,238], but insufficient to decrease the bacterial concentration below the 105 CFU that define an infection. This effect was expected since the Ag-BG concentration was below its recommended 2.5 mg/mL dose. The improved antibacterial action of the Ag-BG/vanc combination was maintained in the Ag-BG@vanc conjugate. Using Ag-BG as a vehicle enabled dose reduction due to the localized delivery of the antibiotic. Specifically, the 0.5 mg Ag-BG and 0.25 mg vancomycin delivered in the Ag-BG@vanc conjugate inhibited more bacteria than 2.5 mg Ag-BG with 0.5 mg vancomycin delivered in combination (**Figure 35** c).

Evaluation of bacterial morphology and microparticles after exposure for 24 h in PBS by SEM showed that, in agreement with previous observations, MRSA tried to colonize the surface of the particles where they faced the presence of nano-sized debris pointed by blue arrows (**Figure 44** b I-II). Bacteria damage was evidenced by changes in their shape and the presence of cytoplasmic content (red arrows) and cell-wall fragments (yellow arrows). Although Ag-BG presented surface deposits when immersed in PBS (**Figure 42** b), the surface remained deposit-free in the presence of bacteria (**Figure 44** b I-II). The interface between Ag-BG@vanc and MRSA retained the Ca-P deposits (white arrows) observed before treatment, although some of them appeared detached from the surface (**Figure 44** b III-IV). The elemental composition of these deposits was Ca-P-based, similar to Ag-BG@vanc before MRSA treatment (**Figure 44** c). The EDS spectrum also showed

a lower contribution of chlorine, which served as an indicator of vancomycin presence, after exposure to bacteria. The antibiotic's presence was noted as thin strings (indicated by green arrows) exiting Ag-BG towards bacteria cells.

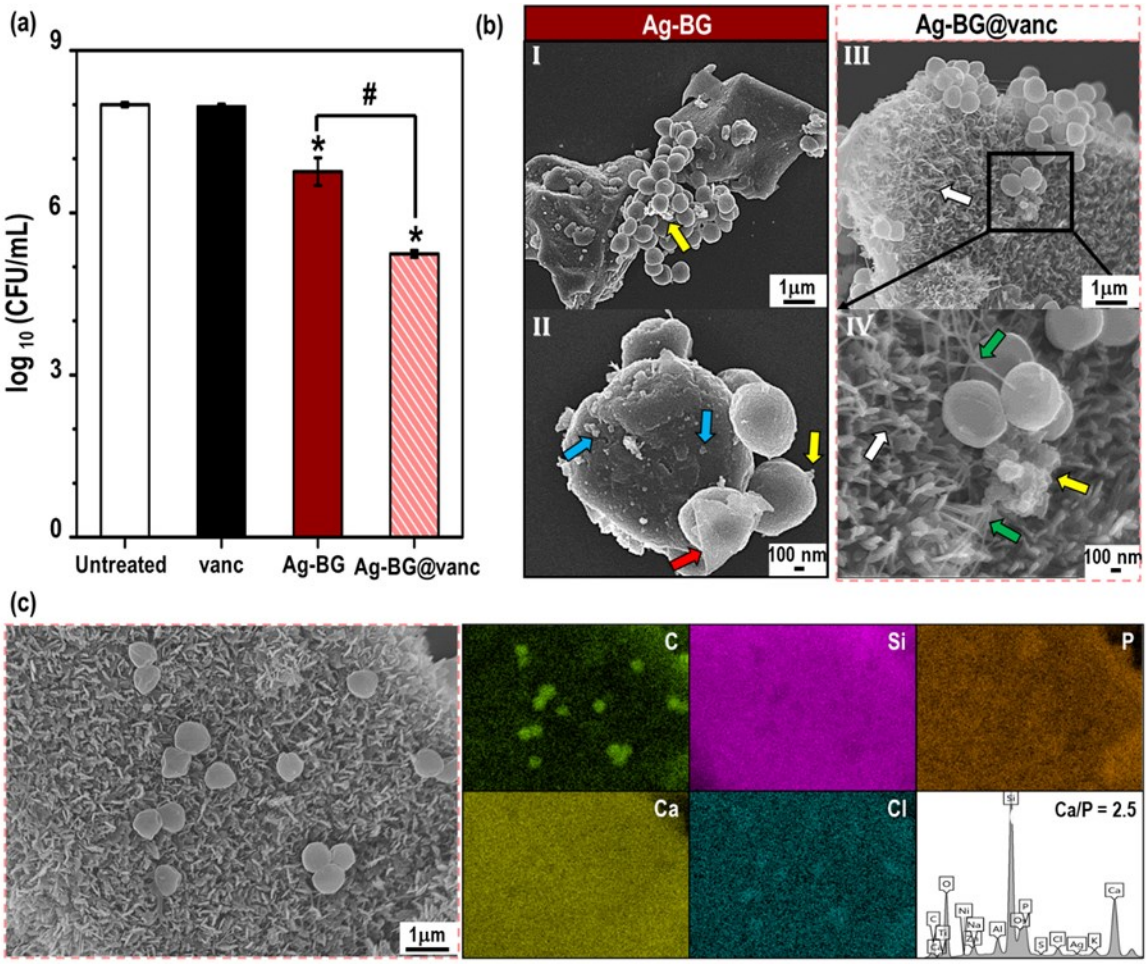

Figure 44: Inhibition of MRSA after 24 h treatment with Ag-BG and Ag-BG@vanc in PBS. (a) Enumeration of colonies. Statistical difference $p<0.05$ between untreated and treated MRSA (*) and between Ag-BG and Ag-BG@vanc (#). (b) Interaction between bacteria and Ag-BG (I-II) or Ag-BG@vanc (III-IV). Morphological features at the particle surface like nano-sized debris and Ca-P deposits are indicated with blue and white arrows, respectively. Vancomycin appears as thin strings exiting the deposits (green arrows). Red and yellow arrows mark cell-wall fragments and cellular content resulted from bacterial damage. (c) Elemental maps in Ag-BG@vanc after MRSA treatment for carbon (C, green), silicon (Si, pink), (Si, fuchsia), phosphorous (P, orange), calcium (Ca, yellow), and chlorine (Cl, cyan), and elemental spectrum.

4.4.4. Interaction of Ag-BG@vanc conjugate and fibroblasts; biocompatibility

The biocompatibility of the antibiotic depot was evaluated following an indirect exposure test similar to previous experiments. Although Ag-BG promotes cell proliferation *in vitro* (**Figure 22**), its surface chemistry was significantly modified during the vancomycin uptake process, and therefore, the biocompatibility must be re-evaluated. Ag-BG@vanc was not cytotoxic according to the lack of statistical difference in cell population vs. untreated cells (**Figure 45**). Both Ag-BG and Ag-BG@vanc had similar positive effects on cell behavior, despite the delayed ion release, key to cell proliferation, expected from the antibiotic/ion co-precipitation on Ag-BG@vanc surface. In contrast, the population of vancomycin-treated cells decreased after 1 and 3 days of exposure, which reverted to normal levels by the end of the experiment.

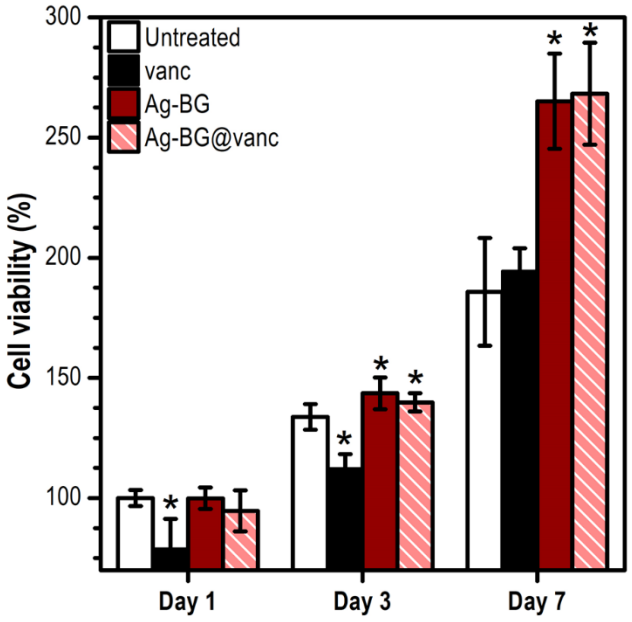

Figure 45: Ag-BG@vanc conjugate (pink-stripes) enhanced cell proliferation at a similar level than Ag-BG (red). Vancomycin at a concentration of 0.06 mg/mL (black) slightly decreased cell viability. The significant difference ($p < 0.05$) between untreated treated cells is indicated with (*).

4.5. From Ag-BG microparticles to Ag-BG nanoparticles

Nanomedicine techniques are based on materials featured to mimic host tissue [187,265]. In this field, nanoparticles hold potential since their size and charge can be modulated to allow intracellular uptake without being harmful to the surrounding tissues. As one of the inhibition mechanisms involved in the antibacterial capabilities of Ag-BG microparticles seemed to rely on the accumulation of nano-sized debris (**Figure 37**), Ag-BGNs are anticipated to hold intense antimicrobial action that would be no longer dependent on microparticles' decomposition. However, as previously mentioned, the incorporation of multifold metallic ions is rarely successful in silicate-based nanoparticles, and therefore, the synthesis of Ag-BGNs is presented as an ambitious goal. In the first part of this section, the conventional Stöber method was first modified to explore the cation incorporation routes in a simplified BGNs composition. Then, the synthesis method was re-evaluated for the development of Ag-BGNs.

4.5.1. Development of ternary system BGNs: incorporation of Ca and P.

In this section, the challenges of incorporating P and Ca in amounts equal to the nominal composition were addressed. A new approach to synthesize nanoparticles in the 62 SiO_2 – 3.2 P_2O_5 - 34.4 CaO (mol.%) where nominal and actual composition agree is reported. First, a Stöber method for submicrometer BGNs (~400 nm) was used as the reference point for this study [71] and then modified in the solvent, stirring time, and order of reagent addition to incorporate the desired concentration of P and Ca^{2+} ions. The results presented here have been previously published as Pajares-Chamorro, N., & Chatzistavrou, X. (2020). "Bioactive Glass Nanoparticles for Tissue Regeneration ", ACS Omega, 5(22), 12716-12726.

4.5.1.1. Morphology and nature of BGN

The particle size, dispersity, and composition of sol−gel-derived BGNs were studied as a function of processing parameters (**Figure 46**). Particles were synthesized following two main protocols: method 1 (M1) and method 2 (M2).

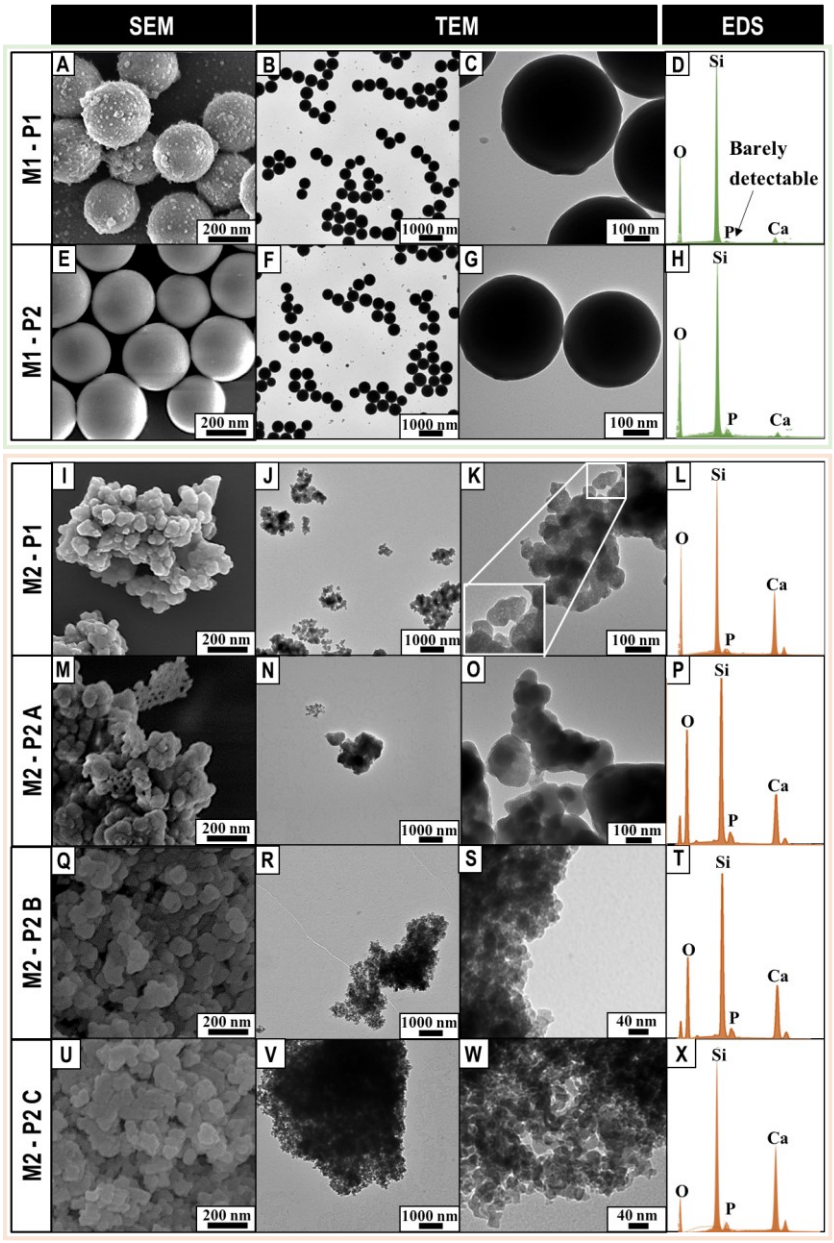

Figure 46: Morphology, distribution, and elemental analysis spectra of BGNs and its aggregates for M1-P1 (A-D), M1-P2 (E-H), M2-P1 (I-L), M2-P2 A (M-P), M2-P2 B (Q-T), and M2-P2 C (U-X) synthesis protocols [266].

Dense, spherical, and monodispersed particles, with a diameter of around ~400 nm, were achieved using the M1 protocols (**Figure 46** A−C, E−G). Particle size was reduced below 100 nm due to the addition of CaNT before catalysis in M2 (**Figure 46** I− K, M−O, Q−S, U−W) and consequently led to a decrease in particle dispersion. BGNs produced by the M2-P1 method presented sizes of ~86 nm, forming aggregates with an average size of around 1−2 μm (**Figure 46** J) and showed mesoporosity (**Figure 46** K, inset). This characterization of the structural pores is presented in section 4.5.1.1.2.

Decreasing the H_2O concentration in Solution B in the M2-P2 A protocol (**Figure 46** M−O) resulted in a trimodal distribution with an average particle size of around ~70 nm (52%), ~190 nm (39%), and ~500 nm (9%), and loss of mesoporosity compared to M2-P1. BGNs synthesized by M2-P2 C (increase in X_1 stirring duration time before the addition of CaNT and Solution B, **Figure 46** Q− S) and M2-P2 C (increase in X_2 stirring time after the addition of CaNT and before the addition of Solution B, **Figure 46** U−W) showed no significant difference in particle size to one another. Both presented a size ~20 nm conforming to bigger aggregates (~1 μm). This observation indicates that the increase in stirring time before Solution B is critical for particle size. However, since no difference was observed between M2-P2 B and M2-P2 C, it is unclear if there is a dependence concerning which step is prolonged (i.e., before or after the addition of CaNT in M2-P2 B and Me-P2 C, respectively) in decreasing particle size or if it is a result of the overall increase in stirring time regardless of the step.

Table 12 summarizes the particle sizes drawn from TEM images, as well as the DLS measurements for comparison. DLS tended to overestimate the size of BGNs because of its predisposition to report aggregate sizes rather than individual particles. However, in general, most DLS data is within the same range as TEM measurements.

Table 12: Particle size of BGN based on TEM Image analysis and DLS measurements [266].

Protocols	M1-P1	M1-P2	M2-P1	M2-P2 A	M2-P2 B	M2-P2 C
Particle size from TEM (nm)	438 ± 17	425 ± 17	86 ± 14	70 ± 13 193 ± 51 495 ± 12	18 ± 2	18 ± 5
Particle size from DLS (nm)	N/A*	500 ± 30	142 ± 20 990 ± 100	120 ± 10 200 ± 30 625 ± 50	15 ± 5 200 ± 100	22 ± 6 300 ± 50

*N/A: non-applicable. The sample was not analyzed.

4.5.1.1.1. Elemental composition of BGNs

Control over the elemental composition of BGNs following a Stöber like method has remained a challenge for years. SEM-EDS spectra semi-quantitatively evaluated the composition of BGNs to elucidate key elemental differences among BGNs from different protocols. The spectra collected were presented in **Figure 46** D, H, L, P, T, X, with the calculated values summarized in **Table 13**. Nanoparticles fabricated by the reference protocol M1-P1 presented significantly low incorporation of P_2O_5 and CaO in agreement with published data [71]. The lack of phosphorous was attributed to the unbalanced hydrolysis rate between TEOS and TEP under basic conditions. This effect was overcome in the M1-P2 and M2 synthesis protocol, where the reagents were dissolved in methanol so that both hydrolysis reactions happened at comparable rates, increasing the final concentration of P_2O_5 in the system. The modification of the solvent was insufficient to reach the intended CaO content since no significant improvement was observed from M1-P1 to M1-P2. Instead, the order of reagent addition was critical for the incorporation of CaO. Synthesizing particles by the M2 protocol where CaNT was incorporated into Solution A before catalysis and stirring for a long enough time allows cation interaction with SiO_2 tetrahedra to increase the CaO content to 35 mol %.

Table 13:Semi-quantitative evaluation of BGNs composition (mol. %) from EDS mapping [266]. The composition was obtained from 3 different regions, and the standard deviation reports the elemental differences among them. Red font is used to highlight the compositions away from the nominal.

	System	SiO_2	P_2O_5	CaO
	Nominal composition (mol. %)	62.1	3.2	34.7
Applied Protocols	M1-P1	93.5 ± 0.7	0.4 ± 0.5	6.1 ± 0.2
	M1-P2	93.1 ± 0.2	3.2 ± 0.1	3.7 ± 0.1
	M2-P1	61.4 ± 0.9	3 ± 0.5	35.6 ± 1.0
	M2-P2 A	63.9 ± 0.9	3.8 ± 0.5	32.3 ± 0.8
	M2-P2 B	64.2 ± 3.0	3.5 ± 0.2	32.3 ± 1.0
	M2-P2 C	62.1 ± 0.4	3.3 ± 0.8	34.6 ± 0.4

4.5.1.1.2. Mesoporosity of M2-P1 particles

The morphological evaluation of the BGNs revealed the presence of pores in particles derived from the M2-P1 synthesis protocol (**Figure 46** K). The mesoporosity was characterized by N_2 adsorption and desorption. M2-P2 presents an isotherm type IV characteristic of a mesoporous sample (**Figure 47** a) and supports the TEM observation. The BET analysis revealed a surface area of 21.95 m^2/g and an overall pore volume of 0.078 cm^3/g. The mesoporosity was distributed in three main approximate sizes: 2 nm, 20 nm, and 90 nm (**Figure 47** b). Considering the particle size and distribution reported in **Figure 46** I-K and **Table 13**, it can be concluded that M2-P1 particles have an average pore size of 20 nm with little presence of smaller pores. Therefore, the larger pores (i.e., 90 nm) are correlated to space between loosely aggregated individual BGNs, demonstrating the particles were not densified together.

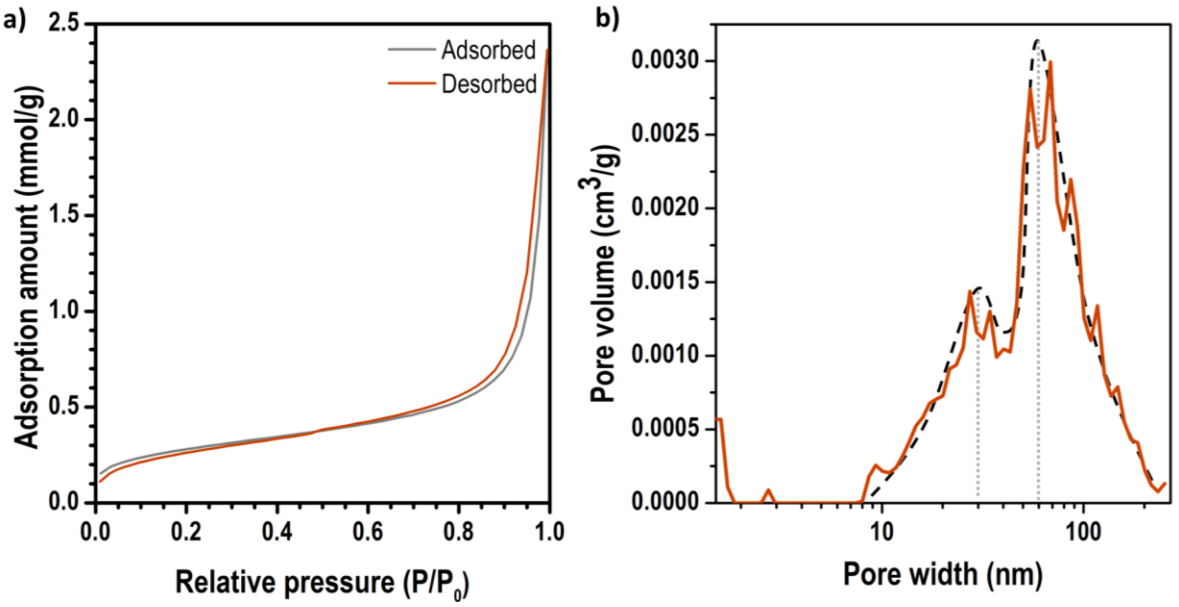

Figure 47: M2-P1 BGNs present mesoporosity in agreement with the N_2 adsorption-desorption isotherm type IV (a). The pore size and distribution obtained by BET analysis (b) demonstrate an average pore size of 20 nm and 90 nm gaps between individual nanoparticles. Modified from [266].

4.5.1.2. Structure of ternary BGN

The structure of BGNs was further assessed by FT-IR (**Figure 48**), XRD (**Figure 49**), and NMR (**Figure 50**) analysis. All FT-IR spectra present characteristic features of amorphous-like silicate-based structures (**Figure 48**), shown in earlier sections. Briefly, M1 BGNs present a dominant SiO_2 structure with vibration modes at 450, 805, 1000−1050, and 1200 cm^{-1} for Si−O−Si bending and stretching. The strong vibration of the Si−O−Si stretching mode at 1000−1050 cm^{-1} overlaps with the P−O bending at 1040 cm^{-1}, in agreement with other silicate glasses' structural characterization. All the BGNs synthesized by M2 protocols developed a shoulder in the 900−1100 cm^{-1} region. The band at 900 cm^{-1} is attributed to Si−O−NBO bonds and demonstrates the SiO_2 network was modified. Therefore, this band's development confirms the presence of Ca^{2+}, which structural role is as modifier ion in the SiO_2 network. The formation of a 900 cm^{-1} band also results in the minor shift of the 1050 cm^{-1} peak to the lower wavenumber.

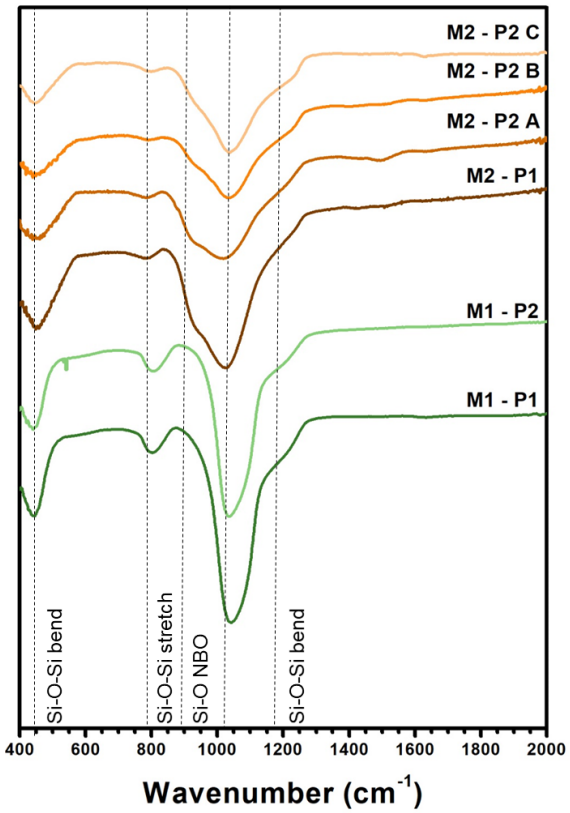

Figure 48: Structural analysis of BGNs from FT-IR vibrations. M1 protocols present a non-modified SiO_2 network, while in M2 protocols, the network was modified by Ca^{2+} ions, evidenced by the shoulder at 900 cm^{-1} [266].

The amorphous structure of M1 and M2 BGNs was further analyzed with XRD (**Figure 49** a). These features were analyzed by fitting the XRD patterns with Gaussian peaks for $R^2 = 0.99$. Five Gaussian peaks were identified to fit the XRD patterns with the maximum for each fitting peak at 2θ: 21.9 ° ± 0.6, 27.4 ° ± 0.5, 31.3 ° ± 0.2, 52.3 ° ± 3, and 70.3 ° ± 0.03 (**Figure 49** b). BGNs developed by the M1-P1 protocol present a strong contribution of the 21.9 °2θ, followed by a weaker one at 27.4 °2θ. Modification of this protocol towards the cation incorporation resulted in the 21.9° 2θ decrease in favor of the increase of 27.4° 2θ. This trend was evident when the XRD pattern of M1-P1 BGNs was compared to that of M1-P2 BGNs, where the only structural difference was the incorporation of P ions in the structure and is more evident in M2 protocols were the overall spectra shifter towards higher 2θ values after Ca^{2+} modified the SiO_2 network.

The fifth peak with a maximum at 70.3° 2θ observed in M1 BGNs disappeared in the M2 BGNs patterns, and instead, two other peaks formed at 31.1 and 52.3 °2θ (**Figure 49** b). These changes in the XRD patterns could also be potentially assigned to the incorporation of Ca^{2+} ions in M2 BGNs that strongly modified the SiO_2 network compared to M1 BGNs.

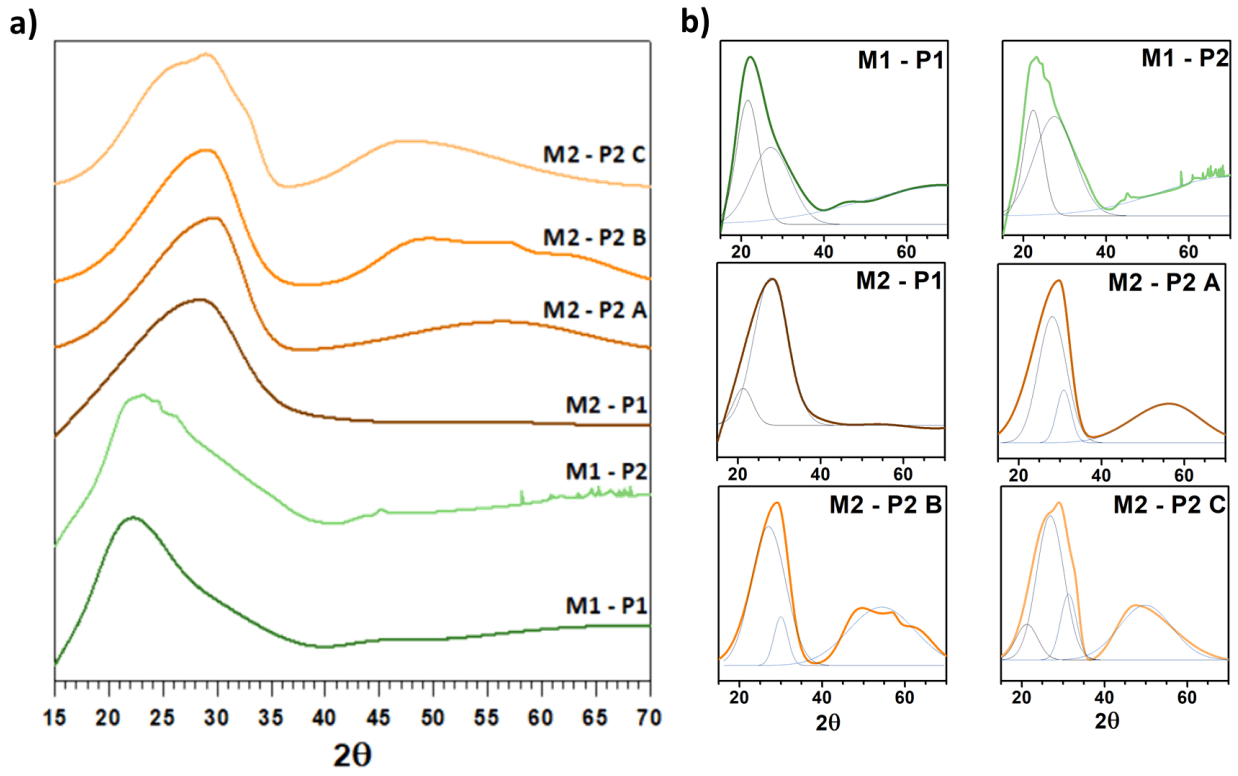

Figure 49: Characterization of the amorphous BGNs structure by XRD analysis (a). The diffraction peaks were deconvoluted with Gaussian curves (b), revealing a significant peak shift towards higher 2θ as the SiO_2 network was modified in M2 BGNs.

The deconvolution of the XRD spectra (**Figure 49** b) in Gaussian peaks was analyzed in terms of area under the curve to demonstrate the evolution of network environments numerically as the synthesis protocol was modified. **Table 14** summarizes the Gaussian deconvolution results, confirming the observation mentioned above regarding peak evolution.

Table 14: Numerical analysis of the Gaussian peak deconvolution of amorphous XRD spectra. The area under the curve evolves during cation incorporation, evidencing a modified SiO_2 network.

Peaks	Peak Maximum (2θ)	Area					
		M1-P1	M1-P2	M2-P1	M2-P2 A	M2-P2 B	M2-P2 C
1st Peak	21.9 ± 0.6	5.28	3.83	1.33	2.71	0	1.44
2nd Peak	27.4 ± 0.5	5.7	7.46	9.4	6.62	8.89	7.35
3rd Peak	31.1 ± 0.2	0	0	0	1.43	1.26	1.95
4th Peak	52.3 ± 3	0	0	0	5.02	7.22	5.37
5th Peak	70.3 ± 0.03	12.45	10.4	0	0	0	0

The shift on the XRD spectra as higher cation concentration was incorporated in BGN revealed different SiO_2 coordination. The network connectivity (NC) was evaluated in terms of Q^n speciation using ^{29}Si MAS-NMR. Two representative samples were analyzed: M1-P2 (**Figure 50** a) and M2-P2 A (**Figure 50** b). The chemical shifts (−δ) were identified for Q^4 (109−112 ppm), Q^3 (100−102 ppm), Q^2 (85−93 ppm), and Q^1 (76−79 ppm) units. The Q^2 species presented two different signals related to (1) silicon associated with hydrogen (~93 ppm) and (2) silicon associated with network modifiers (~85 ppm), in this case, calcium [267]. The structure of M1 BGNs was dominated by Q^4 and Q^3 species. M2 BGNs presented a higher contribution of Q^3 species and showed a significant increase in Q^2 speciation. These observations are congruent with FT-IR and XRD spectra, confirming M1 BGNs had a non-modified SiO_2 network (Q^4 species and Si-O-Si bonds) due to the low incorporation of cations. In contrast, in M2 BGNs, the structure becomes strongly modified.

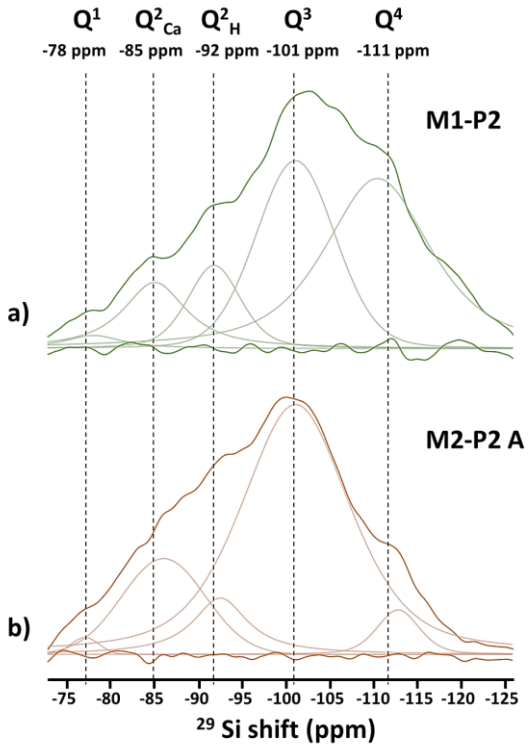

Figure 50: Distribution of Q^n silicon species in M1-P2 (a) and M2-P2 (b) BGNs from solid-state ^{29}Si CP MAS-NMR. The Gaussian deconvolution of the spectra is displayed in lighter colors, with their corresponding Q^n showing higher contribution of Q^4 and Q^3 species in M1, and M2 BGNs, respectively [266].

The NC was calculated from theoretical and experimental models (**Table 15**), as explained in section 3.2.6. Briefly, the theoretical NC was obtained attending SEM-EDS's elemental composition (**Table 13**), assuming phosphorous acted only as network former. The experimental NC was obtained from the Q^2/Q^3 ratio obtained from the Gaussian deconvolution of the MAS-NMR spectra. Note that the experimental value underestimates the network connectivity as it neglects the contribution of Q^4 units in the calculation. Nonetheless, both models confirmed the structure of M1 BGNs was more interconnected than that of M2 BGNs.

Table 15: Network connectivity (NC) in BGNs from theoretical and experimental models demonstrates higher interconnectivity in M1 than M2 BGNs, as expected from cation incorporation [266].

Protocol	Theoretical NC	Experimental NC
M1-P1	3.9	N/A*
M1-P2	4	0.73
M2-P1	3.2	N/A*
M2-P2	3.3	0.36

*N/A: non-applicable. The sample was not analyzed.

4.5.1.2.1. Presence and status of Ca^{2+} ions in M2-P1

The cation incorporation mechanism was studied by analyzing the presence and status of Ca^{2+} at various stages of the synthesis process. In M2-P1 BGNs, CaNT was added before catalysis and stirred for an extended time to interact with the previously formed SiO_2 tetrahedra. These M2-P1 BGNs were collected after condensation and dried at 60 °C to evaluate the incorporation of Ca^{2+} compared to the BGNs after calcination at 700 °C. SEM-EDS demonstrated the presence of CaO in M2-P1 BGNs at the nominal level (~ 35 mol.%) before and after calcination (**Figure 51** a). The status of Ca^{2+} ions was evaluated with FT-IR (**Figure 51** b). M2-P1 BGNs before calcination presented the typical vibration of a non-modified SiO_2 network, similar to the spectra collected for M1 BGNs (**Figure 48**). However, after calcination, the 900 cm-1 should for Si-O-NBO developed. These observations demonstrate Ca^{2+} ions were only trapped within BGNs as the nucleation and condensation of nanoparticles occurred during catalysis but only contributed to the network after calcination.

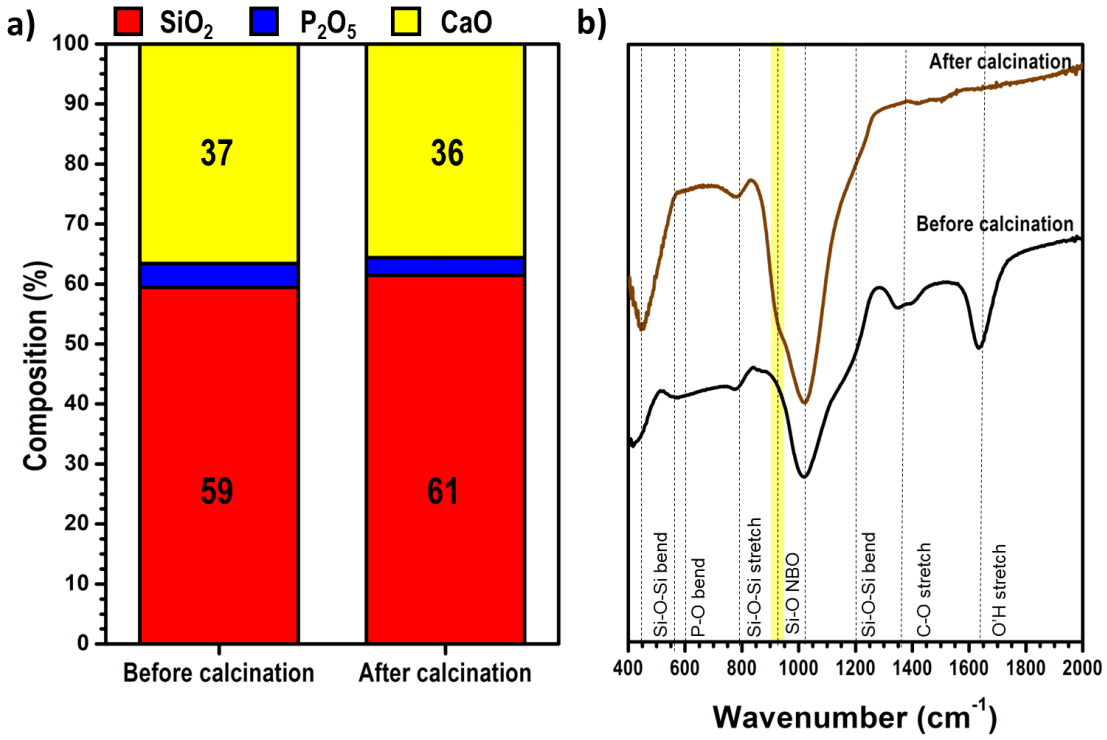

Figure 51: The presence of Ca^{2+} ions above 30 (mol.%) in M2-P1 BGNs before calcination was confirmed semi-quantitively by EDS analysis (a). FT-IR spectrum (b) demonstrates Ca^{2+} ions only modify the SiO_2 network after calcination, as evidenced by the development of a 900 cm^{-1} shoulder. Modified from [266].

4.5.1.3. The degradation of BGNs *in vitro*

The degradation of ternary BGN was evaluated in terms of pH evolution and apatite-forming ability, following the same methodology used in Ag-BG microparticles in section 4.1.

4.5.1.3.1. pH evolution of BGNs

The degradation of BGNs derived from M1-P1, M2-P1, and M2-P2 C was evaluated by immersion in PBS and monitored through the pH of the solution (**Figure 52** a). The results were compared to the behavior of an equivalent compositional system of a larger scale, in this case, 58 S microparticles of < 20 μm. Burst ionic release occurred in M2 BGNs where the solutions presented pH above 8 after 24 h of immersion. After 4 days of immersion, their pH dropped back to neutral

levels (7.5-7.7), indicating a steadier degradation for up to 10 days in solution. On the contrary, M1 BGNs presented a pH below 8 at all times. The 58 S microparticle used as a reference point demonstrated a similar behavior as that of M2 BGNs. This phenomenon is probably correlated to network connectivity of both M2 BGNs and 58 S microparticles being lower than that of M1 BGNs, which presented mainly Q^4 units due to the lack of cation incorporation. On this basis and considering the biological application of these nanoparticles, they were preconditioned in DMEM medium for 4 days, the point at which BGNs are expected to release ions at a more controllable rate. **Figure 52** b shows the pH remained around neutral values after immersing pre-conditioned particles in PBS for up to 4 days.

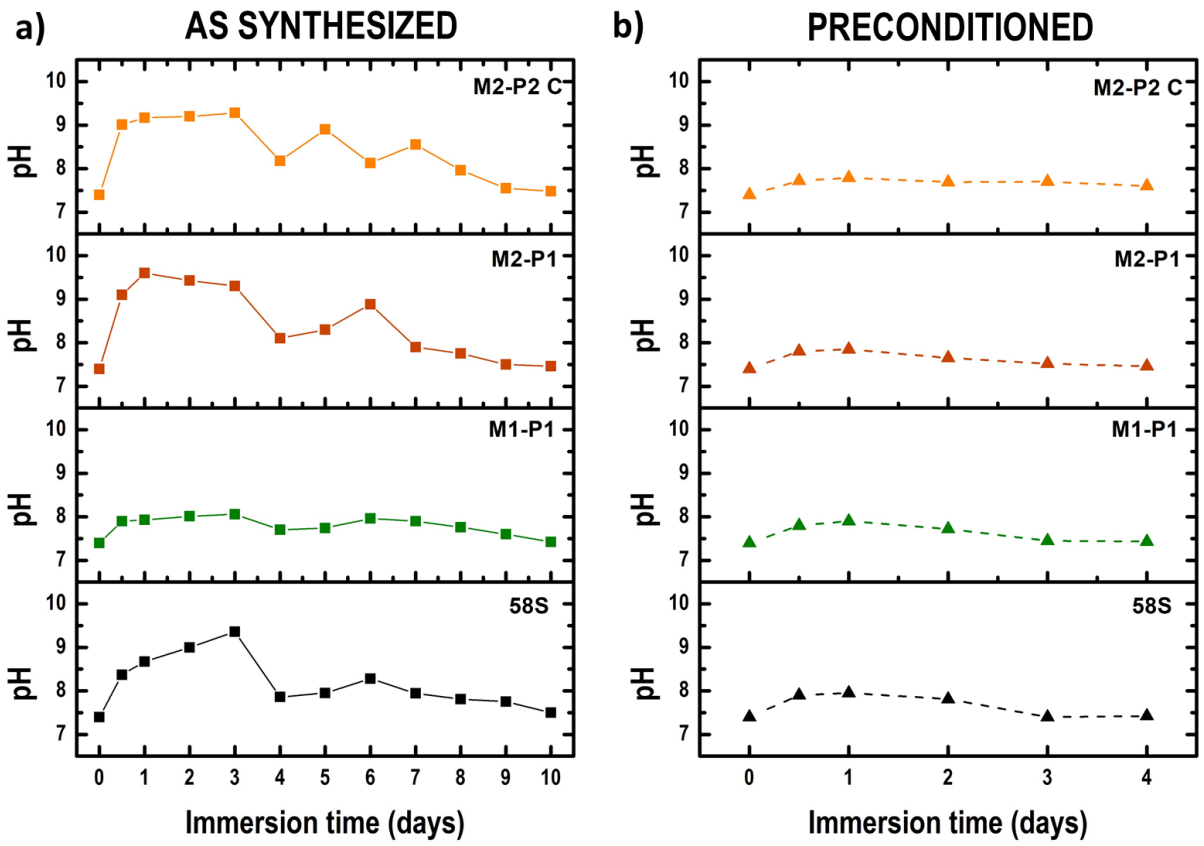

Figure 52: BGNs degrade upon immersion in PBS, causing significant fluctuations in the pH value, which increases above the biological range (7.5-7.7) (a). After preconditioning in DMEM for 4 days, the pH stabilizes around neutral values (b).

4.5.1.3.2. Apatite-forming ability of BGN

The osteoconductive potential of nanoparticles was assessed through *in vitro* biomineralization studies, using the formation of the biological apatite phase in SBF as the indicator of bioactive behavior. After 7 days, the formation of an apatite phase was observed for M1, M2-P1, and M2-P2 A BGNs by FT-IR (**Figure 53**, solid line) and compared to that before SBF (**Figure 53**, dashed line). This deposition was evidenced in both M1 BGNs by developing a broad peak in the region of 575−620 cm^{-1} commonly attributed to P−O bending. In M2 BGNs, this band evolved towards a double peak vibration, although the peak is still quite broad. The wide band at ∼1050 cm^{-1} increased in sharpness and unfolded the side shoulders to form more clear peaks at ∼950 and ∼1200 cm^{-1}. These features indicate the more substantial P−O bending vibration in the structure as the number of P-O increases due to apatite deposition. Additional features were identified in M2 BGNs like carbonate group bands at ∼873 and ∼1450 cm^{-1} that confirmed the formation of a carbonated calcium phosphate phase. Based on these facts, it can be concluded that both M1 and M2 BGNs were able to develop the biological apatite phase. The weaker apatite-forming ability of M1 BGNs than M2 BGNs, as evidenced by the intensity and characteristics of the vibration, as mentioned earlier, is probably a consequence of the alterations in nanoparticles' composition and size.

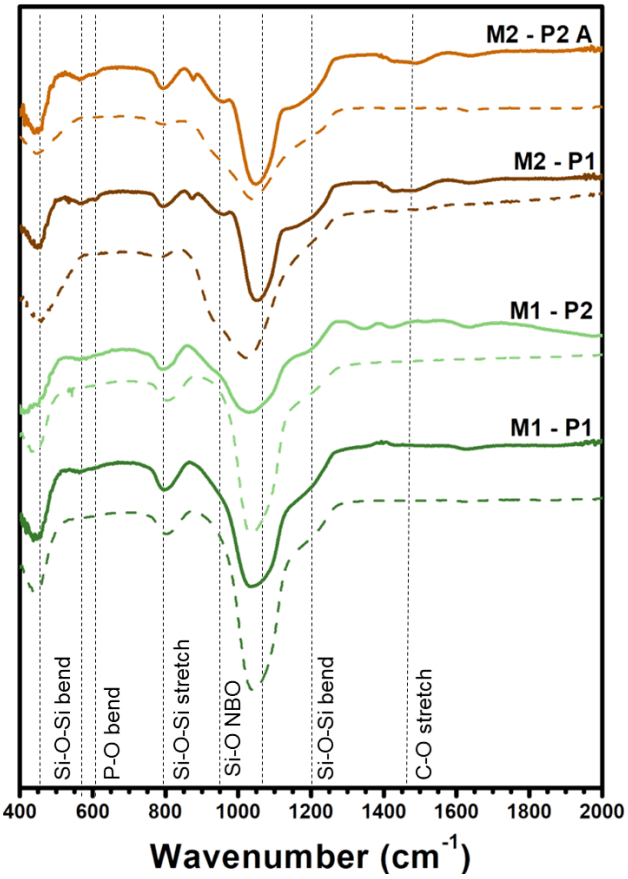

Figure 53: Apatite-forming ability of BGN after 7 days in SBF (solid line) compared to their respective spectra before SBG (dashed line). Carbonate calcium phosphate deposition was evidenced in M1 and M2 BGNS, although the vibration was weaker in M1 BGNs [266].

4.5.1.4. Antibacterial behavior of BGN

The antibacterial effect of three types of BGNs (i.e., M1-P1, M2-P1, and M2-P2 C) was evaluated against MRSA. To reduce the effect of pH in antibacterial behavior, all particles were pre-conditioned for 4 days before the antibacterial test (**Figure 52** b). The 58S microparticle system showing null inhibitory capacity was used as a reference. Conversely, MRSA exposure to BGNs for 24 h significantly decreased their viability (**Figure 54** a). Inhibition achieved with M2 BGNs was considerably more potent than M1-P1 BGNs, providing almost a total ten-fold decrease in bacteria viability. No statistical significance was found between cells treated with M2-P1 versus M2-P2.

Evaluation of MRSA interaction with nanoparticles by SEM imaging showed that untreated bacteria present a spherical shape of 500 nm diameter and a smooth surface, in agreement with previous observations (**Figure 54** b). No signs of damage were evident in bacteria surrounded by M1-P1 BGNs, whose size is close to that MRSA (i.e., 300-400 nm). On the contrary, M2 BGNs of < 100 nm in size coated the bacterial surface allowing the release of cytoplasmic content that was evident around the sample.

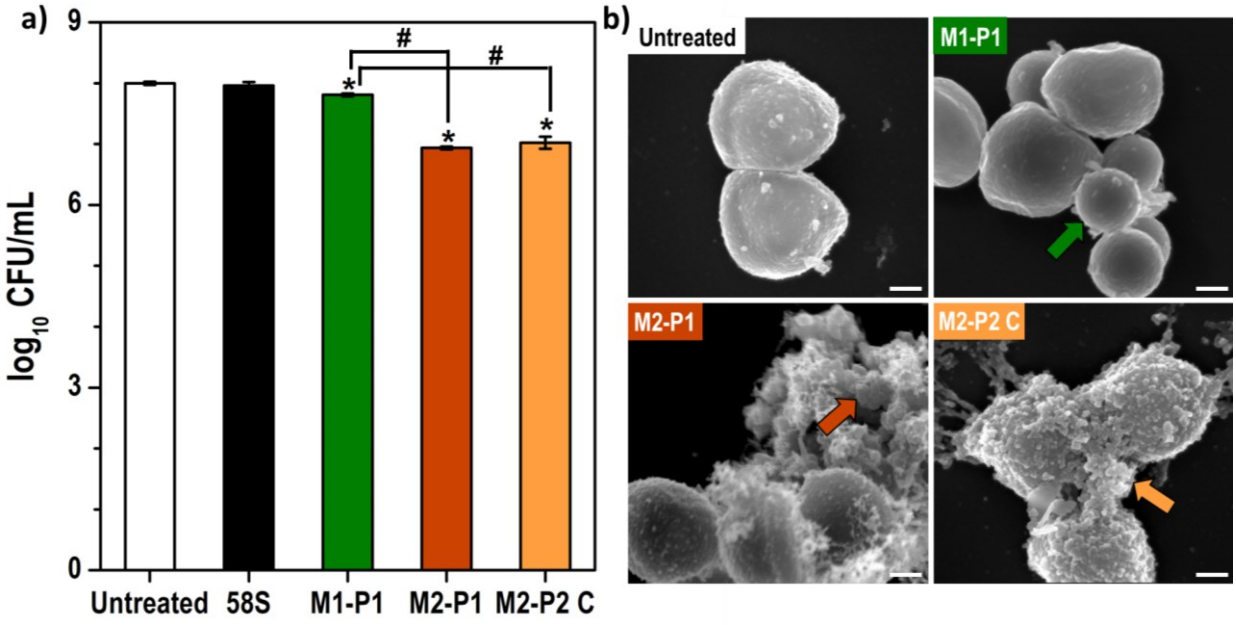

Figure 54: BGNs exhibit mild antibacterial activity against MRSA (a). Suspension of bacteria (OD_{600} = 1 equivalent to ~ 10^8 CFU/mL) were mixed with fresh PBS medium (untreated control, white bar) or 1 mg/mL of 58S (black bar), M1-P1 (green bar) , M2-P1(brown bar) or M2-P2 C (orange bar). The CFUs were enumerated after 24 h with a limit of detection of 100 CFU. The interface between BGNs and bacteria was evaluated in SEM (b), where the color arrows point to nanoparticles. The white scale bar represents 200 nm.

4.5.2. Development of Ag-BGNs for medical applications

The synthesis of Ag-BGNs was performed by modification of the Stöber-like method presented in the previous section. A simplified ternary-BGN composition was processed successfully incorporating P and Ca's intended concentration, therefore, addressing the challenges in ion incorporation in nanoparticles of < 100 nm. This protocol (i.e., M2-P1) was further adapted to yield a composition similar to that of the Ag-BG microparticles previously presented. In this section, Ag-BGNs with a composition of 62.5 SiO_2 – 3.4 P_2O_4 – 29.4 CaO – 3.8 Al_2O_4 – 0.8 Ag_2O (mol. %) were synthesized and characterized to evaluate putative effects of particle size reduction in the biological and antibacterial properties of the system.

4.5.2.1. Morphology, size, and composition of Ag-BGNs

Ag-BGNs were obtained using a modified Stöber method, incorporating Al and Ag to replace the Ca content. Spherical and dense nanoparticles were obtained, as shown by SEM and TEM (**Figure 55** a-b). The particles' morphology was similar to that of M2-P2 BGNs, and the incorporation of two new cations did not influence this morphology.

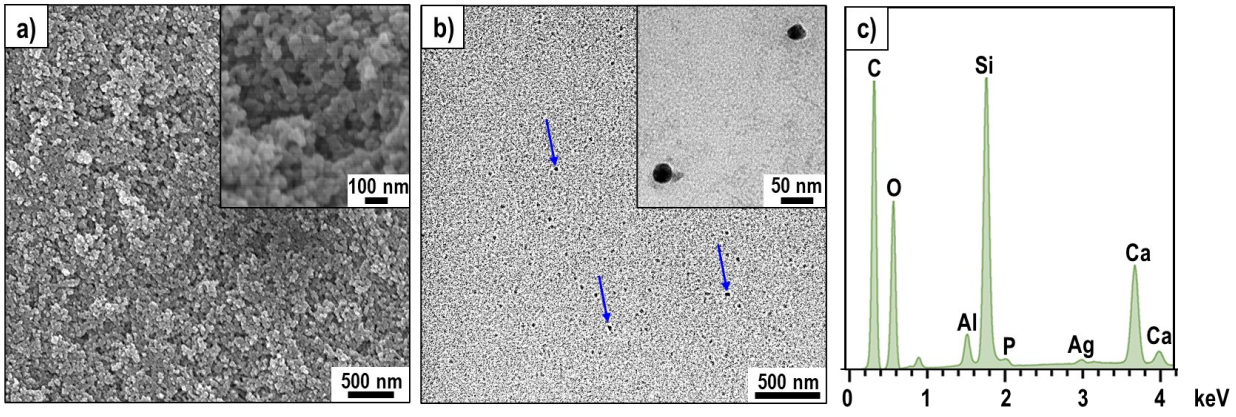

Figure 55: Morphology, distribution, and elemental analysis spectra of Ag-BGNs. Aggregates were observed in powder form (a), but monodispersity is achieved in solution (b). EDS confirmed the incorporation of cations (c).

The nanoparticles appeared in aggregates when in powder form, as observed in SEM (**Figure 55** a). There is a loose connection between nanoparticles forming the aggregates since Ag-BGNs could be uniformly dispersed in the medium. The monodispersity of Ag-BGNs was captured in TEM (**Figure 55** b). The resin was used as dispersing medium since the higher viscosity prevents the separated Ag-BGNs from aggregating to reduce their surface energy. **Table 16** also shows an average particle size of ~10 nm, measured by TEM image analysis and confirmed by DLS. The zeta-potential was negative with a value of ~ -9 mV.

Table 16: Particle size and surface charge of Ag-BGNs based on TEM and DLS measurements.

Ag-BGNs	TEM	DLS
Particle size (nm)	7.40 ± 1.33	8.42 ± 0.62
Zeta-potential (mV)	N/A*	- 8.94 ± 3.84

*N/A: not applicable.

The composition of the Ag-BGNs was semi-quantitatively assessed with EDS. All the ions were successfully incorporated in a similar range as the intended nominal (**Table 17**). The amount of CaO was found around 30 mol.%, in agreement with the M2 BGN protocols previously presented. The concentration of P_2O_5 and Ag_2O was slightly lower than the nominal. However, considering the sensitivity of EDS for the detection of small concentrations, this result may only serve to demonstrate their presence. Other elemental analytical techniques would be required to quantify the exact composition.

Table 17: Semi-quantitative evaluation of Ag-BGNs composition (mol. %) from EDS mapping. The composition was obtained from 3 different regions, and the standard deviation reports the elemental differences among them. Red font is used to highlight the compositions away from the nominal.

System	SiO_2	P_2O_5	CaO	Al_2O_3	Ag_2O
Nominal (mol.%)	62.5	3.4	29.4	3.8	0.8
EDS estimation (mol%)	65.6 ± 3.8	1.9 ± 0.7	27.3 ± 5.7	4.7 ± 1.2	0.5 ± 0.2

4.5.2.2. Status of Ag^+ in the network and network connectivity.

The status of Ag^+ ions in the bioactive glass network was assessed by colorimetry. Visual inspection of the powder showed the Ag-BGNs were colorless (i.e., white powder) (**Figure 56** a). UV-Vis was also used to evaluate the status of Ag. The characteristic peak of Ag and its compounds, which absorb light in the 350-600 nm wavelength range, were absent from the UV-VIS spectra. On this basis, and considering Ag's detection in the EDS (**Figure 55** c), it can be inferred Ag^+ was trapped in ionic form.

The chemical shifts in ^{27}Al MAS-NMR (**Figure 56** b) showed the symmetrical vibration for the magic angle spinning sideband (MASS) at 4.6 – 4.6 ppm and 80 – 100 ppm. The coordination of aluminum in Ag-BGNs was as Al^V and Al^{IV}. The area under the curve was obtained from the Gaussian deconvolutions and used to calculate the population % of species. The structure of Ag-BGNs presented a significantly higher population of Al^{IV} (~ 62 %) than Al^V (~ 21 %). Therefore, the incorporation of aluminum was manly in tetrahedral coordination forming $[AlO_4]^-$ units. It is expected that the negative charge of these aluminum tetrahedra will balance with the positive charge of Ag^+ ions, trapping them within the structure.

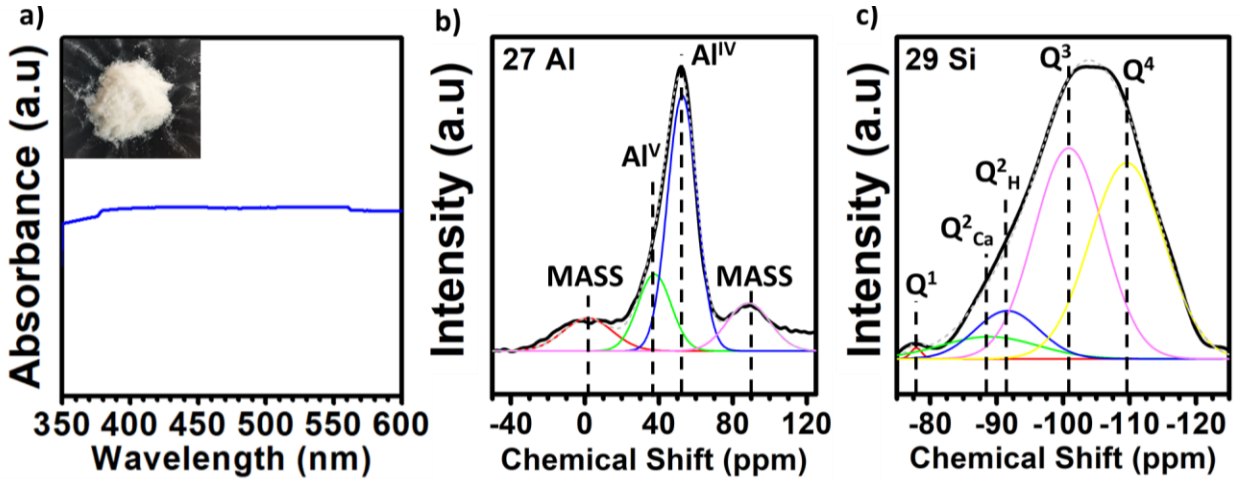

Figure 56: Ag-BGNs did not absorb light in UV-Vis (a), and the powder was colorless (inset), confirming the absence of Ag compounds. ^{27}Al MAS-NMR confirmed the dominant presence of Al^{IV} units (b), used to trapped Ag^{+} ions. The contribution of low Q^n units in ^{29}Si MAS-NMR demonstrated Ag-BGNs had a modified silicate network (c).

The network connectivity was evaluated in terms of Q^n speciation using ^{29}Si MAS-NMR. **Figure 56** c shows the chemical shift (δ) for Q^4 (-109 to -112 ppm), Q^3 (-100 to -102 ppm), Q^2 (-85 to -93 ppm), and Q^1 (-76 to -79 ppm). Similar to BGNs, two different signals were identified for Q^2 species related to hydrogen bonding (~ -93 ppm) and network modifiers bonding (~ -85 ppm). The primary network modifier in Ag-BGNs is Ca^{2+} ion with a concentration of 25 mol.%, and therefore, the chemical shift at -85 ppm was attributed to Q^2_{Ca}. The structure Ag-BGNs was dominated by Q^4 and Q^3 species representing each 30 and 42 % of the spectrum's intensity area, respectively. Therefore, the experimental network connectivity based on **Equation 7** yields approximately 0.67.

4.5.2.3. The degradation of Ag-BGNs *in vitro*

The degradation of Ag-BGNs was evaluated in terms of pH evolution and apatite-forming ability, following the same methodology used in Ag-BG microparticles in section 4.1.

4.5.2.3.1. pH evolution of Ag-BGNs

The degradation of Ag-BGNs was evaluated by immersion in PBS and monitored through the pH of the solution (**Figure 57** a). Like ternary BGNs, the Ag-BGNs present a burst ionic release evidenced by the pH increase above 9 after 24 h immersion. The concentration of alkaline ions remained at toxic pH levels for 4 days and then dropped back to neutral levels. A neutral pH value was maintained after that. Building on this fact, the Ag-BGNs were pre-conditioned in DMEM for 4 days before use in biological and antibacterial assays. The pH of preconditioned Ag-BGNs was monitored for 4 days to confirm the pH was within the biological range (**Figure 57** b).

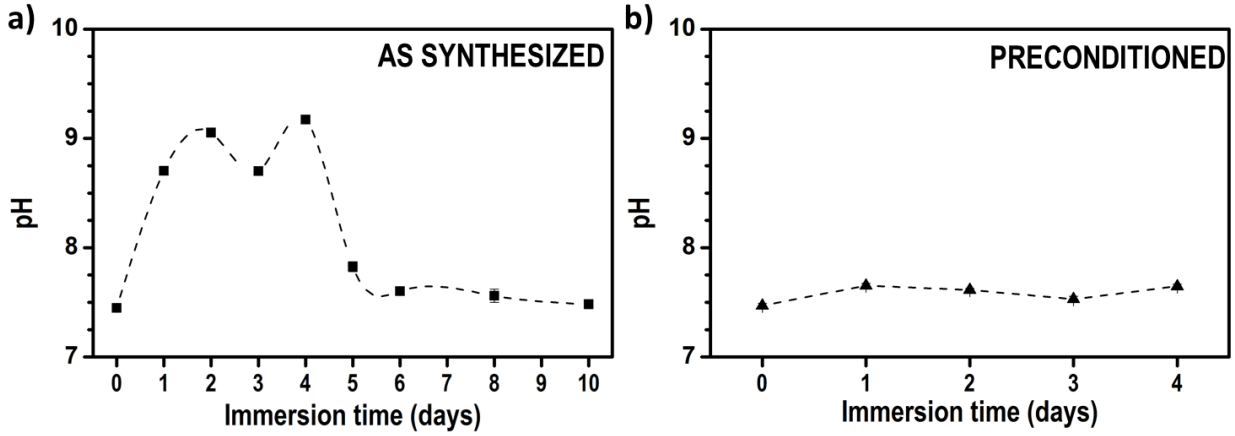

Figure 57: The degradation of the Ag-BGNs upon immersion raised the pH, which stayed at a toxic level (> 8) for up to 4 days before returning to neutral values (a). After preconditioning in DMEM for 4 days, Ag-BGNs degrade at a lower rate, as evidenced by the solution's steady neutral pH (b).

The capability of the Ag-BGNs to form apatite-like phase deposits was evaluated after immersion in SBF at 37 °C under constant agitation to reproduce body conditions. The morphology and

composition of the deposits were characterized by SEM-EDS (**Figure 58**). Ca-P deposit (white arrows) in the shape of needles were randomly observed after 1 and 3 days in SBF. The presence of these needles increased with the immersion time and led to the coalescence of needles to form flower-like structures around Ag-BGNs (blue arrows) after 5 and 7 days of immersion. Exposure for up to 14 days caused the densification of these Ca-P flower-like deposits into well-formed flakes associated with the mineral phase's crystallization. **Figure 58** also reports the semi-quantitative evolution of the Ca/P ratio at the Ag-BGNs surface from EDS spectra compared to the pH in SBF. The Ag-BGNs present a structural Ca/P ratio ~8. The Ca-P ratio decreased to ~1.7 after 7 days f immersion, which is the characteristic Ca/P ratio for biological HCA. Note that the Ca/P before immersion comes from the glass structure, whereas after immersion, the EDS signal comes predominantly from the surface deposits. The pH in a simulated biological environment remained within the neutral range, which suggests a steadier degradation in SBF and the faster deposition of salts and minerals, decreasing alkaline ion content in the SBF solution than in the buffer (as shown in **Figure 57** a).

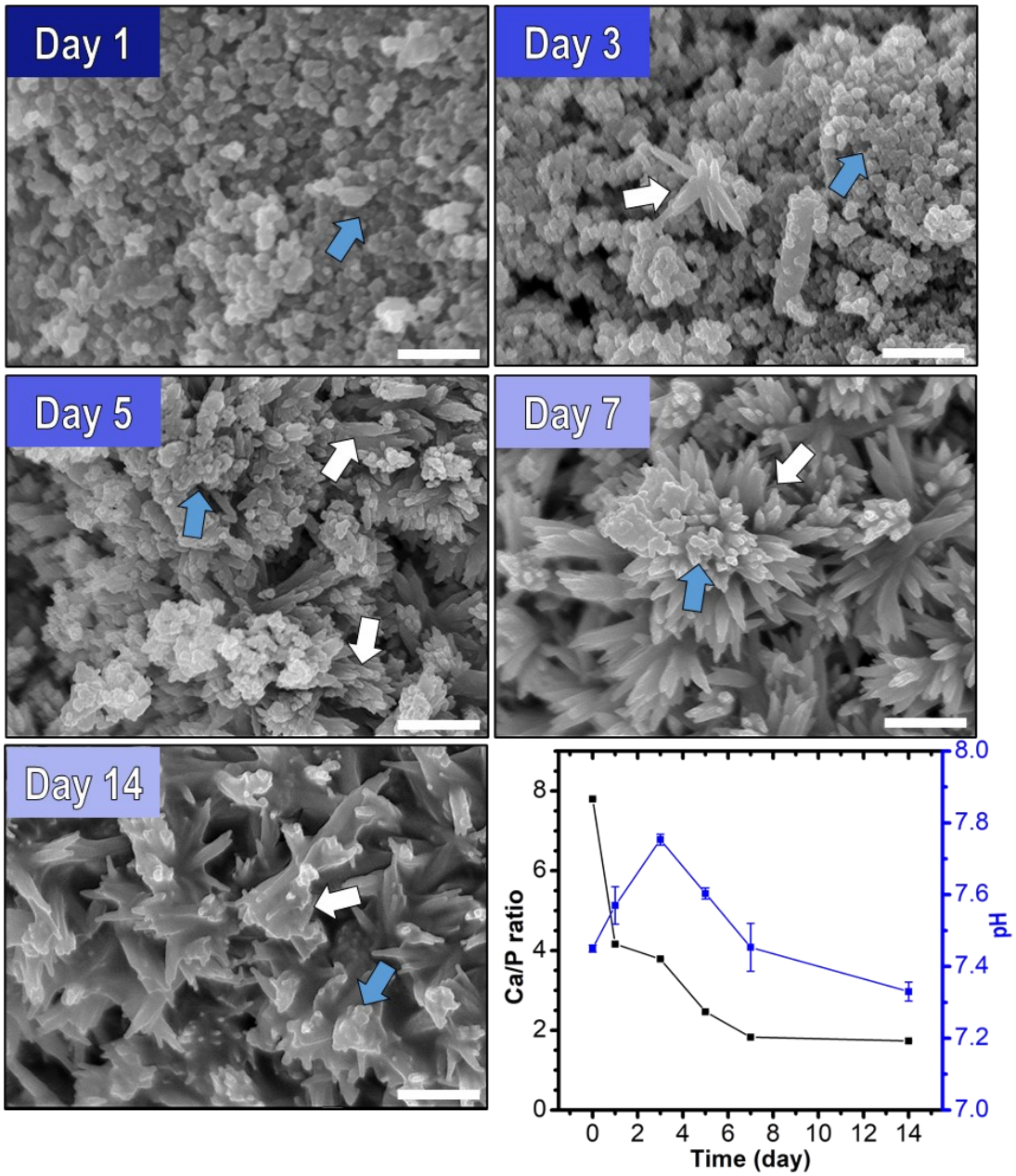

Figure 58: Deposition of biological apatite phase in Ag-BGNs after immersion in SBF. Ca-P needles (white arrows) formed around Ag-BGNs (blue arrows) after 3 days of immersion. The continued deposition caused the coalescence of needles in flower-like deposits after 7 days and their evolution to flakes upon crystallization after 14 days. The white scale bar represents 300 nm. The Ca/P ratio reached a value of 1.7, as obtained semi-quantitatively by EDS. The pH remained within neutral values in SBF.

The structural changes were monitored in FT-IR at various stages of immersion in SBF. **Figure 59** a shows the structure of Ag-BGNs before immersion in SBF with the characteristic vibration

of amorphous silicate-based glasses. For example, bending and stretching modes of the Si-O-Si bond were observed at 450, 805, and 1200 cm^{-1}. The overlap of the P-O bending and the Si-O-Si stretching mode around 1000-1050 cm^{-1} caused the broadening of the peak. The modification of the silica network, due to the successful incorporation of $Al_2O_4^-$, Ca^{2+} and Ag^+, as evidenced by the shoulder band at 900 cm^{-1} attributed to Si-O-NBO bonds. The immersion of Ag-BGNs in SBF induced the development of a broad P-O bending peak in the region of 575-620 cm^{-1}. This contribution evolved to a double peak after 5 days and sharpen after 7 days, indicating the formation of a crystalline phase. The Ca-P phase deposition was also supported by a decrease in the Si-O band intensity at 900 cm^{-1} and 1200 cm^{-1} and the sharpening of the P-O band at 1000 cm^{-1}. The crystalline Ca-P phase was further characterized with XRD and TEM (**Figure 59** b and c, respectively) after 14 days of immersion. **Figure 59** b confirmed as-synthesized Ag-BGNs were amorphous. After 14 days of immersion, a crystalline phase is developed, in agreement with FT-IR, showing diffraction peaks (marked at 26, 28, 32, and 46 °2θ) that matched those of carbonated hydroxyapatite in the ICDD (PDF No. 9003552). Silver-related crystalline phases were not developed after calcination nor after exposure to SBF. At a nanoscale, **Figure 59** c showed the distinctive feature of monodispersed Ag-BGNs (blue arrows) and deposited needles (white arrows) instead of flakes. The SAD pattern revealed strong overlapping of the (211), (112), and (300) diffraction rings, in agreement with XRD observations. The dark field image of these overlapping diffractions (**Figure 59** c) demonstrated the crystallinity belonged to the needle deposits rather than the Ag-BGNs. The amorphous nature of the Ag-BGNs yielded a broad and strong halo around the transmitted spot, causing some amorphous areas to light up in the dark field image.

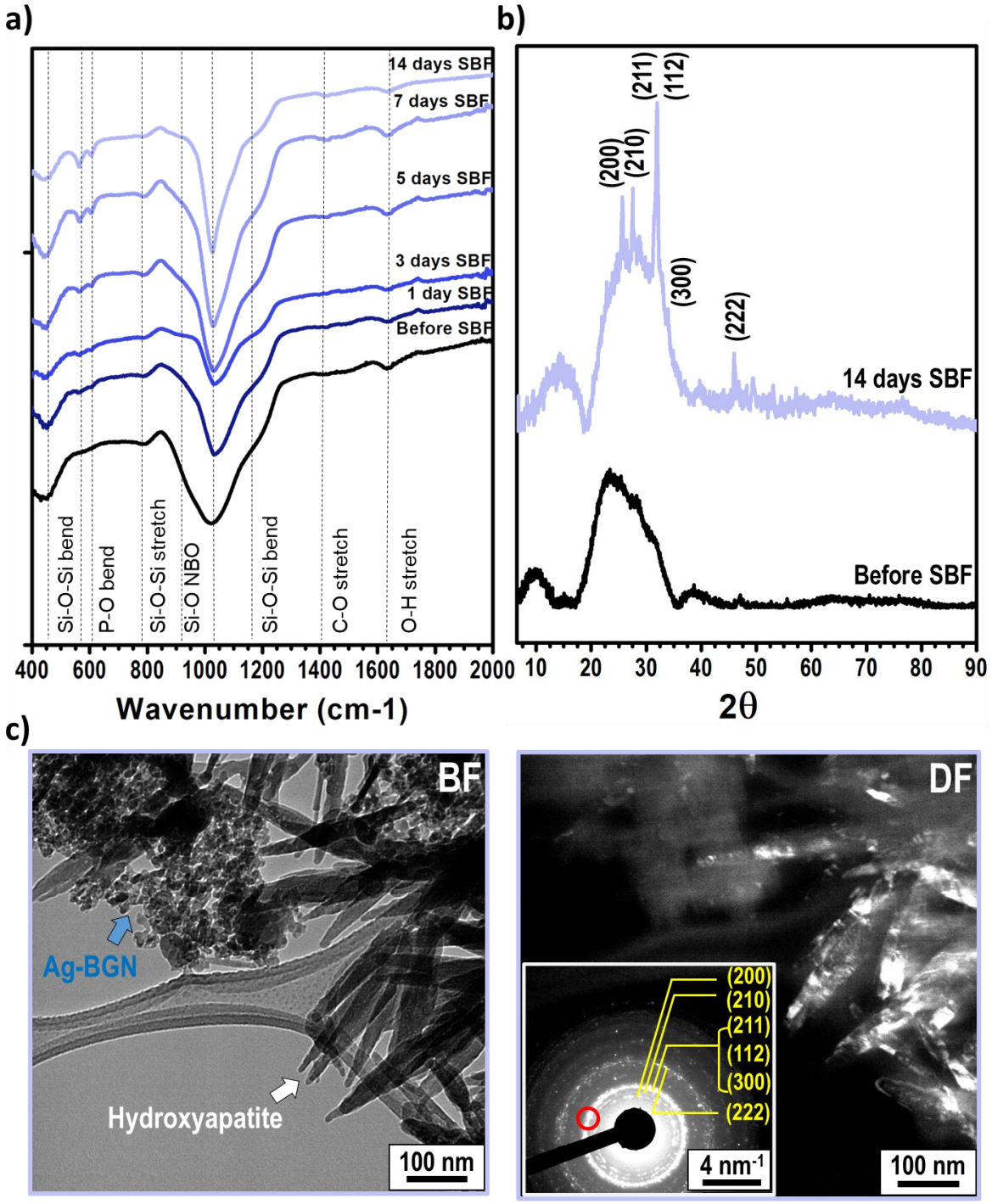

Figure 59: The structure of Ag-BGNs evolves during apatite deposition. FT-IR (a) shows the development of P-O vibrations and an increase in peak sharpness. Carbonated hydroxyapatite peaks were identified by XRD (b) after 14 days in SBF. At the nanoscale, the Ag-BGNs (blue arrows) were surrounded by needles (white arrows) after 14 days in SBF (c), as shown in the bright field (BF) image. The dark field (DF) image evidenced a nanophase distribution with amorphous nanoparticles and semi-crystalline needles. The SAD pattern (inset) further confirmed the deposited phase was carbonated hydroxyapatite. The red circle represents the objective aperture for the DF image.

4.5.2.4. Interaction of Ag-BGNs and microbes: antibacterial behavior

Increasing concentrations of Ag-BGNs nanoparticles were incubated with MRSA under different conditions to analyze their antibacterial behavior. As shown in **Figure 60** a, the MIC of Ag-BGNs under growth-arrested conditions (i.e., dispersing bacteria in PBS) was around 0.05 mg/mL, resulting in MRSA viability < 10^5 CFU/mL after 24h of, which is the minimum bacterial concentration to define an *in vivo* infection [242,243]. The inhibition increased with exposure time and Ag-BGNs concentration. In fact, 0.05 mg/mL of Ag-BGNs already caused a significant 10-fold decrease in CFU after 12 h of co-culture. Bacterial concentration was below the detection limit upon exposure to 0.25 mg/mL Ag-BGNs for 24 h, in clear contrast to the 5 mg/mL Ag-BG microparticles needed to achieve a similar antibacterial effect in PBS (**Figure 27** a).

The antibacterial effect was also significant when bacteria proliferation was allowed, as shown in **Figure 60** b. MRSA exposed to increasing Ag-BGNs concentrations using TSB as dispersing medium significantly decreased viability already after 12 h of treatment, although Ag-BGNs concentrations < 2.5 mg/ml were not able to suppress bacterial growth. This effect is evidenced by the CFU increase from 12 to 24 h for bacteria treated with 2.5 mg/mL of Ag-BGNs. Both of these treatments decreased MRSA viability after 12 h. Still, both Ag-BGN-treated and untreated bacteria kept growing at a similar rate at a longer exposure time, showing almost a ten-fold increase in CFU/mL from 12 to 24 h. However, increasing the concentration of Ag-BGNs above 10 mg/mL bypassed the bacteria growth and decreased the concentration below 10^5 CFU/mL after 24 h. In fact, 20 mg/mL of Ag-BGNs sterilized the solution.

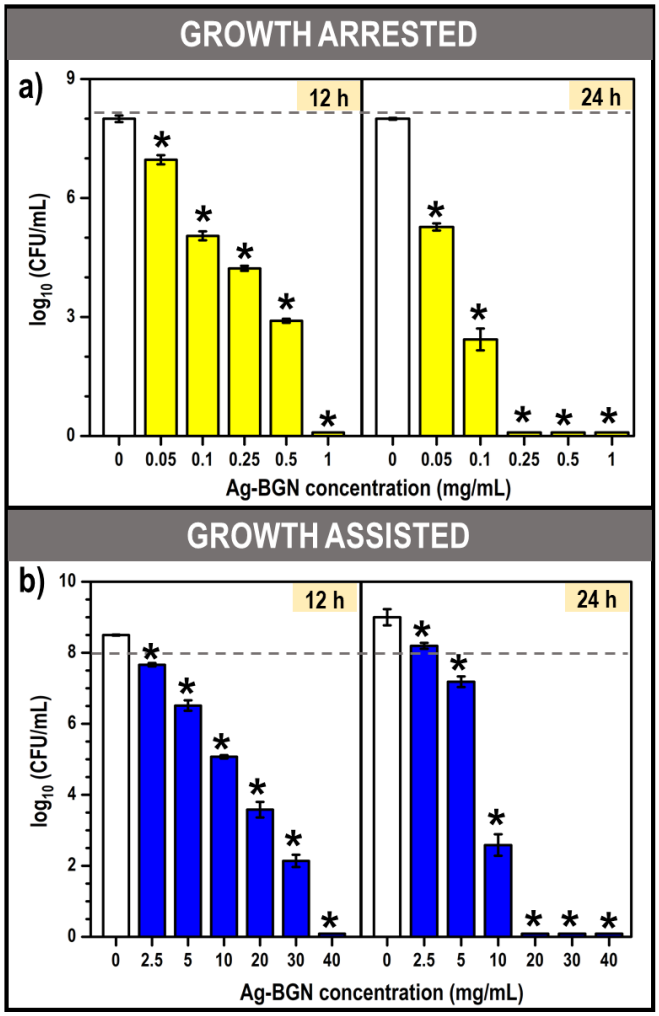

Figure 60: Ag-BGNs inhibit MRSA under growth-arrested (a) and growth-assisted (b) conditions. Suspensions of MRSA (OD_{600} = 1 equivalent to ~ 10^8 CFU/mL, represented by a dashed line) were mixed with fresh PBS (a) or TSB (b) medium (0 mg/mL, untreated control represented by white bars) and increasing concentrations of Ag-BGNs. The CFUs were enumerated after 12 and 24 h with a limit of detection of 100 CFU. (*) Indicates the significant difference between the untreated versus the particle-treated groups ($p < 0.05$).

4.5.2.4.1. Restoration of antibiotics by combination with Ag-BGNs

As previously presented, the combination of Ag-containing materials and antibiotics is synergistic against bacterial growth, showing a strong interaction between Ag-BG microparticles and cell-wall inhibitors. In this section, the antibacterial capabilities of Ag-BGN/ antibiotic were evaluated against MRSA to explore if the synergistic effect observed in microparticles is expanded in the

nanoparticle system. As a reference, MRSA was exposed to 0.5 mg/mL and 2.5 mg/mL Ag-BGNs, concentrations that correspond to the MICs of Ag-BGNs and Ag-BG microparticles, respectively. The Ag-BGN/fosfo were obtained using 0.002 % of fosfomycin (i.e., 0.01 µg/mL of fosfomycin for every 0.5 mg/mL of Ag-BGNs). At both concentrations, Ag-BGNs restored the antibacterial properties of fosfomycin (**Figure 61**), but while synergism was observed at 6 h of co-culture for the smallest Ag-BGNs concentration, sterility was achieved for the combination including 2.5 mg/mL Ag-BGNs. The inhibition of Ag-BGNs and Ag-BGN/fosfo was time-dependent, in agreement with previous observations.

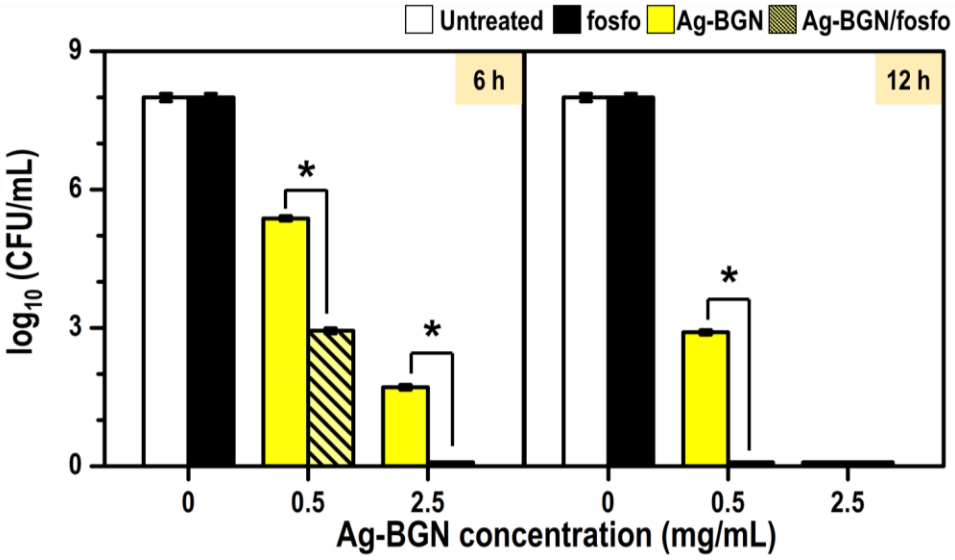

Figure 61: Ag-BGNs resurrect fosfomycin against MRSA. Suspensions of bacteria (OD_{600} = 1 equivalent to ~ 10^8 CFU/mL) were mixed with fresh PBS medium (0 mg/mL, untreated control, white bars), 0.5 µg/mL of fosfomycin (antibiotic control, black bars) and increasing concentration of Ag-BGNs (yellow bars) and their combination with 0.002 % of fosfomycin (Ag-BG/fosfo, patterned bars). The CFUs were enumerated after 6 and 12 h with a limit of detection of 10 CFU. (*) Indicates the significant difference between Ag-BGNs and Ag-BGN/fosfo ($p < 0.05$).

The synergistic capabilities of Ag-BGN/antibiotics were explored for different incubation times to determine the minimum exposure required to observe significant decreases in MRSA viability. For this purpose, combinations of 2.5 mg/mL of Ag-BGNs with either 0.1 µg/mL of oxacillin (**Figure**

62 a) or 0.05 µg/mL of fosfomycin were used (**Figure 62** b). Mild-inhibition was observed already after 30 min of treatment, becoming synergistic after 1 h in co-culture. Although synergism was observed with both antibiotics, the Ag-BGNs/fosfo provided stronger inhibition over time.

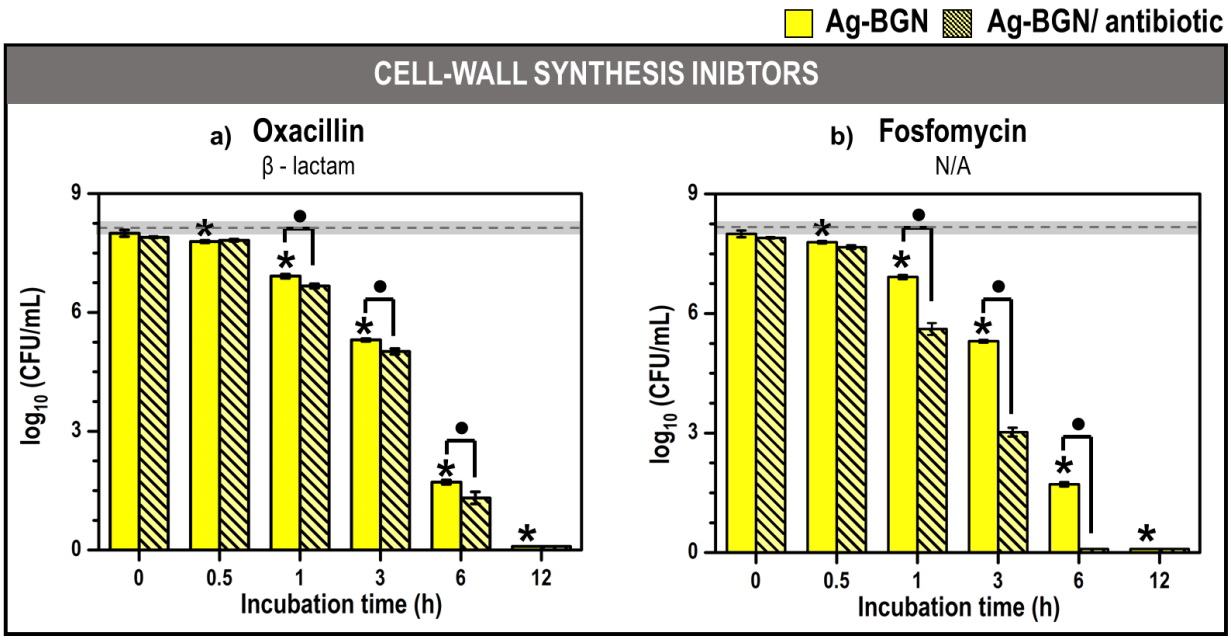

Figure 62: The synergistic effect of Ag-BGNs with oxacillin (a – 0.1 µg/mL) and fosfomycin (b - 0.05 µg/mL) against MRSA was observed after only 1 h of exposure and increased over time. Suspensions of MRSA (OD_{600} = 1 equivalent to ~ 10^8 CFU/mL) were mixed with fresh PBS medium (untreated control – dashed line), antibiotic (grey shade), 2.5 mg/mL of Ag-BGNs (yellow bars) or a combination of substances (pattern bars). Note that antibiotics alone were ineffective against MRSA. The CFUs were enumerated for up to 12 h with a limit of detection of 10 CFU. (*) Indicates the significant difference between Ag-BGN-treated and untreated MRSA and (●) marks the significant difference between Ag-BGNs and Ag-BGN/antibiotic ($p < 0.05$).

4.5.2.5. Interaction of Ag-BGNs and cells: biocompatibility

hBMSCs isolated and expanded from adult bone marrow aspirates present high pluripotency differentiation capacity. As previously shown, these cells in contact with Ag-BG microparticles can be stimulated towards osteogenesis. Therefore, in this section, the biocompatibility of Ag-BGNs was evaluated in terms of hBMSCs cytotoxicity and differentiation to validate the biological use of the system at a nanoscale.

4.5.2.5.1. *In vitro* cytotoxicity of Ag-BGNs

Figure 63 shows no cytotoxic effect over time for Ag-BGN-treated cells. The release of Ag-BGNs degradation products promoted their mitochondrial metabolic activity compared to untreated cells according to measurements with CCK-8. Cell proliferation was significantly accelerated upon exposure to 5 and 10 mg/mL Ag-BGNs concentrations. Proliferation rates were similar for untreated and 20 mg/mL Ag-BGN-treated hBMSCs; however, the latter had significantly higher cell concentration (**Figure 63** b). This result suggests that exposure to 20 mg/mL Ag-BGNs after 4 days of co-culture may favor other cellular processes. As an additional control, cells were exposed to 0.2 mg/mL Ag_2O, simulating the Ag's total content in 20 mg/mL Ag-BGNs. In this case, a 30% decrease in cell viability was detected after 4 days of exposure, indicating the cytotoxicity of the Ag_2O treatment.

Cell health and confluence were evaluated using optical microscopy (**Figure 63** c). Untreated hBMSCs dispersed uniformly through the well and presented spindle-like shapes. Ag-BGN-treatments did not alter cells shape but increased cell concentration so that confluence is reached after 4 days of exposure, 3 days before untreated cells. In contrast, after Ag_2O-treatment, few viable cells remained, and their shape turned to become rounded, indicating their stress.

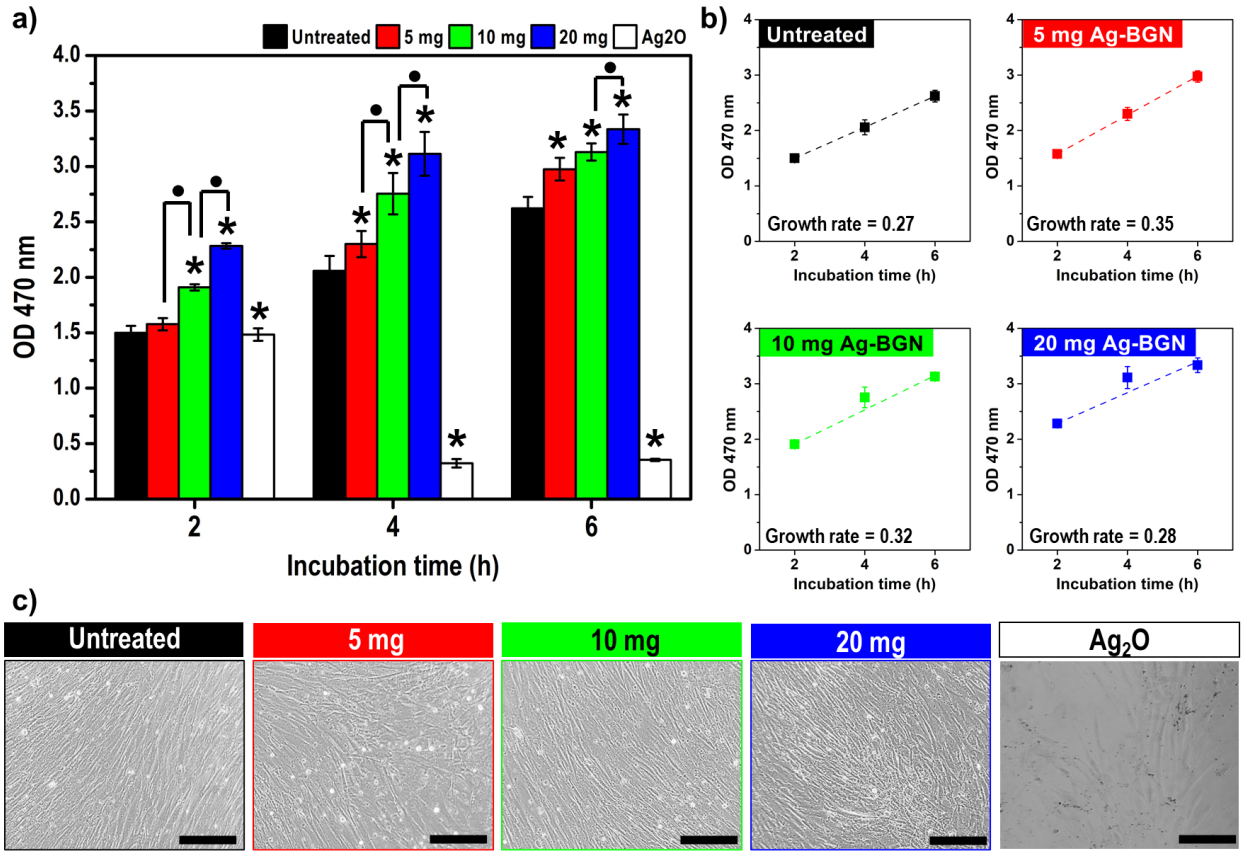

Figure 63: Ag-BGNs promoted the proliferation of hBMSCs. Cell viability via CCK-8, reported by optical density (OD), increased after treatment with 5, 10, and 20 mg/mL of Ag-BGNs and decreased after exposure to 0.2 mg/mL Ag_2O (a). The proliferation rate (b), obtained as OD/time, was faster for the lower concentrations of Ag-BGNs. Optical images (c) show the increase in cell density after Ag-BGNs treatment and the lack of viable cells upon treatment Ag_2O. Cell presented a spindle-like morphology after Ag-BGNs treatment. Scale bar represents 500 µm. Statistical difference between untreated and treated hMBSCs is indicated with (*) and among Ag-BGN-treatments of different concentrations with (●) for $p < 0.05$.

4.5.2.5.2. Osteogenic differentiation on exposure to Ag-BGNs

The osteogenic differentiation was evaluated in terms of mineralization by ARS and gene expression by qRT-PCR. All hBMSC cells showed calcified nodule formation after 14 days of Ag-BGNs treatment, and matured ECM was observed after 10 mg/mL treatment (**Figure 64** a). Quantification of calcified nodules obtained by measuring OD_{405} of the monolayers (**Figure 64** b) confirmed the increase in mineral content with Ag-BGNs concentrations.

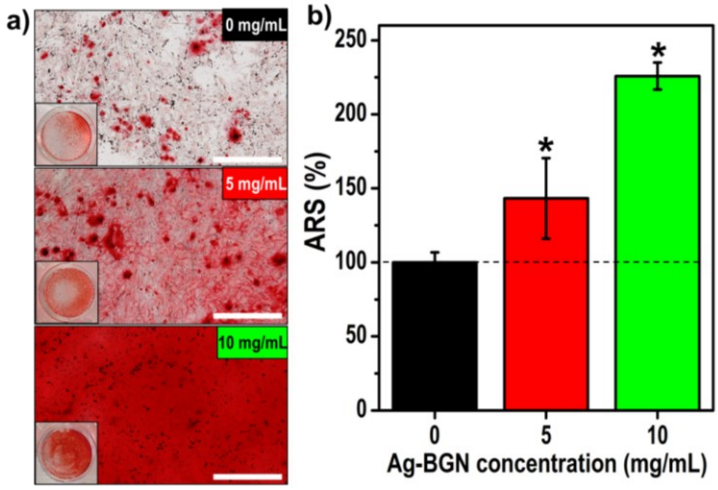

Figure 64: Ag-BGNs provoked cell mineralization after 2 weeks of co-culture. The ARS-stained calcified nodules formed by hBMSCs are shown in (a) for untreated and Ag-BGN-treated groups. Insets show the monolayers formed on 16 mm diameter wells. The scale bars represent 500 µm. Secretion of Ca in the osteogenic medium was quantified by optical density, normalizing the data to 100% of the untreated cells (0 mg/mL, black bar) (b). Statistical difference between untreated and Ag-BG treated cells for $p < 0.05$ is indicated with (*).

A separate group of fibroblasts from the mineralization test was also prepared for microscopy. TEM highlighted significant ultrastructural differences in hBMSCs after exposure to Ag-BGNs. Images of TEM sections were captured without negative staining to identify Ag-BGNs and the mineral deposits due to differentiation, both of which are more electron-dense due to their ceramic nature. Additionally, other sections were negative-stained to gain diffraction of organic components and evaluate the structure and morphology of untreated fibroblasts compared to Ag-BGN-treated cells (**Figure 65**). The structural components were recognized as specific organelles by compatibility of characteristic features with the literature in the images for collagen fibrils, vesicles, calcium minerals, mitochondria, autolysosomes autophagosomes [268–271]. Other analytical techniques with unequivocal staining may be performed to verify these observations. Untreated cells (**Figure 65** a-c) showed a small presence of collagen fibrils and vesicles. The calcium minerals appeared in different shapes and sizes, and mineral nano-granules (~ 50 nm) near and inside the mitochondria (M), in agreement with other reports [269,272].

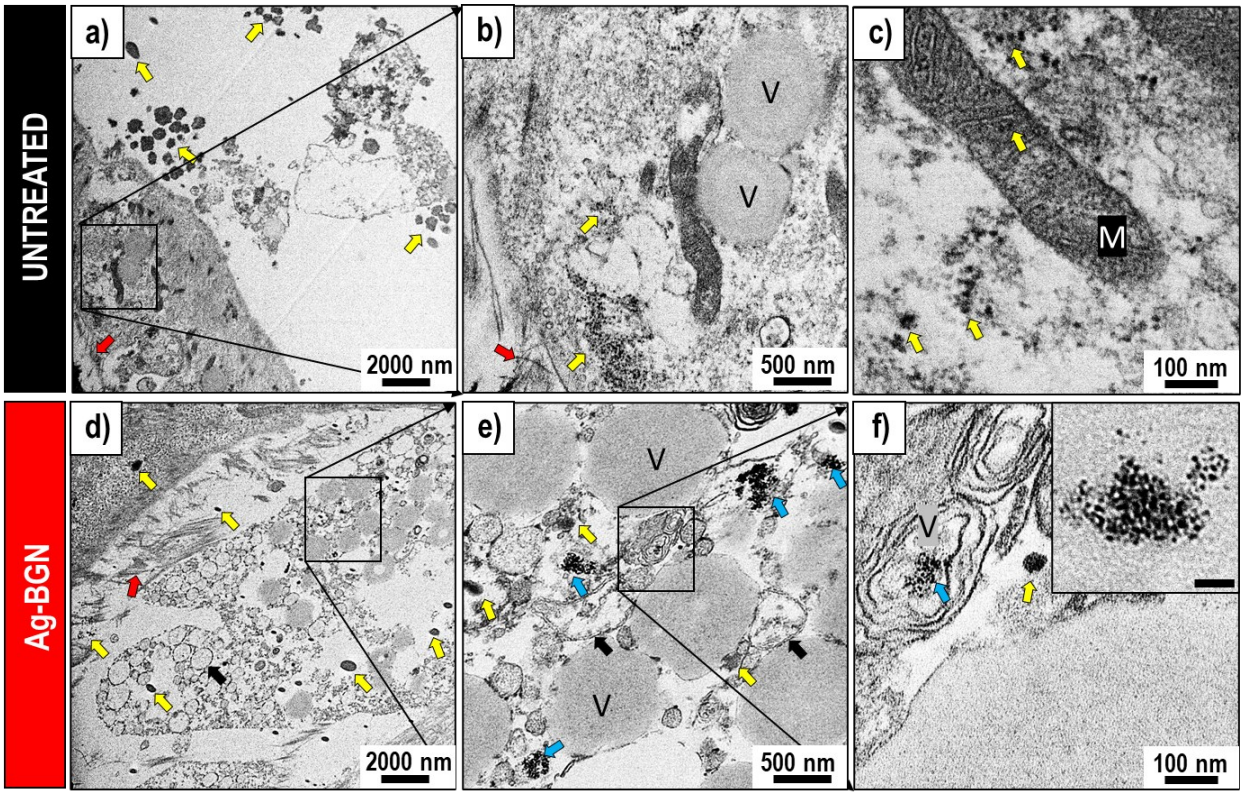

Figure 65: Structure of untreated fibroblasts (a-c) and Ag-BGN-treated (d-f) fibroblasts cultured 14 days in osteogenic medium. Untreated cells present collagen fibrils (red arrows) and mineral deposits of various sizes (yellow arrows), with granules around mitochondria (M). Ag-BGN-treated cells internalized the Ag-BGNs (blue arrows), which were found around a large number of autolysosomes or autophagosomes (black arrow) and vesicles (V). Inset in (f) shows a high magnification of internalized Ag-BGNs. The scale bar represents 50 nm.

In contrast, after Ag-BGNs treatment (**Figure 65** d-f), the concentration of collagen fibrils and vesicles significantly increased. Compared to untreated fibroblasts, the presence of many calcium deposits and granules was found, as well as numerous vesicles compatible with autolysosomes or autophagosomes identified from similar features described in the literature [270,271]. TEM images confirmed the internalization of Ag-BGNs that appeared as ~100 nm clusters; the irregular shape of the particles also suggested their degradation during treatment (**Figure 65** f, inset). Calcium granules and Ag-BGNs were distinguished by their size (i.e., granules were larger than Ag-BGNs), distribution (i.e., Ag-BGNs formed aggregates), and electron density in un-stained sections (i.e.,

Ag-BGNs were significantly darker). Ag-BGNs were intracellularly distributed around vesicles and autophagosomes putatively, indicating their role in nanoparticles' uptake. No significant alterations in developed endoplasmic reticulum and mitochondria (M) were evident in Ag-BGN-treated fibroblasts, neither the presence of particles in the cell nucleus (not shown). Thus, it seems that nanoparticles accumulated in the cytoplasm, being unable to penetrate or be transported through the nuclear membrane. Of note, despite the larger concentration of calcium deposits observed in the TEM images of untreated cells (**Figure 65** a) vs. Ag-BGN-treated (**Figure 65** d), this is not a representative feature according to the higher mineralization detected by ARS after exposure to Ag-BGNs. Therefore, the images may only serve as a qualitative assessment of cellular morphology and structure upon mineralization.

Osteogenic differentiation was also evaluated after 2 weeks of Ag-BGNs treatment in the osteogenic medium following expression by qRT-PCR for 6 different gene markers: *OCN*, *OSX*, *OMD*, *ACAN*, *COL10A1*, and *BSP* (**Figure 66**). Selection of the genes of interest was based on their different roles in osteogenic differentiation: *OCN* is correlated to bone mineral density [240]; *OSX* is an essential transcription factor for osteoblast maturation [273]; *OMD* plays a pivotal role in modulating osteo-differentiation and usually correlates to extracellular matrix (ECM) formation [274]; *ACAN* [275] and *BSP* [239] are integral proteoglycans of the cartilaginous tissue ECM and are expressed at different stages of chondrocyte maturation; *Col10A1* encodes the collagen expressed during endochondral ossification [276]. Signs of mineralization were seen 2 weeks after Ag-BGNs treatment. Upregulations of *OCN*, *OSC*, and *OMD* reached up to 4-fold with 10 mg/mL of Ag-BGNs, but no statistical rise was found upon exposure to 5 mg/mL. Moreover, upregulations of *ACAN*, *Col10A1* and *BSP* was even higher (7-14-fold) than for the other genes, and showed statistical difference for the two Ag-BGNs concentrations studied.

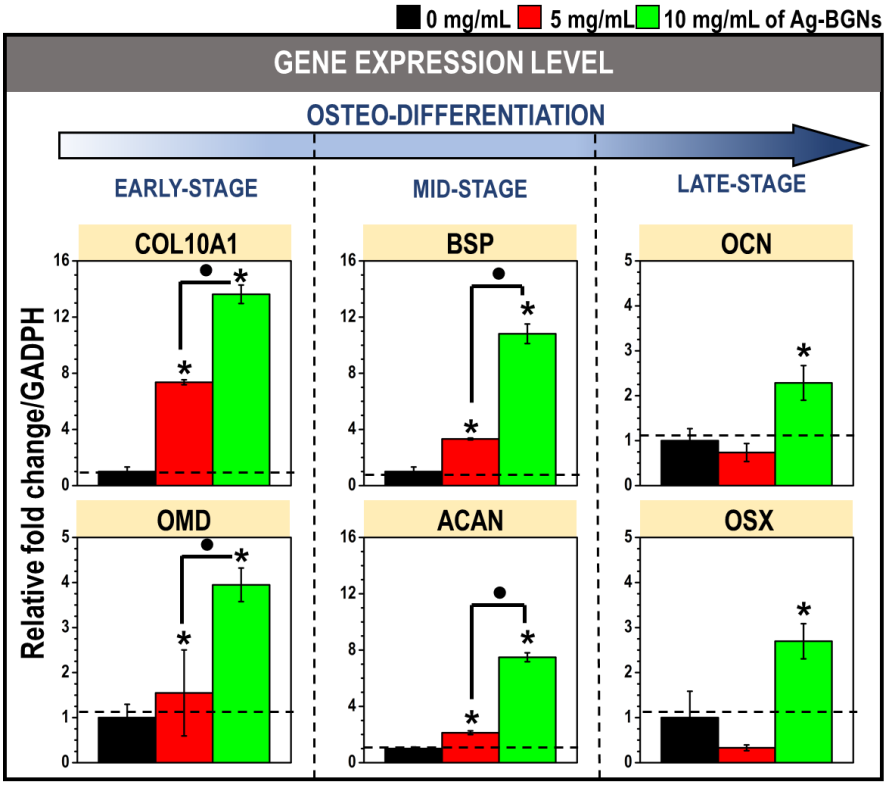

Figure 66: Ag-BGNs upregulated osteogenic gene markers in hBMSCs after 14 days in osteogenic medium. Gene expression was higher for early and mid-stage markers. Late-stage markers were expressed only for 10 mg/mL of Ag-BGNs. Untreated cells (0 mg/mL – black bar) were used as the control for 100 % of expression (dashed line). The statistical significance between untreated and Ag-BGN-treated cells is marked with (*) and between different concentrations of Ag-BGNs with (●) for $p < 0.05$.

4.5.2.6. Bone regenerative capability of Ag-BGNs

The growth of bone tissue in calvaria defects was evaluated with micro-CT (**Figure 67** a-b). The images showed defects with slight bone re-growth after treatment with Ag-BGNs, while the defects remained critically opened in the PBS groups. The quantification of the occupied volume shows a statistical difference between both groups, although very little bone regeneration was observed. Immunohistology (**Figure 67** c) shows non-dense fibrous tissue in the PBS-treated group. Notably, the Ag-BGNs treated group shows greater bone area; however, it was accompanied by a high concentration of macrophages, indicating an inflammatory response. Dense

particulates stained as minerals were dispersed along with the defect. As a general trend, significant implant migration was noticed across Ag-BGN-treated defects. Together these results demonstrated Ag-BGNs treatment triggered mild bone formation.

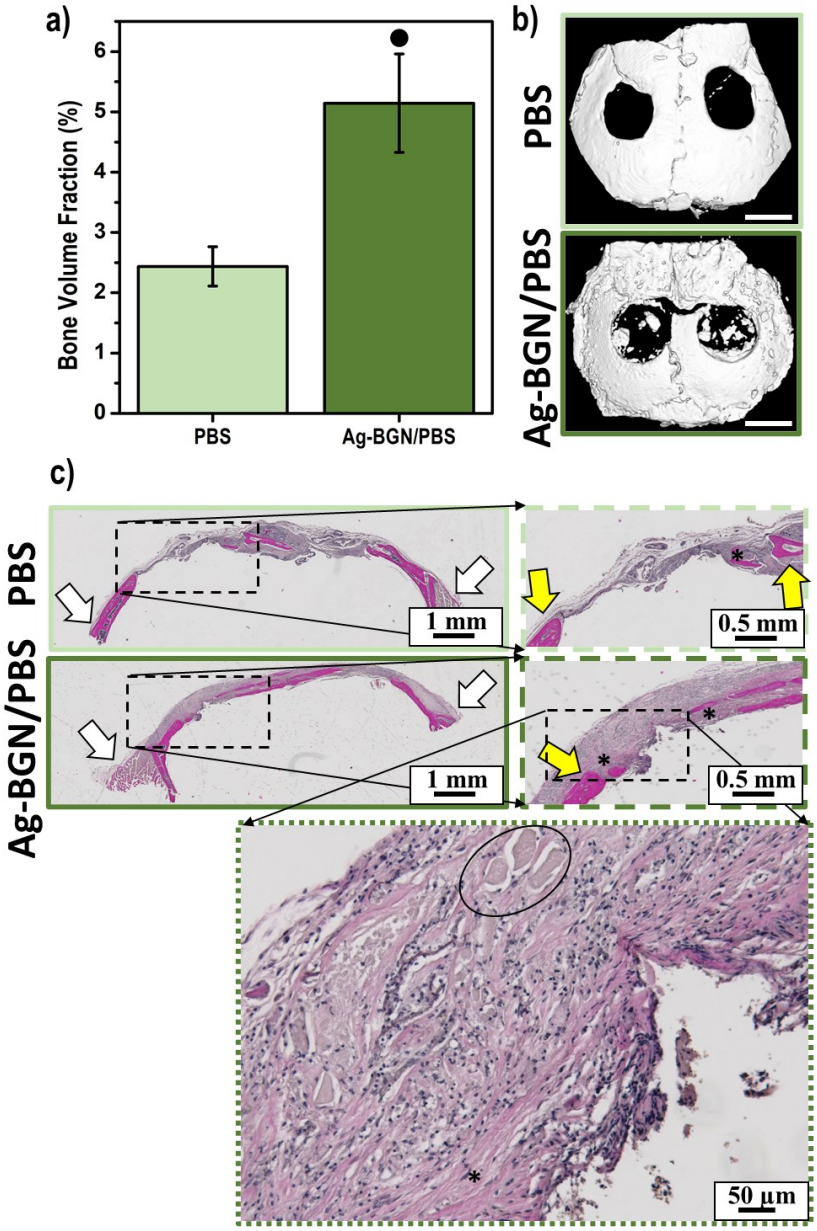

Figure 67: Bone volume fraction formed (a) and micro-CT images of the calvaria after 40 days of treatment, where the white scale bar represents 3 mm (b). Statistical significance ($p < 0.05$) between groups is marked with (●). Histology images of the coronal cross-sections of calvaria are divided in half along the sagittal crest (c), where the presence of new soft tissue and bone is indicated with (*). Yellow arrows represent the edges of the defect and black circumference for particulates. Note that mice treated with PBS present little overall regeneration of calvaria defect.

4.6. Design of medical Ag-BGN/polymer injectable nanocomposite devices

The unique bioactive and antibacterial characteristics of the newly synthesized Ag-BGNs make them attractive for medical applications. The Ag-BGNs were also highly monodispersed when in solution, and therefore, hold potential as building blocks for nanocomposites.

BGN-based hydrogel nanocomposites have emerged as promising materials owed to their ability to mimic tissue microenvironment and their ability to expand, filling irregular defects. In this section, injectable nanocomposites consisting of Ag-BGN dispersed in a hydrogel matrix were explored to provide an easy delivery for osteoregenerative applications. Two natural derived hydrogels were used as matrices: extracellular matrix and collagen type I.

4.6.1. Fabrication and microstructural characterization of the nanocomposite scaffold.

Hydrogel composites were synthesized following temperature-induced polymerization at 37 °C, an easy and inexpensive approach to cure polymers. The hydrogel solution was neutralized to obtain a pH slightly lower than neutral since the preliminary experiment showed faster gelation for acidic pH. The Ag-BGNs were dispersed in PBS and evenly distributed in the hydrogel precursor before polymerization using gentle pipetting and sonication. The nanocomposites were developed with 2 concentrations of Ag-BGNs: 5 and 10 wt.%. The hydrogels with 0 wt.% of Ag-BGNs were used as controls. The time for polymerization was monitored for each nanocomposite and established when the sample did no longer flow when the plate was tilted. **Table 18** summarized the gelation time as a function of Ag-BGNs concentration for collagen and extracellular matrix nanocomposites. Changes in gelation time were observed because of the incorporation of Ag-BGNs. Polymerization was almost unaffected by the concentration of Ag-BGNs in Col/Ag-BGN, although slightly longer time was required for 10 wt.% than 0 and 5 wt.%.

In contrast, the ECM/Ag-BGN samples show a significant increase in gelation time as the concentration of Ag-BGNs increased, which could last for up to 1 day at 37 °C. It is worth mentioning that although the polymerization was confirmed, the samples retained a significant amount of water at their core and did not retain their shapes when removed from the gelation mold (i.e., 24-well plate). This semi-liquid state of the nanocomposites was ideal for injectability confirmed through a syringe with a 27G needle.

Table 18: Time for polymerization at 37 °C for the different Ag-BGN/hydrogel nanocomposites.

Type of hydrogel	Ag-BGNs (wt.%)	pH	Time for polymerization	Code name
Collagen	0	7.3	30 min	Col/Ag-BGN0
	5	7.3	30 min	Col/Ag-BGN5
	10	7.3	60 min	Col/Ag-BGN10
ECM	0	7.3	40 min	ECM/Ag-BGN0
	5	7.3	60 min	ECM/Ag-BGN5
	10	7.3	6 h	ECM/Ag-BGN10
	25	7.5	24 h	ECM/Ag-BGN25
	50	7.5	24 h	ECM/Ag-BGN50

The macro and microarchitecture of Ag-BGN/hydrogels were evaluated for two concentrations of Ag-BGNs (x= 5 and 10 wt.%) and compared to that of hydrogels alone. Under SEM examination, collagen and extracellular matrix hydrogels (**Figure 68**) exhibit a dense fibrillar network. The incorporation of Ag-BGNs in the hydrogel solution before gelation yields small changes in the hydrogel macro and microarchitecture. For instance, the nanocomposites appeared opaquer for higher concentrations of Ag-BGNs (**Figure 68** insets) and presented a white color, the same as the Ag-BGNs powder (**Figure 56** a).

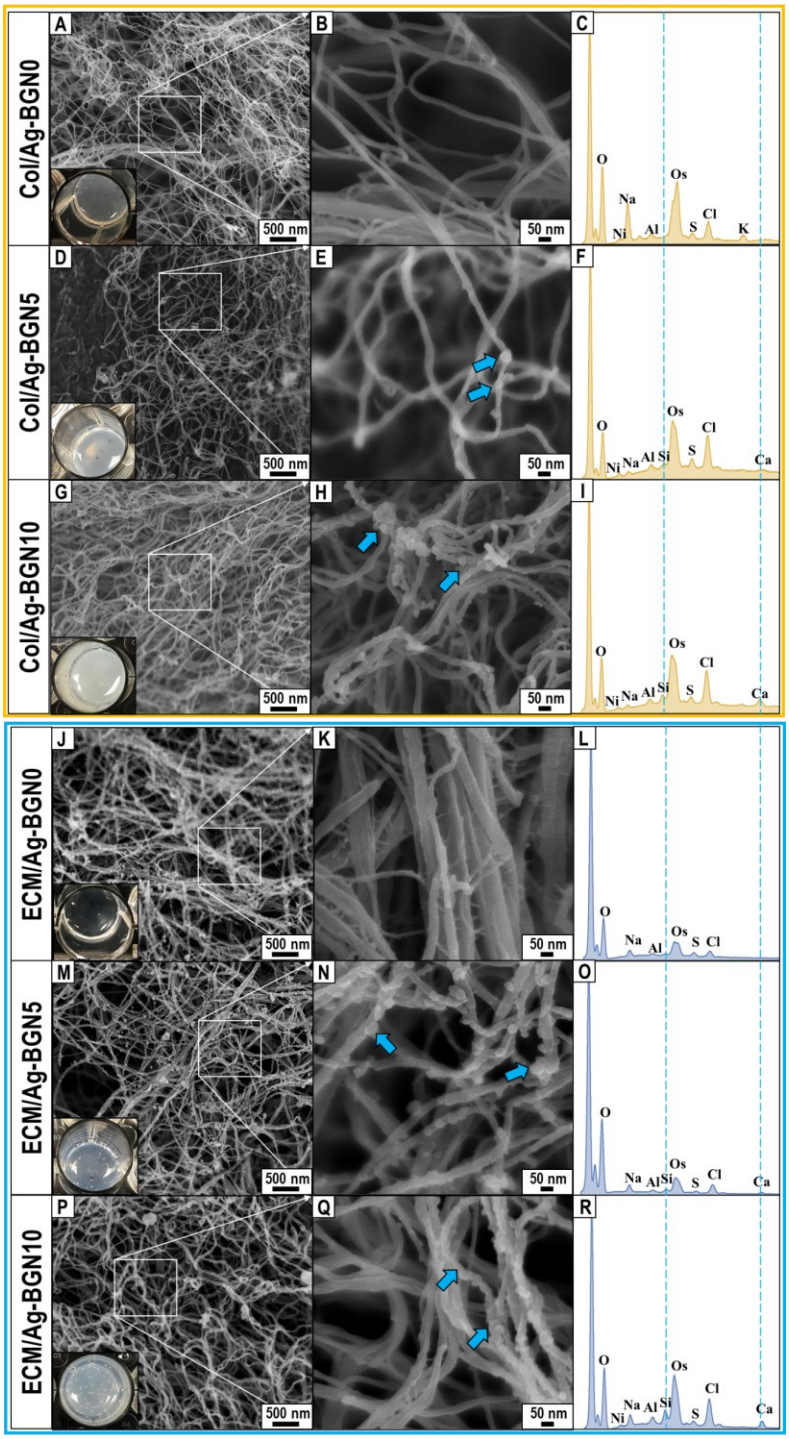

Figure 68: Morphology and elemental composition of the hydrogel alone (A-C and J-L) and the Ag-BGN/hydrogel nanocomposites (D-I and M-R). The insets show the macro architecture of composites, which opacity increased with the Ag-BGNs wt.%. Nanoparticles were homogeneously distributed within collagen (D-I) and extracellular matrix (M-R) fibrils. The increase of Si and Ca peak intensity (marked with a dashed line) in EDS spectra (F, I, O, and R) confirms the presence of Ag-BGNs.

The fibrillar microstructure was preserved after the incorporation of Ag-BGNs, regardless of concentrations. However, the diameter of these fibrils evolved with Ag-BGNs concentrations. The Col/Ag-BGN0 (**Figure 68** A-B) and ECM/Ag-BGN0 (**Figure 68** J-K) samples used as control evidenced larger fibril diameters (23 and 34 nm, respectively) than the nanocomposites (**Table 19**). SEM showed numerous 30-50 nm spherical nanoparticles distributed through the hydrogel network of Ag-BGNs containing samples (**Figure 68** D-E, G-H, M-N, and P-Q). The formation of protein bundles with a particle-like appearance is an anticipated phenomenon after incorporating Ag-BGNs since the fibrils will try to bend to embed the nanoparticles. However, EDS mapping around the 30-50 nm spherical nanoparticles revealed peaks attributed to Si and Ca (**Figure 68** F, I, O, and R) compared to Ag-BGNs free hydrogels (**Figure 68** C and L). The intensity of Si and Ca peaks was higher in the 10 wt.% Ag-BGNs (**Figure 68** I and R) nanocomposites than in the 5 wt.% (**Figure 68** F and O). Therefore, it can be inferred that the 30-50 nm spherical nanoparticles come from the aggregation of individual 10 nm size Ag-BGNs during gelation. In addition to a decrease in fibril diameter, incorporating higher concentrations of Ag-BGNs also caused a dramatic increase in fibril density which were randomly patterned throughout the sample. A higher number of Ag-BGNs were observed in the ECM/Ag-BGN (**Figure 68** N and Q) than in Col/Ag-BGN (**Figure 68** E and H) nanocomposites. Similarly, Si and Ca peaks were more evident in ECM/Ag-BGN (**Figure 68** O and R) than in Col/Ag-BGN (**Figure 68** F and I). This effect was also expected from the fabrication recipe and can be explained by the hydrogels' densities. ECM has a higher density (~8 mg/mL) than collagen (~2.4 mg/mL), and therefore, a higher mass of Ag-BGNs was required to achieve the 5 and 10 wt.% in the nanocomposite.

Table 19: Fibril diameter (nm) for Col/Ag-BGN and ECM/Ag-BGN nanocomposites. The size was measured from SEM images for n=50. The diameter of the fibrils decreases with Ag-BGNs content.

Nanocomposite	Fibril diameter (nm)
Col/Ag-BGN0	22.5 ± 2.2
Col/Ag-BGN5	16.7 ± 1.5
Col/Ag-BGN10	16.1 ± 1.8
ECM/Ag-BGN0	33.61 ± 5.1
ECM/Ag-BGN5	26.14 ± 2.5
ECM/Ag-BGN10	20.5 ± 1.9

The structure of the nanocomposites was also evaluated in FT-IR. The Col/Ag-BGN (**Figure 69** a) and ECM/Ag-BGN (**Figure 69** b) nanocomposites developed a new peak at 450 cm^{-1} after Ag-BGNs incorporation. This vibration may be correlated to Si-O-Si bending mode. The relative intensity of this vibration increases slightly with Ag-BGNs concentration. Additionally, the FT-IR spectra of Col/Ag-BGN0 (i.e., collagen control) exhibited various bands between 1140 and 1600 cm^{-1} that characterize the collagen hydrogel structure [277]. For example, bending of C=C (~ 1600 cm^{-1}), the scissoring band of the CCH_2 group (~ 1450 cm^{-1}), the C-H vibration of CH_3 groups (~ 1350 cm^{-1}), and the symmetric and antisymmetric stretching of the O-R groups (~ 1140 cm^{-1}) [277,278]. The collagen also consisted of amide I, II, and III bands; the N-H in-plane bend vibrations were noted at 1240, 1550, and 1640 cm^{-1} [279]. Most of these bands are also observed in the Col/Ag-BGN5 and Col/Ag-BGN10 nanocomposites. In contrast, the ECM/Ag-BGNx nanocomposites only showed peaks related to the silica network. Therefore, FT-IR confirmed the presence of Ag-BGNs in the nanocomposites, in agreement with the SEM-EDS results.

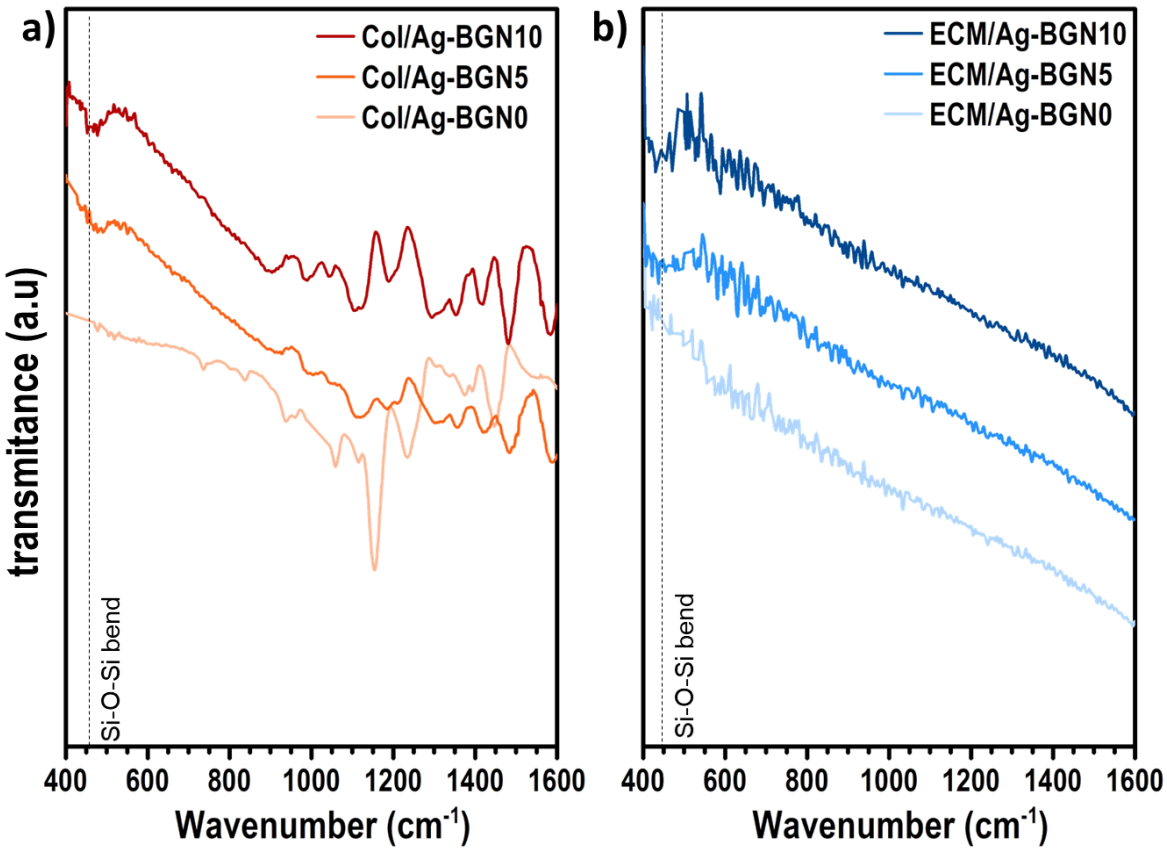

Figure 69: The hydrogel nanocomposites developed a vibration due to the incorporation of Ag-BGN. The intensity of Si-O bend mode increased with Ag-BGNs content in Col/Ag-BGNx (a) and ECM/Ag-BGNx (b). The x denotes the different concentrations of Ag-BGNs (i.e., 0, 5, and 10).

4.6.2. Interaction of Ag-BGN/hydrogel nanocomposites with bacteria.

The antibacterial activity of Col/Ag-BGNx and ECM/Ag-BGNx was evaluated against planktonic growth-arrested MRSA. The viability was characterized by colony counting after 24 h of incubation with the samples. Exposure to Col/Ag-BGN0 (**Figure 70** b) and ECM/Ag-BGN0 (**Figure 70** c) induced a CFUs increase, whereas bacterial viability significantly decreased when Ag-BGNs was delivered with the collagen CFUs decreasing below untreated levels. In contrast, only the highest Ag-BGNs concentration induced a reduction in bacterial CFUs when using ECM

as a matrix. In general, although both nanocomposites showed antibacterial action, this was significantly lower than of Ag-BGNs alone after 24 h.

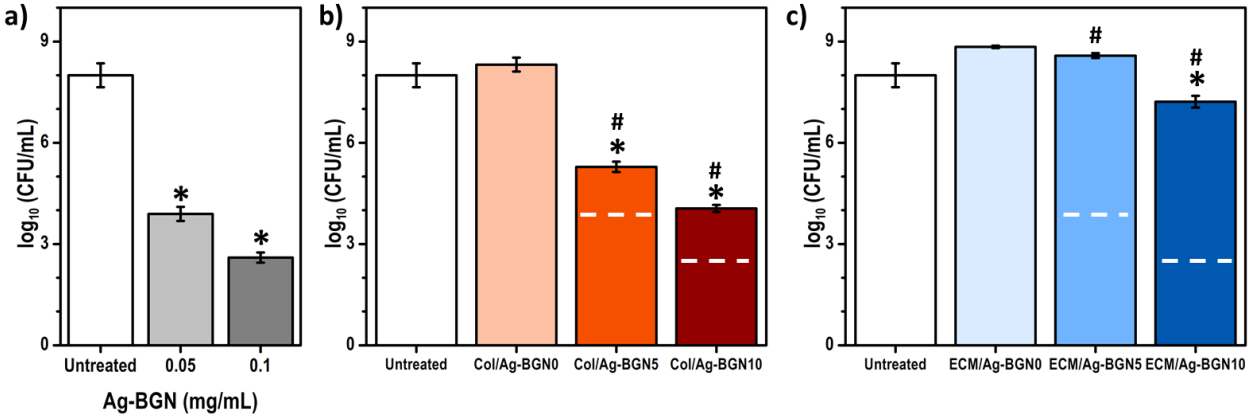

Figure 70: Ag-BGN/hydrogel nanocomposites are antibacterial against MRSA. The antibacterial capability of Ag-BGNs alone (a) is presented as reference for 0.05 mg/mL and 0.1 mg/mL of Ag-BGNs, the concentrations delivered in the nanocomposites for x=5 and x=10, respectively. The Col/Ag-BGNx (b) and ECM/Ag-BGNx (c) reduced the viability of MRSA, although they show higher CFU than Ag-BGNs alone. The dashed lines indicate the CFUs obtained for Ag-BGNs alone at the specified concentration. Note that collagen (Col/Ag-BGN0) and ECM (ECM/Ag-BGN0) alone are not antibacterial. Suspensions of bacteria (OD_{600} = 1 equivalent to ~ 10^8 CFU/mL) were mixed with fresh PBS medium (0 mg/mL, untreated control, white bars), 0.4 mL of Col/Ag-BGNx or 0.1 mL of ECM/Ag-BGNx. The CFUs were enumerated after 24 h with a limit of detection of 100 CFU. The significant difference between untreated and treated groups is indicated with (*) while between Ag-BGNs alone and the nanocomposites is indicated with (#) ($p < 0.05$).

4.6.3. Interaction of ECM/Ag-BGN nanocomposites with cells: biocompatibility

Assessment of cytotoxicity and cell proliferation was performed only with ECM/Ag-BGNx as a representative group. The ECM/Ag-BGN nanocomposites evaluated were x= 25 and 50 wt.%. The dose was increased so that the effect of Ag-BGNs product release would be notable during the assay. Specifically, 0.4 and 0.8 mg of Ag-BGNs were delivered to hBMSCs. **Figure 71** a shows higher cell viability in the ECM/Ag-BGN groups compared to the untreated control. Cell proliferation with Ag-BGNs nanocomposites was dose-dependent, in agreement with the effect observed in **Figure 63**. The proliferation rate (**Figure 71** b) increased significantly with Ag-BGNs

concentration. Cells showed the characteristic spindle-like shape of fibroblasts and were randomly oriented. Despite the faster growth of fibroblasts, the confluence was not achieved after 7 days of treatment, which may be due to the low initial cell concentration ($5 \cdot 10^3$ cells/well).

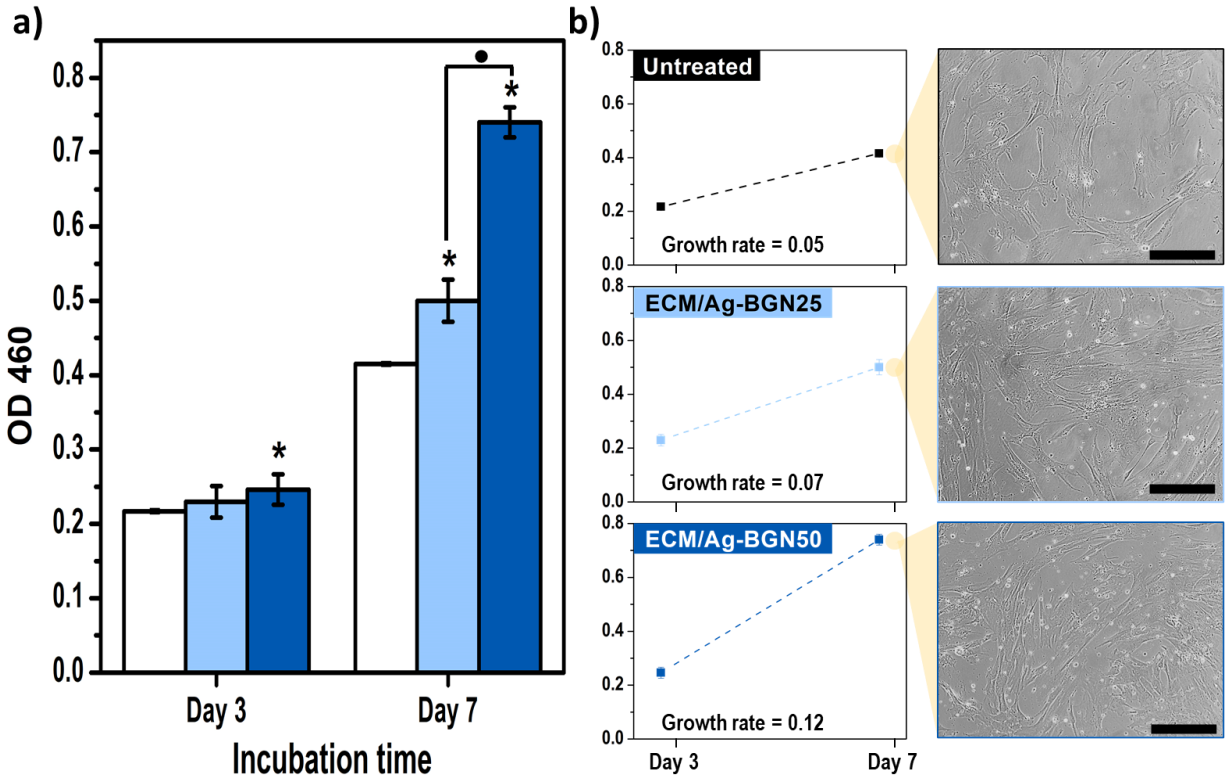

Figure 71: ECM/Ag-BGNx nanocomposites induced faster fibroblast proliferation. The metabolic activity of fibroblasts was evaluated by CCK-8, recording the optical density at 460 nm (OD_{460}) for 1 week of co-treatment (a), showing statistical difference among untreated and treated groups (*) and between ECM/Ag-BGN of different Ag-BGNs concentration (●) for $p < 0.05$. (b) The proliferation rate (OD_{460}/time) and cell confluence after 7 days of co-culture were higher in the presence of Ag-BGNs. The scale bar represents 500 µm.

5. DISCUSSION

Novel materials are needed to obtain improved clinical outcomes in orthopedics. Materials with enhanced regenerative properties and antibacterial action can become the materials of choice for bone fractures and diseases where the often underlying or secondary infection can compromise the outcome.

In this work, Ag-doped bioactive glass particles, in micro- (i.e., Ag-BG) and nano- (i.e., Ag-BGNs) sizes, have been presented a suitable material to meet the demanding needs for medical treatments. The interdependent relationship among the particle's microstructure and composition and their biological and antibacterial properties were studied following the scientific foundation of the Materials Science tetrahedron. These two components (structure and properties) can be tailored during processing to design optimum performance materials. Two different processing routes were investigated to obtain particles of different sizes and, therefore, custom the properties of the material for orthopedic applications. The first part of this section focuses on the biological and antibacterial properties of Ag-BG microparticles and concludes with the hypothesis that both properties would be enhanced by decreasing particle size to the nanoscale. Therefore, in the second part, different synthesis protocols were evaluated to address the challenges in metallic ion incorporation in BGNs before developing Ag-BGNs. The bioactive and antibacterial properties of Ag-BGNs were then assessed in similar set-ups as those in Ag-BG microparticles to establish a comparison of the benefits and drawbacks of nanoscale treatment. Finally, the delivery method of Ag-BGNs employing injectable nanocomposites is discussed.

5.1. Degradation and biological performance of Ag-BG microparticles *in vitro*

The ideal material for tissue engineering should possess biocompatibility and degrade safely to trigger a positive chain of reactions in the human body. As previously presented, Ag-BG microparticles have a homogeneous structure consisting of Si, Ca, P, Al, Ag, Na, and K atoms forming a semi-crystalline network. The surface of Ag-BG presents a negative zeta-potential (~ -17 mV), which is necessary for bioactive behavior as it favors apatite deposition [14].

5.1.1. Degradation of Ag-BG microparticles: bioactive response

Ag-BG degrades when immersed in a buffer, releasing alkaline species from its structure. The study of the ion release revealed a steady degradation of the glass network. After 4 days (Figure 13), the pH values present neutral levels, and longer immersion time for up to a month did not show further fluctuations [14].

Ag-BG is a silicate-based material with a Ca/P ratio close to 4, and is expected to induce apatite formation when immersed in SBF. The roughness and negative charge at the surface favor the protonation of the Si-O groups at the microparticles' outermost layer, creating focal points for the heterogeneous nucleation and crystallization of mineral phases [280]. The presence of an early Ca-P phase was confirmed after 3 days of immersion (**Figure 21** a). More prolonged soaking in SBF allowed the crystallization of stoichiometric apatite forming flakes (**Figure 21** c).

5.2. Interaction of Ag-BG microparticles with fibroblasts: effect on cell proliferation and differentiation

The biological properties of Ag-BG microparticles have been previously studied in the context of dental applications, showing promising results [14,281]. Here, those properties were investigated in context for the bone application. Like the effect on dental pulp cells, Ag-BG was not cytotoxic to pre-osteoblast hBMSCs at any concentration (**Figure 22** a). Although the OD dropped after 2 days of culture, it did not reduce the relative cell viability below 70 % of the untreated control, and therefore can be considered biocompatible in agreement with ISO 10993. The material's degradation caused the release of Si, Ca, P, Na, and K ions from the bioactive glass network [14]. The release rate of Si and Ca significantly increased with the immersion time. The concentration of ions in solution is expected to reach 15-25 and 30-40 ppm, for Si and Ca, respectively, between 6 and 10 days of co-culture (**Figure 6**). The delivery of P is relatively stable (~ 0.8-1.1 ppm) during the *in vitro* experiment (**Figure 6**). The concentration of Si, Ca, and P species enhanced the rate of cell proliferation compared to untreated cells (**Figure 22** b). The release of Ag^+ ions occurred at 0.44 ppm/h (**Figure 6**). The concentration of Ag^+ in solution remained stable at 0.7 ppm, and therefore, was well below the 1.66 ppm cytotoxic concentration for human cells [157,282,283].

Ag-BG microparticles also promoted osteogenic gene expression in hBMSCs (**Figure 23**). As previously mentioned, bone sialoprotein (*BSP*) and osteocalcin are non-collagenous proteins related to the extracellular matrix's development and maturation during cell differentiation [239,240]. Both BSP and OCN expression serves as an indicator of terminal osteoblastic differentiation, as they do not upregulate in immature osteoblasts [284,285]. The relative expression of these genes significantly increased upon Ag-BG exposure. In contrast, *RunX2* acts as a regulator in the cell proliferation cycle, and its level decreases as the division of cells progress

[241]. On this basis, *RunX2* is upregulated in the early stages of the cell differentiation, while *BSP* and *OCN* indicate mid- and late-stage mineralization. Compared to *BSP* and *OCN*, the lower expression of *RunX2* demonstrates the extracellular matrix was mineralizing significantly fast after Ag-BG treatment.

The presence of Ag-BG triggered an enhanced formation of the mineral phase within 10 days, as identified by ARS (**Figure 24**). Cell mineralization occurred in the osteogenic medium (Figure 17 b) and the growth medium (**Figure 24** a) without osteogenic supplements. This effect may be due to the super-saturation of the solution that triggers cell secretion and mineral formation [286]. The supersaturation will occur faster in the osteogenic medium since it is enriched, explaining the higher concentration of minerals. The key finding here is that soluble Si and Ca ions were sufficient to promote cell mineralization without supplements, proving the Ag-BG microparticles' osteogenic properties. Both Si and Ca synergize, affecting the metabolism of osteoblastic cells and are involved in the upregulation of *OCN* [287,288]. In particular, intracellular Ca ions may trigger various mitogen-activated protein kinases [289]. The upregulation of *OCN* and the high mineral secretion evidenced the effect of these two ions when increasing Ag-BG microparticles concentrations, thereby delivering higher Si and Ca content. Despite the non-specificity of ARS, false staining due to Ca inside the Ag-BG did not occur since acellular wells lacked a stained monolayer after exposure to the ARS solution (**Figure 24** b).

The medium's saturation is also expected to trigger a surface reaction and the consequent deposition of Ca-rich phases in Ag-BG microparticles, similarly to SBF's soaking (**Figure 21**). The mineral deposition in Ag-BG's surface after the cell differentiation assay was confirmed in **Figure 25** a-d. Previous reports have shown that the high concentration of HCO_3^- in DMEM favors the formation of calcite minerals instead of apatite-like phases in BGs [290,291]. However, the

results presented in **Figure 25** for Ag-BG microparticles proved otherwise. FT-IR showed an increase in intensity for P-O vibration (**Figure 25** e). The formation of an apatite-like phase is the only explanation for this vibration since calcite lacks phosphorous in its composition.

Additionally, the XRD peaks (**Figure 25** f) matched those of hydroxyapatite in the ICCD. The previous presence of hydroxyapatite in the semi-crystalline structure of as-synthesized Ag-BG is the most likely cause for the discrepancies with the literature. The growth of a pre-existing crystalline phase in the glass structure is more energetically favorable than the formation of a new phase (i.e., calcite). Moreover, the preferable formation of hydroxyapatite is also supported by its lower enthalpy of formation (~ 13,314 kJ/mol [292]) compared to calcite's (~ 1207 kJ/mol [293]).

5.3. Interaction Ag-BG microparticles and tissue *in vivo*: bone regeneration.

Despite the promising properties of Ag-containing bioactive glasses in different bone-derived cells *in vitro*, their behavior *in vivo* was studied for the first time in this project. The regenerative capability of Ag-BG reported in pulp dentin [14] was also observed in bone (**Figure 26**). Specifically, Ag-BG had a remarkable effect on increasing bone regeneration in the calvaria defects owed to the physicochemical properties derived from their structure. The Si and Ca ions released from Ag-BG have the most significant role in intracellular and extracellular pathways for osteogenesis, as observed in the *in vitro* cell differentiation [287,294]. Sol-gel glasses, like these Ag-BG microparticles, are synthesized by the densification of smaller particles during the gelation process. During the degradation of Ag-BG, nano-size debris may be leached from the surface and gobbled by cells. The intracellular dissolution of the nano-size debris could result in a localized increase of Si and Ca ion content, inducing specific signaling for cell proliferation and differentiation. This effect has previously been observed after exposing mammalian cells to BGNs.

5.4. Interaction of Ag-BG microparticles with microbes: antibacterial properties

Inorganic antimicrobial agents have attracted interest for control of microbial populations since their safety and stability are usually higher than organic antimicrobials. Additionally, some inorganic materials present the advantage of additional therapeutic properties [7,295–297]. This is the case of bioactive glasses, which, as previously shown, can play a role in tissue regeneration. Despite the number of studies proving the remarkable antimicrobial potential of bioactive glasses against a wide variety of strains and conditions [298,299], the mechanisms of inhibition have yet to be understood. In this section, the interaction of Ag-BG microparticles with pathogens was assessed to elucidate the role of structure, composition, and degradation profile of Ag-BG in the inhibition mechanism. The spectrum of action of Ag-BG was evaluated in combination with different antibiotics to expand the knowledge on how inorganic materials can be used to restore the action of drugs against resistant-strains.

5.4.1. Performance of Ag-BG against pathogenic bacteria

The antibacterial capability of an Ag-doped BG (Ag-BG) and its Ag-free counterpart (BG) were evaluated in parallel, as both materials present a similar structure and degradation profile and only differ in terms of composition since BG is devoid of Ag^+ ions.

Ag-BG and BG presented strong inhibitory capabilities against MRSA in growth-arrested conditions, with similar MIC (~2.5 mg/mL) after 24 h of treatment (**Figure 27** a-b). Ag-BG demonstrated a notably stronger antibacterial effect than BG alone. In contrast, inhibition of metabolically active MRSA (i.e., TSB) required higher treatment concentrations for both Ag-BG and BG (**Figure 27** c-d). Bacterial viability decreased upon exposure to 10 mg/mL of Ag-BG. However, the number of CFUs was higher (~ 10^9 CFU/mL) than at the beginning of the experiment

(~ 10^8 CFU/mL). This result indicates that at 10 mg/mL, there is not sufficient antibacterial action to suppress bacteria growth, which was achieved for concentrations higher than 20 mg/mL. In the case of BG, no antibacterial action was observed for concentrations lower than 100 mg/mL, similar to the effect observed in other non-doped bioactive glasses [300,301]. The ability of both materials to inhibit a biofilm (**Figure 30**) formation shows a similar trend to that observed in growth-arrested MRSA. Specifically, Ag-BG sterilized the plate at a concentration of 5 mg/mL and above, while BG only compromised the biofilm's viability to some extent without eliminating bacteria. Both Ag-BG and BG present more antibacterial potential against dormant bacteria, which functionalities are reduced to survive [302]. Specifically, bacteria stop proliferating by limiting new cell-wall synthesis [303], where cells are the most sensitive to treatments. Dormant bacteria are typically less permeability to antimicrobials, hindering their effect [304]. Once damaged, bacteria recovery leads to the reactivation of several functionalities, including cell-wall biosynthesis [305]. These observations suggest bioactive glasses play a pivotal role in bacteria envelope's integrity (i.e., affecting the cells' permeability), favoring extracellular inhibition pathways since the antibacterial effect was stronger when bacteria did not produce cell-wall at a regular rate.

5.4.2. Effect of the structure, composition, and degradation of bioactive glass particles in the inhibition of bacteria.

Antibacterial properties of BGs have been associated with increasing pH and osmotic effects as a result of network degradation. Although neither Ag-BG nor BG changed the overall pH during immersion [14], local fluctuations may occur intracellularly, affecting various cellular functions (i.e., enzyme activity for cellular metabolism). The osmotic effect is also considered a possible antibacterial pathway in Ag-BG and BG microparticles. For instance, the release of Ca^{2+} ions may unbalance the bacterial intracellular Ca^{2+} causing cell membrane depolarization and apoptotic or

necrotic bacteria cell death [306]. There has been some speculation as to the role of oxidative stress in the inhibition process based on the mechanism observed in other inorganic materials [300]. Oxidative stress is the intracellular imbalance of ROS and the enzymes involved in ROS detoxification [307]. ROS are byproducts of normal oxygen metabolism [308]. In this work, both Ag-BG and BG presented significantly different inhibition potential in aerobic and anaerobic environments (**Figure 29**), unraveling the role of oxidative stress in the antibacterial capability of the bioactive glasses for the first time. Although the identification of particular ROS is beyond the scope of this work, previous studies in ZnO, MgO, and CaO particles demonstrated the presence of superoxide (O_2), hydrogen peroxide (H_2O_2), and hydroxyl radical (OH^-) during inhibition [309,310]. Each of these oxygen radicals presents a different antibacterial potential. For example, while H_2O_2 is relatively permeable to the cell membrane, the O_2^- radical is not able to diffuse through it [311]. Instead, O_2^- tends to produce other radicals like hydroperoxyl (HO_2^-) or hydroxyls (OH^-) extracellularly, which are more potent oxidants [312]. These reactions may also be catalyzed with intracellular or extracellular metallic ions in the Fenton reactions [313]. On this basis, the ROS from the glass structure are anticipated from the action of O_2^- radicals, from the dismutation of oxides [314] forming the network (i.e., SiO_2, P_2O_5, CaO, etc.), as well as the hydroxyl groups, which are a usual constituent of bioactive glass structures. This may explain why sol-gel-derived bioactive glasses, whose surface is silanol-rich (Si-OH), presented stronger antibacterial effect than melt-derived bioactive glasses with similar compositions.

In contrast, the antibacterial properties of Ag-containing BGs have been historically attributed solely to the heavy metal ions [128,129,322,323,160,315–321]. Regardless of its status within the glass (i.e., ion form, surface functionalization, etc.), Ag acts as a broad-spectrum biocide, damaging bacteria at almost all sub-cellular levels [324,325]. Nonetheless, Ag^+ ions are known to

present more potent antibacterial behavior than metallic Ag and its oxides. For example, at an extracellular level, Ag^+ ions destabilize the cell membrane [326] and increase its permeability due to their high affinity with negatively charged groups (i.e., teichoic acids and phospholipids) [327–329]. Once inside the cytoplasm, Ag^+ ions can cause irreversible DNA condensation [330,331] and obstruct the respiratory chain [332–334]. Additionally, its inhibition mechanism has been related to oxidative stress, inducing hydroxyl and peroxide radicals [335,336]. Yamanaka *et al*. also reported Ag's bactericidal action in the denaturation of the 30S ribosomal subunit [337]. The concentration of Ag^+ ions released from Ag-BG after 24 h of immersion in an aqueous solution was previously observed to be approximately 0.4 ppm [14], which is sufficient to damage the bacterial cell envelope [157]. These mechanisms are also expected in Ag-BG because of Ag^+ ion release, explaining the 20 % inhibition difference between Ag-BG and BG microparticles (**Figure 27**). The experimental design allowed to estimate ROS contribution in the Ag^+ ions mechanism. The comparison of antibacterial action between Ag-BG and BG against anaerobic MRSA indicates that approximately 75% of the total inhibition associated with Ag^+ ions in Ag-BG comes from ROS (**Figure 29**).

In addition to the release of ions and radicals, Ag-BG and BG's antibacterial activity has also been related to physical mechanisms. For instance, microparticle degradation causes the release of nano-sized debris and ionic species in solution [237]. The presence of this nano-sized debris was confirmed in TEM images (**Figure 32** and **Figure 37**). These nano-sized debris damage the cell envelope, puncturing the membrane, inducing nano-pores through which nanoparticles can travel to accumulate within the cytoplasm, where the other mechanisms are expected to take over to advance the inhibition. Degradation of Ag-BG and BG microparticles, releasing antibacterial species (i.e., ions, radicals, nano-size debris) is dependent on their surface area [338] and the time

of immersion [237]. Specifically, Marsh *et al*. [339] demonstrated that the morphology of the nano-sized debris played a relevant role in its antibacterial effect, as scaffolds produced with the Ag-BG microparticles presented in our work showed less inhibition in 3D-structure than in pulverized form. As more degradation products are released (i.e., ions, radicals, and debris), inhibition will be higher, explaining the decrease in CFUs with increasing microparticles concentration (**Figure 27**). This effect was also observed in the time-dependent inhibition (**Figure 28** a) since fewer MRSA were observed for longer co-culture. The degradation of Ag-BG progresses with immersion time, releasing a higher concentration of antibacterial products, resulting in enhanced inhibition.

5.4.2.1. Proposed model of the mechanisms of inhibition in Ag-BG and BG

Inhibition level against growth-arrested MRSA at a concentration of 2.5 mg/mL of Ag-BG and BG (**Figure 29**) was considered to estimate the contribution of each mechanism (**Figure 72**). It must be noted that the contribution of each mechanism was drawn from a 24 h inhibition. As the degradation of Ag-BG and BG advances, the contribution of each mechanism may change.

The proposed inhibition model predicts a dominant contribution of ROS from the bioactive glass network to the inhibitory process. Specifically, ROS from the network contribute about 40 % and 83 % in Ag-BG and BG inhibitory capability, respectively. As previously mentioned, the degradation products of the bioactive glass microparticles will lead to the creation of nano-pores and an osmotic effect due to unbalanced ionic concentration, with an approximate contribution of 8% and 17 % in Ag-BG and BG, respectively. Finally, in Ag-BG, Ag^+ ions were demonstrated to play a dominant role in the level of inhibition (~ 52 %) due to a broad range of previously reported mechanisms. Here, oxidative stress was identified as the most contributing mechanism in Ag^+ ion

inhibitory action (~ 75 % of Ag contribution). Although these are all the antibacterial mechanisms identified, other less dominant processes yet to be described may also be taking place.

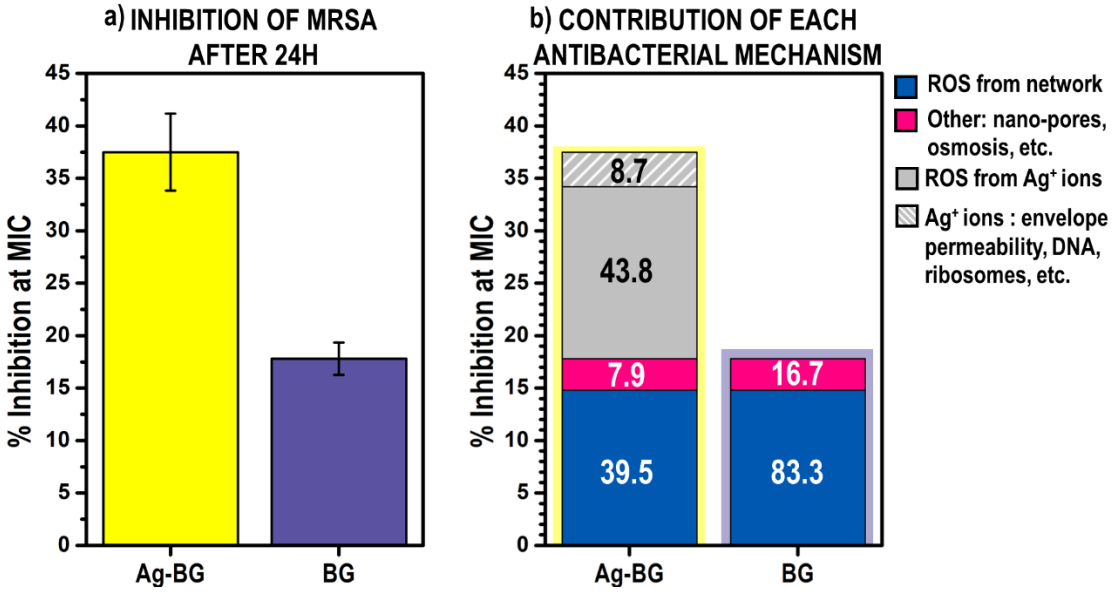

Figure 72: Predicted model of inhibition mechanisms. (a) The inhibitory capability of 2.5 mg/mL of Ag-BG and BG after 24 h (a). The inhibition difference between Ag-BG and BG is only correlated to the presence of Ag. The antibacterial mechanism can be divided into (1) creation of ROS from the bioactive glass network, (2) effect of degradation products (nano-pores, osmosis, etc.), and (3) mechanisms of Ag^+ ions from which ROS are the most dominant. The numbers inside the bars indicate the % contribution of each mechanism, considering the total inhibition as 100 % for each material.

Interestingly, while the release of ROS from bioactive glasses has been reported to be detrimental for proliferation of eukaryotic cells in some bioactive glasses [340,341], such effect was not observed in the Ag-BG microparticles used in this work. In fact, when ROS generation was balanced with ROS scavenging, cell differentiation, proliferation [343–345] and bone nodule formation [346] are promoted, which is a possible scenario in Ag-BG treatment. Ag-BG microparticles demonstrated an overall positive effect in fibroblast proliferation, differentiation, and bone re-growth [238], which in light of these occurring mechanisms, may be correlated to the absorption of Si and Ca species [287–289,294,342] and intracellular ROS production.

5.4.3. Effect of prolonged Ag-BG treatments on MRSA: development of tolerance to particle treatment

Successive treatments of MRSA with Ag-BG induced a bimodal phenotype distribution (**Figure 31** b). Two distinct clones were identified: those with the same size as WT (clone type I) and the small-colony variants (clone type II). The phenotype of the colony correlated with their sensitivity to treatment (**Figure 31** c). Clone type I behaved similar to WT, while clone type II was increasingly sensitive to the treatment. The development of small colony variants has been observed in other works as a response mechanism for staphylococcal survival amidst a hostile environment [347], although in the present work, they have a somewhat counter-productive effect. The macroscopic phenotype was correlated to modification at a structural level (**Figure 31**). For example, clone type II grew in multi-cellular clusters due to a low on-going cell division and a severely impaired daughter cell separation [347]. Asymmetrical location of the septa is probably responsible for the incomplete cell-division [348,349]. Interruption of the cell cycle was also related to structural features, like when the cell membrane blends with the wall, becoming undistinguishable [350]. This was also observed in clone type II. Campbell *et al*. [351] attributed these features to increased osmotic stress, which caused a parallel up-regulation of cell-wall stress, wall teichoic acids, and protein stabilization genes and proteins. Clone type II cell-wall was generally thicker and more diffused in the TEM images than the well-defined envelope observed in WT and clone type I. Thickening of the cell-wall may be associated with decreased intracellular ATP and membrane potential [350]. The diffuse appearance of the cell-wall is related to enhanced adherence for colonization [347], which may also be demonstrated by the development of appendices [352], such as the ones observed in clone type II. The development of adhesive proteins has been reported in *E. coli* as a phenotypic change to reduce the colloidal stability of Ag

nanoparticles and hinder their antibacterial advances [353]. On this basis, MRSA may develop the adhesive appendices to hold the nano-size debris from Ag-BG degradation and prevent the boring of nano-pores. Nonetheless, the accumulation of nanoparticles was still observed in G3-clone type II after Ag-BG treatment (**Figure 33**). It must be noted that despite the contribution of other mechanisms, the main antibacterial effect was obtained from the release of Ag^+ ions. Although Ag resistance has been reported for some organisms, they are rare and difficult to transfer and maintain [354]. Here, successive Ag-BG treatments did not decrease in inhibitory effect, and therefore, the development of resistance is not anticipated. Furthermore, the resulting clones after Ag-BG treatment were re-sensitized to cell-wall targeting antibiotics (**Figure 34**), supporting the hypothesis that Ag-BG increases envelope permeability. Although the antibacterial properties of Ag-BG were thoroughly evaluated in this work, its therapeutic window should be further assessed considering other environmental factors. Previous research has shown that absorption of protein and amino-acids may lead to the formation of Ag^+ complexes [355] or the obstruction of ion release from the bioactive glass structure, reducing its antibacterial effect [356,357]. Although, the planktonic and biofilm *in vitro* models may mimic these reactions at some extent, an *in vivo* infection model would be the closest approach to reproduce the interaction among Ag-BG, bacteria and tissue [323]. Therefore, the study of the antibacterial properties of Ag-BG *in vivo* is highly encouraged as a future line of work.

5.4.4. Restoration of antibiotics that MRSA resists by combination with bioactive microparticles

The ability of Ag-BG to potentiate the action of antibiotics was explored for antibiotics with different targets to understand the driving force in the interaction among Ag-BG, antibiotic, and bacteria. Antibiotics with three main targets were explored: cell-wall inhibitors, protein synthesis inhibitors, and DNA disruptors. The combinations were assessed with sub-inhibitory concentrations to evaluate the capability of Ag-BG to restore or expand the antibacterial capability of the drugs. The potent inhibition by the Ag-BG/ antibiotic combination cannot be attributed to an additive effect of the two agents since antibacterial properties were not reported for each of the antibiotics alone.

In terms of cell-wall inhibitors, MRSA is inherently resistant to oxacillin and fosfomycin. In the growth-arrested conditions, vancomycin is also inert to bacterial cells. β-Lactams such as oxacillin elicit antibacterial activity by targeting the cell envelope and inhibiting peptidoglycan synthesis by penicillin-binding protein 2 (PBP2) [245]. Resistance against β-lactams can be expected in MRSA by encoding PBP2a. In this situation, the antibiotic can only inhibit PBP2 but not PBP2a, which will take over the biosynthesis process and resists the drug [358]. The bacteria strain used in this work is resistant to fosfomycin, which was selected due to its broad-spectrum activity and the lack of toxicity [359,360]. Its mechanism of action is to inhibit the initial step of cell wall biosynthesis by inducing product dissociation of the MurA enzyme and suppressing PBP production [246,361]. Finally, glycopeptides such as vancomycin are potent inhibitors of cell wall synthesis. In this case, the target is the D-Ala-D-Ala dipeptide terminus present in the partially crosslinked cell wall and the Lipid II intermediate [362]. The antibiotic creates five hydrogen bonds with this terminus,

preventing it from attaching PBPs for transglycosylation and transpeptidation [247]. Thus, vancomycin is expected to be especially antibacterial during highly active cell-wall biosynthesis processes like in cell-division where the division septum ends up destroyed [363,364]. Under growth-arrested conditions, cell division is not expected to occur as PBS is a starvation medium. Consistent with this, vancomycin did not reduce the viability of MRSA under the high concentration tested in PBS but was highly toxic in TSB (**Figure S3**, Appendix B).

Synergy was observed upon exposure to oxacillin, fosfomycin, or vancomycin, with Ag-BG (**Figure 35** a-c). In all cases and similar to Ag-BG delivered alone, the combination of Ag-BG/cell-wall inhibitors showed time-dependent lethality. Synergy was observed after 12 h of exposure and is enhanced with the culture time. Bactericidal properties are expected for longer than 24 h since Ag-BG alone was lethal after 48 h (**Figure 28**).

The combinatorial approach was also assessed with four protein inhibitors: gentamycin, tobramycin, erythromycin, and chloramphenicol. Gentamycin and tobramycin are aminoglycoside antibiotics that interrupt protein synthesis by targeting the 30S ribosomal subunit. MRSA is not resistant to either aminoglycoside, and the collected data did not reveal any alteration on their mechanisms because of Ag-BG (**Figure 35** d-e). Like aminoglycosides, erythromycin, a macrolide, inhibits protein synthesis, although its target resides in the 50S ribosomal subunit [365]. The antibacterial action of erythromycin consists of two processes: blocking ribosome exit tunnel and tRNA translocation [365]. MRSA presents erythromycin-resistance [256] by several mechanisms, including reduced permeability, active reflux, target modification, and methylating enzymes [256,366]. The combination of Ag-BG/ery did not show any antibacterial advantage beyond the inhibition provided by Ag-BG (**Figure 35** f). Chloramphenicol is also a potent protein synthesis inhibitor whose reversible binding prevents peptide chain elongation at the 50S subunit

[367]. Although MRSA is not resistant to chloramphenicol (MIC~ 8 μg/mL [368]), it can tolerate a high antibiotic concentration under growth-arrested conditions similar to the phenomenon observed in vancomycin. This lack of activity may be due to the bacteriostatic nature of chloramphenicol [258] or the reduced ribosome activity in dormant bacteria [369,370]. While several reports have proven chloramphenicol does not interfere with the cell-wall synthesis [371,372], its presence may lead to severe accretion of cell-wall material [373] and unbalanced membrane synthesis, causing envelope thickening [374]. The combination of Ag-BG/cpl was strongly synergistic, presenting CFUs below the limit of detection of the experiment (**Figure 35** g).

Lastly, ciprofloxacin targets DNA gyrase, an essential component in DNA replication, by increasing its special requirement within the cell [259]. Although several reports described the effect of sub-inhibitory concentrations of ciprofloxacin in increased outer membrane permeabilization in Gram negatives [375,376], the precise ciprofloxacin's mode of action on bacterial membranes is still unknown [377]. For example, Verma *et al*. [378] reported that ciprofloxacin might cause alteration in the composition of macromolecules (i.e., phospholipids, sugars, proteins), compromising the integrity of the cell-wall. Resistance to ciprofloxacin is rare, with a MIC ~ 0.5 μg/mL, although under growth-arrested conditions, MRSA can tolerate higher concentrations (5 μg/mL) due to the decreased permeability. The combination of Ag-BG/cipro at sub-inhibitory concentrations demonstrated strong synergism (**Figure 35** h).

5.4.4.1. Proposed model for the resurrection of antibiotic action

The potential mechanism of action is based on the by-products created during the degradation of Ag-BG microparticles. The released ions and nano-sized pieces can damage the cell envelope opening nano-tunnels/channels for the antibiotic to penetrate and act. As the antibiotics target the cell wall, permeability increases, allowing for enhanced exposure to ions and antibiotics. A similar mechanism is expected for BG/fosfo (**Figure 40**), although significantly lower efficacy was observed due to the absence of the additional Ag^{+} ions inhibition, particularly those affecting the cell-envelope integrity.

The synergistic action of Ag-BG and BG with the cell-wall targeting antibiotics is only understood if cell-wall biosynthesis is taking place in static cell conditions. After the cell-wall gets damaged, biosynthesis will be activated for its reconstruction. As a result, these drugs will penetrate through the wall and will be able to find active targets to inhibit the synthesis process so that the cell structure is unrepairable. The process has been schematically presented in **Figure 73**. Notably, the presence of nano-sized debris in the TEM images was more evident in Ag-BG/antibiotic (**Figure 37** S-X) combinations than in Ag-BG alone (**Figure 37** M-O), suggesting the presence of antibiotic may hasten the degradation of the microparticles. The proposed mechanism is fascinating in the case of Ag-BG/oxa since the mutated PBP2a would now be also exposed to the antibiotic making the mutated enzyme less effective against the oxacillin.

Therefore, this model predicts that the first step of inhibition depends on Ag-BG degradation damaging the cell-wall. This step is supported by the finding that Ag-BG/vanc was bactericidal only for Ag-BG concentrations at or above the MIC (**Figure 38**). This initial damage is considered the driving force for the re-activation of antibiotics. In agreements with previous discussions,

combinations of higher Ag-BG concentrations, keeping the same antibiotic concentrations, elevated the bactericidal action as more by-products for the physicochemical degradation were released.

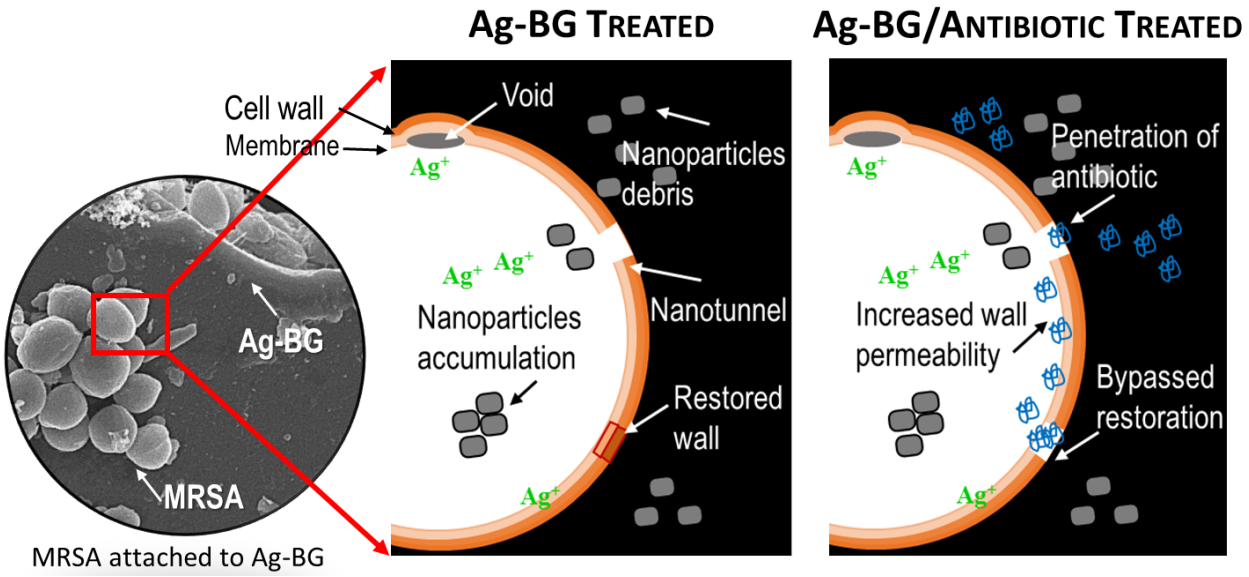

Figure 73: The proposed resurrection of antibiotics model in the combination of Ag-BG/antibiotics. The process is explained for MRSA, although it may occur similarly in other pathogens. The degradation products Ag-BG or BG compromise the integrity of the bacteria cell-envelope. The nano-sized debris released from the structure bore nano-tunnels through the cell-wall and accumulate in the cytoplasm. The release of Ag^{+}, osmotic effect, and ROS from the bulk or the debris cause additional cell disruption. The bacteria trigger the urgent re-activation of cell-wall synthesis to clog the pores and restore the wall. The addition of an antibiotic with cell-wall inhibiting or disrupting pathways will bypass the restoration.

In agreement with this mechanism are the features observed in MRSA exposed to vancomycin alone versus Ag-BG/vanc. Basri *et al*. reported that MRSA cells exposed to vancomycin harbored an irregularly thick cell wall lacking a division septum [379]. However, this is not observed in this work as vancomycin is not activated on cells suspended in PBS (**Figure 37** J, K, L). Notably, the combination of Ag-BG/vanc activates vancomycin allowing this antibiotic to cause pronounced ultrastructural changes (i.e., swelling of bacteria), leading to decreased viability (**Figure 37** V, W, X).

Other results also support this hypothesis. First, there was a lack of synergism with gentamycin, tobramycin, and erythromycin. These antibiotics have no primary nor secondary effect on the cell envelope. In contrast, chloramphenicol and ciprofloxacin, with reported side effects to cell-wall structure and synthesis process, were synergistic with Ag-BG. Second, the advanced inhibition observed in the Ag-BG/antibiotic in metabolically active MRSA (**Figure 36**), where cell-wall synthesis occurs regularly. As anticipated, the combinations did not show the same level of synergism in TSB due to bacteria's ability to clog the pores faster than in PBS. For example, Ag-BG/fosfo was stronger in PBS (~65 % inhibition) than in TSB (~35 % inhibition).

The concentration of antibiotics was critical for the synergism. For example, a concentration of 0.1 mg/mL of vancomycin in Ag-BG/vanc was insufficient to reduce bacterial viability beyond what was observed with 2.5 mg/ml of Ag-BG alone (**Figure 39** a). The synthesis of new cell-wall is probably considerably low with the treatment of 2.5 mg/mL of Ag-BG alone, and it can be concluded that the amount of damage that occurs when cells are exposed to this amount of Ag-BG is not sufficient to increase vancomycin binding to D-Ala-D-Ala dipeptide at concentrations lower than 0.3 mg/mL. This result supports the notion that low quantities of D-Ala-D-Ala dipeptide require increasing vancomycin concentration in Ag-BG/vanc to or above 0.3 mg/mL. This finding also supports the model that Ag-BG/vanc bactericidal activity is based on the activation of cell-wall synthesis that occurs in response to Ag-BG-dependent cell wall damage, a process that is further inhibited by vancomycin. This mechanism of action is also supported using a sub-lethal concentration of vancomycin (0.5 mg/mL). In this case, increasing Ag-BG concentration also elevates Ag-BG/vanc synergy (**Figure 39** c). Similar antibiotic concentration dependencies were observed in Ag-BG/cpl and Ag-BG/cipro, although they may not be directly related to cell-wall synthesis. For example, higher chloramphenicol concentrations may favor the inhibition of more

ribosomes, hindering the synthesis of proteins required to re-activate the emergency process for wall restoration. In ciprofloxacin, both the antibiotic and the Ag^+ ions may synergize intracellularly to condensate the DNA, leading to bacterial death. Therefore, increasing the ciprofloxacin concentration will lead to more intracellular uptake, which is anticipated to cause more DNA damage, although side-effects on the cell-wall are anticipated. Therefore, the capability of Ag-BG to restore antibiotics is restricted to drugs with major or minor effects on the cell-wall.

Overall, this section provides a fundamental understanding of the interaction between Ag-BG and bacteria. The results explain how the antibacterial performance may be tailored for specific needs by controlling the degradation profile and products of the microparticles. The combined delivery of Ag-BG with antibiotics enhances the antibacterial activity of Ag-BG alone, showing promising results for the treatment of infections recycling antibiotics. The performance of Ag-BG and Ag-BG/antibiotics to eradicate an *in vivo* infection is recommended for future investigation in wound healing models. Because of the ability of Ag-BG to trigger bone re-growth, as presented in previous sections, it is also hypothesized that Ag-BG is a promising treatment for regeneration infected bone defects.

5.5. Ag-BG as therapeutic carrier against antibiotic-resistant infections

Delivering therapeutic compounds to the target site is a significant problem in treating many diseases [380]. The most conventional drug applications are oral administration and injection. The effectiveness of these methods is limited due to poor biodistribution and lack of selectivity since the drug is not explicitly targeted to the area that needs treatment [381]. These limitations may be overcome using a drug delivery system [382]. The drug is directly transported to the place of action, enhancing drug concentration at the target and minimizing the undesirable effect on other tissue. Local drug release systems also offer the ability to tailor the release kinetics so the dose can be controlled over time [383–385]. Cell-specific targeting can be achieved by attaching drugs to individually designed carriers [386]. An ideal drug carrier system would be inherently non-cytotoxic and degrade or be excreted from the body after its cargo release.

In this project, drug delivery systems were explored within the scope of antibiotic-resistant infection treatments, especially those affecting bone tissue. Resistance to antibiotics usually occurs due to a decrease in cell-wall permeability, and therefore, a precise delivery mechanism must overcome the cell-wall barrier [387]. The concept of this treatment is advanced by incorporating a vehicle that is not a mere bystander but instead presents antibacterial properties of its own. Although the delivery of antibiotics in this kind of set-up has been a target of research before, it has failed to provide the much-needed recovery of the surrounding tissue [386]. Therefore, in this work, a new strategy is proposed to simultaneously eradicate an infection while promoting tissue regeneration during fracture repair. All of these demands can be met using Ag-BG microparticles as delivery vehicles. Ag-BG microparticles can penetrate bacteria by creating nano-tunnel [17], as demonstrated in previous sections. Additionally, Ag-BG's combination with antibiotics, like vancomycin, proved an advanced inhibitory capability against MRSA [17]. Ag-BG also promotes

tissue regrowth in critical bone defects [238]. Therefore, Ag-BG microparticles were proposed as carriers for vancomycin delivery to draw on the combination of osteostimulation, antibacterial properties, and drug delivery.

5.5.1. Mechanism of vancomycin incorporation and release in Ag-BG@vanc

The immobilization of vancomycin at the Ag-BG microparticles was performed following a co-precipitation method [260–262], consisting of Ag-BG immersion in a highly concentrated antibiotic solution. Ag-BG interaction with an antibiotic in a medium will lead to its incorporation by absorption, adsorption, and/or encapsulation [388].

Vancomycin was successfully immobilized in the Ag-BG microparticles with an uptake efficiency above 50 %. Chemical incorporation is proposed by combining the mechanism mentioned above and is schematically illustrated in **Figure 74**. For instance, vancomycin absorption may occur within the pores of the carrier [264,389]. In this case, Ag-BG microparticles present low porosity with seldom pores in the range of 2-20 nm size. Therefore, the absorption mechanism is unlikely to play a dominant role in antibiotic incorporation. The adsorption mechanism is governed by electrostatic interaction, and it is usually exploited to bond negatively charged surfaced with positively charged antibiotics. Ag-BG presents a surface charge of –17 mV [163] due to the presence of silanol groups, naturally occurring in sol-gel-derived glasses. The immersion in the medium will trigger the Ag-BG microparticles' bioactive response, creating additional silanols and carboxyls [390]. These negatively charged groups act as nucleation sites and are anticipated to bond with ionizable groups from the vancomycin structure (i.e., protons, carbon rings, and amine groups) [391]. The presence of both Si-OH and COOH was observed in FT-IR (**Figure 41**), confirming vancomycin's successful conjugation by adsorption. The bioactive response triggered

in Ag-BG microparticles upon immersion would increase ionic species' concentration such as Ca^{2+}, Na^{+}, and K^{+} in solution. The medium's supersaturation due to the high antibiotic concentration and the increase of alkaline species will promote an amorphous Ca-P phase, similarly to the effect observed in SBF. The deposition of this phase will promote the entrapment of vancomycin at the surface interface [262]. Previous reports have shown that free Ca^{2+} ions in solution may also bind to carboxyl groups from the antibiotic, like tetracycline [392–394]. These intermediate complexes will also deposit at the microparticle surface during extraction at the end of the uptake process. A similar effect is expected to occur with vancomycin. The role of this entrapment mechanism by Ca-P phase deposition was demonstrated in the Ag-BG@vanc by the increase of P-O vibration (**Figure 41**), and the deposits observed in SEM (**Figure 42**).

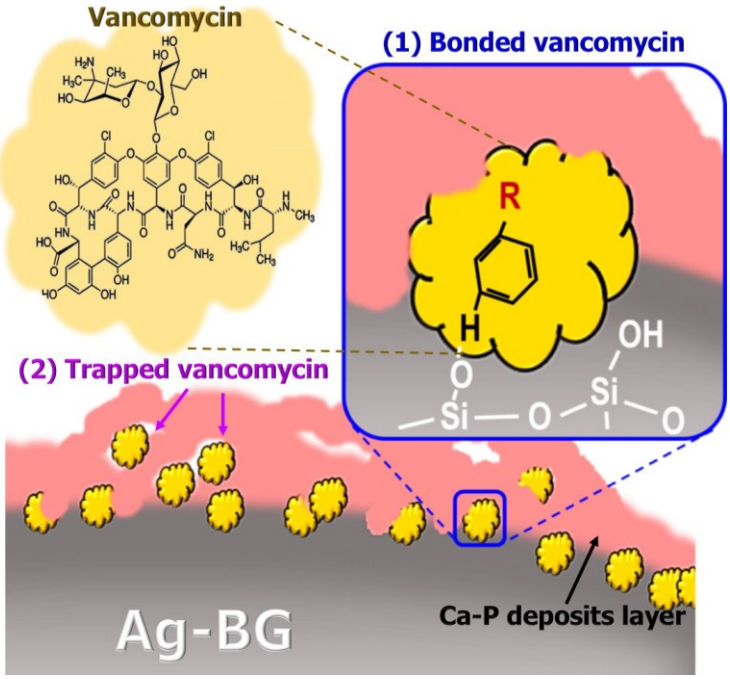

Figure 74: Schematic representation of vancomycin immobilization process. The two dominating mechanisms were adsorption and entrapment. (1) Vancomycin bonds with Ag-BG surface groups to get adsorbed. Here Si-OH is used as a representative nucleation site to bond with protons from the drug structure. Note that other functional groups play a role in the immobilization process. The molecular chain of vancomycin (yellow cloud) is displayed for reference and abbreviated as R in the mechanism. (2) Vancomycin is trapped with Ca-P deposits (illustrated as a pink matrix).

The pharmacokinetics of the conjugate will be governed by which of the loading mechanisms dominates the antibiotic uptake [388]. The release of absorbed antibiotics is probably the mechanism that offers the least control since it is not physically attached to the particle. The release of adsorbed molecules will depend on the electrostatic affinity between the nucleation site and the functional group. For example, amine groups present the highest electrostatic affinity [395] of vancomycin's functional groups and lead to a more effective bonding. Therefore, the vancomycin molecules bonded through amine groups would presumably exhibit a slower release rate. In contrast, the Ca-P phase help regulate the antibiotic release [396]. Their high solubility (2.5×10^{-3} g/L) favors the transfer of molecules from the microparticle's surface [397].

The release profile of the Ag-BG@vanc conjugate was evaluated under two different conditions to assess their behavior during application. The conjugate releases a systemic concentration of antibiotic, reaching its full release after 12 h of immersion and continued a more steady release for up to 3 days in physiological conditions (**Figure 43** a-c). In contrast, at 2 °C, the release followed a perfect Gaussian profile finishing the release of vancomycin after 4 days of immersion (**Figure 43** b-d). Total delivery capacity was not achieved since only 40 % of the vancomycin loaded was released by the end of the test. As expected, the release rate at 2 °C was slower than at 37 °C since the Ag-BG degradation is catalyzed by temperature. In general, a lower concentration of vancomycin was detected at 37 ºC compared to 2 ºC. This process may be explained due to the re-precipitation of the antibiotic *in vitro* as the solution saturates. Previous research has shown this effect in bioactive glasses loaded with a significant antibiotic concentration [263,264], and similar behavior is expected in Ag-BG@vanc. Nonetheless, the antibiotic's re-precipitation is more unlikely to occur during *in vivo* treatment, as the surrounding tissues absorb the antibiotic and ions released from the conjugate. The degradation of vancomycin after prolonged exposure to 37 °C

challenges the ability to assess the conjugate's full delivery potential. The release at 2 °C was maintained for longer times, confirming the system is still capable of delivering vancomycin for more extended periods. On this basis, it is anticipated that the Ag-BG@vanc conjugate will sustain drug release for at least a week, which is the average time for infection treatments. The main limitation of the delivery mechanism presented in this section is the partial control over the conjugate uptake and release profile. Further optimization of the carrier fabrication process is proposed as a promising line for future work, and the alternatives will be discussed later in this document.

5.5.2. Toxicity of Ag-BG@vanc to bacteria and fibroblasts

The Ag-BG@vanc conjugate was antibacterial against MRSA and proved synergistic, in agreement with previous results (**Figure 44**). The use of Ag-BG as a delivery vehicle enabled dose reduction to provide enhanced inhibition. Specifically, a combination of 2.5 mg/mL of Ag-BG and 0.3 mg/mL was necessary to synergize previous combinatorial therapies (**Figure 39**). However, vancomycin delivery as cargo instead of in solution provided significant inhibition for a combination of 0.5 mg/mL of Ag-BG and 0.25 mg/mL of vancomycin (concentration released after 24 h at 37 °C). As previously presented, the Ag-BG mechanism of inhibition consists of several processes: the release of trace elements (i.e., Ag^+), osmotic effect, presence of ROS, and degradation in nano-size debris [17]. Although Ag^+ ions play a pivotal role in the inhibition mechanism of Ag-BG, it is not the only factor contributing to synergism. In fact, previous results demonstrated that Ag-free BG, with an equivalent composition to Ag-BG devoid of Ag, could synergize with antibiotics, too [237]. Therefore, the inhibitory action of Ag-BG@vanc is anticipated from the collaborative action of Ag^+, osmotic effect, nano-sized debris, and drug. On this basis, Ag-BG@vanc will be more toxic after 48 h than at 24 h, following a similar trend to

Ag-BG alone (**Figure 28**) [17], as the degradation of the structure continues and disable the infection throughout treatment. The synergistic mechanism of Ag-BG with vancomycin against growth-arrested MRSA may also be extrapolated to possible scenarios against VRSA since vancomycin was ineffective in this experimental set-up. The mechanism of resistance to vancomycin is related to a thickening of the cell-wall and, therefore, reduced permeability towards antibiotic penetration [398–400]. The peptidoglycans would trap vancomycin molecules before they can reach the D-Ala-D-Ala dipeptide terminus in the Lipid II intermediate inside the cytoplasm [401,402]. The Ag-BG@vanc conjugate is anticipated to overcome the wall, following the mechanisms described previously, and aid the penetration of vancomycin to find its target causing significant damage to VRSA. The inhibition rate and antibacterial power can be controlled by the concentration of Ag-BG@vanc conjugate delivered and the exposure time. In this case, the released vancomycin concentration (0.3 mg/mL after 24 h) was above its MIC (~0.47 μg/mL) [363,403] by several folds, which ensure bacteria inhibition.

The bacteria-material interaction study did not demonstrate any significant morphological change in bacteria between the Ag-BG and Ag-BG@vanc treatments. However, based on the previous analysis (**Figure 37**), the bacteria structure is expected to undergo critical changes upon exposure to vancomycin. The combination of Ag-BG/vanc revealed swollen bacteria with evident marks of nano-size debris penetration. Similar features would be expected in Ag-BG@vanc conjugate treated MRSA. Their validation must be done with advanced microscopy techniques, like TEM, since SEM sample preparation cannot preserve the structure of damaged bacteria, and it is proposed as a future line of investigation. Interestingly, while the morphological assessment did not reveal much information about the bacteria structure, it provided insights on Ag-BG and its interaction with bacteria. Previous results showed the Ag-BG's surface developed Ca-P deposits

and salts after immersion in just PBS (**Figure 42** b); however, those deposits vanished in the presence of MRSA (**Figure 44** b I-II). Such observation suggests the medium supersaturation was not taking place upon immersion of Ag-BG in PBS as the bacteria nurture from the ions released, confirming the uptake of ionic species by biological entities. In contrast, the deposits observed in Ag-BG@vanc before exposure to bacteria remained at the surface, although some of them appeared detached. After treatment, the elemental analysis confirmed the nature of the deposits as Ca-P, and thereby, they did not change during antibiotic release (**Figure 44** c). These Ca-P deposits most likely served as a regulator for the release kinetics. The antibiotic release could also be noted in the elemental analysis since the relative contribution of chlorine to the EDS spectrum was significantly lower after exposure to MRSA (**Figure 44** c) than after fabrication (**Figure 42** c).

The promising biological properties of Ag-BG *in vitro* were maintained in the Ag-BG@vanc conjugate. Although the presence of surface deposits was expected to significantly delay the ion release, and therefore, provide lower incidence in cell proliferation, no statistical difference was observed between the effect of Ag-BG alone and Ag-BG@vanc. In contrast, vancomycin-treated cells suffered a significant decrease in viability at the beginning of the treatment. The possible adverse effect of vancomycin was subdued in the Ag-BG@vanc conjugate thanks to the Ca-P mineral deposits caging the drug. Previous research has shown that Ca and P's presence holds a significant role in enhancing cell proliferation and the upregulation of osteoblastic genes for osteogenesis [163,238]. Ag-BG@vanc-treated cells were directly exposed to these ions, as they were already present at the conjugate surface. In contrast, the concentration of Ca and P was lower in Ag-BG-treated cells, as they release slowly upon degradation of the microparticles.

This section reinforces the concept of Ag-BG´s degradation as a critical parameter to deliver a double set of properties. The antibacterial and bioactive properties of the Ag-BG@vanc conjugate

observed here would be further potentiated *in vivo* since the presence of eukaryotic cells, like osteoblasts, can accelerate and remodel the degradation of BGs [404–406]. The Ag-BG@vanc conjugate is a feasible approach to develop multipurpose bone fillers for diseases like osteomyelitis and osteoporosis. For example, Mistry *et al*. [407] have recently shown the ability of an antibiotic-loaded bioactive glass-based cement to eradicate bone sepsis and osteogenesis. The use of Ag-BG as a carrier would advance the recovery by providing antibacterial pathways to bolster antibiotic action beyond the role of a mere drug vehicle. The antibiotic immobilization process presented here provides enough adaptability to load other antibiotics for specialized targeting introducing minimal modifications. Therefore, the use of Ag-BG as a multi-functional carrier for vancomycin holds excellent potential for clinical treatments in scenarios where bone tissue must be cleared of persistent infection before regeneration.

5.6. From Ag-BG microparticles to Ag-BG nanoparticles

The degradation study of Ag-BG microparticles and their performance suggested a significant contribution of nano-size debris in the properties observed. To draw on this mechanism, the Ag-BG formulation was translated into a nano-scaled system. The primary hypothesis of this work was that the accelerated degradation behavior of nanoparticles, due to their high surface area, would make them the strongest weapon against pathogens and provoke faster cellular behaviors thanks to material internalization. On this basis, this section of the dissertation focuses on the development and characterization of novel Ag-BGNs. As previously stated, cation incorporation is a significant challenge in this field. Therefore, the first step consisted of modifying the Stöber method to design and optimize a protocol to incorporate P and Ca. Understanding the cation incorporation process enabled the controlled synthesis of Ag-BGNs with sizes similar to the nano-size debris observed from the degradation of Ag-BG microparticles.

5.6.1. Synthesis of ternary system BGN

Silicate-based BGNs can be considered silica nanoparticles in which various network modifier ions are introduced within the structure. As such, the Stöber-method[408] can be adapted for their fabrication. In this section of the project, ternary system BGNs with a composition of 62 SiO_2 – 3.2 P_2O_5 - 34.4 CaO (mol.%) were synthesized utilizing polymer-free, one-step basic catalysis approaches inspired by the Stöber method. The processing protocols were designed to understand which steps governed cation incorporation and particle size to tailor BGNs performance.

5.6.1.1. Mechanism of incorporation of P and Ca in BGNs.

As previously mentioned, the main unresolved issue in Stöber-like approaches is the persisting discrepancy between the nominal composition and the actual one obtained after the fabrication [56,72,73]. Specifically, the incorporation of P and Ca^{2+}, vital elements for bone bonding [74], ions remains a significant challenge. Congruent with this observation, the M1-P1 BGNs obtained from a reference protocol [74] presented a significantly low amount of P_2O_5 and CaO.

On the one hand, the incorporation of P ions depends on TEP's hydrolysis (i.e., P ions precursor), performed in a solution containing TEOS as the reagent for SiO_2. In solution, there is an unbalanced hydrolysis rate between TEOS and TEP. Specifically, TEP's hydrolysis under elevated pH, such as the one used in the Stöber method, is significantly slower than TEOS. In other words, SiO_2 nanoparticles start to condensate while there are still very few free P ions in the solution [30]. Because of this unbalanced reaction, most of the TEP reagent is wasted during the synthesis, producing final BGNs with a low amount of P_2O_5. To address this challenge, de Oliveira *et al*. [409] applied methanol as the solvent since the shorter carbon chain favors faster hydrolysis of TEP, comparable to TEOS. The amount of P_2O_5 was significantly higher, but it did not meet the

nominal composition [409]. On this basis, the M1-P2 protocol was designed using methanol as the solvent in Solution A and submitting the solution to extended homogenization before nanoparticle nucleation. Although EDS confirmed the incorporation of P within the desired range in the BGN structure, it may only serve to assess the effectiveness of the applied protocol toward the incorporation. The errors associated with this technique make it unsuitable for determining the exact composition for such low amounts. Therefore, other techniques like ion coupled plasma (ICP) or atomic probe tomography (APT) are recommended for future investigation to measure the composition accurately. One of the key findings in the M1-P2 protocol was the consistency in particle size and dispersity observed with M1-P1. This observation indicates that by introducing methanol, the chemical modification was insufficient to decrease the surface charge below the isoelectric point of the structure, which is the main reason for BGNs' monodispersity [68]. The slightly smaller particle size in M1-P2 BGNs is associated with faster hydrolysis in methanol [408,410–412]. Based on these results, the M1-P2 protocol can serve as an approach to fabricate BGNs consisting primarily of SiO_2-P_2O_5. Additionally, like other Stöber-like protocols [72,88], M1-P2 offers control of particle size and dispersity by tailoring both the reagent concentration in Solution B and the stirring time X_3.

On the other hand, the compositional gap observed in CaO is associated with its reported mechanism of incorporation. Calcination above 400 ºC is necessary to activate the diffusion of Ca^{2+} ions into the SiO_2 network and, consequently, cause its modification [413]. Keeping on this fact, most protocols, including the M1 approach followed in this project, perform the incorporation of CaO by immersing previously formed SiO_2 nanoparticles in a CaNT bath. In this process, the incorporation of Ca^{2+} ions relies on their electrostatic attraction with hydroxyl species (OH^-) at the nanoparticle surface. Then, the BGNs are washed and calcinated to trigger Ca^{2+} ions diffusion.

The concentration of CaO is limited by the number of hydroxyl groups available to bond. The electrostatic attraction between these two species is reasonably weak, and most of the bonds will not survive the washing steps [76], yielding to BGNs with less than 10 mol.% of CaO. Attending to this mechanism, the change in the hydrolysis pace induced with methanol in M1-P2 has little effect on incorporating Ca^{2+} ions, explaining the similarities between M1-P1 and M1-P2 in terms of CaO content. In this project, the incorporation of calcium was achieved by introducing a significant change in the synthesis process. Specifically, in the M2 approach, CaNT was added into Solution A and stirred for a long enough time to allow cation interaction with SiO_2 tetrahedra. Catalysis of the solution after 24 h caused nanoparticle formation and allowed trapping of Ca^{2+} ions within the structure. Although this approach was found on another protocol [74], the status of Ca^{2+} as modifier ion or trapped ion on their BGNs was not assessed in their results. Additionally, the calcium detected from EDS mapping could come from calcium carbonate molecules or calcium-rich components without being adequately incorporated in the network [72,90]. Here, the ion-trapping mechanism is supported by the chemical and structural analysis of M2 BGNs before and after heat treatment, performing washes in the latter to dilute and eliminate other calcium-containing compounds. Before calcination at 400 ºC, BGNs presented ~35 mol.% of CaO in SEM-EDS but lacked the characteristic Si-O-NBO vibration in FT-IR (**Figure 51**), demonstrating Ca^{2+} was within the BGNs but not modifying the SiO_2 network. During calcination, the diffusion of these trapped ions was activated to form Si-O-Ca NBOs. The network modification was evidenced by the newly developed FT-IR vibration at 900 cm^{-1} and increased Q^3 and Q^2 units in the NMR spectrum. The mechanism of P and Ca^{2+} ion incorporation is schematically presented in **Figure 75**.

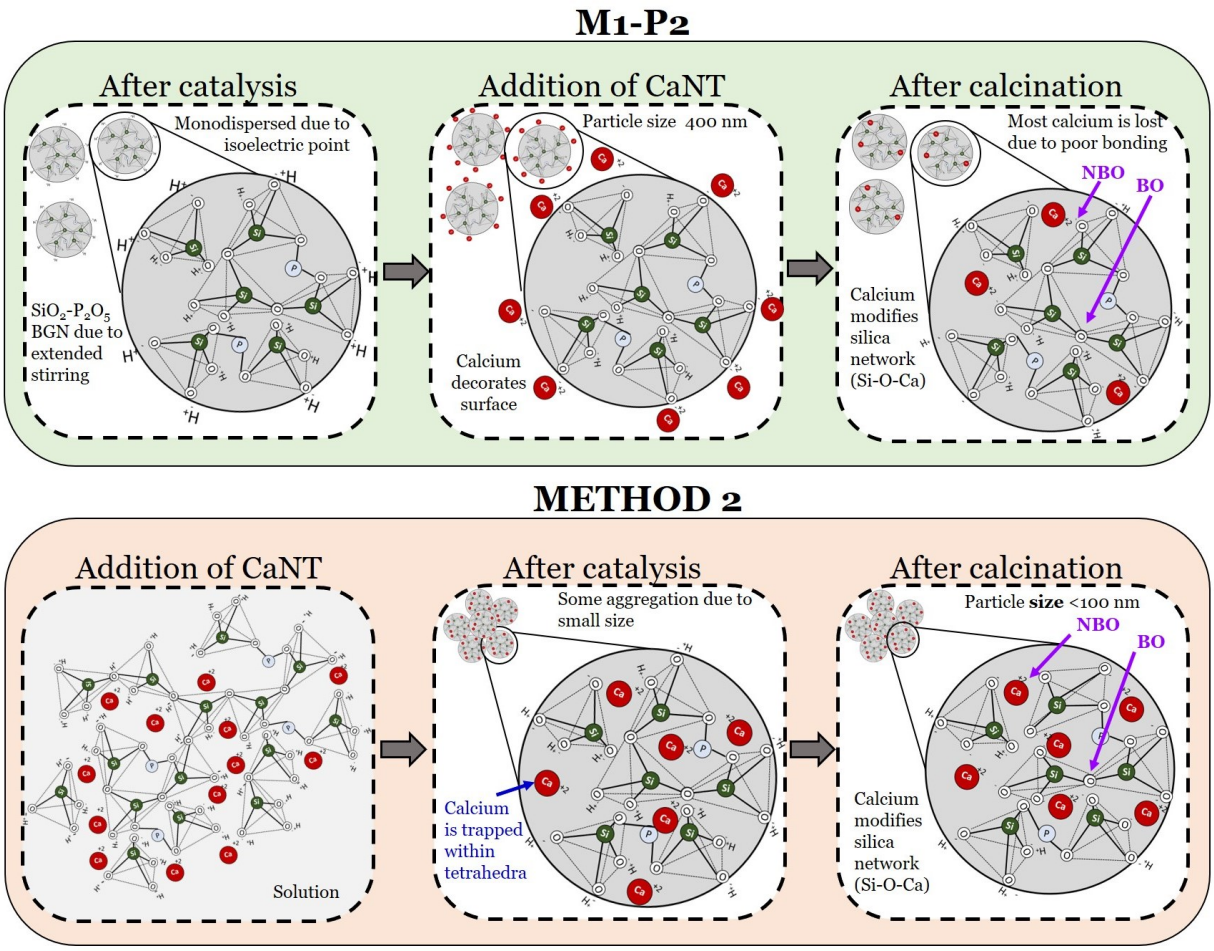

Figure 75: Proposed mechanisms for P (light blue circle) and Ca^{2+} (red circle) ions position within BGNs when M1-P2 and M2 protocols are applied. Tetrahedra are formed by Si (green circle) and O (white circle) ions in both protocols. In protocol M1- P2, pure silica nanoparticles are formed, and Ca^{2+} ions remain on their surface prior to calcination, while in protocol M2, Ca ions are already present within the nanoparticles. Calcination in both protocols allows Ca^{2+} ion incorporation into the glass structure, bridging oxygens (BO) and non-bridging oxygens (NBO) marked in purple [266].

Although the calcination step has little effect on the incorporation of CaO, it controls the status of Ca^{2+} within BGNs and, therefore, nanoparticles' behavior. For example, trapped Ca^{2+} (i.e., before calcination) will leach at an uncontrollable rate which could be harmful to cells. In contrast, the presence of Si−O−Ca NBO bonds (i.e., after calcination) not only allows the controlled release of Ca^{2+} but also accelerates the degradation of a silicate network since it is less interconnected. Hence, while the concentration of CaO was achieved at both stages, heat treatment is critical to control

the system's properties. Modified silica networks are usually preferred since they would deliver both the Si and Ca necessary to trigger the positive effects on cells reported in previous sections.

5.6.1.2. Role of stirring time in the synthesis of BGNs

This study also revealed a significant effect of stirring time prior to catalysis and condensation in both the composition and size of BGNs. As previously mentioned, increasing the stirring time before catalysis allowed P and Ca^{2+} ions to position around SiO_2 tetrahedra. The time allowed for solution homogenization was at least 24 h in between reagent addition. This extended stirring was vital to achieving complete hydrolysis of the TEP molecules since stirring time X_1 below 24 h yielded BGNS with a significantly lower amount of P_2O_5. Although the results indicate 24 h was the minimum time to hydrolyze all the TEP (**Figure S1** in Appendix A), further experiments would determine the minimum time to maintain optimal Ca^{2+} ion incorporation. In this regard, the significance of stirring time has been noticed in other works, although never highlighted before. Lukowiak *et al*. achieved 28 wt.% CaO in europium-doped BGN in a two-step catalysis method by homogenizing the solution for 20 h [56], whereas only 12 wt.% was obtained after 8 h [414].

Stirring solutions for a total of 72 h before catalysis (as in M2-P2 B and C) yielded a significant reduction in particle size (~20 nm) following their aggregation due to instability, in agreement with other reports [68,415]. It is worth noticing that BGNs were not densified together as DLS (**Table 12**) capture the size of individual nanoparticles. Therefore, alternative post-nucleation surface treatments can be explored to improve their dispersity. The prolonged stirring not only allowed ion incorporation but also affected the network connectivity. For an extended period, the hydrolysis in methanol made Si−O−Si bonds more susceptible to chain breakdown during catalysis since it promotes hydrolysis reactions over condensation [408,410]. Although methanol is known

to yield irregular shape particles, the combination with high temperatures (i.e., calcination) leads to more uniform nanoparticles [54,89,416,417]. Furthermore, the additional stirring time allowed the maximum harnessing of TEOS, TEP, and CaNT precursors, as proved by the higher mass of material collected after calcination.

Interestingly, the early addition of CaNT in the M2 protocols neutralized the overall effect of the stirring time after catalysis. Several works have reported an increase in particle size with longer stirring after particle nucleation as more dissolved monomers bond to the nuclei [30,62]. In this study, M2 - derived - BGNs were collected after different stirring times X_3 (after catalysis) from 5 min to 6 h, and all presented similar sizes and composition (**Figure S2** in Appendix A). Moreover, the concentration of water and ammonium in the catalytic solution held little effect on particle size control, which was instead governed by the stirring time before catalysis. Although further investigations would be required to determine this effect's background, it is hypothetically correlated to changes in the isoelectric point during particle nucleation due to an increase in alkaline species.

5.6.1.3. Degradation of ternary BGNs and their interaction with bacteria.

The biological behavior was evaluated in terms of pH evolution and apatite deposition. The pH suffered a sudden increase due to a burst release of alkaline species in the medium and remained toxic (pH > 8) for up to 3 days. This phenomenon was counteracted by pre-conditioning the BGNs for 4 days in DMEM before use.

The ability to develop the biological apatite is attributed to the accumulation of dissolution products [33]. The bioactivity process has been presented in detail in section 2.3.1. Briefly, P and Ca^{2+} ions are initially exchanged in solution, leaving an increased concentration of silanol bonds

(Si−OH) at the surface of nanoparticles. These silanols repolymerize, creating a silica-rich layer. Further ion migration of P and Ca species occurs from the core of the particle toward the surface and reacts to create an amorphous calcium phosphate layer. The supersaturated solution causes the deposition of hydroxyl and carbonate groups as well as more P and Ca^{2+} ions and later the crystallization of the calcium-phosphate phase to HCA [33,418,419]. The rate of HCA layer formation is greatly influenced by the composition and, consequently, the structure of the BGNs. The substitution of Si by other ions such as P and the modification of the network by Ca^{2+} ions created a less connected network in which hydrolysis of Si−O−Si is not as necessary for dissolution silicate chains. On this basis, M2-BGNs undergo a faster bioactive response than M1-BGNs since they exhibit half network connectivity (NC) due to higher calcium incorporation. The NC was below the ideal reported by Edén [420] ($2 < NC < 2.6$) and insufficient to generate a dense apatite phase after 7 days in SBF. Despite the low calcium content in M1 BGNs, a calcium phosphate deposition was observed. This result agrees with previous reports that proved bioactive behavior of sol−gel glasses with up to 90 mol % SiO_2 [57]. The bioactive response is also affected by the particle size [421,422]. A smaller particle size induces a higher ion dissolution rate due to the higher surface-to-volume ratio. Thus, ion release in M2 BGNs (particle size, <100 nm) is intrinsically higher than that in M1 protocols (~400 nm).

The effect of particle size was also observed in the antibacterial behavior. Treating MRSA with 58S microparticles did not decrease bacteria viability. In contrast, BGNs were antibacterial after 24 h. The antibacterial capability of M1-P1 was mild and could be explained by the local release of alkaline species at a faster rate than 58S due to the higher surface area, causing osmotic difference around the bacterial envelope [423,424]. The osmotic effect would also be expected in the inhibitory mechanism of M2-BGNs. However, in this case, the antibacterial behavior benefits

from the decrease in particle size, which creates mechanical damage to the cell-wall, following a similar process as Ag-BG microparticles. Although further studies would be required to unravel this mechanism in ternary BGNs, the presence of nanoparticles coating thoroughly the MRSA's surface may support this mechanism. Keeping on these facts, the prime hypothesis of Ag-BGNs providing advanced bioactive and antibacterial properties compared to their micrometer counterpart gains ground.

5.6.2. Development and characterization of Ag-BGNs

Biomaterials with enhanced antibacterial and regenerative properties are valuable in orthopedics, specifically in cases where underlying infections compromise patient recovery. The thorough evaluation of the antibacterial and biological behavior of Ag-BG microparticles suggested that by decreasing the particle size, these unique dual set of properties could be significantly potentiated [17,238]. This hypothesis was evaluated by synthesizing Ag-BGNs and evaluating their behavior compared to their micro-size equivalent.

5.6.2.1. Size, dispersity, and structure of Ag-BGNs

The synthesis of multi-fold metallic ion BGNs by Stöber-like methods is challenging and requires specific modification to incorporate the cations at the desired concentration. Previous work (section 4.5.1) focused on optimizing a Stöber-like method for incorporating P and Ca [266], and in this section, said protocol was further modified to incorporate additional ions in a quinary system. The Ag-BGNs were developed for a composition of SiO_2 59.6-CaO 25.5-P_2O_5 5.1-Al_2O_3 7.2 - Ag_2O 2.2 (wt.%) that is similar to that Ag-BG microparticles (SiO_2 58.6–CaO 24.9–P_2O_5 7.2–Al_2O_3 4.2–Na_2O 2.1–K_2O 3 (wt.%)) sans Na_2O and K_2O. Both Na^+ and K^+ ions act modifying the silica network to promote a faster but stilled controlled degradation. Their incorporation in Ag-

BGNs was neglected as the higher surface area due to their small size already promotes the degradation process. The M2-P1 method for ternary BGNs provided the best control over cation incorporation and particle size. Therefore, it was selected for the Ag-BGNs synthesis. The M2-P1 protocol was adapted to incorporate the additional salts before the nanoparticle nucleation by basic catalysis with water and ammonium hydroxide. The early addition of $Al(NO_3)_3$ and $AgNO_3$ is expected to cause the incorporation of their free ionic species in the nanoparticles by ion trapping following the mechanism reported for Ca^{2+} ions [266]. Although EDS proved all the ions were incorporated within the desired level, other analytical techniques are recommended for future work to assess the exact concentration of each oxide, especially those with a lower presence like P_2O_5 and Ag_2O, which reported concentration seemed slightly lower than intended. Regular shape and size Ag-BGNs of ~10 nm were produced after calcination, with high dispersity when in solution as proved in DLS and TEM. The zeta potential was around – 9 mV, which was not enough to provide colloidal stability via inter-particle electrostatic repulsion. However, as observed in TEM, the Ag-BGNs were easily dispersed in a medium. It is worth noticing the particle size reduction from M2-P1 BGNs (~90 nm) to Ag-BGNs (~10 nm), utilizing the same Solution B for catalysis. The main difference between these protocols was the total stirring time before catalysis: 48 h and 96 h, in M2-P1 and Ag-BGNs, respectively. This observation supports the dominant role of stirring time in the particle size as presented previously. Moreover, it suggests that solvents' concentration in Solution B loses its effect in particle size if the solution is thoroughly homogenized. A similar decrease in particle size to ~ 10-20 nm was observed among the M2-P2 protocols, which used a different Solution B than M2-P1, only by increasing the stirring time before catalysis, strengthening this hypothesis.

The structure of the Ag-BGNs was amorphous and consisted of SiO_4 tetrahedral units forming a 3D interconnected network with a small number of orthophosphates (**Figure 56** c). The network connectivity was reduced due to the incorporation of $[Al_2O^4]^-$ units, Ag^+, and Ca^{2+} ions that formed NBO bonds opening the network. As previously mentioned, the NBO groups facilitate the exchange of ions from the BG structure with the H^+ protons in the aqueous solution [61]. The larger the concentration of NBO bonds, the faster the dissolution rate, which yields to higher ion release and higher bioactivity [7,128]. In the Ag-BGNs, most of the NBOs would be produced by Ca^{2+} ions since it is the network modifier with a higher compositional presence, and each ion causes 2 NBO to compensate for the electric charge. Although Ag-O bonds' formation may decrease the dissolution rate [151] because of the high covalent affinity binding [126], the concentration of Ag^+ in these Ag-BGNs was not enough to form a significant number of Ag-O bonds. Moreover, all the Ag^+ ions are expected to remain ionic. The ratio Al/Ag > 1 ensures enough $[Al_2O^4]^-$ units are available to balance the electric charge of Ag^+ ions [14,319] and, therefore, trapped them as ions within the Ag-BGNs. The status of Ag^+ ions was confirmed by the lack of UV-VIS absorbance peaks in the range of 360-550 nm (**Figure 56** a), where metallic Ag, AgO, and Ag_2O present their maximum light absorption [425,426].

The degradation of Ag-BGNs was assessed in terms of the pH evolution and apatite-forming ability. For instance, the pH suddenly increased upon exposure in medium (**Figure 57**), suggesting a faster release of alkaline species due to degradation. Ag-BGNs were highly reactive, developing mild apatite-deposition after 1-3 days of immersion in SBF (**Figure 58** and **Figure 59**) compared to the 7 days required in Ag-BG microparticles to observe a similar effect (**Figure 21**). The faster bioactivity was correlated to the low network connectivity and the higher surface reactivity of

small-size particles [421,422]. The negative zeta-potential value of Ag-BGNs is also favorable for apatite deposition [427].

5.6.2.2. Interaction of Ag-BGNs and bacteria, and comparison with the antibacterial performance of Ag-BG microparticles

The antibacterial effect of the Ag-BGNs was evaluated under 2 environmental conditions: growth-arrested and growth-assisted, as both are representative of the metabolic state of bacteria that Ag-BGNs might face during clinical application. Growth-assisted conditions reproduce a more virulent environment where bacteria are prone to colonize tissue and surfaces to create an infection, while growth-arrested conditions represent a mature biofilm.

Ag-BGNs presented strong antibacterial properties against MRSA under both conditions. The antibacterial effect may not be attributed to the pH since the Ag-BGNs were pre-conditioned before the assay to omit the initial burst ion release. Like Ag-BG microparticles, the antibacterial mechanism of Ag-BGNs is mainly correlated to the release of trace elements like Ag^+ ions and the mechanical damage of the bacteria cell-wall. As previously presented, Ag^+ ions are more antibacterial than Ag compounds and can affect almost all the microorganism's sub-cellular levels [324,325]. The MIC significantly decreased moving from micro-scale (**Figure 27** a and c) to nano-scale (**Figure 60**). For example, the MIC of the Ag-BGNs was 98% lower than Ag-BG microparticles' MIC under growth-arrested conditions (i.e., 0.05 mg/mL of Ag-BGNs vs. 2.5 mg/mL of Ag-BG). This effect was also observed under growth-assisted conditions, where the MIC was reduced 75 % (i.e., 5-10 mg/mL of Ag-BGNs vs. 20-30 mg/mL of Ag-BG). The potent inhibitory capability of Ag-BGNs may be associated with faster mechanical damage of MRSA and a faster release of trace elements than in the Ag-BG microparticles. It is worth noticing that under

growth-assisted conditions, although the CFUs were lower in Ag-BGN-treated than untreated, the groups treated with a low concentration of Ag-BGNs (i.e., 5 mg/mL) presented more bacteria than at the beginning of the experiment. This suggests that either the inhibition rate was slower than the proliferation rate, or the bacteria were able to re-built their cell-wall recovering from the damage.

In **Figure 76**, the antibacterial effect of Ag-BG and Ag-BGNs can be compared under the same conditions. Specifically, MRSA was treated with 2.5 mg/mL of particles in PBS for up to 48 h. The antibacterial action was significantly faster after treatment with Ag-BGNs than Ag-BG microparticles. Bacteria inhibition was already observed after only 1 h of exposure to Ag-BGNs. However, one of the most noticeable effects occurred at 12 h of treatment, where Ag-BG microparticles started to provide significant inhibition while the Ag-BGNs had sterilized the solution.

The combinatorial treatment of particles and oxacillin followed a similar trend in both microparticles and nanoparticles (**Figure 76**). Synergism was only observed once the Ag-BGNs had caused significant bacterial damage, agreeing with the process observed for Ag-BG microparticles (**Figure 38**), suggesting both systems follow a similar mechanism (i.e., creating nano-tunnels for antibiotic penetration). The combination Ag-BGN/oxa was toxic sooner than Ag-BG/oxa owed to the nanoparticles' faster antimicrobial capability. Interestingly, the level of synergism, defined as the difference between the agent alone and in combination, is significantly less evident in Ag-BGN/oxa than in the microparticle counterpart. This effect is hypothesized to come from the mechanism of antibiotic resurrection. As mentioned previously, the nano-size debris opened tunnels for antibiotic penetration, and the lethargic bacteria are expected to re-activate the biosynthesis of cell-wall to clog these pores. Once the biosynthesis starts, oxacillin will find its target and bypass the envelope's restoration [17]. In Ag-BGNs, the nano-tunnels are

puncture significantly faster than Ag-BG microparticles since the system does not need to degrade to release the debris. Although this damage will allow oxacillin penetration, the faster antibacterial behavior is expected to leave a shorter notice to start new cell-wall biosynthesis, and therefore, it would be more challenging for oxacillin to find active targets and synergize. This behavior was also observed in the Ag-BGN/fosfo combination, where the synergism level was slightly lower than in Ag-BG/fosfo. Interestingly, the synergism level with 0.5 mg/mL of Ag-BGNs in Ag-BGN/fosfo (**Figure 61**) was significantly higher than that observed using 2.5 mg/mL Ag-BGNs in the combination (**Figure 76**), although at a different time point of the co-culture. The lower concentration of Ag-BGNs (i.e., 0.5 mg/mL) delays the antibacterial action to 6 – 12 h, which is slower than the 1-3 h observed for the higher concentration (i.e., 2.5 mg/mL). Under growth-arrested conditions, 6 – 12 h are supposedly enough time to re-activate significant cell-wall biosynthesis to clog the pores and potentiate the synergism, supporting the proposed mechanism. Nonetheless, this hypothesis could be further investigated by exposing MRSA to Ag-BGN/antibiotic combinations under growth-assisted conditions so that the bacteria are already in a metabolically active state to produce new cell-wall right away. The concentration of Ag-BGNs should be carefully selected for the synergism in TSB medium, and it is recommended to be over 10 mg/mL so that the bacteria viability upon exposure to Ag-BGNs only decreases from that at 0 h of treatment. If the proposed mechanism is correct, the level of synergism would be significant even at short time points.

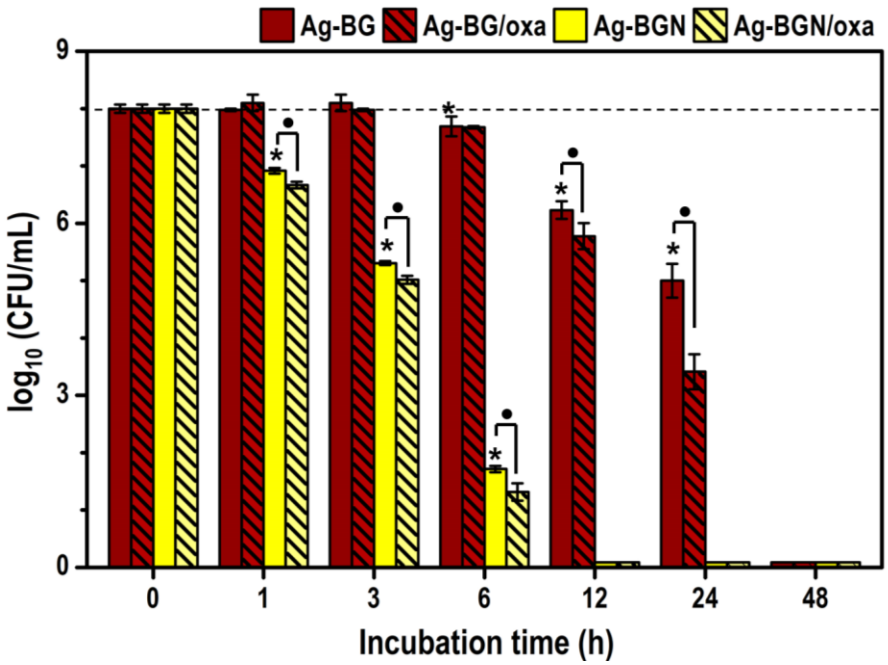

Figure 76: Ag-BGNs inhibits MRSA faster than Ag-BG microparticles. This figure is a reprint combining the antibacterial properties presented in different results sections for comparison. Suspensions of MRSA (OD_{600} = 1 equivalent to ~ 10^8 CFU/mL) were mixed with fresh PBS medium (untreated control – dashed line), 2.5 mg/mL of Ag-BG or Ag-BGNs (red and yellow bars, respectively), or a combination of substances with 0.1 µg/mL of oxacillin (oxa - pattern bars). Note that antibiotics alone were ineffective against MRSA. The CFUs were enumerated for up to 48 h with a limit of detection of 10 CFU. (*) Indicates the significant difference between particle-treated and untreated MRSA and (●) marks the significant difference between particles and particles/oxa ($p < 0.05$).

5.6.2.3. Interaction of Ag-BGNs and cells, and comparison with the biological behavior of Ag-BG microparticles

The biological properties of Ag-BGNs were studied for the first time in co-culture with hBMSCs. Ag-BGNs were not cytotoxic at any concentration (**Figure 63**). Although the ion-releasing profile of the Ag-BGNs was not assessed, it is anticipated to release Si, Ca, P, and Al species as the glass network degrades. Similar to Ag-BG microparticles, the release of Si and Ca enhances the rate of proliferation compared to untreated cells. The ion delivery and uptake by cellular organelles are expected both extracellularly and intracellularly as the nanoparticles get internalized. The effect on delivering Ag^+ ions was investigated by exposing the cells to Ag_2O at the Ag-BGNs network

concentration. Treatment with Ag_2O decreased in viability (**Figure 63** a), showing almost no alive cells in the plate (**Figure 63** c). In contrast, Ag-BGN-treated wells were confluent with healthy spindle-like cells. This result suggests a steady release of Ag^+ ions below cytotoxic limits and with a strong antibacterial effect.

The cell proliferation was significantly influenced by particle size. Ag-BGNs promoted faster proliferation than Ag-BG microparticles (**Figure 77**). The proliferation rate of Ag-BGN-treated cells was higher than Ag-BG microparticles, although they showed a more negligible difference with the untreated control. For instance, Ag-BGNs enhanced 1.3 times faster proliferation than the control, whereas, with Ag-BG microparticles, the cell proliferation was 2 times faster. This effect could be correlated to several factors related to the experimental design and the behavior of particles. First, the cell viability test in Ag-BG microparticles was performed with higher cell density (30 K cells/well) than in Ag-BGNs (15 K cells/well), and consequently, their growth rate is slower due to higher confluence. Second, the Ag-BG microparticles caused a slight drop in the cell population at the beginning of the treatment, causing the fitting line to have s steeper slope. It is also worth mention, the dependency of relative cell viability with the concentration of particles. In the case of Ag-BG microparticles, the cell viability did not change significantly between untreated and the different concentrations of Ag-BG. In contrast, significantly higher cell viability was observed as the Ag-BGNs concentration increased, which may be associated with the ion concentrations released from the network. Although BGs tend to dissolve faster in culture medium than in PBS due to the high affinity of organic molecules with cations in the glass [428], the degradation of Ag-BG is expected to be significantly slower than Ag-BGNs due to the highly compact silica network and lower surface area. Additionally, most Ag-BGNs are supposedly internalized by cells, whereas only small debris nano-size fragments from Ag-BG microparticles

may reach the cell. Therefore, Ag-BGNs will deliver higher concentrations of ions, both extracellularly and intracellularly, than Ag-BG microparticles.

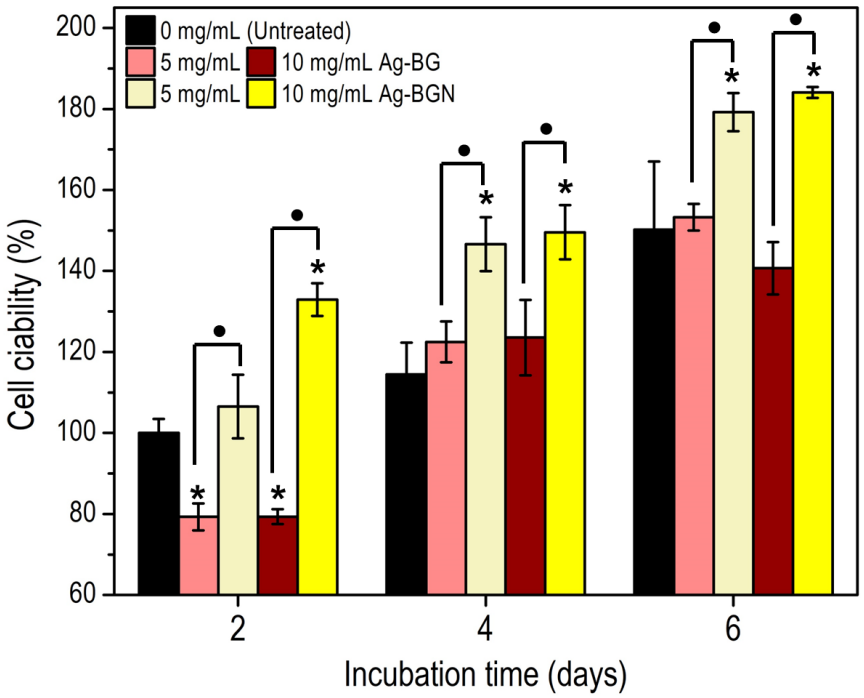

Figure 77: Ag-BGNs promotes faster cell proliferation than Ag-BG microparticles. This figure is a reprint combining the cell proliferation presented in different results sections for comparison. The cell viability was obtained by normalizing the optical density (OD) with the untreated control after 2 days of incubation. Statistical difference between untreated and treated hMBSCs is indicated with (*) and between Ag-BG microparticles and Ag-BGNs-treatments of same concentrations with (●) for $p < 0.05$.

Following previous research, the ionic release products from Ca-containing BGNs induced osteogenic differentiation to osteoblasts [428,429]. Mature ECM, which forms during osteogenic differentiation, was observed after treatment with the Ag-BGNs (**Figure 64** a). The results indicate a significant relationship between calcified nodule formation and Ag-BGNs concentration (**Figure 64** b). Cell differentiation was also evidenced in gene markers. *Col10A1* and *OMD* served as early-stage markers [430,431] of osteoblast differentiation and were significantly upregulated after treatment with both 5 and 10 mg/mL Ag-BGNs, indicating the degradation products of the

nanoparticles caused the production of mineralized ECM [432]. The higher expression of mid-stage markers (*BSP* and *ACAN*) [430], related to mineralization and ECM maturation [433–435], proved the Ag-BGNs positive effect. Late-stage makers *OCN* and *OSX* [430] signal differentiation has occurred [434,435], and both were upregulated in cells treated with 10 mg/mL of Ag-BGNs but not in the 5 mg/mL groups. Together, the expression level of these genes indicates differentiation occurs in all the cells and is promoted upon Ag-BGNs treatment. The high expression levels of *Col10A1*, *BSP*, and *ACAN* compared to other gene markers (note the relative expression goes up to 16) might be correlated to an early synergism between ion dissolution products and osteogenic supplements, causing the expression of proteins. In fact, this synergism between BGN products and supplements was previously reported by Naruphontjirakul *et al*.[429] in a separate glass system. Osteogenesis occurred faster for the higher concentration of Ag-BGNs (i.e., 10 mg/mL) than in lower concentrations (5 mg/mL) since, in the former, the cells showed evidence of late-stage differentiation. This observation is congruent with the proliferation rate results since proliferation and differentiation are competitive processes. **Figure 63** b demonstrated slower proliferation with 5 mg/mL than 10 mg/mL and 20 mg/mL of Ag-BGNs, whereas the concentration effect was reversed in cell differentiation. Therefore, confirming higher concentrations of Ag-BGNs favor cell differentiation over cell proliferation.

Figure 78 presents the cell differentiation after Ag-BG treatment compared to Ag-BGNs when both are used at a concentration of 10 mg/mL. The mid-stage gene marker *BSP* was more expressed after Ag-BGNs than Ag-BG microparticles, and late-stage gene marker *OCN* follows a similar behavior. These results suggest faster cell differentiation when exposed to Ag-BGNs than Ag-BG microparticles, although most of cells are still at the mid-stage of the process. It is hypothesized that while Ag-BGNs promote faster cell proliferation due to the accelerated ionic

release, their earlier degradation does not support the delivery of a high concentration of ions for the long incubation times required to provoke complete differentiation. The higher levels of proliferation and differentiation may also be correlated to intracellular uptake. The degradation of Ag-BG microparticles is slower, providing a lower concentration of ions to the cells but constant during the experiment.

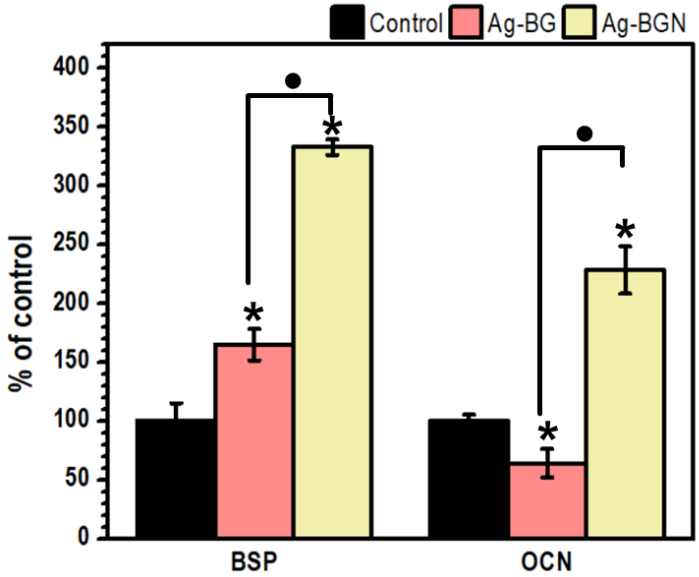

Figure 78: Ag-BGNs induce faster cell differentiation than Ag-BG at the same concentration (10 mg/mL). Gene markers like bone sialoprotein (*BSP*) osteocalcin (*OCN*) are more expressed in Ag-BGNs. This figure is a reprint combining the cell differentiation in different results sections for comparison. Statistical difference between untreated and treated hMBSCs is indicated with (*) and between Ag-BG microparticles and Ag-BGNs-treatments with (●) for $p < 0.05$.

5.6.2.4. Internalization of Ag-BGNs during co-culture

The phenomenon of cellular uptake is crucial in cell behaviors, including cell proliferation, differentiation, and tissue organization [436,437]. The nanoparticles' internalization depends on their surface chemistry, size, and shape [438–440]. In Ag-BGNs, the intracellular uptake was demonstrated in differentiated cells after 14 days of co-culture. Although the specific cellular pathways for cell internalization was not addressed in this study, most previous research point to

endocytic trafficking [441,442] as the main pathway for cellular uptake of particles with less than 200 nm diameter [443]. Endocytosis consists of vesicle formation to capture the nanoparticles in the extracellular environments and then carry them into the cytoplasm. Once endocytosis is completed, different endosomes transport the material until the nanoparticles escape and translocate into the cytosol [444–446]. The size of individual Ag-BGNs (~10 nm) and their aggregates (~100 nm, as observed in Figure 57 f) make them perfect candidates for endocytic trafficking. The vast number of vesicles, autolysosomes, and autophagosomes found in Ag-BGN-treated fibroblasts, significantly more prominent than in untreated cells, may solidify this idea of the endocytic pathway in Ag-BGNs uptake. Nonetheless, the role of endocytosis as well as the specific endocytic route is recommended as a subject of study in the future to better design the delivery systems of Ag-BGN-based treatments. For instance, research has shown that the surface functionalization of nanoparticles with other components can promote or neglect endocytosis [447]. Although there is no way to predict which endocytic pathway the Ag-BGNs uptake will follow, other studies in fibroblasts and mesenchymal cells have suggested endocytosis via clathrin-pitted mechanism for the internalization of Si-based nanoparticles [105,448]. It should also be noted that while endocytosis has been the target of study as the main cellular uptake mechanism, research has shown internalization of nanoparticles in cells treated with pharmacological endocytosis inhibitors, suggesting the less dominant existence of alternative cellular pathways [105,429,449].

The Ag-BGNs accumulated near subcellular organelles (mitochondria and Golgi bodies) or around the cytosol instead of encapsulated in vesicles. This distribution of nanoparticles near organelles has also been observed in other systems cultured with mammalian cells [445,449]. The significance of this observation is that Ag-BGNs were able to escape the endocytic system and

then scatter through the cytoplasm, where they degrade, releasing ions for cell proliferation and differentiation. The ability of nanoparticles to exit endosomes has been associated with their negative charge [448], which is ~ 9 mV in Ag-BGNs. The Ag-BGNs degradation was evidenced by their irregular shapes (**Figure 65** f). Note that Ag-BGNs were not found inside the nucleus, in agreement with the observation by Lin *et al*. [450].

A separate area of study regarding cellular uptake would be the "wrapping time", defined as how fast the cell-membrane encloses nanoparticles [451,452]. Previous work in this area, performed primarily in mesoporous silica nanoparticles, found the cellular uptake took about 2 h [453] and followed a sigmoidal behavior with the dose [448]. A similar effect would be expected to occur in Ag-BGN-treatments, where the number of nanoparticles internalized by the cells would increase with the concentration of the nanoparticles in the culture medium.

5.6.2.5. Interaction of Ag-BGNs and tissues, and comparison with the bone regeneration by Ag-BG microparticles.

The developed Ag-BGNs sustained mild bone re-growth in critical calvaria defects; however, less bone volume fraction was obtained than after Ag-BG microparticles treatment. The mechanisms of bone re-growth were based on the release of degradation products, especially soluble Si and Ca, described in section 5.3. Additionally, Ag-BGNs are expected to be internalized by tissues. Immunohistology suggests significant tissue inflammation after Ag-BGNs treatment. These results may indicate a not significant improvement of regenerative properties by down-scaling the Ag-BG system. The inflammation process is an expected reaction to foreign material in the body. In the case of Ag-BGNs, the inflammation is suspected of coming from an overdose of material. Further studies are required to evaluate the type and concentration of macrophages and determine

the reaction towards materials implantation. The Ag-BGNs concentration delivered was 10 mg/mL, the same as in Ag-BG microparticles. However, Ag-BGNs reactivity and degradation are notably faster, as demonstrated in section 4.5.2.3, releasing higher ions concentration in shorter periods. To prove the bone regenerative properties of Ag-BGNs, the experimental design may require adjustments in terms of Ag-BGNs dose. Alternatively, the degradation of Ag-BGNs might be excessively fast to support bone re-growth over time. Therefore, the composition of Ag-BGNs can be adjusted to decrease the rate of degradation by, for example, lowering the CaO content, which the major network modifier in the system. Additionally, large particulates were found around the newly formed tissue. The morphology and size indicate these particulates were not Ag-BGNs aggregates as they were firmly densified. Based on the degradation behaviors of Ag-BGNs, these particulates might be HCA deposits from the bioactive response. Further investigation with Raman spectroscopy on the histology section may bring new light to the nature of these particulates.

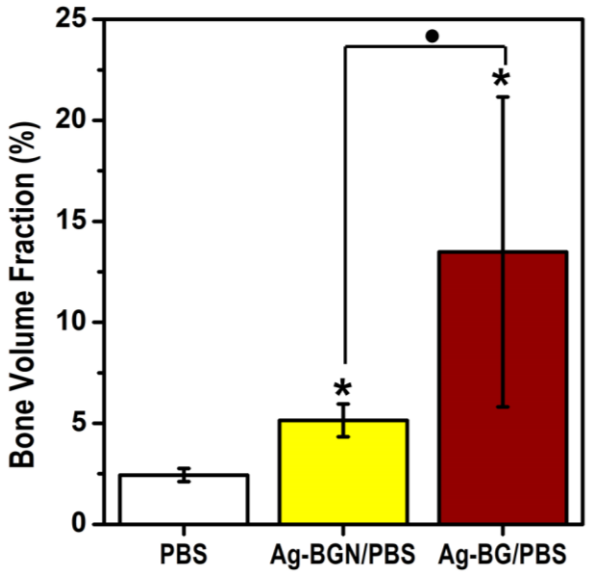

Figure 79: Ag-BG microparticles trigger more bone re-growth after a month of implantation. This figure is a reprint combining the *in vivo* results presented in different results sections for comparison. Statistical difference between PBS and particle treated is indicated with (*) and between Ag-BGNs and Ag-BG with (●) for $p < 0.05$.

5.7. Design of medical Ag-BGN/polymer nanocomposites devices

There is an increasing interest in designing treatments for osteoregenerative applications. As has been highlighted in this document, multi-functional bioactive materials hold promise in clinical scenarios where an underlying infection can compromise the outcome. The ability of Ag-BGNs to provoke cell proliferation and trigger bone re-growth has been shown in sections 4.5.2.5 and 4.5.2.6. Additionally, Ag-BGNs present advanced antibacterial properties proving the inhibition of planktonic antibiotic-resistant bacteria within a few hours of treatment (section 4.5.2.4). Therefore, in this section, the clinical delivery of Ag-BGNs was explored by designing a minimally invasive injectable approach. Nanocomposites were fabricated by dispersion of Ag-BGNs in a polymeric matrix. The matrix's selection prioritized biocompatibility, suitable porous structure, and homogeneous microstructure with the intended host tissue [454,455]. Two natural-based hydrogel matrices (i.e., extracellular matrix (ECM) and Collagen Type I (Col)) were used to draw on their favorable structure, such as their interconnected pores for cell infiltration and angiogenesis, which guide the regeneration of surrounding tissue [456,457]. These natural matrices have been proposed for the regeneration of damaged tissues [458,459], showing promising results in defective tissues when filled with bioceramic materials [460–462]. In this sense, the design of nanocomposites filled Ag-BGNs could further advance the clinical outcomes owing to the enhanced capabilities of nano-design systems.

ECM and Col polymerize by combining pH and thermal activation, which offers the advantage of injectability in clinical applications. The samples would be delivered in a liquid-like state, allowing the material to flow and fill the bone defect (even if it presents an irregular shape) and then self-polymerize under physiological conditions [456]. The incorporation of Ag-BGNs in the hydrogel matrices significantly affected the polymerization process. The higher the Ag-BGNs

concentrations, the slower the polymerization occurred. However, 5 wt.% of Ag-BGNs did not strongly delay the polymerization of the hydrogel. The Ag-BGN/hydrogel nanocomposites are anticipated to polymerize through covalent bonds and physical crosslinking, similar to other hydrogels [463]. The covalent bonds occurred by radical chain polymerization, while the physical crosslinking is expected between Ag-BGNs and the polymeric chains. The slower polymerization in the nanocomposites with higher Ag-BGNs wt.% is probably a result of the physical crosslinking as nanoparticles' presence disrupt the oriented arrangements of the polymer chains. The approximately 10 cm^{-1} shift and the broadening of some FT-IR peaks in the Col/Ag-BGNx nanocomposites (**Figure 69** a) support the hypothesis of chemical interaction between the $(COO)^-$ groups in the collagen and nanoparticles in agreement with other works [277].

The fibrillar structure of the hydrogels was preserved after Ag-BGNs incorporation (**Figure 68**). However, the structure evolved towards a denser packaging with visible protein bundles. The presence of Ag-BGNs disturbing the covalent bonding between monomers lead to a high concentration of shorter polymer chains. As a result, more and thinner fibrils were clearly visible in the Col/Ag-BGN10 nanocomposite compared to Col/Ag-BGN0. Interestingly, despite their low zeta potential value, Ag-BGNs showed good dispersibility in the hydrogel matrix, agreeing with their dispersion in resin (**Figure 55**). In the ECM/Ag-BGN10 nanocomposite, individual nanoparticles were adsorbed on the fibril surface, similar to the effect observed in colloidal silica [464,465]. In general, the SEM images suggest Ag-BGNs concentration up to 10 wt.% did not significantly perturb the hydrogels' structure, which retained significant porosity. This observation is congruent with previous work [22,463,466] in bioceramic nanocomposites that only showed significant structural changes for filler concentrations above 20 wt.%.

The antibacterial and biological performance of the nanocomposites were also evaluated. Planktonic MRSA mixed with either Col/Ag-BGNx or ECM/Ag-BGNx are anticipated to migrate through the open pores to colonize the fibrils, similar to the effect observed in Ag-BG microparticles (**Figure 28** b). The nanocomposites' antibacterial model is expected to follow the same inhibition mechanisms as Ag-BGNs alone, presented in a previous section. Briefly, these mechanisms consist of Ag^+ ions, mechanical damage of the envelope, oxidative stress, and osmotic effect. The bacteria viability was significantly higher when exposed to the Ag-BGN/hydrogel nanocomposites than the Ag-BGNs alone (**Figure 70**). Several processes may explain this outcome. First, the interaction between Ag-BGNs and polymer chains may reduce the nanoparticles' degradability as a significant part of their surface area is covered with hydrogel rather than exposed to the medium. Second, the above-mentioned antibacterial mechanisms are delayed because of the matrix. For instance, Ag-BGNs would need to detach from the fibrils and get released in solution before they can mechanically damage the bacteria envelope. Besides, the released cations from the network degradation might need to diffuse through the fibrils before reaching the microbes. Both nanoparticle detachment and ion release would occur as the hydrogel degrades; however, this time-dependent process would be significantly slower than when Ag-BGNs are delivered free in a suspension. As degradation continues, the antibacterial product concentration is expected to increase to provide significantly higher inhibition, as observed in the other time-dependent antibacterial properties (**Figure 60**). The stronger bonding between Ag-BGNs and ECM than with Col is presumably responsible for the lower antibacterial effect observed in ECM/Ag-BGNx. Interestingly, the Col/Ag-BGN0 and ECM/Ag-BGN0 (i.e., hydrogel controls devoid of nanoparticles) showed a slight increase in bacteria concentration after 24 h (**Figure 70**). These hydrogels are nutrient-rich [467] and may provide a suitable but not significant

nurturing source for bacteria, similarly to their effect in eukaryotic cells [468]. These nutrients may counter-effect the antibacterial properties of the Ag-BGNs in the nanocomposite, contributing to the lower antibacterial efficacy observed. In contrast, the nutrients and fibrils structure of the hydrogel matrices are expected to provide the appropriate microenvironment for cell attachment and proliferation required for tissue regeneration [469,470]. The exposure of fibroblasts to ECM/Ag-BGNx revealed significant cell proliferation after 1 week. The release of ions from the Ag-BGNs network degradation (i.e., Si, P, and Ca) is anticipated to enhance cell growth. Based on the behavior of Ag-BGNs alone (**Figure 64** and **Figure 66**), the ion-mediated reactions are also expected to trigger osteogenic function in fibroblasts by inducing cell mineralization and gene up-regulation. ECM holds regenerative properties of its own, provoking cell proliferation and differentiation due to the release of biomolecules with inherent biological properties [471]. However, the ECM properties are presumably lower than in the presence of bioceramics, based on other works [472,473]. Therefore, cell proliferation was promoted by a synergistic action between the hydrogel and the Ag-BGNs. The highly hydrated structure of matrices may also cause problems with the degradability of the nanoparticles. Specifically, there are concerns of Ag-BGNs degradation due to the abundance of water, which may cause nanoparticle dissolution before use. On this basis, the preparation of the nanocomposites shall only be performed right before application.

To summarize, Ag-BGNs can be effectively incorporated in a Col or ECM matrix to obtain an injectable nanocomposite. Polymerization is anticipated within a few hours for Ag-BGNs concentrations < 10 wt.%. The nanocomposites showed good biological behavior and long-lasting antibacterial action. This capability makes them ideal for filling defective tissue fractures where the clinical application calls for biocompatibility, antibacterial activity, and matrix formation.

6. SUMMARY AND CONCLUSION

This thesis investigated the design and synthesis of bioactive glass particles for orthopedic applications. Although the field of regenerative medicine is constantly expanding, there is still a need for treatments that can effectively heal tissues and prevent or eradicate infections. Material Science has played a critical for the development of prosthetics, and now, using the fundamental understanding of materials microstructure and degradation, materials can carve their way as the top choices for clinical applications.

In this work, a previously presented Ag-doped bioactive glass formulation in the form of microparticles (Ag-BG) was thoroughly investigated to correlate their physical performance *in vitro* and *in vivo* with their composition and structure. Next, their antibacterial potential was explored against resistant pathogens to unravel the mechanism of inhibition this material provides. Additionally, this work demonstrated the capability of Ag-BG to resurrect antibiotics, providing hope to fight antibiotic-resistance by giving old drugs a second life. To draw on this capacity, antibiotic depots were developed using Ag-BG as a vehicle for vancomycin delivery. The proposed antibacterial model described nano-size debris's role in the inhibition, suggesting both biological and antibacterial properties could be significantly enhanced by down-scaling the Ag-BG formulation to nanoparticles.

Therefore, the Stöber method was revisited to develop BGNs reliably. The synthesis of BGNs has presented a constant challenge in cation incorporation. Therefore, the synthesis method was first modified to incorporate Ca and P at the nominal range and then adjusted to develop Ag-BGNs. The properties of the Ag-BGNs were evaluated following similar experimental set-ups than in Ag-BG microparticles to compare the effect of size and morphology on the biological and antibacterial

performance models described before. Finally, an injectable nanocomposite was designed, demonstrating the potential for incorporating monodispersed Ag-BGNs in hydrogel matrices for a straight-forward clinical delivery.

The specific conclusions and highlights of this dissertation have been described in the following sub-section, bringing to context all the knowledge acquired in completing this work. Finally, this section concludes the thesis work by providing guidance and recommendation for future work.

6.1. Conclusions

6.1.1. Degradation of Ag-BG microparticles

(1) The Ag-BG microparticles were biodegradable upon immersion in medium (i.e., PBS, SBF, or DMEM) by cleavage BO and NBO bonds. The biological and antibacterial studies revealed two types of degradation products: ionic species from the glass network and nano-size debris. The degradation products maintained a neutral pH value in the solution through the process.

(2) The release of ionic species modified the chemistry and morphology of the microparticle surface, preparing it for the deposition of a new phase. Precipitation of stoichiometric hydroxyapatite was observed within 7 days, demonstrating the bioactivity of the system.

6.1.2. Interaction between Ag-BG and cells and tissues: biological performance

(1) The on-site degradation of Ag-BG in the presence of cells was not cytotoxic for concentrations ranging between 2.5 – 12.5 mg/mL. The composition of the bioactive glass was rich in Si, Ca, and P species. When these ions are leached from the network and absorbed by cells, they provoke cell proliferation. The release of Ag^{+} ions remained below toxic limits to mammalian cells. The secondary degradation in nano-size debris may also favor intracellular uptake of

nanoparticles, providing a localized delivery of ions and, therefore, hastening the biological processes. The Ag-BG structure also provided ROS from the surface silanols (Si-OH) and the dismutation of network oxides (O^{2-} species). These ROS seemed to benefit cell behaviors, similarly to other works.

(2) Prolonged exposure to Ag-BG (at a concentration between 5 – 12.5 mg/mL) induced cell differentiation into osteoblastic lineage in the presence and absence of differentiating factors. The higher density of the mineral monolayer in the osteogenic medium was correlated to a synergism between Ag-BG degradation products and differentiating factors.

(3) The degradation of Ag-BG followed a similar process in the presence of cells, depositing apatite at the surface. The thickness of the deposit was significantly lower than in the acellular degradation test. This observation is correlated to a lower medium saturation since the cells can absorb and metabolize the degradation products, decreasing the concentration in the solution.

(4) The *in vivo* tests using a calvarial defect model in mice demonstrated that Ag-BG microparticles induce bone regrowth after 30 days. Histology and micro-CT images revealed defects filled with new tissue. Therefore, demonstrating Ag-BG microparticles are an excellent material for the regeneration of damaged bone.

6.1.3. Interaction between Ag-BG and pathogens: antibacterial behavior

(1) Ag-BG is a potent antimicrobial against MRSA. The antibacterial capabilities were demonstrated in planktonic and biofilm bacteria, revealing Ag-BG's potential to target an on-going or a mature infection.

(2) The inhibition model was described for Ag-BG as a contribution of simultaneous mechanisms. The strongest antibacterial action (~ 52 % contribution) comes from the release

of Ag^{+} ions from the structure at levels that toxic to microbiota. The degradation of Ag-BG upon immersion releases additional species. For instance, ROS cannot be adequately metabolized by bacteria, causing oxidative stress (~ 40 % contribution) or elevated cation concentrations like Ca^{2+} ions that unbalance the osmosis around the cell envelope. Finally, the model describes nano-size debris's contribution, causing mechanical damage to the cell-wall, puncturing holes to penetrate and accumulate at the cytoplasm (~ 8 % contribution). In general, Ag-BG had a more significant effect on the cell envelope affecting its integrity and permeability.

(3) Prolonged exposure to Ag-BG induced the evolution of MRSA to small-colony variants, which became increasingly sensitive to treatment. Therefore, no resistance to treatment is anticipated.

(4) Ag-BG's ability to restore the antibacterial action of antibiotics was evaluated for different bacteria targets using 2.5 mg/mL of microparticles. The results demonstrated that the resurrection of antibiotics only occurred when the drug presented primary or secondary effects on the cell-wall. The proposed synergistic model consisted of the penetration of the antibiotic through the created nano-tunnels. Therefore, in order to restore antibiotics, Ag-BG needs to cause significant damage on its own. Bacteria would try to clog the pores, reactivating cellular functions like cell-wall biosynthesis, where the antibiotic will then find its target from inside the bacterium and bypass the restoration. This model was supported by the antibacterial mechanism of the antibiotics as well as the synergism observed when bacteria were actively growing.

6.1.4. Development of therapeutic carriers using Ag-BG as antibiotic vehicle

(1) Vancomycin was successfully conjugated with Ag-BG microparticles to create an antibiotic depot against resistant bacteria. Drug immobilization was anticipated by pore absorption, chemical bonding, and entrapment. The results suggest a decisive role of the two latter mechanisms due to the FT-IR vibration of Si-OH and COOH bonds and the presence of Ca-P-rich deposits at the Ag-BG surface. The loading efficiency was around 50 %.

(2) The pharmacokinetics of the Ag-BG@vanc conjugate reached a maximum release peak after 12 h at 37 °C and showed a total delivery capacity of about 40 %. The presence of Ca-P deposits presumably controlled the release. The low delivery capacity may be associated with a re-precipitation process, which is unlikely to occur during clinical application as biological entities absorb the antibiotics.

(3) The Ag-BG@vanc conjugate allowed to decrease the dose of agents to provide a similar inhibition level to the Ag-BG/vanc combination. This effect was correlated to Ag-BG's faster degradation as their surface was modified by the presence of the antibiotic and the localized delivery.

(4) The Ag-BG@vanc conjugate was not cytotoxic. Therefore, the Ag-BG shows excellent potential as a carrier to bolster antibiotic action and advance the tissue's recovery.

6.1.5. Synthesis and characterization of Ag-BGNs

(1) A Stöber method was modified to developed ternary system BGNs with a composition consisting of 62 SiO_2 – 3.2 P_2O_5 - 34.4 CaO (mol.%) yielded nanoparticles of nominal composition with sizes < 100 nm.

(2) The cation incorporation model was proposed in two steps. First, methanol was able to balance TEOS and TEP's hydrolysis, yielding to the incorporation of P within the network. Second, CaNT was added before nanoparticle nucleation to trap the Ca^{2+} ions within the structure. Calcination at 700 °C was performed to induce Ca^{2+} ions diffusion and the formation of NBO within the silica network. This model was confirmed by comparing the composition and structure of the BGNs developed by different models at different fabrication stages. For instance, the network connectivity significantly decreased upon successful incorporation of Ca^{2+} as a network modifier. Based on this model, incorporating additional elements at nominal composition can be controlled by the amount of reagent added to develop a new formulation for specific applications.

(3) Extended homogenization of solution was key for incorporating the elements and was demonstrated to affect particle size. This phenomenon could be explained as a side effect of methanol solvent, which promotes hydrolysis over condensation, leading to shorter silica chains as the reaction continues. This effect was also confirmed in the fabrication of Ag-BGNs. As the hydrolysis of both TEOS and TEP was fulfilled with increasing stirring time, a higher mass of nanoparticles was obtained at the end of the heat treatment.

(4) The role of composition and morphology was observed in the apatite-forming ability and antibacterial properties. The M2-P2 presented greater capabilities than the other BGNs correlated to a higher modified silica network due to the higher calcium content and the higher surface area. These elements trigger a faster material degradation, which was also evident by the pH value evolution.

(5) A method for synthesizing spherical monodispersed Ag-BGNs in the system SiO_2 59.6-CaO 25.5-P_2O_5 5.1-Al_2O_3 7.2 - Ag_2O 2.2 (wt.%) was successfully derived from the modified

Stöber approach for BGNs. Cation incorporation was achieved within nominal levels following the previously presented model.

(6) The extended stirring for the homogenization of solution after nitrate addition caused significant size reduction, providing Ag-BGNs < 10 nm. Although the nanoparticles tended to appear in aggregates of 200 nm, they were easily detached and monodispersed in polymeric matrices without surface modification.

(7) The degradation of Ag-BGNs was significantly faster than in their micrometer counterparts. The Ag-BGNs structure was completely amorphous compared to the semi-crystalline structure of Ag-BG microparticles. The ion release caused significant changes in the pH, forcing particle pre-condition before application to reduce toxicity. Additionally, carbonated hydroxyapatite started to deposit after 1 day, with significant deposits after 3 and crystallization after 7 days. This faster degradation was correlated to the higher surface area and the fully amorphous structure of Ag-BGNs. Amorphous materials are more reactive than semi-crystalline ones due to their instability and their need to find equilibrium.

(8) Ag-BGNs were highly antibacterial, demonstrating significantly faster and stronger inhibition than Ag-BG microparticles. Specifically, the MIC was reduced by about 90 %. Additionally, 2.5 mg/mL of Ag-BGNs (which was the MIC of Ag-BG microparticles) provided inhibition after only 1 h of co-culture and sterilized the solution after 12 h. Therefore, demonstrating the hypothesis of Ag-BGNs as a more potent antibacterial weapon.

(9) The inhibition model of Ag-BGNs is expected to follow the exact mechanisms as Ag-BG microparticles with Ag^+ ion, osmotic effect, mechanical damage of the cell-wall, and ROS. Nonetheless, owed to their size, the mechanical damage through nano-sized debris is anticipated to play a more dominant role. The presence of all these mechanisms explains why

Ag-BGNs are still synergized with antibiotics. This confirms that reducing the system to a nano-scale only enhanced the overall antibacterial performance of the system.

(10) Ag-BGNs were not cytotoxic. The degradation products from the Ag-BGNs structure only promoted cell proliferation faster than Ag-BG microparticles. Although the release rate of ionic species was not evaluated for Ag-BGNs, the results suggest the concentration of Si, Ca, and P is enough to trigger cell response while Ag remains below cytotoxic limits. In fact, the controlled release of Ag^{+} was indirectly confirmed by comparison of cell response upon exposure to Ag_2O, which toxic to fibroblasts. The small size of the Ag-BGNs also favored intracellular uptake by endocytosis, as suggested by the fibroblasts' TEM images.

(11) The Ag-BGNs were also able to provoke cell differentiation. In general, the level of differentiation was higher in Ag-BGNs than Ag-BG microparticles. This may be associated with the faster degradation of Ag-BGNs, which is expected to leach higher ion concentration at the beginning of the treatment.

(12) Ag-BGNs triggered significant tissue re-growth. However, the volume of new bone was lower than in the case of Ag-BG microparticles. This effect may be correlated to the faster degradation of Ag-BGNs, which does not sustain the ion release to promote tissue formation for extended periods.

6.1.6. Design of Ag-BGN/polymer nanocomposite devices

(1) Injectable hydrogel nanocomposites were fabricated by dispersion of Ag-BGNs in collagen or extracellular matrix. The presence of nanoparticles delayed the matrix's polymerization under physiological conditions but did not disrupt the 3D porous fibril network.

(2) The hydrogel fibril diameter decreased with Ag-BGNs concentration due to the interruption of monomer-monomer cross-linking. Higher concentrations of fibrils with diameters in the

range of 20-300 nm were found in SEM. Nonetheless, more work is required to prove the interaction of Ag-BGNs with amine and carboxyl acid groups in the hydrogels.

(3) The Ag-BGNs aggregation around fibrils was not significant, as most nanoparticles appeared homogeneously dispersed across the fibrils' length. The few aggregates found had sub-micrometer sizes (< 200 nm), suggesting nano-size properties may still be maintained.

(4) The combination of Ag-BGNs with the natural hydrogel matrices was synergistic to nurture biological entities due to the rich-protein content. The interaction of the nanocomposites with bacteria and cells shows a less prominent effect on bacteria inhibition and enhanced cell proliferation/differentiation. This effect was suggested due to slowed degradation process of Ag-BGNs.

(5) The work done in Ag-BGN/polymer nanocomposites shows potential for the homogeneous incorporation of nanoparticles in a hydrogel matrix for straight-forward injectable delivery to fill complex and defective minor bone fractures and trigger tissue regeneration.

7. RESEARCH GAPS AND DIRECTION FOR FUTURE WORK

This research aimed to identify the relationship among microstructure, morphology, and composition in bioactive glasses to draw a beneficial interaction with tissues and eradicate or prevent an infection. This dissertation has presented a conceptual theory, empirical findings, and models to design and develop optimum inorganic bioactive materials for the potential treatment of osteo-degenerative diseases. The findings presented here are not free of limitations inherent in the research questions and methods used. Consequently, this document concludes by disclosing research paths to help foster further research in this topic.

(1) *Re-examine the composition of nanoparticles with quantitative techniques.* In the synthesis of BGNs and Ag-BGNs, the actual composition was almost identical to the nominal one for all the oxide concentrations. The explanation of this phenomenon has been elaborated in section 5.6.1.1. Although the composition was controlled with standardized processing parameters, quantitative techniques to demonstrate enhanced metallic ion incorporation are strongly demanded. The analysis performed was semi-quantitative, and although the results are reliable, the method sensitivity is insufficient to verify small quantities. Additional techniques like ICP-AES, APT, and TEM-EDX are encouraged to re-examine and validate the proposed synthesis approach to address this issue.

(2) *Address the limitations on particle size control and monodispersity*. The synthesis approach for BGNs revealed a significant decrease in particle size due to long stirring time, neutralizing the time-effect of the catalyzing solution on particle growth observed in other works [30]. Modification of the fabrication method in terms of solution concentration and optimum stirring time for hydrolysis of each reagent may provide more insights into the particle growth

mechanism and built-up on the model of BGN formation by trapping high cation content. One of the biggest concerns in the product outcome was aggregates' formation, although the results showed those were easily detached. Individual BGNs were metastable and quickly returned to an aggregate state after stimuli. Therefore, surface functionalization processes are recommended to maintain the particles' monodispersity, for example, by coating the BGNs surface with a biocompatible polymer like polyethylene glycol (PEG). The presence of the polymer would provide a barrier to repeal one nanoparticle to another [474], and it is expected to reduce the surface reactivity. Consequently, the degradation of the BGNs and their interaction with biological entities would need re-assessment. The PEGylation of nanoparticle surface may prevent internalization by macrophages *in vivo* and avoid protein corona formation [475]. Additionally, PEG may favor the attachment of other ligands to investigate alternative applications.

(3) *Build on the effect of composition in Ag-BGNs reactivity*. The development of Ag-BGNs with the desired composition in a nano-metric size (~ 10 nm) was achieved in this research. Although the degradation product concentration is yet to be determined in terms of ionic release, the pH evaluation demonstrated the material's high reactivity. While nanoparticles have high degradability owed to their surface area, the low network connectivity may also play a role. Therefore, the synthesis of Ag-BGNs with different concentrations of CaO from 15-30 %, in substitution of SiO_2, is recommended as future work to gain control over Ag-BGNs degradability through the network connectivity. It should be noted that by gaining this control on Ag-BGNs degradation, their effect on cellular responses can also be tailored for specific therapies.

(4) *Assess the proposed model of Ag-BG microparticle and Ag-BGNs degradation*. The particle-bacteria interaction provided insights into the inhibition mechanism to draw a hypothetical particle degradation model *in vitro*. However, several questions remained unanswered. For instance, the antibacterial behavior proposed the release of ROS that were toxic to microbiota. The degradation of the particles shall be similar in the presence of bacteria and eukaryotic cells. Therefore, the presence and effect of ROS resulting from particle degradation can be further proved in eukaryotic cellular activities. Additionally, the TEM images revealed the presence of internalized nanoparticles in MRSA after Ag-BG treatment. The degradation model proposed that these nanoparticles were nano-sized debris from the bulk structure of Ag-BG microparticles. However, the experimental technique used did not report the nature of these nanoparticles. Therefore, analytical techniques are encouraged to demonstrate they were originated from the degradation of the Ag-BG. The use of TEM-EDX is proposed to assess the Si content of the nanoparticles. It must be noted that careful sample preparation and optimum electron voltage and current conditions are required since the ultra-thin sections are prone to burning in the microscope column upon intense exposure to the beam. The intracellular accumulation of nanoparticles is also anticipated in Ag-BGNs but has yet to be shown. Finally, the mechanism model surmised the antagonistic effect of Ag-BG and Ag-BGNs in the permeability of the bacteria envelope. This hypothetical mechanism needs further evaluation, maybe by Live/Dead staining or membrane potential measurements.

(5) *Expand the conceptual framework of antibiotic resurrection by combinatorial therapies*. The ability of Ag-BG and Ag-BGNs to restore the action of antibiotics was demonstrated in simulated *in vitro* conditions. The therapeutic potential of this model should follow a further study against biofilms, where bacteria are protected by a protein matrix that hinders antibiotic

penetration. Additionally, the system's capabilities to eradicate bacteria shall be addressed in animal models for acute and chronic infections since the degradation of Ag-BG and Ag-BGNs *in vivo* may follow different profiles and lead to unexpected cellular responses.

(6) *Examine a new context for conjugation of Ag-BG and antibiotics*. The drug immobilization model was proposed by a combination of mechanisms: pore absorption, chemical adsorption bonding, and deposit entrapment. The experimental approach used in this work did not show an outstanding control of the antibiotic concentration incorporated nor released. Further work is recommended to optimize the process and examine alternative approaches to improve the loading efficiency and tailor species release. Some recommendations are listed next. Antibiotic uptake by absorption can be improved by increasing the microparticles' porosity during the synthesis. The loading process may also be performed under vacuum, substituting the air in the pores by the antibiotic solution, increasing chances for molecule absorption. The release of absorbed antibiotics is probably the least controlled mechanism since the drug is not physically attached to the particle; however, it may be tailored by surface modification of the particles after drug loading.

(7) Stimuli-responsive systems have been successfully developed on the surface of silica nanoparticles [476]. Castillo *et al*. [477] used Au nanoparticles to cap the pores of mesoporous silica nanoparticles. The Au nanoparticles were bonded to Diels-Alder cycloaddition adducts that acted as thermal-responsive units enhancing or suppressing drug release upon heating cycles. Polymer and lipids may also be used to entrap antibiotics within the nanoparticles' pores. For example, Mattingly *et al*. [478] successfully coated mesoporous silica nanoparticles with a cationic lipid shell to control doxorubicin release. The adsorption mechanism strongly depends on the nucleation units at the particle surface and the ionizable groups in the antibiotics. Therefore, some antibiotics like fosfomycin, which main active groups are hydroxyls, would be highly

challenging to adsorb. The adsorption mechanism could be promoted by providing active targets for antibiotic bonding at particle surfaces [11]. In other words, functionalize the surface to increase the nucleation sites is an affordable approach. For example, Escoto and Cai successfully conjugated antibiotics and mesoporous silica nanoparticles using PEG spacers [12,13]. Finally, antibiotic entrapment could be favored by accelerating the mineral deposition. Increasing the density of the apatite layer can significantly increase the loading amount. Therefore, performing the loading process on an ion-saturated solution, like SBF instead of PBS, holsters the Ca-P phase development and encourages antibiotic entrapment as a loading mechanism [164].

(8) *Innovate delivery methods for Ag-BGNs*. The preliminary study of injectable hydrogel nanocomposites showed Ag-BGNs were a promising building block for scaffolds. The matrix facilitates on-site delivery for clinical application, and promising properties were observed. Nonetheless, research questions remained answered to understand the interaction between Ag-BGNs and the hydrogel, which is critical for a proper nanocomposite design. For example, the effect of the matrix in the degradation profile of Ag-BGNs and the effect of released ions on the integrity of the fibril structure. Engineering novel nanocomposites with Ag-BGNs broadens the spectrum of application of the system where the knowledge gathered in this dissertation may be merged for a single-step clinical technology. A promising line of work is the use of antibiotic-loaded injectable nanocomposites. Antibiotic-loaded hydrogels have been previously studied, showing a rapid and uncontrollable release of the drug that is not suitable for long-term applications. In this case, Ag-BGNs are proposed as carriers for antibiotic and building blocks in a polymeric matrix so that the degradation of Ag-BGNs controls the drug release. In order to design such material with multi-functional properties, a profound understanding of Ag-BGNs and hydrogel interaction is required. The selection of antibiotics offers a window of possibilities since

the Ag-BGNs formulation presents restorative capabilities to recycle old antibiotics against resistant pathogens. Lastly, Ag-BGNs could also be used as building blocks for other polymeric matrices, envisioning additional applications. For example, Ag-BGNs could be distributed in poly(ε caprolactone) (PCL) and chitosan (CS) electrospun fibers for the development of mats for wound healing applications.

APPENDICES

APPENDIX A: Optimization of synthesis parameters for nanoparticle fabrication

- Effect of stirring time X_1 in the incorporation of P_2O_5 in M2-P1 BGNs

The proposed mechanism of incorporating P ions was based on two parameters: hydrolysis rate and stirring time. To confirm this mechanism, the synthesis of M2-P1 BGNs was performed, allowing a stirring time X_1 of 4, 8, 12, or 18 h. The SEM-EDS data was collected and compared to that obtained in BGNs stirred for X_1=24 h. The concentration of P_2O_5 in mol.% was calculated, and the averaged triplicate sample is summarized in **Figure S1**. It must be noted that EDS is a semi-quantitative approach for the determination of oxide concentration. Therefore, these results only served to guide the optimization of the stirring time X_1. An in-depth analysis of BGNs composition with additional techniques like ICP and APT is highly encouraged to determine the exact composition.

Longer stirring times allowed TEP to hydrolysis further, releasing P molecules in the solution to homogenize with SiO_2 tetrahedra. However, the nominal composition of M2-P1 BGNs was only achieved after 24 h. The trend observed confirmed the slow hydrolysis of TEP in methanol, and thus, extended stirring was required to hydrolyze the reagent fully.

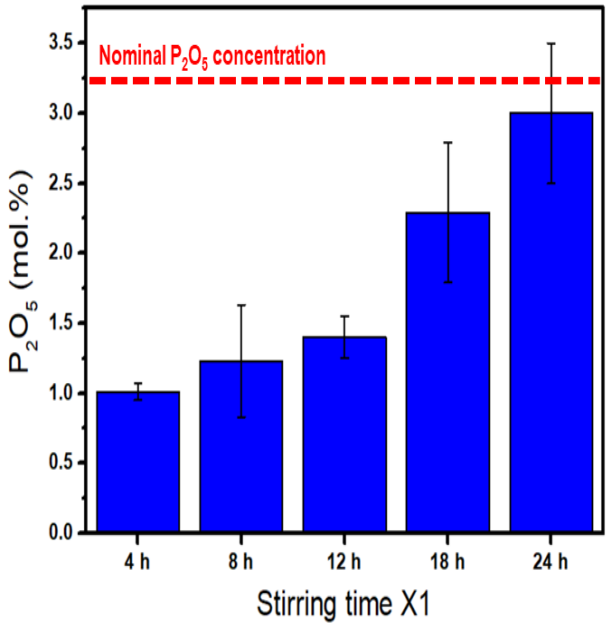

Figure S1: The concentration of P_2O_5 in M2-P1BGNs increased with the stirring time X_1 before particle nucleation. Hydrolysis of TEP was not completed until after 24 h. The concentration at each time point was obtained by semi-quantitative EDS analysis.

- Effect of stirring time X_3 in particle size and composition of M2-P1 BGNs

One-step basic catalyzed synthesis protocols have often described the effect of different stirring times X_3, collecting particles at different points after their nucleation. Specifically, extended stirring allowed the continuous and homogeneous growth of particles by the Ostwald ripening phenomenon. The protocol introduced in this work showed a neutralization of particle growth based on the stirring time after catalysis. In **Figure S2**, M2-P1 BGNs, collected after different stirring times, presented a similar particle size of about 90 nm. The elemental analysis confirmed the overall composition was maintained during the stirring time. Thus, the nominal composition was achieved prior to catalysis in the first nucleated BGNs, thanks to the previously extended homogenization of the solution. Note that the SEM images do not show monodispersed individual BGNs. This observation is considered an artifact of the imaging conditions, as the previous analysis performed and presented in section 4.5.1 showed clear individual spherical nanoparticles.

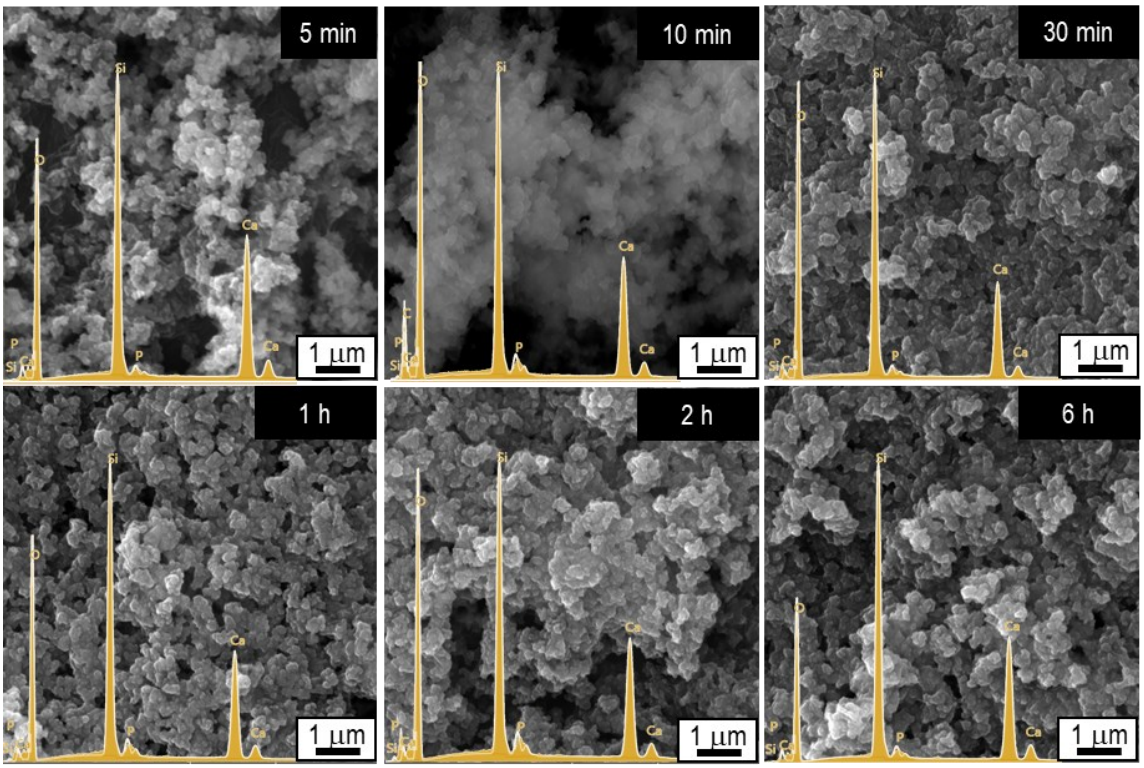

Figure S2: The incorporation of CaNT neutralized the effect of stirring time X_3 in particle growth before particle nucleation and the extended stirring. M2-P1 BGNs presented similar sizes and compositions at all collection times. The X_3 stirring times are indicated in the upper right corner of each picture. The EDS spectra are also presented in orange as an inset in the images.

APPENDIX B. Preliminary characterization of antibiotics effect in MRSA

The antibacterial capabilities of different antibiotics were explored before their use in combinatorial therapies with Ag-BG or Ag-BGNs. MRSA was exposed to oxacillin, fosfomycin, vancomycin, and ciprofloxacin (**Figure S3**), and gentamycin, tobramycin, erythromycin, and chloramphenicol (**Figure S4**). The results indicate MRSA resists oxacillin, fosfomycin, and erythromycin. Tolerance to antibiotic or reduced sensitivity due to experimental conditions was found for vancomycin, ciprofloxacin, and chloramphenicol in PBS, although MSA was sensitive to all in TSB. Finally, growth-arrested MRSA presents high sensitivity to gentamycin and tobramycin. The MICs for the antibiotic under each condition were summarized in **Table 6**.

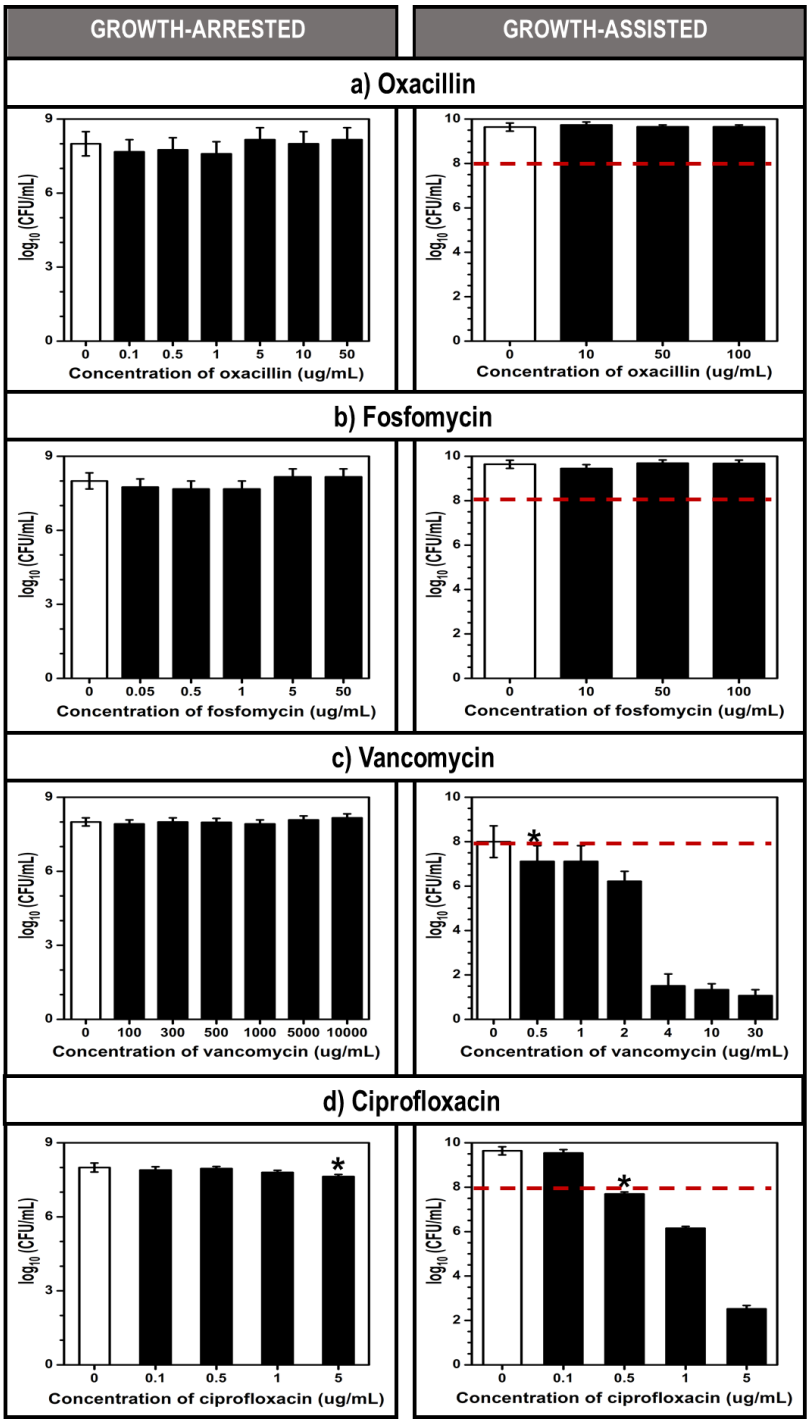

Figure S3: Basal activity of oxacillin (a), fosfomycin (b), vancomycin (c), and ciprofloxacin (d) under growth-arrested (PBS) and growth-assisted (TSB) conditions against MRSA. Suspensions of bacteria (OD_{600} = 1 equivalent to ~ 10^8 CFU/mL, dashed line) were mixed with fresh PBS or TSB medium (d-f) (0 mg/mL, untreated control represented by white bars) and increasing concentrations antibiotic (black bars). MRSA is resistant to fosfomycin and oxacillin and fosfomycin. MRSA tolerates vancomycin and presents reduced sensitivity to ciprofloxacin in PBS, but it is susceptible to both in TSB. The CFUs were enumerated after 24 h with a limit of detection of 100 CFU. (*) Indicates the MIC.

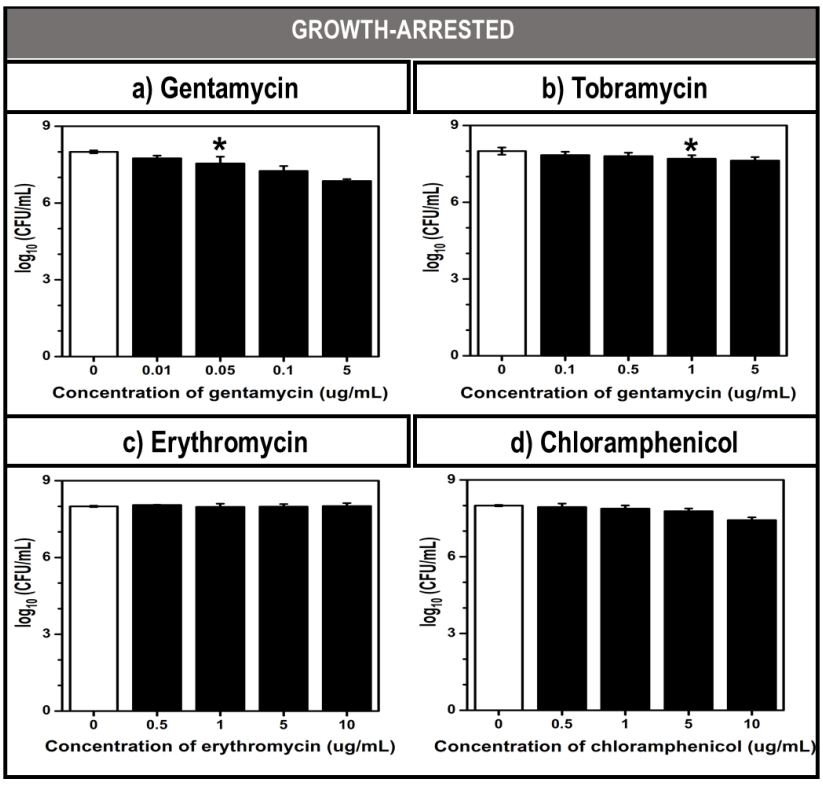

Figure S4: Basal activity of gentamycin (a), tobramycin (b), erythromycin (c), and chloramphenicol (d) against growth-arrested MRSA. Suspensions of bacteria (OD_{600} = 1 equivalent to ~ 10^8 CFU/mL, dashed line) were mixed with fresh PBS (0 mg/mL, untreated control represented by white bars) and increasing concentrations antibiotic (black bars).MRSA is sensitive to gentamycin and tobramycin and resists erythromycin. In growth-arrested conditions, MRSA tolerates chloramphenicol. The CFUs were enumerated after 24 h with a limit of detection of 100 CFU. (*) Indicates the MIC.

APPENDIX C. Characterization of small colony variants after several generations

The structure of MRSA after sequential Ag-BG treatment was studied in TEM to understand the evolution of the bacteria after generations (**Figure S5**). As described in **Figure 32**, colony type II had a similar 500 nm diameter size to WT while its cell-wall became thinner through generations. Treating G3-clone type I with Ag-BG still showed the affinity of bacteria to colonize particle surface and the presence of nano-size debris in the cells, preferent near the envelope. Clone type II showed thinning of the cell-wall and thickening at G3, forming multi-cellular clusters.

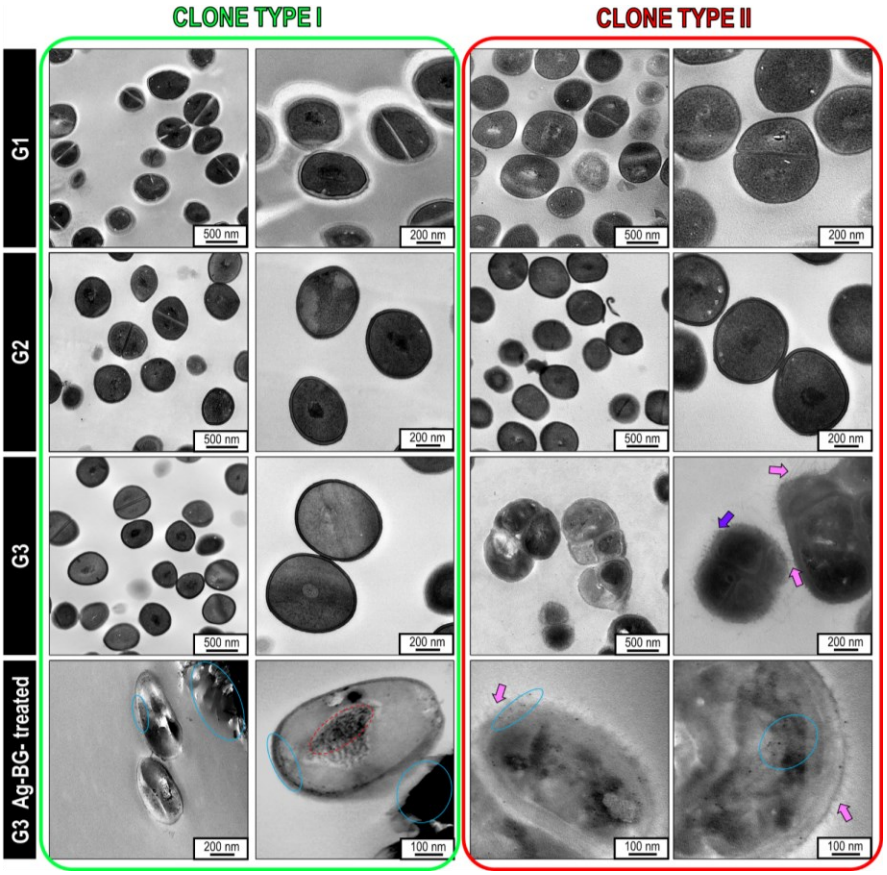

Figure S5: Structural features of MRSA phenotypes after sequential treatment with 2.5 mg/mL of Ag-BG in PBS for 24 h. Clone type I shows a cell-wall thickness below 40 nm and a bacterium diameter of 500 nm. Clone type II shows a similar cell-wall thickness to clone type I for G1 and G2 and suffered a significant thickening in G3. Clone type II at G3 forms multi-cellular clusters with surfaces crumbs and hair-like extension. Similar to the WT, the G3 clones appeared near Ag-BG microparticles (blue circles). Intracellular debris was found at the cytoplasm and near the cell-wall (blue circles), and around condensed DNA (dashed red circle).

Fibrils and crumbs around the surface of G3-clone type II appeared connecting bacteria units (**Figure S5**), supporting the hypothesis of increased adherence. SEM-EDS (**Figure S6**) demonstrate these features were organic and probably a result of increased protein concentration at the envelope.

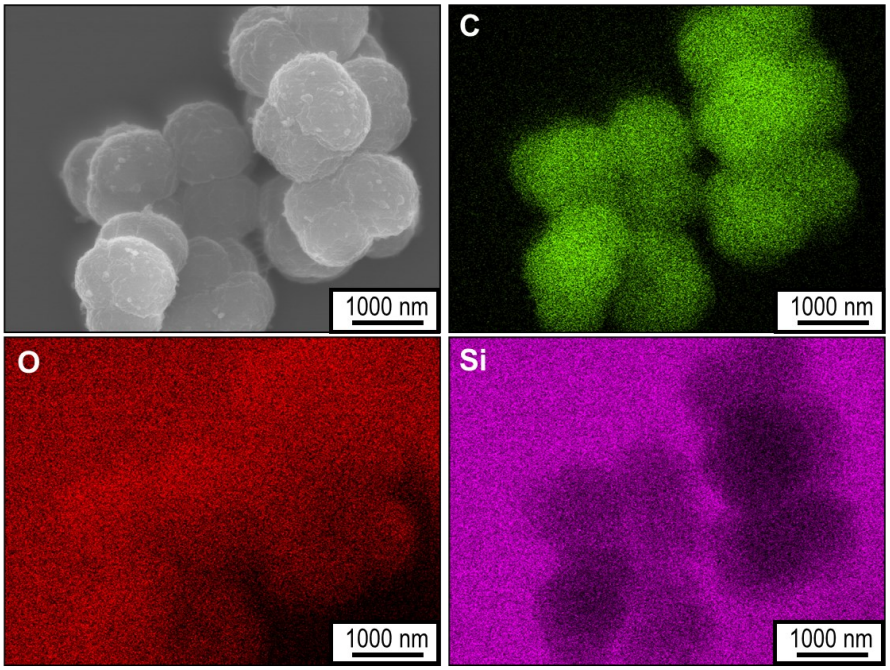

Figure S6: Crumb and fibrils in G3-clone type II contained high traces of carbon (C, green) and oxygen (O, red) in SEM-EDS maps, revealing their organic nature. Bacteria lacked silicon (Si, pink) content (the principal component of Ag-BG) which instead presented higher elemental contribution around them, indicating it belonged to the glass slides underneath. Samples were prepared following previously described methods with 15 s metallization in Os. The maps were collected at 15 keV as accelerating voltage.

APPENDIX D. Composition of Simulated Body Fluid

The formulation of SBF was developed by Kokubo *et al*. [228] for the *in vitro* evaluation of bioactivity in inorganic materials. SBF contains inorganic ions at a concentration that reproduces human blood plasma composition to mimic body conditions in a laboratory (**Table S1**).

Table S1: Composition of SBF in comparison to human blood plasma [228].

Ion	Concentration (mmol/dm^3)	
	SBF	**Human blood plasma**
Na^+	142.0	142.0
K^+	5.0	5.0
Mg^{2+}	1.5	1.5
Ca^{2+}	2.5	2.5
Cl^-	147.8	103.0
HCO_3^-	4.2	27.0
HPO_4^{2-}	1.0	1.0
SO_4^{2-}	0.5	0.5

BIBLIOGRAPHY

BIBLIOGRAPHY

[1] S. Mantero, A. Remuzzi, A. Ahluwalia, S. Mantero, Fondamenti di ingegneria dei tessuti per la medicina rigenerativa, Pàtron, 2009.

[2] J.R. Porter, T.T. Ruckh, K.C. Popat, Bone tissue engineering: A review in bone biomimetics and drug delivery strategies, Biotechnol. Prog. 25 (2009) NA-NA. doi:10.1002/btpr.246.

[3] E.S. Place, N.D. Evans, M.M. Stevens, Complexity in biomaterials for tissue engineering, Nat. Mater. (2009). doi:10.1038/nmat2441.

[4] M.M. Stevens, Biomaterials for bone tissue engineering, Mater. Today. 11 (2008) 18–25. doi:10.1016/S1369-7021(08)70086-5.

[5] J.M. Werier, Focus On Bone graft substitutes in oncology, paediatrics, and hip arthroplasty, J. Bone Jt. Surg. (2012).

[6] V. Miguez-Pacheco, L.L. Hench, A.R. Boccaccini, Bioactive glasses beyond bone and teeth: Emerging applications in contact with soft tissues, Acta Biomater. 13 (2015). doi:10.1016/j.actbio.2014.11.004.

[7] J.R. Jones, Reprint of: Review of bioactive glass: From Hench to hybrids, Acta Biomater. 23 (2015) S53–S82. doi:10.1016/j.actbio.2015.07.019.

[8] D.S. Brauer, Bioactive Glasses-Structure and Properties, Angew. Chemie Int. Ed. 54 (2015) 4160–4181. doi:10.1002/anie.201405310.

[9] A. Hoppe, N.S. Güldal, A.R. Boccaccini, A review of the biological response to ionic dissolution products from bioactive glasses and glass-ceramics, Biomaterials. 32 (2011) 2757–2774. doi:10.1016/J.BIOMATERIALS.2011.01.004.

[10] N.J. Lakhkar, I.H. Lee, H.W. Kim, V. Salih, I.B. Wall, J.C. Knowles, Bone formation controlled by biologically relevant inorganic ions: Role and controlled delivery from phosphate-based glasses, Adv. Drug Deliv. Rev. (2013). doi:10.1016/j.addr.2012.05.015.

[11] J.R. Morones-Ramirez, J.A. Winkler, C.S. Spina, J.J. Collins, Silver Enhances Antibiotic Activity Against Gram-Negative Bacteria, Sci. Transl. Med. 5 (2013) 190ra81-190ra81. doi:10.1126/SCITRANSLMED.3006276.

[12] Y. Wang, X. Ding, Y. Chen, M. Guo, Y. Zhang, X. Guo, H. Gu, Antibiotic-loaded, silver core-embedded mesoporous silica nanovehicles as a synergistic antibacterial agent for the treatment of drug-resistant infections, Biomaterials. 101 (2016) 207–216. doi:10.1016/J.BIOMATERIALS.2016.06.004.

[13] A.R. Shahverdi, A. Fakhimi, H.R. Shahverdi, S. Minaian, Synthesis and effect of silver nanoparticles on the antibacterial activity of different antibiotics against Staphylococcus aureus and Escherichia coli., Nanomedicine. 3 (2007) 168–71. doi:10.1016/j.nano.2007.02.001.

[14] X. Chatzistavrou, J.C. Fenno, D. Faulk, S. Badylak, T. Kasuga, A.R. Boccaccini, P. Papagerakis, Fabrication and characterization of bioactive and antibacterial composites for dental applications, Acta Biomater. 10 (2014) 3723–3732. doi:10.1016/j.actbio.2014.04.030.

[15] X. Chatzistavrou, K.M. Paraskevopoulos, V. Salih, A.R. Boccaccini, T. Kasuga, Ag-Doped Sol-Gel Derived Novel Composite Materials for Dental Applications, Key Eng. Mater. 493–494 (2011) 637–642. doi:10.4028/www.scientific.net/KEM.493-494.637.

[16] X. Chatzistavrou, E. Kontonasaki, A. Bakopoulou, A. Theocharidou, A. Sivropoulou, K.M. Paraskevopoulos, P. Koidis, A.R. Boccaccini, T. Kasuga, Development of new sol-gel derived Ag-doped biomaterials for dental applications, MRS Proc. 1417 (2012) mrsf11-1417-kk06-09. doi:10.1557/opl.2012.743.

[17] N. Pajares-Chamorro, J. Shook, N.D. Hammer, X. Chatzistavrou, Resurrection of antibiotics that methicillin-resistant Staphylococcus aureus resists by silver-doped bioactive glass-ceramic microparticles, Acta Biomater. 96 (2019) 537–546. doi:10.1016/J.ACTBIO.2019.07.012.

[18] R. Langer, Biomaterials in drug delivery and tissue engineering: One laboratory's experience, Acc. Chem. Res. 33 (2000) 94–101. doi:10.1021/ar9800993.

[19] K. Rezwan, Q.Z. Chen, J.J. Blaker, A.R. Boccaccini, Biodegradable and bioactive porous polymer/inorganic composite scaffolds for bone tissue engineering, Biomaterials. 27 (2006) 3413–3431. doi:10.1016/J.BIOMATERIALS.2006.01.039.

[20] C. Wang, H. Shen, Y. Tian, Y. Xie, A. Li, L. Ji, Z. Niu, D. Wu, D. Qiu, Bioactive nanoparticle-gelatin composite scaffold with mechanical performance comparable to cancellous bones, ACS Appl. Mater. Interfaces. (2014). doi:10.1021/am5029582.

[21] A. El-Fiqi, J.H. Lee, E.-J. Lee, H.-W. Kim, Collagen hydrogels incorporated with surface-aminated mesoporous nanobioactive glass: Improvement of physicochemical stability and mechanical properties is effective for hard tissue engineering, Acta Biomater. 9 (2013) 9508–9521. doi:10.1016/J.ACTBIO.2013.07.036.

[22] A. Liu, Z. Hong, X. Zhuang, X. Chen, Y. Cui, Y. Liu, X. Jing, Surface modification of bioactive glass nanoparticles and the mechanical and biological properties of poly(l-lactide) composites, Acta Biomater. 4 (2008) 1005–1015. doi:10.1016/j.actbio.2008.02.013.

[23] A.R. Boccaccini, M. Erol, W.J. Stark, D. Mohn, Z. Hong, J.F. Mano, Polymer/bioactive glass nanocomposites for biomedical applications: A review, Compos. Sci. Technol. 70

(2010) 1764–1776. doi:10.1016/j.compscitech.2010.06.002.

[24] I.A. Rahman, V. Padavettan, Synthesis of Silica nanoparticles by Sol-Gel: Size-dependent properties, surface modification, and applications in silica-polymer nanocompositesa review, J. Nanomater. (2012). doi:10.1155/2012/132424.

[25] C. Vichery, J.-M. Nedelec, Bioactive Glass Nanoparticles: From Synthesis to Materials Design for Biomedical Applications, Materials (Basel). 9 (2016) 288. doi:10.3390/ma9040288.

[26] M. Erol-Taygun, K. Zheng, A.R. Boccaccini, Nanoscale Bioactive Glasses in Medical Applications, Int. J. Appl. Glas. Sci. 4 (2013) 136–148. doi:10.1111/ijag.12029.

[27] V. Wagner, A. Dullaart, A.-K. Bock, A. Zweck, The emerging nanomedicine landscape, Nat. Biotechnol. (2006). doi:10.1038/nbt1006-1211.

[28] C. Vichery, J.-M. Nedelec, Bioactive Glass Nanoparticles: From Synthesis to Materials Design for Biomedical Applications, Materials (Basel). 9 (2016) 288. doi:10.3390/ma9040288.

[29] C. Vichery, J.-M. Nedelec, C. Vichery, J.-M. Nedelec, Bioactive Glass Nanoparticles: From Synthesis to Materials Design for Biomedical Applications, Materials (Basel). 9 (2016) 288. doi:10.3390/ma9040288.

[30] K. Zheng, A.R. Boccaccini, Sol-gel processing of bioactive glass nanoparticles: A review, Adv. Colloid Interface Sci. 249 (2017) 363–373. doi:10.1016/j.cis.2017.03.008.

[31] R. Larry, L. Hench, The story of Bioglass, J Mater Sci Mater Med. 17 (2006) 967–978. doi:10.1007/s10856-006-0432-z.

[32] L.L. Hench, R.J. Splinter, W.C. Allen, T.K. Greenlee, Bonding mechanisms at the interface of ceramic prosthetic materials, J. Biomed. Mater. Res. 5 (1971) 117–141. doi:10.1002/jbm.820050611.

[33] D.M. Sanders, L.L. Hench, Mechanisms of Glass Corrosion, J. Am. Ceram. Soc. 56 (1973) 373–377. doi:10.1111/j.1151-2916.1973.tb12689.x.

[34] D.S. Brauer, Bioactive Glasses-Structure and Properties, Angew. Chemie Int. Ed. 54 (2015) 4160–4181. doi:10.1002/anie.201405310.

[35] D.W. Kingery, H.K. Bowen, D.R. Uhlmann, Introduction to Ceramics, John Wiley & Sons, Ltd, 1976.

[36] J.S. Reed, Principles of Ceramics Processing Second Edition, John Wiley & Sons, Ltd, 1995.

[37] M.. Toplis, B. Reynard, Temperature and time-dependent changes of structure in phosphorus containing aluminosilicate liquids and glasses: in situ Raman spectroscopy at high temperature, J. Non. Cryst. Solids. 263–264 (2000) 123–131. doi:10.1016/S0022-3093(99)00628-6.

[38] B.O. Mysen, P. Richet, Silicate Glasses and Melts: Properties and Structure, Elsevier Sci. (2005).

[39] L.L. Hench, The story of Bioglass®, J. Mater. Sci. Mater. Med. 17 (2006) 967–978. doi:10.1007/s10856-006-0432-z.

[40] L.L. Hench, Bioceramics: From Concept to Clinic, J. Am. Ceram. Soc. (1991). doi:10.1111/j.1151-2916.1991.tb07132.x.

[41] Ö.H. Andersson, K.H. Karlsson, On the bioactivity of silicate glass, J. Non. Cryst. Solids. 129 (1991) 145–151. doi:10.1016/0022-3093(91)90090-S.

[42] K.E. Wallace, R.G. Hill, J.T. Pembroke, P. V Hatton, In¯uence of sodium oxide content on bioactive glass properties, n.d.

[43] S.M. Rabiee, N. Nazparvar, M. Azizian, D. Vashaee, L. Tayebi, Effect of ion substitution on properties of bioactive glasses: A review, Ceram. Int. 41 (2015) 7241–7251. doi:10.1016/J.CERAMINT.2015.02.140.

[44] G. Kaur, O.P. Pandey, K. Singh, D. Homa, B. Scott, G. Pickrell, A review of bioactive glasses: Their structure, properties, fabrication and apatite formation, J. Biomed. Mater. Res. - Part A. 102 (2014). doi:10.1002/jbm.a.34690.

[45] Málek, Svoboda, Kinetic Processes in Amorphous Materials Revealed by Thermal Analysis: Application to Glassy Selenium, Molecules. 24 (2019) 2725. doi:10.3390/molecules24152725.

[46] S. Janssens, G. Van den Mooter, Review: physical chemistry of solid dispersions, J. Pharm. Pharmacol. 61 (2009) 1571–1586. doi:10.1211/jpp.61.12.0001.

[47] O.P. Filho, G.P. La Torre, L.L. Hench, Effect of crystallization on apatite-layer formation of bioactive glass 45S5, J. Biomed. Mater. Res. 30 (1996) 509–514. doi:10.1002/(SICI)1097-4636(199604)30:4<509::AID-JBM9>3.0.CO;2-T.

[48] The effect of residual glassy phase in a bioactive glass-ceramic on the formation of its surface apatite layer in vitro, 1992.

[49] P. Sepulveda, J.R. Jones, L.L. Hench, Bioactive sol-gel foams for tissue repair, J. Biomed. Mater. Res. 59 (2002) 340–348. doi:10.1002/jbm.1250.

[50] T.J. Brunner, R.N. Grass, W.J. Stark, Glass and bioglass nanopowders by flame synthesis,

Chem. Commun. 0 (2006) 1384–1386. doi:10.1039/b517501a.

[51] W.J. Stark, S.E. Pratsinis, Aerosol flame reactors for manufacture of nanoparticles, Powder Technol. 126 (2002) 103–108. doi:10.1016/S0032-5910(02)00077-3.

[52] C.J. Brinker, G.W. Scherer, Sol-Gel Science: The Physics and Chemistry of Sol-Gel Processing, 2013. doi:10.1016/C2009-0-22386-5.

[53] R. Li, A.E. Clark, L.L. Hench, An investigation of bioactive glass powders by sol-gel processing, J. Appl. Biomater. 2 (1991) 231–239. doi:10.1002/jab.770020403.

[54] W. Stöber, A. Fink, E. Bohn, Controlled growth of monodisperse silica spheres in the micron size range, J. Colloid Interface Sci. 26 (1968) 62–69. doi:10.1016/0021-9797(68)90272-5.

[55] R.K. Iler, The Chemistry of Silica. Solubility, Polymerization, Colloid and Surface Properties, and Biochemistry., 1979. doi:10.1002/ange.19800920433.

[56] A. Lukowiak, J. Lao, J. Lacroix, J.-M. Nedelec, Bioactive glass nanoparticles obtained through sol–gel chemistry, Chem. Commun. 49 (2013) 6620. doi:10.1039/c3cc00003f.

[57] Q. Hu, Y. Li, G. Miao, N. Zhao, X. Chen, Size control and biological properties of monodispersed mesoporous bioactive glass sub-micron spheres, RSC Adv. 4 (2014) 22678–22687. doi:10.1039/C4RA01276C.

[58] M.M. Azevedo, G. Jell, M.D. O'Donnell, R. V. Law, R.G. Hill, M.M. Stevens, Synthesis and characterization of hypoxia-mimicking bioactive glasses for skeletal regeneration, J. Mater. Chem. (2010). doi:10.1039/c0jm01111h.

[59] L.L. Hench, J.K. West, The sol-gel process, Chem. Rev. (1990). doi:10.1021/cr00099a003.

[60] V.K. Lamer, R.H. Dinegar, Theory, Production and Mechanism of Formation of Monodispersed Hydrosols, J. Am. Chem. Soc. (1950). doi:10.1021/ja01167a001.

[61] G.H. Bogush, C.F. Zukoski IV, Uniform silica particle precipitation: An aggregative growth model, J. Colloid Interface Sci. 142 (1991) 19–34. doi:10.1016/0021-9797(91)90030-C.

[62] K. Lee, A.N. Sathyagal, A. V. McCormick, A closer look at an aggregation model of the Stober process, Colloids Surfaces A Physicochem. Eng. Asp. (1998). doi:10.1016/S0927-7757(98)00566-4.

[63] G.H. Bogush, C.F. Zukoski IV, Studies of the kinetics of the precipitation of uniform silica particles through the hydrolysis and condensation of silicon alkoxides, J. Colloid Interface Sci. 142 (1991) 1–18. doi:10.1016/0021-9797(91)90029-8.

[64] R. Mohler, Encyclopedia of physical science and technology, Press, New York, 2003.

[65] P.J. Feeney, D.H. Napper, R.G. Gilbert, Coagulative Nucleation and Particle Size Distributions in Emulsion Polymerization, 1984.

[66] M.T. Harris, R.R. Brunson, C.H. Byers, The base-catalyzed hydrolysis and condensation reactions of dilute and concentrated TEOS solutions, J. Non. Cryst. Solids. 121 (1990) 397–403. doi:10.1016/0022-3093(90)90165-I.

[67] A.K. Van Helden, J.W. Jansen, A. Vrij, Preparation and characterization of spherical monodisperse silica dispersions in nonaqueous solvents, J. Colloid Interface Sci. (1981). doi:10.1016/0021-9797(81)90417-3.

[68] D.. Green, J.. Lin, Y.-F. Lam, M.Z.-C. Hu, D.W. Schaefer, M.. Harris, Size, volume fraction, and nucleation of Stober silica nanoparticles, J. Colloid Interface Sci. 266 (2003) 346–358. doi:10.1016/S0021-9797(03)00610-6.

[69] A. Van Blaaderen, J. Van Geest, A. Vrij, Monodisperse colloidal silica spheres from tetraalkoxysilanes: Particle formation and growth mechanism, J. Colloid Interface Sci. 154 (1992) 481–501. doi:10.1016/0021-9797(92)90163-G.

[70] O. Tsigkou, S. Labbaf, M.M. Stevens, A.E. Porter, J.R. Jones, Monodispersed Bioactive Glass Submicron Particles and Their Effect on Bone Marrow and Adipose Tissue-Derived Stem Cells, Adv. Healthc. Mater. 3 (2014) 115–125. doi:10.1002/adhm.201300126.

[71] K. Zheng, N. Taccardi, A.M. Beltrán, B. Sui, T. Zhou, V.R.R. Marthala, M. Hartmann, A.R. Boccaccini, Timing of calcium nitrate addition affects morphology, dispersity and composition of bioactive glass nanoparticles, RSC Adv. 6 (2016) 95101–95111. doi:10.1039/C6RA05548F.

[72] S.L. Greasley, S.J. Page, S. Sirovica, S. Chen, R.A. Martin, A. Riveiro, J. V. Hanna, A.E. Porter, J.R. Jones, Controlling particle size in the Stöber process and incorporation of calcium, J. Colloid Interface Sci. 469 (2016) 213–223. doi:10.1016/J.JCIS.2016.01.065.

[73] S. Labbaf, O. Tsigkou, K.H. Müller, M.M. Stevens, A.E. Porter, J.R. Jones, Spherical bioactive glass particles and their interaction with human mesenchymal stem cells in vitro, Biomaterials. 32 (2011) 1010–1018. doi:10.1016/j.biomaterials.2010.08.082.

[74] K. Zheng, N. Taccardi, A.M. Beltrán, B. Sui, T. Zhou, V.R.R. Marthala, M. Hartmann, A.R. Boccaccini, Timing of calcium nitrate addition affects morphology, dispersity and composition of bioactive glass nanoparticles, RSC Adv. 6 (2016) 95101–95111. doi:10.1039/C6RA05548F.

[75] S. Lin, C. Ionescu, K.J. Pike, M.E. Smith, J.R. Jones, Nanostructure evolution and calcium distribution in sol–gel derived bioactive glass, J. Mater. Chem. 19 (2009) 1276. doi:10.1039/b814292k.

[76] A.-C.J.H. Johnson, P. Greenwood, M. Hagström, Z. Abbas, S. Wall, Aggregation of

Nanosized Colloidal Silica in the Presence of Various Alkali Cations Investigated by the Electrospray Technique, Langmuir. 24 (2008) 12798–12806. doi:10.1021/la8026122.

[77] X. Kesse, C. Vichery, A. Jacobs, S. Descamps, J.-M. Nedelec, Unravelling the Impact of Calcium Content on the Bioactivity of Sol–Gel-Derived Bioactive Glass Nanoparticles, ACS Appl. Bio Mater. 3 (2020) 1312–1320. doi:10.1021/acsabm.0c00036.

[78] B. Yu, C.A. Turdean-Ionescu, R.A. Martin, R.J. Newport, J. V. Hanna, M.E. Smith, J.R. Jones, Effect of calcium source on structure and properties of sol-gel derived bioactive glasses, Langmuir. 28 (2012) 17465–17476. doi:10.1021/la303768b.

[79] G. Poologasundarampillai, J.R. Jones, B. Yu, G. Poologasundarampillai, C. Turdean-Ionescu, M.E. Smith, J.R. Jones, A New Calcium Source for Bioactive Sol-Gel Hybrids Organic-inorganic hybrids View project A New Calcium Source for Bioactive Sol-Gel Hybrids, Bioceram. Dev. Appl. 1 (2011). doi:10.4303/bda/D110178.

[80] A. Kozon, D., Zheng, K., Boccardi, E., Liu, Y., Liverani, L., & Boccaccini, Synthesis of Monodispersed Ag-Doped Bioactive Glass Nanoparticles via Surface Modification, Materials (Basel). 9 (2016) 225–233. doi:10.3390/ma9040225.

[81] P. Naruphontjirakul, S.L. Greasley, S. Chen, A.E. Porter, J.R. Jones, Monodispersed strontium containing bioactive glass nanoparticles and MC3T3-E1 cellular response, in: Biomed. Glas., Walter de Gruyter GmbH, 2016: pp. 72–81. doi:10.1515/bglass-2016-0009.

[82] Q. Liang, Q. Hu, G. Miao, B. Yuan, X. Chen, A facile synthesis of novel mesoporous bioactive glass nanoparticles with various morphologies and tunable mesostructure by sacrificial liquid template method, Mater. Lett. 148 (2015) 45–49. doi:10.1016/j.matlet.2015.01.122.

[83] Y. Li, B.P. Bastakoti, Y. Yamauchi, Smart Soft-Templating Synthesis of Hollow Mesoporous Bioactive Glass Spheres, Chem.-A Eur. J. (2015) 8038–42.

[84] Y. Li, X. Chen, C. Ning, B. Yuan, Q. Hu, Facile synthesis of mesoporous bioactive glasses with controlled shapes, Mater. Lett. 161 (2015) 605–608. doi:10.1016/j.matlet.2015.09.057.

[85] M. Gaumet, A. Vargas, R. Gurny, F. Delie, Nanoparticles for drug delivery: The need for precision in reporting particle size parameters, Eur. J. Pharm. Biopharm. 69 (2008) 1–9. doi:10.1016/j.ejpb.2007.08.001.

[86] S.Y. Fu, X.Q. Feng, B. Lauke, Y.W. Mai, Effects of particle size, particle/matrix interface adhesion and particle loading on mechanical properties of particulate-polymer composites, Compos. Part B Eng. 39 (2008) 933–961. doi:10.1016/j.compositesb.2008.01.002.

[87] G.H. Bogush, M.A. Tracy, C.F. Zukoski IV, Preparation of monodisperse silica particles: Control of size and mass fraction, J. Non. Cryst. Solids. (1988). doi:10.1016/0022-3093(88)90187-1.

[88] K.S. Rao, K. El-Hami, T. Kodaki, K. Matsushige, K. Makino, A novel method for synthesis of silica nanoparticles, J. Colloid Interface Sci. 289 (2005) 125–131. doi:10.1016/J.JCIS.2005.02.019.

[89] S.K. Park, K. Do Kim, H.T. Kim, Preparation of silica nanoparticles: Determination of the optimal synthesis conditions for small and uniform particles, Colloids Surfaces A Physicochem. Eng. Asp. (2002). doi:10.1016/S0927-7757(01)00683-5.

[90] O. Tsigkou, S. Labbaf, M.M. Stevens, A.E. Porter, J.R. Jones, Monodispersed Bioactive Glass Submicron Particles and Their Effect on Bone Marrow and Adipose Tissue-Derived Stem Cells, Adv. Healthc. Mater. 3 (2014) 115–125. doi:10.1002/adhm.201300126.

[91] R. Zerrouk, A. Foissy, R. Mercier, Y. Chevallier, J.C. Morawski, Study of Ca2+-induced silica coagulation by small angle scattering, J. Colloid Interface Sci. 139 (1990) 20–29. doi:10.1016/0021-9797(90)90441-P.

[92] G.M. Luz, J.F. Mano, Nanoengineering of bioactive glasses: Hollow and dense nanospheres, J. Nanoparticle Res. 15 (2013) 1–11. doi:10.1007/s11051-013-1457-0.

[93] A. Hoppe, N.S. Güldal, A.R. Boccaccini, A review of the biological response to ionic dissolution products from bioactive glasses and glass-ceramics, Biomaterials. 32 (2011) 2757–2774. doi:10.1016/j.biomaterials.2011.01.004.

[94] O. Peitl, E. Dutra Zanotto, L.L. Hench, Highly bioactive P2O5–Na2O–CaO–SiO2 glass-ceramics, J. Non. Cryst. Solids. 292 (2001) 115–126. doi:10.1016/S0022-3093(01)00822-5.

[95] M. Montazerian, E. Dutra Zanotto, History and trends of bioactive glass-ceramics, J. Biomed. Mater. Res. Part A. 104 (2016) 1231–1249. doi:10.1002/jbm.a.35639.

[96] P. Habibovic, J.E. Barralet, Bioinorganics and biomaterials: Bone repair, Acta Biomater. 7 (2011) 3013–3026. doi:10.1016/j.actbio.2011.03.027.

[97] J.C. Elliott, R.M. Wilson, S.E.P. Dowker, Apatite structures, Int. Cent. Diffr. Data. (2002). doi:10.4028/www.scientific.net/MSF.278-281.151.

[98] J.R. Jones, P. Sepulveda, L.L. Hench, Dose-dependent behavior of bioactive glass dissolution, J. Biomed. Mater. Res. 58 (2001) 720–726. doi:10.1002/jbm.10053.

[99] J.-Y. Sun, Y.-S. Yang, J. Zhong, D.C. Greenspan, The effect of the ionic products of Bioglass® dissolution on human osteoblasts growth cyclein vitro, J. Tissue Eng. Regen. Med. 1 (2007) 281–286. doi:10.1002/term.34.

[100] M. Cerruti, D. Greenspan, K. Powers, Effect of pH and ionic strength on the reactivity of Bioglass® 45S5, Biomaterials. 26 (2005) 1665–1674. doi:10.1016/J.BIOMATERIALS.2004.07.009.

[101] J.-Y. Sun, Y.-S. Yang, J. Zhong, D.C. Greenspan, The effect of the ionic products of Bioglass® dissolution on human osteoblasts growth cyclein vitro, J. Tissue Eng. Regen. Med. 1 (2007) 281–286. doi:10.1002/term.34.

[102] L.L. Hench, I.D. Xynos, J.M. Polak, Bioactive glasses for in situ tissue regeneration, J. Biomater. Sci. Polym. Ed. 15 (2004) 543–562. doi:10.1163/156856204323005352.

[103] C. Wu, W. Fan, J. Chang, Functional mesoporous bioactive glass nanospheres: Synthesis, high loading efficiency, controllable delivery of doxorubicin and inhibitory effect on bone cancer cells, J. Mater. Chem. B. 1 (2013) 2710–2718. doi:10.1039/c3tb20275e.

[104] T. Waltimo, T.J. Brunner, M. Vollenweider, W.J. Stark, M. Zehnder, Antimicrobial effect of nanometric bioactive glass 45S5., J. Dent. Res. 86 (2007) 754–757. doi:10.1177/154405910708600813.

[105] T.H. Chung, S.H. Wu, M. Yao, C.W. Lu, Y.S. Lin, Y. Hung, C.Y. Mou, Y.C. Chen, D.M. Huang, The effect of surface charge on the uptake and biological function of mesoporous silica nanoparticles in 3T3-L1 cells and human mesenchymal stem cells, Biomaterials. (2007). doi:10.1016/j.biomaterials.2007.03.006.

[106] D. Napierska, L.C.J. Thomassen, V. Rabolli, D. Lison, L. Gonzalez, M. Kirsch-Volders, J.A. Martens, P.H. Hoet, Size-Dependent Cytotoxicity of Monodisperse Silica Nanoparticles in Human Endothelial Cells, Small. 5 (2009) 846–853. doi:10.1002/smll.200800461.

[107] N. Lewinski, V. Colvin, R. Drezek, Cytotoxicity of Nanoparticles, Small. 4 (2008) 26–49. doi:10.1002/smll.200700595.

[108] Q. He, Z. Zhang, Y. Gao, J. Shi, Y. Li, Intracellular Localization and Cytotoxicity of Spherical Mesoporous Silica Nano- and Microparticles, Small. 5 (2009) 2722–2729. doi:10.1002/smll.200900923.

[109] M.C. Garnett, P. Kallinteri, Nanomedicines and nanotoxicology: some physiological principles, Occup. Med. (Chic. Ill). 56 (2006) 307–311. doi:10.1093/occmed/kql052.

[110] M. Cho, W.S. Cho, M. Choi, S.J. Kim, B.S. Han, S.H. Kim, H.O. Kim, Y.Y. Sheen, J. Jeong, The impact of size on tissue distribution and elimination by single intravenous injection of silica nanoparticles, Toxicol. Lett. 189 (2009) 177–183. doi:10.1016/j.toxlet.2009.04.017.

[111] K. Hirota, H. Ter, Endocytosis of Particle Formulations by Macrophages and Its Application to Clinical Treatment, in: Mol. Regul. Endocytosis, InTech, 2012. doi:10.5772/45820.

[112] S.J. Soenen, B. Manshian, S.H. Doak, S.C. De Smedt, K. Braeckmans, Fluorescent non-porous silica nanoparticles for long-term cell monitoring: Cytotoxicity and particle functionality, Acta Biomater. 9 (2013) 9183–9193. doi:10.1016/j.actbio.2013.04.026.

[113] J. Ajita, S. Saravanan, N. Selvamurugan, Effect of size of bioactive glass nanoparticles on mesenchymal stem cell proliferation for dental and orthopedic applications, Mater. Sci. Eng. C. 53 (2015) 142–149. doi:10.1016/j.msec.2015.04.041.

[114] R. Detsch, M. Rübner, P.L. Strissel, D. Mohn, E. Strasser, W.J. Stark, R. Strick, A.R. Boccaccini, Nanoscale bioactive glass activates osteoclastic differentiation of RAW 264.7 cells, Nanomedicine. 11 (2016) 1093–1105. doi:10.2217/nnm.16.20.

[115] L.L. Hench, Adhesion to bone, Biocompat. Orthop. Implant. (1982) 129–170.

[116] C.A. Shapoff, D.C. Alexander, A.E. Clark, Clinical use of a bioactive glass particulate in the treatment of human osseous defects., Compend. Contin. Educ. Dent. 18 (1997) 352–4, 356, 358 passim.

[117] T.B. Lovelace, J.T. Mellonig, R.M. Meffert, A.A. Jones, P. V. Nummikoski, D.L. Cochran, Clinical Evaluation of Bioactive Glass in the Treatment of Periodontal Osseous Defects in Humans, J. Periodontol. 69 (1998) 1027–1035. doi:10.1902/jop.1998.69.9.1027.

[118] L.L. Hench, Bioceramics: From Concept to Clinic, (1991).

[119] I.D. Xynos, A.J. Edgar, L.D.K. Buttery, L.L. Hench, J.M. Polak, Ionic Products of Bioactive Glass Dissolution Increase Proliferation of Human Osteoblasts and Induce Insulin-like Growth Factor II mRNA Expression and Protein Synthesis, Biochem. Biophys. Res. Commun. 276 (2000) 461–465. doi:10.1006/bbrc.2000.3503.

[120] J. Wilson, S.B. Low, Bioactive ceramics for periodontal treatment: Comparative studies in the patus monkey, J. Appl. Biomater. 3 (1992) 123–129. doi:10.1002/jab.770030208.

[121] W. Zhai, H. Lu, L. Chen, X. Lin, Y. Huang, K. Dai, K. Naoki, G. Chen, J. Chang, Silicate bioceramics induce angiogenesis during bone regeneration, Acta Biomater. 8 (2012) 341–349. doi:10.1016/j.actbio.2011.09.008.

[122] L.C. Gerhardt, K.L. Widdows, M.M. Erol, C.W. Burch, J.A. Sanz-Herrera, I. Ochoa, R. Stämpfli, I.S. Roqan, S. Gabe, T. Ansari, A.R. Boccaccini, The pro-angiogenic properties of multi-functional bioactive glass composite scaffolds, Biomaterials. 32 (2011) 4096–4108. doi:10.1016/j.biomaterials.2011.02.032.

[123] A. Hoppe, N.S. Güldal, A.R. Boccaccini, A review of the biological response to ionic dissolution products from bioactive glasses and glass-ceramics, Biomaterials. 32 (2011) 2757–2774. doi:10.1016/J.BIOMATERIALS.2011.01.004.

[124] A. Leu, S.M. Stieger, P. Dayton, K.W. Ferrara, J.K. Leach, Angiogenic response to bioactive glass promotes bone healing in an irradiated calvarial defect, Tissue Eng. - Part A. 15 (2009) 877–885. doi:10.1089/ten.tea.2008.0018.

[125] S.J. Froum, M.A. Weinberg, D. Tarnow, Comparison of Bioactive Glass Synthetic Bone

Graft Particles and Open Debridement in the Treatment of Human Periodontal Defects. A Clinical Study, n.d.

[126] S.K. Nandi, A. Mahato, B. Kundu, P. Mukherjee, Doped Bioactive Glass Materials in Bone Regeneration, in: Adv. Tech. Bone Regen., 2016. doi:10.5772/63266.

[127] M. Rahmati, M. Mozafari, Selective Contribution of Bioactive Glasses to Molecular and Cellular Pathways, ACS Biomater. Sci. Eng. (2020). doi:10.1021/acsbiomaterials.8b01078.

[128] A.A. El-Rashidy, G. Waly, A. Gad, A.A. Hashem, P. Balasubramanian, S. Kaya, A.R. Boccaccini, I. Sami, Preparation and in vitro characterization of silver-doped bioactive glass nanoparticles fabricated using a sol-gel process and modified Stöber method, J. Non. Cryst. Solids. 483 (2018) 26–36. doi:10.1016/j.jnoncrysol.2017.12.044.

[129] N. Gargiulo, A.M. Cusano, F. Causa, D. Caputo, P.A. Netti, Silver-containing mesoporous bioactive glass with improved antibacterial properties, J. Mater. Sci. Mater. Med. 24 (2013) 2129–2135. doi:10.1007/s10856-013-4968-4.

[130] M. Diba, A.R. Boccaccini, Silver-containing bioactive glasses for tissue engineering applications, in: Precious Met. Biomed. Appl., 2014. doi:10.1533/9780857099051.2.177.

[131] M. Mozafari, F. Moztarzadeh, Silver-doped bioactive glasses: What remains unanswered?, InterCeram Int. Ceram. Rev. (2013).

[132] J.C. Aurégan, T. Bégué, Bioactive glass for long bone infection: A systematic review, Injury. 46 (2015) S3–S7. doi:10.1016/S0020-1383(15)30048-6.

[133] I. Allan, H. Newman, M. Wilson, Antibacterial activity of particulate Bioglass® against supra- and subgingival bacteria, Biomaterials. 22 (2001) 1683–1687. doi:10.1016/S0142-9612(00)00330-6.

[134] D. Zhang, O. Leppäranta, E. Munukka, H. Ylänen, M.K. Viljanen, E. Eerola, M. Hupa, L. Hupa, Antibacterial effects and dissolution behavior of six bioactive glasses, J. Biomed. Mater. Res. Part A. 9999A (2009) NA-NA. doi:10.1002/jbm.a.32564.

[135] M. Vaahtio, E. Munukka, O. Leppäranta, D. Zhang, E. Eerola, H.O. Ylänen, T. Peltola, Effect of Ion Release on Antibacterial Activity of Melt-Derived and Sol-Gel-Derived Reactive Ceramics, Key Eng. Mater. 309–311 (2006) 349–354. doi:10.4028/www.scientific.net/kem.309-311.349.

[136] A.A. Ahmed, A.A. Ali, D.A.R. Mahmoud, A.M. El-Fiqi, Preparation and characterization of antibacterial P2O5-CaO-Na2O-Ag2O glasses, J. Biomed. Mater. Res. Part A. 98A (2011) 132–142. doi:10.1002/jbm.a.33101.

[137] D. Batalu, A.M. Stanciuc, L. Moldovan, G. Aldica, P. Badica, Evaluation of pristine and Eu2O3-added MgB 2 ceramics for medical applications: Hardness, corrosion resistance,

cytotoxicity and antibacterial activity, Mater. Sci. Eng. C. 42 (2014) 350–361. doi:10.1016/j.msec.2014.05.046.

[138] M. Zehnder, T. Waltimo, B. Sener, E. Söderling, Dentin enhances the effectiveness of bioactive glass S53P4 against a strain of Enterococcus faecalis, Oral Surgery, Oral Med. Oral Pathol. Oral Radiol. Endodontology. 101 (2006) 530–535. doi:10.1016/j.tripleo.2005.03.014.

[139] J.S. Moya, B. Cabal, J. Sanz, A.C. Da Silva, S. Mello-Castanho, R. Torrecillas, F. Rojo, Mechanism of calcium lixiviation in soda-lime glasses with a strong biocide activity, Mater. Lett. 70 (2012) 113–115. doi:10.1016/j.matlet.2011.11.104.

[140] A.A. Ahmed, A.A. Ali, D.A.R. Mahmoud, A.M. El-Fiqi, Preparation and characterization of antibacterial P 2O 5-CaO-Na 2O-Ag 2O glasses, J. Biomed. Mater. Res. - Part A. 98 A (2011) 132–142. doi:10.1002/jbm.a.33101.

[141] V. Mortazavi, M. Mehdikhani Nahrkhalaji, M.H. Fathi, S.B. Mousavi, B. Nasr Esfahani, Antibacterial effects of sol-gel-derived bioactive glass nanoparticle on aerobic bacteria, J. Biomed. Mater. Res. - Part A. 94 (2010) 160–168. doi:10.1002/jbm.a.32678.

[142] M. Gubler, T.J. Brunner, M. Zehnder, T. Waltimo, B. Sener, W.J. Stark, Do bioactive glasses convey a disinfecting mechanism beyond a mere increase in pH?, Int. Endod. J. 41 (2008) 670–678. doi:10.1111/j.1365-2591.2008.01413.x.

[143] A.S. Bakry, Y. Tamura, M. Otsuki, S. Kasugai, K. Ohya, J. Tagami, Cytotoxicity of 45S5 bioglass paste used for dentine hypersensitivity treatment, J. Dent. 39 (2011) 599–603. doi:10.1016/j.jdent.2011.06.003.

[144] Y.N. Slavin, J. Asnis, U.O. Häfeli, H. Bach, Metal nanoparticles: Understanding the mechanisms behind antibacterial activity, J. Nanobiotechnology. 15 (2017) 65. doi:10.1186/s12951-017-0308-z.

[145] A. Shrestha, A. Kishen, Antibacterial Nanoparticles in Endodontics: A??Review, J. Endod. 42 (2016) 1417–1426. doi:10.1016/j.joen.2016.05.021.

[146] A.C. Marsh, N.P. Chamorro, X. Chatzistavrou, Long-term performance and failure of orthopedic devices, Bone Repair Biomater. (2019) 379–410. doi:10.1016/B978-0-08-102451-5.00015-9.

[147] S. Chernousova, M. Epple, Silver as antibacterial agent: Ion, nanoparticle, and metal, Angew. Chemie - Int. Ed. 52 (2013) 1636–1653. doi:10.1002/anie.201205923.

[148] Z. Lu, K. Rong, J. Li, H. Yang, R. Chen, Size-dependent antibacterial activities of silver nanoparticles against oral anaerobic pathogenic bacteria, J. Mater. Sci. Mater. Med. 24 (2013) 1465–1471. doi:10.1007/s10856-013-4894-5.

[149] J.P. Ruparelia, A.K. Chatterjee, S.P. Duttagupta, S. Mukherji, Strain specificity in antimicrobial activity of silver and copper nanoparticles, Acta Biomater. 4 (2008) 707–716. doi:10.1016/j.actbio.2007.11.006.

[150] K.Y. Yoon, J. Hoon Byeon, J.H. Park, J. Hwang, Susceptibility constants of Escherichia coli and Bacillus subtilis to silver and copper nanoparticles, Sci. Total Environ. 373 (2007) 572–575. doi:10.1016/j.scitotenv.2006.11.007.

[151] G. Borkow, J. Gabbay, Copper as a Biocidal Tool, Curr. Med. Chem. 12 (2005) 2163–2175. doi:10.2174/0929867054637617.

[152] M. Rai, A. Yadav, A. Gade, Silver nanoparticles as a new generation of antimicrobials, Biotechnol. Adv. 27 (2009) 76–83. doi:10.1016/j.biotechadv.2008.09.002.

[153] J.L. Clement, P.S. Jarrett, Antibacterial Silver, Met. Based. Drugs. 1 (1994) 467–482. doi:10.1155/MBD.1994.467.

[154] K.D. Rosenman, A. Moss, S. Kon, Argyria: clinical implications of exposure to silver nitrate and silver oxide, J Occup Med. 21 (1979) 430–435.

[155] M. Bellantone, N.J. Coleman, L.L. Hench, Bacteriostatic action of a novel four-component bioactive glass, J. Biomed. Mater. Res. 51 (2000) 484–490. doi:10.1002/1097-4636(20000905)51:3<484::AID-JBM24>3.0.CO;2-4.

[156] M. Bellantone, H.D. Williams, L.L. Hench, B.B. Activity, Broad-Spectrum Bactericidal Activity of Ag 2 O-Doped Bioactive Glass Broad-Spectrum Bactericidal Activity of Ag 2 O-Doped Bioactive Glass, Antimicrob. Agents Chemother. 46 (2002) 1940–1945. doi:10.1128/AAC.46.6.1940.

[157] P. Saravanapavan, J.E. Gough, J.R. Jones, L.L. Hench, Antimicrobial Macroporous Gel-Glasses: Dissolution and Cytotoxicity, Key Eng. Mater. 254–256 (2004) 1087–1090. doi:10.4028/www.scientific.net/KEM.254-256.1087.

[158] J.J. Blaker, S.N. Nazhat, A.R. Boccaccini, Development and characterisation of silver-doped bioactive glass-coated sutures for tissue engineering and wound healing applications, Biomaterials. (2004). doi:10.1016/j.biomaterials.2003.08.007.

[159] A. Balamurugan, G. Balossier, D. Laurent-Maquin, S. Pina, A.H.S. Rebelo, J. Faure, J.M.F. Ferreira, An in vitro biological and anti-bacterial study on a sol-gel derived silver-incorporated bioglass system, Dent. Mater. 24 (2008) 1343–1351. doi:10.1016/j.dental.2008.02.015.

[160] N. Nezafati, F. Moztarzadeh, S. Hesaraki, M. Mozafari, A. Samadikuchaksaraei, L. Hajibaki, M. Gholipour, Effect of silver concentration on bioactivity and antibacterial properties of SiO2-CaO-P2O5 sol-gel derived bioactive glass, in: Key Eng. Mater., Trans Tech Publications Ltd, 2012: pp. 74–79. doi:10.4028/www.scientific.net/KEM.493-494.74.

[161] H. Palza, B. Escobar, J. Bejarano, D. Bravo, M. Diaz-Dosque, J. Perez, Designing antimicrobial bioactive glass materials with embedded metal ions synthesized by the sol-gel method, Mater. Sci. Eng. C. 33 (2013) 3795–3801. doi:10.1016/j.msec.2013.05.012.

[162] J. Pratten, S.N. Nazhat, J.J. Blaker, A.R. Boccaccini, In vitro attachment of staphylococcus epidermidis to surgical sutures with and without Ag-containing bioactive glass coating, J. Biomater. Appl. 19 (2004) 47–57. doi:10.1177/0885328204043200.

[163] X. Chatzistavrou, J.C. Fenno, D. Faulk, S. Badylak, T. Kasuga, A.R. Boccaccini, P. Papagerakis, Fabrication and characterization of bioactive and antibacterial composites for dental applications, Acta Biomater. 10 (2014) 3723–3732. doi:10.1016/J.ACTBIO.2014.04.030.

[164] J. Hum, A.R. Boccaccini, Bioactive glasses as carriers for bioactive molecules and therapeutic drugs: A review, in: J. Mater. Sci. Mater. Med., 2012. doi:10.1007/s10856-012-4580-z.

[165] J.R.J. Delben, O.M. Pimentel, M.B. Coelho, P.D. Candelorio, L.N. Furini, F. Alencar Dos Santos, F.S. De Vicente, A.A.S.T. Delben, Synthesis and thermal properties of nanoparticles of bioactive glasses containing silver, J. Therm. Anal. Calorim. 97 (2009) 433–436. doi:10.1007/s10973-009-0086-4.

[166] V. Simon, C. Albon, S. Simon, Silver release from hydroxyapatite self-assembling calcium-phosphate glasses, J. Non. Cryst. Solids. 354 (2008) 1751–1755. doi:10.1016/j.jnoncrysol.2007.08.063.

[167] A. Vulpoi, L. Baia, S. Simon, V. Simon, Silver effect on the structure of SiO 2-CaO-P 2O 5 ternary system, Mater. Sci. Eng. C. 32 (2012) 178–183. doi:10.1016/j.msec.2011.10.015.

[168] P. Saravanapavan, M.H. Patel, L.L. Hench, Effect of composition and texture on controlled rate of release of an antibacterial agent from bioactive gel-glasses, in: Key Eng. Mater., Trans Tech Publications Ltd, 2003: pp. 233–236. doi:10.4028/www.scientific.net/kem.240-242.233.

[169] A.M. El-Kady, A.F. Ali, R.A. Rizk, M.M. Ahmed, Synthesis, characterization and microbiological response of silver doped bioactive glass nanoparticles, Ceram. Int. 38 (2012) 177–188. doi:10.1016/j.ceramint.2011.05.158.

[170] A.R.M. Coates, Y. Hu, J. Holt, P. Yeh, Antibiotic combination therapy against resistant bacterial infections: synergy, rejuvenation and resistance reduction, Expert Rev. Anti. Infect. Ther. 18 (2020) 5–15. doi:10.1080/14787210.2020.1705155.

[171] S. Ghosh, S. Patil, M. Ahire, R. Kitture, S. Kale, K. Pardesi, S. Cameotra, J. Bellare, D.D. Dhavale, A. Jabgunde, B.A. Chopade, Synthesis of silver nanoparticles using Dioscorea bulbifera tuber extract and evaluation of its synergistic potential in combination with antimicrobial agents, Int. J. Nanomedicine. (2012).

[172] A.R. Shahverdi, A. Fakhimi, H.R. Shahverdi, S. Minaian, Synthesis and effect of silver nanoparticles on the antibacterial activity of different antibiotics against Staphylococcus aureus and Escherichia coli, Nanomedicine Nanotechnology, Biol. Med. 3 (2007) 168–171. doi:10.1016/j.nano.2007.02.001.

[173] S.S. Birla, V. V. Tiwari, A.K. Gade, A.P. Ingle, A.P. Yadav, M.K. Rai, Fabrication of silver nanoparticles by Phoma glomerata and its combined effect against Escherichia coli, Pseudomonas aeruginosa and Staphylococcus aureus, Lett. Appl. Microbiol. (2009). doi:10.1111/j.1472-765X.2008.02510.x.

[174] K. Jyoti, M. Baunthiyal, A. Singh, Characterization of silver nanoparticles synthesized using Urtica dioica Linn. leaves and their synergistic effects with antibiotics , J. Radiat. Res. Appl. Sci. (2016). doi:10.1016/j.jrras.2015.10.002.

[175] J.K. Patra, M.S. Ali, I.G. Oh, K.H. Baek, Proteasome inhibitory, antioxidant, and synergistic antibacterial and anticandidal activity of green biosynthesized magnetic Fe3O4 nanoparticles using the aqueous extract of corn (Zea mays L.) ear leaves, Artif. Cells, Nanomedicine Biotechnol. (2017). doi:10.3109/21691401.2016.1153484.

[176] E. Shahbazi, F. Morshedzadeh, D. Zaeifi, Bacteriostatic Potency of Fe2O3 Against Enterococcus faecalis in Synergy with Antibiotics by DDST Method., Avicenna J. Med. Biotechnol. 11 (2019) 176.

[177] N.B.A. Abdulrahman, Z.M. Nssaif, Antimicrobial Activity of Zinc Oxide, titanium Dioxide and Silver Nanoparticles Against Mithicillin-Resistant Staphylococcus aureus Isolates | Tikrit Journal of Pure Science, Tikrit J. Pure Sci. 21 (2018) 49–53.

[178] F.Y. Ahmed, U.F. Aly, R.M. Abd El-Baky, N.G.F.M. Waly, Comparative study of antibacterial effects of titanium dioxide nanoparticles alone and in combination with antibiotics on MDR pseudomonas aeruginosa strains, Int. J. Nanomedicine. (2020). doi:10.2147/IJN.S246310.

[179] U.H. Abo-Shama, H. El-Gendy, W.S. Mousa, R.A. Hamouda, W.E. Yousuf, H.F. Hetta, E.E. Abdeen, Synergistic and antagonistic effects of metal nanoparticles in combination with antibiotics against some reference strains of pathogenic microorganisms, Infect. Drug Resist. (2020). doi:10.2147/IDR.S234425.

[180] S. Iram, J.A. Khan, N. Aman, A. Nadhman, Z. Zulfiqar, M.A. Yameen, Enhancing the anti-enterococci activity of different antibiotics by combining with metal oxide nanoparticles, Jundishapur J. Microbiol. (2016). doi:10.5812/jjm.31302.

[181] R.K. Kankala, W.Z. Lin, C.H. Lee, Combating antibiotic resistance through the synergistic effects of mesoporous silica-based hierarchical nanocomposites, Nanomaterials. (2020). doi:10.3390/nano10030597.

[182] V.M. Wu, S. Tang, V. Uskoković, Calcium Phosphate Nanoparticles as Intrinsic Inorganic

Antimicrobials: The Antibacterial Effect, ACS Appl. Mater. Interfaces. (2018). doi:10.1021/acsami.8b12784.

[183] S. Ghosh, V. Wu, S. Pernal, V. Uskoković, Self-Setting Calcium Phosphate Cements with Tunable Antibiotic Release Rates for Advanced Antimicrobial Applications, ACS Appl. Mater. Interfaces. (2016). doi:10.1021/acsami.6b01160.

[184] K. Rezwan, Q.Z. Chen, J.J. Blaker, A.R. Boccaccini, Biodegradable and bioactive porous polymer/inorganic composite scaffolds for bone tissue engineering, Biomaterials. 27 (2006) 3413–3431. doi:10.1016/J.BIOMATERIALS.2006.01.039.

[185] V. Guarino, F. Causa, L. Ambrosio, Bioactive scaffolds for bone and ligament tissue, Expert Rev. Med. Devices. 4 (2007) 405–418. doi:10.1586/17434440.4.3.405.

[186] A.K. Gaharwar, N.A. Peppas, A. Khademhosseini, Nanocomposite hydrogels for biomedical applications, Biotechnol. Bioeng. 111 (2014) 441–453. doi:10.1002/bit.25160.

[187] J.K. Carrow, A.K. Gaharwar, Bioinspired Polymeric Nanocomposites for Regenerative Medicine, Macromol. Chem. Phys. 216 (2015) 248–264. doi:10.1002/macp.201400427.

[188] F. Quintero, J. Pou, R. Comesaña, F. Lusquiños, A. Riveiro, A.B. Mann, R.G. Hill, Z.Y. Wu, J.R. Jones, Laser Spinning of Bioactive Glass Nanofibers, Adv. Funct. Mater. 19 (2009) 3084–3090. doi:10.1002/adfm.200801922.

[189] A.X. Liu, J.C. Wei, X.S. Chen, X. Bin Jing, Y. Cui, Y. Liu, Novel composites of poly(l-lactide) and surface modified bioactive SiO 2-CAO-P2O5 gel nanoparticles:, Chinese J. Polym. Sci. (English Ed. 27 (2009) 415–426. doi:10.1142/S0256767909004084.

[190] M. Peter, N.S. Binulal, S. V. Nair, N. Selvamurugan, H. Tamura, R. Jayakumar, Novel biodegradable chitosan-gelatin/nano-bioactive glass ceramic composite scaffolds for alveolar bone tissue engineering, Chem. Eng. J. 158 (2010) 353–361. doi:10.1016/j.cej.2010.02.003.

[191] N.A. Peppas, J.Z. Hilt, A. Khademhosseini, R. Langer, Hydrogels in Biology and Medicine: From Molecular Principles to Bionanotechnology, Adv. Mater. 18 (2006) 1345–1360. doi:10.1002/adma.200501612.

[192] A.S. Hoffman, Hydrogels for biomedical applications, Adv. Drug Deliv. Rev. 64 (2012) 18–23. doi:10.1016/j.addr.2012.09.010.

[193] G. Orive, R.M. Hernández, A.R. Gascón, R. Calafiore, T.M.S. Chang, P. De Vos, G. Hortelano, D. Hunkeler, I. Lacík, A.M.J. Shapiro, J.L. Pedraz, Cell encapsulation: Promise and progress, Nat. Med. 9 (2003) 104–107. doi:10.1038/nm0103-104.

[194] H. Uludag, P. De Vos, P.A. Tresco, Technology of mammalian cell encapsulation, Adv. Drug Deliv. Rev. 42 (2000) 29–64. doi:10.1016/S0169-409X(00)00053-3.

[195] N.C. Hunt, L.M. Grover, Cell encapsulation using biopolymer gels for regenerative medicine, Biotechnol. Lett. 32 (2010) 733–742. doi:10.1007/s10529-010-0221-0.

[196] J.L. Drury, D.J. Mooney, Hydrogels for tissue engineering: Scaffold design variables and applications, Biomaterials. 24 (2003) 4337–4351. doi:10.1016/S0142-9612(03)00340-5.

[197] J.K. Kim, H.J. Kim, J.Y. Chung, J.H. Lee, S.B. Young, Y.H. Kim, Natural and synthetic biomaterials for controlled drug delivery, Arch. Pharm. Res. 37 (2014) 60–68. doi:10.1007/s12272-013-0280-6.

[198] B. Stevens, Y. Yang, A. Mohandas, B. Stucker, K.T. Nguyen, A review of materials, fabrication methods, and strategies used to enhance bone regeneration in engineered bone tissues, J. Biomed. Mater. Res. Part B Appl. Biomater. 85B (2008) 573–582. doi:10.1002/jbm.b.30962.

[199] J.D. Kretlow, L. Klouda, A.G. Mikos, Injectable matrices and scaffolds for drug delivery in tissue engineering, Adv. Drug Deliv. Rev. 59 (2007) 263–273. doi:10.1016/j.addr.2007.03.013.

[200] Q. Hou, P.A. De Bank, K.M. Shakesheff, Injectable scaffolds for tissue regeneration, J. Mater. Chem. 14 (2004) 1915–1923. doi:10.1039/b401791a.

[201] S. Utech, A.R. Boccaccini, A review of hydrogel-based composites for biomedical applications: enhancement of hydrogel properties by addition of rigid inorganic fillers Morphogenetic protein-2 BMPs Recombinant human bone morphogenic proteins BMSC Bone marrow stromal cells CA Collagen-alginate, J. Mater. Sci. 51 (2016) 271–310. doi:10.1007/s10853-015-9382-5.

[202] J.R. Jones, A.G. Clare, Bio-Glasses, John Wiley & Sons, Ltd, Chichester, UK, 2012. doi:10.1002/9781118346457.

[203] J.P. Chen, M.J. Tsai, H.T. Liao, Incorporation of biphasic calcium phosphate microparticles in injectable thermoresponsive hydrogel modulates bone cell proliferation and differentiation, Colloids Surfaces B Biointerfaces. 110 (2013) 120–129. doi:10.1016/j.colsurfb.2013.04.028.

[204] Y. Wang, C. Yang, X. Chen, N. Zhao, Development and Characterization of Novel Biomimetic Composite Scaffolds Based on Bioglass-Collagen-Hyaluronic Acid-Phosphatidylserine for Tissue Engineering Applications, Macromol. Mater. Eng. 291 (2006) 254–262. doi:10.1002/mame.200500381.

[205] J. Koo, Polymer Nanocomposites, (n.d.).

[206] T.P. Nguyen, B.H.P. Doan, D.V. Dang, C.K. Nguyen, N.Q. Tran, Enzyme-mediated in situ preparation of biocompatible hydrogel composites from chitosan derivative and biphasic calcium phosphate nanoparticles for bone regeneration, Adv. Nat. Sci. Nanosci.

Nanotechnol. 5 (2014) 015012. doi:10.1088/2043-6262/5/1/015012.

[207] M.C. Lai, K.C. Chang, S.C. Hsu, M.C. Chou, W.I. Hung, Y.R. Hsiao, H.M. Lee, M.F. Hsieh, J.M. Yeh, In situ gelation of PEG-PLGA-PEG hydrogels containing high loading of hydroxyapatite: In vitro and in vivo characteristics, Biomed. Mater. 9 (2014) 015011. doi:10.1088/1748-6041/9/1/015011.

[208] S.L. Flegler, J.W. Heckman, K.L. Klomparens, Scanning and transmission electron microscopy: an introduction, Oxford University Press, 1994. doi:10.5860/choice.31-4353.

[209] J.I. Goldstein, D.E. Newbury, J.R. Michael, N.W.M. Ritchie, J.H.J. Scott, D.C. Joy, Scanning electron microscopy and x-ray microanalysis, 2017. doi:10.1007/978-1-4939-6676-9.

[210] R. Castaing, J. Descamps, Sur les bases physiques de l'analyse ponctuelle par spectrographie X, J. Phys. Le Radium. (1955). doi:10.1051/jphysrad:01955001604030400.

[211] D.B. Williams, C.B. Carter, Transmission electron microscopy: A textbook for materials science, 2009. doi:10.1007/978-0-387-76501-3.

[212] W.H. BRAGG, W.L. Bragg, The reflection of X-rays by crystals, Proc. R. Soc. London. Ser. A, Contain. Pap. a Math. Phys. Character. 88 (1913) 428–438. doi:10.1098/rspa.1913.0040.

[213] J. Lim, S.P. Yeap, H.X. Che, S.C. Low, Characterization of magnetic nanoparticle by dynamic light scattering, Nanoscale Res. Lett. (2013). doi:10.1186/1556-276X-8-381.

[214] A. Einstein, Über die von der molekularkinetischen Theorie der Wärme geforderte Bewegung von in ruhenden Flüssigkeiten suspendierten Teilchen, Ann. Phys. (1905). doi:10.1002/andp.19053220806.

[215] J. Jiang, G. Oberdörster, P. Biswas, Characterization of size, surface charge, and agglomeration state of nanoparticle dispersions for toxicological studies, J. Nanoparticle Res. (2009). doi:10.1007/s11051-008-9446-4.

[216] K.E. Sapsford, K.M. Tyner, B.J. Dair, J.R. Deschamps, I.L. Medintz, Analyzing nanomaterial bioconjugates: A review of current and emerging purification and characterization techniques, Anal. Chem. (2011). doi:10.1021/ac200853a.

[217] B.D. Cullity, J.W. Weymouth, Elements of X-Ray Diffraction, Am. J. Phys. (1957). doi:10.1119/1.1934486.

[218] R.K. Mishra, J. Cherusseri, A. Bishnoi, S. Thomas, Nuclear Magnetic Resonance Spectroscopy, in: Spectrosc. Methods Nanomater. Charact., 2017. doi:10.1016/B978-0-323-46140-5.00013-3.

[219] R.G. Hill, D.S. Brauer, Predicting the bioactivity of glasses using the network connectivity or split network models, J. Non. Cryst. Solids. 357 (2011) 3884–3887. doi:10.1016/J.JNONCRYSOL.2011.07.025.

[220] S. Prasad, A. Gaddam, A. Jana, S. Kant, P.K. Sinha, S. Tripathy, K. Annapurna, J.M.F. Ferreira, A.R. Allu, K. Biswas, Structure and Stability of High CaO- and P_2O_5 -Containing Silicate and Borosilicate Bioactive Glasses, J. Phys. Chem. B. 123 (2019) 7558–7569. doi:10.1021/acs.jpcb.9b02455.

[221] R. Borges, J.F. Schneider, J. Marchi, Structural characterization of bioactive glasses containing rare earth elements (Gd and/or Yb), J. Mater. Sci. 54 (2019) 11390–11399. doi:10.1007/s10853-019-03715-1.

[222] I. Elgayar, A.E. Aliev, A.R. Boccaccini, R.G. Hill, Structural analysis of bioactive glasses, J. Non. Cryst. Solids. 351 (2005) 173–183. doi:10.1016/j.jnoncrysol.2004.07.067.

[223] M.D. O'Donnell, S.J. Watts, R. V. Law, R.G. Hill, Effect of P2O5 content in two series of soda lime phosphosilicate glasses on structure and properties - Part I: NMR, J. Non. Cryst. Solids. 354 (2008) 3554–3560. doi:10.1016/j.jnoncrysol.2008.03.034.

[224] D.S. Brauer, N. Karpukhina, R. V. Law, R.G. Hill, Structure of fluoride-containing bioactive glasses, J. Mater. Chem. 19 (2009) 5629–5636. doi:10.1039/b900956f.

[225] A. Tilocca, A.N. Cormack, Structural Effects of Phosphorus Inclusion in Bioactive Silicate Glasses, J. Phys. Chem. B. 111 (2007) 14256–14264. doi:10.1021/jp075677o.

[226] S. Brunauer, P.H. Emmett, E. Teller, Adsorption of Gases in Multimolecular Layers, J. Am. Chem. Soc. (1938). doi:10.1021/ja01269a023.

[227] D.F. Swinehart, The Beer-Lambert law, J. Chem. Educ. (1962). doi:10.1021/ed039p333.

[228] T. Kokubo, H. Kushitani, S. Sakka, T. Kitsugi, T. Yamamuro, Solutions able to reproducein vivo surface-structure changes in bioactive glass-ceramic A-W3, J. Biomed. Mater. Res. 24 (1990) 721–734. doi:10.1002/jbm.820240607.

[229] D.O. Freytes, S.F. Badylak, T.J. Webster, L.A. Geddes, A.E. Rundell, Biaxial strength of multilaminated extracellular matrix scaffolds, Biomaterials. (2004). doi:10.1016/j.biomaterials.2003.09.015.

[230] D.W. Youngstrom, R. Senos, R.L. Zondervan, J.D. Brodeur, A.R. Lints, D.R. Young, T.L. Mitchell, M.E. Moore, M.H. Myers, W.J. Tseng, K.M. Loomes, K.D. Hankenson, Intraoperative delivery of the Notch ligand Jagged-1 regenerates appendicular and craniofacial bone defects, Npj Regen. Med. (2017). doi:10.1038/s41536-017-0037-9.

[231] M. Assad, N. Jackson, Biocompatibility Evaluation of Orthopedic Biomaterials and Medical Devices: A Review of Safety and Efficacy Models, in: Encycl. Biomed. Eng., 2019.

doi:10.1016/B978-0-12-801238-3.11104-3.

[232] P.D. Fey, J.L. Endres, V.K. Yajjala, T.J. Widhelm, R.J. Boissy, J.L. Bose, K.W. Bayles, A genetic resource for rapid and comprehensive phenotype screening of nonessential Staphylococcus aureus genes., MBio. 4 (2013) e00537-12. doi:10.1128/mBio.00537-12.

[233] J. Huerta-Cepas, K. Forslund, L.P. Coelho, D. Szklarczyk, L.J. Jensen, C. von Mering, P. Bork, Fast Genome-Wide Functional Annotation through Orthology Assignment by eggNOG-Mapper, Mol. Biol. Evol. 34 (2017) 2115–2122. doi:10.1093/molbev/msx148.

[234] J. Huerta-Cepas, D. Szklarczyk, D. Heller, A. Hernández-Plaza, S.K. Forslund, H. Cook, D.R. Mende, I. Letunic, T. Rattei, L.J. Jensen, C. Von Mering, P. Bork, EggNOG 5.0: A hierarchical, functionally and phylogenetically annotated orthology resource based on 5090 organisms and 2502 viruses, Nucleic Acids Res. 47 (2019) D309–D314. doi:10.1093/nar/gky1085.

[235] K.L. Klomparens, S.L. Flegler, G.R. Hooper, G.R. Hooper, Procedures for transmission and scanning electron microscopy for biological and medical science, (1986).

[236] X. Chatzistavrou, S. Velamakanni, K. Direnzo, A. Lefkelidou, J.C. Fenno, T. Kasuga, A.R. Boccaccini, P. Papagerakis, Designing dental composites with bioactive and bactericidal properties, Mater. Sci. Eng. C. 52 (2015) 267–272. doi:10.1016/j.msec.2015.03.062.

[237] N. Pajares-Chamorro, J. Shook, N.D. Hammer, X. Chatzistavrou, Resurrection of antibiotics that methicillin-resistant Staphylococcus aureus resists by silver-doped bioactive glass-ceramic microparticles, Acta Biomater. (2019). doi:10.1016/j.actbio.2019.07.012.

[238] N. Pajares-Chamorro, Y. Wagley, C. V. Maduka, D.W. Youngstrom, A. Yeger, S.F. Badylak, N.D. Hammer, K. Hankenson, X. Chatzistavrou, Silver-doped bioactive glass particles for in vivo bone tissue regeneration and enhanced methicillin-resistant Staphylococcus aureus (MRSA) inhibition, Mater. Sci. Eng. C. 120 (2021) 111693. doi:10.1016/j.msec.2020.111693.

[239] L.W. Fisher, O.W. McBride, J.D. Termine, M.F. Young, Human bone sialoprotein. Deduced protein sequence and chromosomal localization, J. Biol. Chem. (1990).

[240] N.K. Lee, H. Sowa, E. Hinoi, M. Ferron, J.D. Ahn, C. Confavreux, R. Dacquin, P.J. Mee, M.D. McKee, D.Y. Jung, Z. Zhang, J.K. Kim, F. Mauvais-Jarvis, P. Ducy, G. Karsenty, Endocrine Regulation of Energy Metabolism by the Skeleton, Cell. (2007). doi:10.1016/j.cell.2007.05.047.

[241] I.A. San Martin, N. Varela, M. Gaete, K. Villegas, M. Osorio, J.C. Tapia, M. Antonelli, E.E. Mancilla, B.P. Pereira, S.S. Nathan, J.B. Lian, J.L. Stein, G.S. Stein, A.J. Van Wijnen, M. Galindo, Impaired cell cycle regulation of the osteoblast-related heterodimeric transcription factor Runx2-Cbfβ in osteosarcoma cells, J. Cell. Physiol. (2009). doi:10.1002/jcp.21894.

[242] R. Edwards, K.G. Harding, Bacteria and wound healing, Curr. Opin. Infect. Dis. 17 (2004) 91–96. doi:10.1097/00001432-200404000-00004.

[243] C. Desrousseaux, V. Sautou, S. Descamps, O. Traoré, Modification of the surfaces of medical devices to prevent microbial adhesion and biofilm formation, J. Hosp. Infect. 85 (2013) 87–93. doi:10.1016/j.jhin.2013.06.015.

[244] P.R. Gonzales, M.W. Pesesky, R. Bouley, A. Ballard, B.A. Biddy, M.A. Suckow, W.R. Wolter, V.A. Schroeder, C.-A.D. Burnham, S. Mobashery, M. Chang, G. Dantas, Synergistic, collaterally sensitive β-lactam combinations suppress resistance in MRSA, Nat. Chem. Biol. 11 (2015) 855–861. doi:10.1038/nchembio.1911.

[245] C. Walsh, T. Wencewicz, Antibiotics: Challenges, Mechanisms, Opportunities, 2nd Edition, American Society of Microbiology, 2016. doi:10.1128/9781555819316.

[246] F.M. Kahan, J.S. Kahan, P.J. Cassidy, H. Kropp, THE MECHANISM OF ACTION OF FOSFOMYCIN (PHOSPHONOMYCIN), Ann. N. Y. Acad. Sci. 235 (1974) 364–386. doi:10.1111/j.1749-6632.1974.tb43277.x.

[247] D. Zeng, D. Debabov, T.L. Hartsell, R.J. Cano, S. Adams, J.A. Schuyler, R. McMillan, J.L. Pace, Approved Glycopeptide Antibacterial Drugs: Mechanism of Action and Resistance., Cold Spring Harb. Perspect. Med. 6 (2016) a026989. doi:10.1101/cshperspect.a026989.

[248] S. Shakil, R. Khan, R. Zarrilli, A.U. Khan, Aminoglycosides versus bacteria - A description of the action, resistance mechanism, and nosocomial battleground, J. Biomed. Sci. (2008). doi:10.1007/s11373-007-9194-y.

[249] B.D. Davis, Mechanism of bactericidal action of aminoglycosides, Microbiol. Rev. (1987). doi:10.1128/mmbr.51.3.341-350.1987.

[250] R.E.W. Hancock, F. Bellido, Antibiotic uptake: Unusual results for unusual molecules, J. Antimicrob. Chemother. (1992). doi:10.1093/jac/29.3.235.

[251] F. Walter, Q. Vicens, E. Westhof, Aminoglycoside-RNA interactions, Curr. Opin. Chem. Biol. (1999). doi:10.1016/S1367-5931(99)00028-9.

[252] J. Woodcock, D. Moazed, M. Cannon, J. Davies, H.F. Noller, Interaction of antibiotics with A- and P-site-specific bases in 16S ribosomal RNA, EMBO J. (1991). doi:10.1002/j.1460-2075.1991.tb07863.x.

[253] J. Davies, L. Gorini, B.D. Davis, Misreading of RNA codewords induced by aminoglycoside antibiotics., Mol. Pharmacol. (1965).

[254] M.I. Recht, S. Douthwaite, J.D. Puglisi, Basis for prokaryotic specificity of action of aminoglycoside antibiotics, EMBO J. (1999). doi:10.1093/emboj/18.11.3133.

[255] J. Poehlsgaard, S. Douthwaite, The bacterial ribosome as a target for antibiotics, Nat. Rev. Microbiol. (2005). doi:10.1038/nrmicro1265.

[256] N. Ardic, M. Ozyurt, B. Sareyyupoglu, T. Haznedaroglu, Investigation of erythromycin and tetracycline resistance genes in methicillin-resistant staphylococci, Int. J. Antimicrob. Agents. (2005). doi:10.1016/j.ijantimicag.2005.06.013.

[257] E. Cundliffe, K. McQuillen, Bacterial protein synthesis: The effects of antibiotics, J. Mol. Biol. (1967). doi:10.1016/0022-2836(67)90249-5.

[258] S. Schwarz, C. Kehrenberg, B. Doublet, A. Cloeckaert, Molecular basis of bacterial resistance to chloramphenicol and florfenicol, FEMS Microbiol. Rev. (2004). doi:10.1016/j.femsre.2004.04.001.

[259] M. LeBel, Ciprofloxacin: Chemistry, Mechanism of Action, Resistance, Antimicrobial Spectrum, Pharmacokinetics, Clinical Trials, and Adverse Reactions, Pharmacother. J. Hum. Pharmacol. Drug Ther. (1988). doi:10.1002/j.1875-9114.1988.tb04058.x.

[260] M. Stigter, J. Bezemer, K. de Groot, P. Layrolle, Incorporation of different antibiotics into carbonated hydroxyapatite coatings on titanium implants, release and antibiotic efficacy, J. Control. Release. 99 (2004) 127–137. doi:10.1016/j.jconrel.2004.06.011.

[261] M. Miola, C. Vitale-Brovarone, C. Mattu, E. Verné, Antibiotic loading on bioactive glasses and glass-ceramics: An approach to surface modification, J. Biomater. Appl. 28 (2013) 308–319. doi:10.1177/0885328212447665.

[262] J. Rivadeneira, G.M. Luz, M.C. Audisio, J.F. Mano, A.A. Gorustovich, Novel antibacterial bioactive glass nanocomposite functionalized with tetracycline hydrochloride, Biomed. Glas. 1 (2015). doi:10.1515/bglass-2015-0012.

[263] J. Rivadeneira, A.L. Di Virgilio, M.C. Audisio, A.R. Boccaccini, A.A. Gorustovich, Evaluation of antibacterial and cytotoxic effects of nano-sized bioactive glass/collagen composites releasing tetracycline hydrochloride, J. Appl. Microbiol. 116 (2014) 1438–1446. doi:10.1111/jam.12476.

[264] C. Soundrapandian, A. Mahato, B. Kundu, S. Datta, B. Sa, D. Basu, Development and effect of different bioactive silicate glass scaffolds: In vitro evaluation for use as a bone drug delivery system, J. Mech. Behav. Biomed. Mater. 40 (2014) 1–12. doi:10.1016/j.jmbbm.2014.08.007.

[265] L.M. Cross, A. Thakur, N.A. Jalili, M. Detamore, A.K. Gaharwar, Nanoengineered biomaterials for repair and regeneration of orthopedic tissue interfaces, Acta Biomater. 42 (2016) 2–17. doi:10.1016/j.actbio.2016.06.023.

[266] N. Pajares-Chamorro, X. Chatzistavrou, Bioactive Glass Nanoparticles for Tissue Regeneration, ACS Omega. (2020). doi:10.1021/acsomega.0c00180.

[267] P.N. Gunawidjaja, A.Y.H. Lo, I. Izquierdo-Barba, A. García, D. Arcos, B. Stevensson, J. Grins, M. Vallet-Regí, M. Edén, Biomimetic Apatite Mineralization Mechanisms of Mesoporous Bioactive Glasses as Probed by Multinuclear 31 P, 29 Si, 23 Na and 13 C Solid-State NMR, J. Phys. Chem. C. 114 (2010) 19345–19356. doi:10.1021/jp105408c.

[268] E.G. Canty, K.E. Kadler, Procollagen trafficking, processing and fibrillogenesis, J. Cell Sci. (2005). doi:10.1242/jcs.01731.

[269] S.G. Wolf, Y. Mutsafi, T. Dadosh, T. Ilani, Z. Lansky, B. Horowitz, S. Rubin, M. Elbaum, D. Fass, 3D visualization of mitochondrial solid-phase calcium stores in whole cells, Elife. (2017). doi:10.7554/eLife.29929.

[270] A. Dai, L. Yu, H.W. Wang, WHAMM initiates autolysosome tubulation by promoting actin polymerization on autolysosomes, Nat. Commun. (2019). doi:10.1038/s41467-019-11694-9.

[271] S.J. Yoon, C.J. Lim, H.J. Chung, J.H. Kim, Y.H. Huh, K. Park, S. Jeong, Autophagy activation by Crepidiastrum Denticulatum extract attenuates environmental pollutant-induced damage in dermal fibroblasts, Int. J. Mol. Sci. (2019). doi:10.3390/ijms20030517.

[272] D. dan Pei, J. long Sun, C. hui Zhu, F. cong Tian, K. Jiao, M.R. Anderson, C. Yiu, C. Huang, C. xiong Jin, B.E. Bergeron, J. hua Chen, F.R. Tay, L. na Niu, Contribution of Mitophagy to Cell-Mediated Mineralization: Revisiting a 50-Year-Old Conundrum, Adv. Sci. (2018). doi:10.1002/advs.201800873.

[273] K.M. Sinha, X. Zhou, Genetic and molecular control of osterix in skeletal formation, J. Cell. Biochem. (2013). doi:10.1002/jcb.24439.

[274] W. Lin, L. Gao, W. Jiang, C. Niu, K. Yuan, X. Hu, R. Ma, Z. Huang, The role of osteomodulin on osteo/odontogenic differentiation in human dental pulp stem cells, BMC Oral Health. (2019). doi:10.1186/s12903-018-0680-6.

[275] I.M.H. Li, K. Liu, A. Neal, P.D. Clegg, S. De Val, G. Bou-Gharios, Differential tissue specific, temporal and spatial expression patterns of the Aggrecan gene is modulated by independent enhancer elements, Sci. Rep. (2018). doi:10.1038/s41598-018-19186-4.

[276] J. Gu, Y. Lu, F. Li, L. Qiao, Q. Wang, N. Li, J.A. Borgia, Y. Deng, G. Lei, Q. Zheng, Identification and characterization of the novel Col10a1 regulatory mechanism during chondrocyte hypertrophic differentiation, Cell Death Dis. (2014). doi:10.1038/cddis.2014.444.

[277] L.J. Zhang, X.S. Feng, H.G. Liu, D.J. Qian, L. Zhang, X.L. Yu, F.Z. Cui, Hydroxyapatite/collagen composite materials formation in simulated body fluid environment, Mater. Lett. 58 (2004) 719–722. doi:10.1016/j.matlet.2003.07.009.

[278] R.J. Koegel, J.P. Greenstein, M. Winitz, S.M. Birnbaum, R.A. Mccallum, V. 77, R.J.

Koegel, J.P. Greenstein, M. Winitz, S.M. Birnbaum, R.A. Mccallum, Studies on Diastereoisomeric-Amino Acids and Corresponding-Hydroxy Acids. V. Infrared Spectra, n.d.

[279] P. Sasmal, H. Begam, Extraction of Type-I Collagen from Sea Fish and Synthesis of Hap/Collagen Composite, Procedia Mater. Sci. 5 (2014) 1136–1140. doi:10.1016/j.mspro.2014.07.408.

[280] J. Kim, L. Gu, L. Breschi, L. Tjäderhane, K.K. Choi, D.H. Pashley, F.R. Tay, Implication of ethanol wet-bonding in hybrid layer remineralization, J. Dent. Res. (2010). doi:10.1177/0022034510363380.

[281] X. Chatzistavrou, R.R. Rao, D.J. Caldwell, A.W. Peterson, B. McAlpin, Y.-Y. Wang, L. Zheng, J. Christopher Fenno, J.P. Stegemann, P. Papagerakis, Collagen/fibrin microbeads as a delivery system for Ag-doped bioactive glass and DPSCs for potential applications in dentistry, J. Non. Cryst. Solids. 432 (2016) 143–149. doi:10.1016/J.JNONCRYSOL.2015.03.024.

[282] A.R. Shahverdi, A. Fakhimi, H.R. Shahverdi, S. Minaian, Synthesis and effect of silver nanoparticles on the antibacterial activity of different antibiotics against Staphylococcus aureus and Escherichia coli, Nanomedicine Nanotechnology, Biol. Med. (2007). doi:10.1016/j.nano.2007.02.001.

[283] K.-H. Cho, J.-E. Park, T. Osaka, S.-G. Park, The study of antimicrobial activity and preservative effects of nanosilver ingredient, Electrochim. Acta. 51 (2005) 956–960. doi:10.1016/J.ELECTACTA.2005.04.071.

[284] C. Qin, O. Baba, W.T. Butler, P ost-translational M odifications of SIBLING P roteins and T heir R oles in O steogenesis and D entinogenesis, Crit. Rev. Oral Biol. Med. 15 (2004) 126–136. doi:10.1177/154411130401500302.

[285] R.T. Franceschi, The Developmental Control of Osteoblast-Specific Gene Expression: Role of Specific Transcription Factors and the Extracellular Matrix Environment, Crit. Rev. Oral Biol. Med. 10 (1999) 40–57. doi:10.1177/10454411990100010201.

[286] V.G. Varanasi, J.B. Owyoung, E. Saiz, S.J. Marshall, G.W. Marshall, P.M. Loomer, The ionic products of bioactive glass particle dissolution enhance periodontal ligament fibroblast osteocalcin expression and enhance early mineralized tissue development., J. Biomed. Mater. Res. A. 98 (2011) 177–84. doi:10.1002/jbm.a.33102.

[287] D. Dufrane, C. Delloye, I.J. McKay, P.N. De Aza, S. De Aza, Y.J. Schneider, M. Anseau, Indirect cytotoxicity evaluation of pseudowollastonite, J. Mater. Sci. Mater. Med. 14 (2003) 33–38. doi:10.1023/A:1021545302732.

[288] N. Saffarian Tousi, M.F. Velten, T.J. Bishop, K.K. Leong, N.S. Barkhordar, G.W. Marshall, P.M. Loomer, P.B. Aswath, V.G. Varanasi, Combinatorial effect of Si4 +, Ca2 +, and

Mg2 + released from bioactive glasses on osteoblast osteocalcin expression and biomineralization, Mater. Sci. Eng. C. 33 (2013) 2757–2765. doi:10.1016/J.MSEC.2013.02.044.

[289] S. Maeno, Y. Niki, H. Matsumoto, H. Morioka, T. Yatabe, A. Funayama, Y. Toyama, T. Taguchi, J. Tanaka, The effect of calcium ion concentration on osteoblast viability, proliferation and differentiation in monolayer and 3D culture, Biomaterials. 26 (2005) 4847–4855. doi:10.1016/J.BIOMATERIALS.2005.01.006.

[290] G. Lusvardi, G. Malavasi, L. Menabue, V. Aina, C. Morterra, Fluoride-containing bioactive glasses: Surface reactivity in simulated body fluids solutions, Acta Biomater. (2009). doi:10.1016/j.actbio.2009.06.009.

[291] M. Mozafari, S. Banijamali, F. Baino, S. Kargozar, R.G. Hill, Calcium carbonate: Adored and ignored in bioactivity assessment, Acta Biomater. (2019). doi:10.1016/j.actbio.2019.04.039.

[292] N.J. Flora, C.H. Yoder, H.D.B. Jenkins, Lattice Energies of Apatites and the Estimation of ΔH f°(PO43-,g), Inorg. Chem. (2004). doi:10.1021/ic030255o.

[293] S. Zumdahl, D. Decoste, Chemical Principles, 8th Ed. TEXTBOOK, 2006. doi:10.1002/0471743984.vse5459.pub2.

[294] P. Valerio, M.M. Pereira, A.M. Goes, M.F. Leite, The effect of ionic products from bioactive glass dissolution on osteoblast proliferation and collagen production, Biomaterials. 25 (2004) 2941–2948. doi:10.1016/J.BIOMATERIALS.2003.09.086.

[295] D. Arcos, M. Vallet-Regí, Sol-gel silica-based biomaterials and bone tissue regeneration, Acta Biomater. 6 (2010) 2874–2888. doi:10.1016/j.actbio.2010.02.012.

[296] S.M. Best, A.E. Porter, E.S. Thian, J. Huang, Bioceramics: Past, present and for the future, J. Eur. Ceram. Soc. (2008). doi:10.1016/j.jeurceramsoc.2007.12.001.

[297] M. Vallet-Regí, Evolution of bioceramics within the field of biomaterials, Comptes Rendus Chim. 13 (2010) 174–185. doi:10.1016/j.crci.2009.03.004.

[298] J.S. Fernandes, P. Gentile, R.A. Pires, R.L. Reis, P. V Hatton, Multifunctional bioactive glass and glass-ceramic biomaterials with antibacterial properties for repair and regeneration of bone tissue, Acta Biomater. (2017). doi:10.1016/j.actbio.2017.06.046.

[299] S. Kargozar, F. Baino, S. Hamzehlou, R.G. Hill, M. Mozafari, Bioactive glasses entering the mainstream, Drug Discov. Today. 23 (2018) 1700–1704. doi:10.1016/j.drudis.2018.05.027.

[300] E. Munukka, O. Leppäranta, M. Korkeamäki, M. Vaahtio, T. Peltola, D. Zhang, L. Hupa, H. Ylänen, J.I. Salonen, M.K. Viljanen, E. Eerola, Bactericidal effects of bioactive glasses

on clinically important aerobic bacteria, J. Mater. Sci. Mater. Med. 19 (2008) 27–32. doi:10.1007/s10856-007-3143-1.

[301] D. Zhang, O. Leppäranta, E. Munukka, H. Ylänen, M.K. Viljanen, E. Eerola, M. Hupa, L. Hupa, Antibacterial effects and dissolution behavior of six bioactive glasses, J. Biomed. Mater. Res. - Part A. 93 (2010) 475–483. doi:10.1002/jbm.a.32564.

[302] J.D. Oliver, Recent findings on the viable but nonculturable state in pathogenic bacteria, FEMS Microbiol. Rev. 34 (2010) 415–425. doi:10.1111/j.1574-6976.2009.00200.x.

[303] E.C. Hett, E.J. Rubin, Bacterial Growth and Cell Division: a Mycobacterial Perspective, Microbiol. Mol. Biol. Rev. 72 (2008) 126–156. doi:10.1128/mmbr.00028-07.

[304] K. Lewis, Persister cells, dormancy and infectious disease, Nat. Rev. Microbiol. 5 (2007) 48–56. doi:10.1038/nrmicro1557.

[305] J. Dworkin, I.M. Shah, Exit from dormancy in microbial organisms, Nat. Rev. Microbiol. 8 (2010) 890–896. doi:10.1038/nrmicro2453.

[306] B. Cabal, L. Alou, F. Cafini, R. Couceiro, D. Sevillano, L. Esteban-Tejeda, F. Guitián, R. Torrecillas, J.S. Moya, A new biocompatible and antibacterial phosphate free glass-ceramic for medical applications, Sci. Rep. 4 (2014) 1–9. doi:10.1038/srep05440.

[307] G. Pizzino, N. Irrera, M. Cucinotta, G. Pallio, F. Mannino, V. Arcoraci, F. Squadrito, D. Altavilla, A. Bitto, Oxidative Stress: Harms and Benefits for Human Health, Oxid. Med. Cell. Longev. 2017 (2017). doi:10.1155/2017/8416763.

[308] T.P.A. Devasagayam, J.C. Tilak, K.. Boloor, K.. Sane, S. Ghaskadabi, R. Lele, Free Radicals and Antioxidants in Human Health: Current Status and Future Prospects | Request PDF, J. Assoc. Physicians India. 52 (2004) 794–804.

[309] J. Sawai, Quantitative evaluation of antibacterial activities of metallic oxide powders (ZnO, MgO and CaO) by conductimetric assay, J. Microbiol. Methods. 54 (2003) 177–182. doi:10.1016/S0167-7012(03)00037-X.

[310] J. Sawai, E. Kawada, F. Kanou, H. Igarashi, A. Hashimoto, T. Kokugan, M. Shimizu, Detection of active oxygen generated from ceramic powders having antibacterial activity., J. Chem. Eng. JAPAN. 29 (1996) 627–633. doi:10.1252/jcej.29.627.

[311] K. Kobayashi, Life time of active oxygens and their physiological significance -, Protein, Nucleic Acid Enzym. (1988) 2678–2683.

[312] E.R. Bucker, S.E. Martin, Superoxide dismutase activity in thermally stressed Staphylococcus aureus., Appl. Environ. Microbiol. 41 (1981).

[313] S.B. Farr, T. Kogoma, Oxidative stress responses in Escherichia coli and Salmonella

typhimurium., Microbiol. Mol. Biol. Rev. 55 (1991).

[314] D.H. Bae, J.H. Yeon, S.Y. Park, D.H. Lee, S. Do Ha, Bactericidal effects of CaO (scallop-shell powder) on foodborne pathogenic bacteria, Arch. Pharm. Res. 29 (2006) 298–301. doi:10.1007/BF02968574.

[315] C. Shuai, Y. Xu, P. Feng, G. Wang, S. Xiong, S. Peng, Antibacterial polymer scaffold based on mesoporous bioactive glass loaded with in situ grown silver, Chem. Eng. J. 374 (2019) 304–315. doi:10.1016/j.cej.2019.03.273.

[316] A.M. El-Kady, A.F. Ali, R.A. Rizk, M.M. Ahmed, Synthesis, characterization and microbiological response of silver doped bioactive glass nanoparticles, Ceram. Int. 38 (2012) 177–188. doi:10.1016/j.ceramint.2011.05.158.

[317] H. Zhu, C. Hu, F. Zhang, X. Feng, J. Li, T. Liu, J. Chen, J. Zhang, Preparation and antibacterial property of silver-containing mesoporous 58S bioactive glass, Mater. Sci. Eng. C. 42 (2014) 22–30. doi:10.1016/j.msec.2014.05.004.

[318] A.W. Wren, A. Coughlan, P. Hassanzadeh, M.R. Towler, Silver coated bioactive glass particles for wound healing applications, J. Mater. Sci. Mater. Med. 23 (2012) 1331–1341. doi:10.1007/s10856-012-4604-8.

[319] M. Kawashita, S. Tsuneyama, F. Miyaji, T. Kokubo, H. Kozuka, K. Yamamoto, Antibacterial silver-containing silica glass prepared by sol-gel method, Biomaterials. 21 (2000) 393–398. doi:10.1016/S0142-9612(99)00201-X.

[320] M. Bellantone, N.J. Coleman, L.L. Hench, Novel sol-gel derived bioactive glass featuring antibacterial properties, Key Eng. Mater. 192–195 (2001) 597–600. doi:10.4028/www.scientific.net/kem.192-195.597.

[321] M. Bellantone, H.D. Williams, L.L. Hench, Broad-spectrum bactericidal activity of Ag(2)O-doped bioactive glass., Antimicrob. Agents Chemother. 46 (2002) 1940–5. doi:10.1128/AAC.46.6.1940-1945.2002.

[322] M. Gholipourmalekabadi, M. Sameni, A. Hashemi, F. Zamani, A. Rostami, M. Mozafari, Silver- and fluoride-containing mesoporous bioactive glasses versus commonly used antibiotics: Activity against multidrug-resistant bacterial strains isolated from patients with burns, Burns. 42 (2016) 131–140. doi:10.1016/J.BURNS.2015.09.010.

[323] K. Zheng, P. Balasubramanian, T.E. Paterson, R. Stein, S. MacNeil, S. Fiorilli, C. Vitale-Brovarone, J. Shepherd, A.R. Boccaccini, Ag modified mesoporous bioactive glass nanoparticles for enhanced antibacterial activity in 3D infected skin model, Mater. Sci. Eng. C. 103 (2019) 109764. doi:10.1016/j.msec.2019.109764.

[324] L.G. Ovington, The truth about silver., Ostomy. Wound. Manage. 50 (2004) 1S-10S.

[325] B. Reidy, A. Haase, A. Luch, K. Dawson, I. Lynch, Mechanisms of Silver Nanoparticle Release, Transformation and Toxicity: A Critical Review of Current Knowledge and Recommendations for Future Studies and Applications, Materials (Basel). 6 (2013) 2295–2350. doi:10.3390/ma6062295.

[326] C.-N. Lok, C.-M. Ho, R. Chen, Q.-Y. He, W.-Y. Yu, H. Sun, P.K.-H. Tam, J.-F. Chiu, C.-M. Che, Proteomic Analysis of the Mode of Antibacterial Action of Silver Nanoparticles, J. Proteome Res. 5 (2006) 916–924. doi:10.1021/pr0504079.

[327] I. Sondi, B. Salopek-Sondi, Silver nanoparticles as antimicrobial agent: a case study on E. coli as a model for Gram-negative bacteria, J. Colloid Interface Sci. 275 (2004) 177–182. doi:10.1016/J.JCIS.2004.02.012.

[328] T. Hamouda, A. Myc, B. Donovan, A.Y. Shih, J.D. Reuter, J.R. Baker, A novel surfactant nanoemulsion with a unique non-irritant topical antimicrobial activity against bacteria, enveloped viruses and fungi, Microbiol. Res. 156 (2001) 1–7. doi:10.1078/0944-5013-00069.

[329] P. Dibrov, J. Dzioba, K.K. Gosink, C.C. Häse, Chemiosmotic mechanism of antimicrobial activity of Ag(+) in Vibrio cholerae., Antimicrob. Agents Chemother. 46 (2002) 2668–70. doi:10.1128/AAC.46.8.2668-2670.2002.

[330] W.-R. Li, X.-B. Xie, Q.-S. Shi, S.-S. Duan, Y.-S. Ouyang, Y.-B. Chen, Antibacterial effect of silver nanoparticles on Staphylococcus aureus, BioMetals. 24 (2011) 135–141. doi:10.1007/s10534-010-9381-6.

[331] M.M. Cox, The bacterial RecA protein: structure, function, and regulation, in: Springer, Berlin, Heidelberg, 2007: pp. 53–94. doi:10.1007/978-3-540-71021-9_3.

[332] O. Gordon, T. Vig Slenters, P.S. Brunetto, A.E. Villaruz, D.E. Sturdevant, M. Otto, R. Landmann, K.M. Fromm, Silver coordination polymers for prevention of implant infection: thiol interaction, impact on respiratory chain enzymes, and hydroxyl radical induction., Antimicrob. Agents Chemother. 54 (2010) 4208–18. doi:10.1128/AAC.01830-09.

[333] J.R. Morones, J.L. Elechiguerra, A. Camacho, K. Holt, J.B. Kouri, J.T. Ramírez, M.J. Yacaman, The bactericidal effect of silver nanoparticles, Nanotechnology. 16 (2005) 2346–2353. doi:10.1088/0957-4484/16/10/059.

[334] M. Raffi, F. Hussain, T.M. Bhatti, J.. Akhter, A. Hameed, M.M. Hasan, Antibacterial Characterization of Silver Nanoparticles against, J. Mater. Sci. Technol. 24 (2008).

[335] J.S. Kim, E. Kuk, K.N. Yu, J.-H. Kim, S.J. Park, H.J. Lee, S.H. Kim, Y.K. Park, Y.H. Park, C.-Y. Hwang, Y.-K. Kim, Y.-S. Lee, D.H. Jeong, M.-H. Cho, Antimicrobial effects of silver nanoparticles., Nanomedicine. 3 (2007) 95–101. doi:10.1016/j.nano.2006.12.001.

[336] Q.L. Feng, J. Wu, G.Q. Chen, F.Z. Cui, T.N. Kim, J.O. Kim, A mechanistic study of the

antibacterial effect of silver ion on Escherichia coli and Staphylococcus aureus, J Biomed Mater Res. 52 (2000) 662–668.

[337] M. Yamanaka, K. Hara, J. Kudo, Bactericidal actions of a silver ion solution on Escherichia coli, studied by energy-filtering transmission electron microscopy and proteomic analysis., Appl. Environ. Microbiol. 71 (2005) 7589–93. doi:10.1128/AEM.71.11.7589-7593.2005.

[338] Q. Chen, C. Zhu, G.A. Thouas, Progress and challenges in biomaterials used for bone tissue engineering: bioactive glasses and elastomeric composites, Prog. Biomater. 1 (2012) 2. doi:10.1186/2194-0517-1-2.

[339] A.C. Marsh, N.P. Mellott, M. Crimp, A. Wren, N. Hammer, X. Chatzistavrou, Ag-doped Bioactive Glass-Ceramic 3D Scaffolds: Microstructural, Antibacterial, and Biological Properties, J. Eur. Ceram. Soc. (2021). doi:10.1016/j.jeurceramsoc.2021.01.011.

[340] L. Bergandi, V. Aina, S. Garetto, G. Malavasi, E. Aldieri, E. Laurenti, L. Matera, C. Morterra, D. Ghigo, Fluoride-containing bioactive glasses inhibit pentose phosphate oxidative pathway and glucose 6-phosphate dehydrogenase activity in human osteoblasts, Chem. Biol. Interact. 183 (2010) 405–415. doi:10.1016/j.cbi.2009.11.021.

[341] V. Aina, A. Perardi, L. Bergandi, G. Malavasi, L. Menabue, C. Morterra, D. Ghigo, Cytotoxicity of zinc-containing bioactive glasses in contact with human osteoblasts, Chem. Biol. Interact. (2007). doi:10.1016/j.cbi.2007.03.002.

[342] D.. Reffitt, N. Ogston, R. Jugdaohsingh, H.F.. Cheung, B.A.. Evans, R.P.. Thompson, J.. Powell, G.. Hampson, Orthosilicic acid stimulates collagen type 1 synthesis and osteoblastic differentiation in human osteoblast-like cells in vitro, Bone. 32 (2003) 127–135. doi:10.1016/S8756-3282(02)00950-X.

[343] A.A. Barbosa, S.A. Júnior, R.L. Mendes, R.S. de Lima, A. de Vasconcelos Ferraz, Multifunctional hydroxyapatite with potential for application in theranostic nanomedicine, Mater. Sci. Eng. C. 116 (2020) 111227. doi:10.1016/j.msec.2020.111227.

[344] G. Afreen, M. Shoeb, S. Upadhyayula, Effectiveness of reactive oxygen species generated from rGO/CdS QD heterostructure for photodegradation and disinfection of pollutants in waste water, Mater. Sci. Eng. C. 108 (2020) 110372. doi:10.1016/j.msec.2019.110372.

[345] Y. Yuan, L. Zhao, C. Shen, Y. He, F. Yang, G. Zhang, M. Jia, R. Zeng, C. Li, R. Qiao, Reactive oxygen species-responsive amino acid-based polymeric nanovehicles for tumor-selective anticancer drug delivery, Mater. Sci. Eng. C. 106 (2020) 110159. doi:10.1016/j.msec.2019.110159.

[346] F. Kermani, S. Mollazadeh, S. Kargozar, J. Vahdati Khakhi, Solution combustion synthesis (SCS) of theranostic ions doped biphasic calcium phosphates; kinetic of ions release in simulated body fluid (SBF) and reactive oxygen species (ROS) generation, Mater. Sci. Eng. C. 118 (2021) 111533. doi:10.1016/j.msec.2020.111533.

[347] L.A. Onyango, R.H. Dunstan, J. Gottfries, C. von Eiff, T.K. Roberts, Effect of Low Temperature on Growth and Ultra-Structure of Staphylococcus spp, PLoS One. 7 (2012) e29031. doi:10.1371/journal.pone.0029031.

[348] B.C. Kahl, G. Belling, R. Reichelt, M. Herrmann, R.A. Proctor, G. Peters, Thymidine-dependent small-colony variants of Staphylococcus aureus exhibit gross morphological and ultrastructural changes consistent with impaired cell separation, J. Clin. Microbiol. 41 (2003) 410–413. doi:10.1128/JCM.41.1.410-413.2003.

[349] W. Sianglum, P. Srimanote, W. Wonglumsom, K. Kittiniyom, S.P. Voravuthikunchai, Proteome Analyses of Cellular Proteins in Methicillin-Resistant Staphylococcus aureus Treated with Rhodomyrtone, a Novel Antibiotic Candidate, PLoS One. 6 (2011) e16628. doi:10.1371/journal.pone.0016628.

[350] M. Liu, K. Yang, J. Wang, J. Zhang, Y. Qi, X. Wei, M. Fan, Young astringent persimmon tannin inhibits methicillin-resistant Staphylococcus aureus isolated from pork, LWT. 100 (2019) 48–55. doi:10.1016/j.lwt.2018.10.047.

[351] J. Campbell, A.K. Singh, J.G. Swoboda, M.S. Gilmore, B.J. Wilkinson, S. Walker, An antibiotic that inhibits a late step in wall teichoic acid biosynthesis induces the cell wall stress stimulon in Staphylococcus aureus, Antimicrob. Agents Chemother. 56 (2012) 1810–1820. doi:10.1128/AAC.05938-11.

[352] N.K. Archer, M.J. Mazaitis, J. William Costerton, J.G. Leid, M.E. Powers, M.E. Shirtliff, Staphylococcus aureus biofilms: Properties, regulation and roles in human disease, Virulence. 2 (2011) 445–459. doi:10.4161/viru.2.5.17724.

[353] A. Panáček, L. Kvítek, M. Smékalová, R. Večeřová, M. Kolář, M. Röderová, F. Dyčka, M. Šebela, R. Prucek, O. Tomanec, R. Zbořil, Bacterial resistance to silver nanoparticles and how to overcome it, Nat. Nanotechnol. (2018). doi:10.1038/s41565-017-0013-y.

[354] E.J. Woods, C.A. Cochrane, S.L. Percival, Prevalence of silver resistance genes in bacteria isolated from human and horse wounds, Vet. Microbiol. 138 (2009) 325–329. doi:10.1016/j.vetmic.2009.03.023.

[355] S. Kittler, C. Greulich, J. Diendorf, M. Köller, M. Epple, Toxicity of silver nanoparticles increases during storage because of slow dissolution under release of silver ions, Chem. Mater. 22 (2010) 4548–4554. doi:10.1021/cm100023p.

[356] C. Greulich, D. Braun, A. Peetsch, J. Diendorf, B. Siebers, M. Epple, M. Köller, The toxic effect of silver ions and silver nanoparticles towards bacteria and human cells occurs in the same concentration range, RSC Adv. 2 (2012) 6981–6987. doi:10.1039/c2ra20684f.

[357] K. Zheng, M. Kapp, A.R. Boccaccini, Protein interactions with bioactive glass surfaces: A review, Appl. Mater. Today. 15 (2019) 350–371. doi:10.1016/j.apmt.2019.02.003.

[358] M.G. Pinho, M. Kjos, J.-W. Veening, How to get (a)round: mechanisms controlling growth and division of coccoid bacteria, Nat. Rev. Microbiol. 11 (2013) 601–614. doi:10.1038/nrmicro3088.

[359] S. Alvarez, M. Jones, S.L. Berk ', In Vitro Activity of Fosfomycin, Alone and in Combination, against Methicillin-Resistant Staphylococcus aureus, Antimicrob. Agents Chemother. 28 (1985) 689–690.

[360] G. Peters, F. Schumacher-Perdreau, G. Pulverer, [Comparison of activity of fosfomycin, oxacillin and penicillin G against staphylococci and micrococci (author's transl)]., Dtsch. Med. Wochenschr. 105 (1980) 1541–3. doi:10.1055/s-2008-1070908.

[361] S. Eschenburg, M. Priestman, E. Schö, Evidence That the Fosfomycin Target Cys 115 in UDP-N-acetylglucosamine Enolpyruvyl Transferase (MurA) Is Essential for Product Release*, (2004). doi:10.1074/jbc.M411325200.

[362] D.H. Williams, The glycopeptide story – how to kill the deadly 'superbugs,' Nat. Prod. Rep. 13 (1996) 469–477. doi:10.1039/NP9961300469.

[363] B.P. Howden, J.K. Davies, P.D.R. Johnson, T.P. Stinear, M.L. Grayson, Reduced vancomycin susceptibility in Staphylococcus aureus, including vancomycin-intermediate and heterogeneous vancomycin-intermediate strains: resistance mechanisms, laboratory detection, and clinical implications., Clin. Microbiol. Rev. 23 (2010) 99–139. doi:10.1128/CMR.00042-09.

[364] S. Gardete, A. Tomasz, Mechanisms of vancomycin resistance in Staphylococcus aureus, J. Clin. Invest. 124 (2014) 2836–2840. doi:10.1172/JCI68834.

[365] H. Blode, S. Zeun, S. Parke, T. Zimmermann, B. Rohde, U. Mellinger, M. Kunz, Evaluation of the effects of rifampicin, ketoconazole and erythromycin on the steady-state pharmacokinetics of the components of a novel oral contraceptive containing estradiol valerate and dienogest in healthy postmenopausal women, Contraception. 86 (2012) 337–344. doi:10.1016/j.contraception.2012.01.010.

[366] J.K. Marr, A.T. Lim, L.G. Yamamoto, Erythromycininduced Resistance to Clindamycin in Staphylococcus aureus, Hawaii Med. J. 64 (2005).

[367] F. van Bambeke, M.-P. Mingeot-Leclercq, Y. Glupczynski, P.M. Tulkens, Mechanisms of Action, in: Infect. Dis. (Auckl)., Elsevier, 2017: pp. 1162-1180.e1. doi:10.1016/b978-0-7020-6285-8.00137-4.

[368] M. Fayyaz, I.A. Mirza, A. Hussain, In Vitro Susceptibility of Chloramphenicol Against Methicillin-Resistant Staphylococcus aureu Diagnosis of malaria View project Carbapenem resistant enterobacteriacea and non enterobacteriacea View project, 2014.

[369] J.A. Cram, New insights into relationships between active and dormant organisms,

phylogenetic diversity and ecosystem productivity, Mol. Ecol. 24 (2015) 5767–5769. doi:10.1111/mec.13449.

[370] D.L. Kalpaxis, P. Karahalios, M. Papapetropoulou, Changes in ribosomal activity in Escherichia coli cells during prolonged culture in sea salts medium, J. Bacteriol. 180 (1998) 3114–3119. doi:10.1128/jb.180.12.3114-3119.1998.

[371] K.L. Chung, AUTORADIOGRAPHIC STUDIES OF BACTERIAL CELL WALL REPLICATION I. CELL WALL GROWTH OF BACILLUS CEREUS IN THE PRESENCE OF CHLORAMPHENICOLl, Can. J. Microbiol. 13 (1967).

[372] R. Hancock, J.T. Park, Cell-wall synthesis by Staphylococcus aureus in the presence of chloramphenicol, Nature. 181 (1958) 1050–1052. doi:10.1038/1811050a0.

[373] L. Johannsen, H. Labischinski, P. Giesbrecht, Changes in the chemical structure of walls of Staphylococcus aureus grown in the presence of chloramphenicol, 1983. doi:10.1111/j.1574-6968.1983.tb00309.x.

[374] D.G. Smith, R. Marchant, Unbalanced cell-wall synthesis in chloramphenicol-grown Rhodotorula glutinis, 1969.

[375] W.H. Voigt, H.J. Zeiler, Influence of ciprofloxacin on the ultrastructure of grampositive and gramnegative bacteria, in: 24 Th Intersci. Conf. Animicrobial Agents, 1984.

[376] K. Cohen, J.S. McConnell, Endotoxin release from bacteria exposed to ciprofloxacin and other bactericidal antibiotics, in: 14 Th Int. Congr. Chemother., 1985.

[377] A. Dalhoff, Interaction of Aminoglycosides and Ciprofloxacin with Bacterial Membranes, in: Influ. Antibiot. Host-Parasite Relatsh. II, Springer Berlin Heidelberg, 1985: pp. 16–27. doi:10.1007/978-3-642-70748-3_2.

[378] I. Verma, A. Rohilla, G.K. Khuller, Alterations in macromolecular composition and cell wall integrity by ciprofloxacin in Mycobacterium smegmatis, Lett. Appl. Microbiol. 29 (1999) 113–117. doi:10.1046/j.1365-2672.1999.00597.x.

[379] D.F. Basri, N. Jaffar, N.M. Zin, L.S. Raj, Electron Microscope Study of Gall Extract from Quercus infectoria in Combination with Vancomycin against MRSA Using Post-Antibiotic Effect Determination, Int. J. Pharmacol. 9 (2013) 150–156. doi:10.3923/ijp.2013.150.156.

[380] D. Nevozhay, U. Kańska, R. Budzyńska, J. Boratyński, Current status of research on conjugates and related drug delivery systems in the treatment of cancer and other diseases, Postepy Hig. Med. Dosw. (Online). (2007).

[381] M. Vallet-Regí, M.M. García, M. Colilla, Biomedical applications of mesoporous ceramics: Drug delivery, smart materials and bone tissue engineering, 2012. doi:10.1201/b12959.

[382] S.S. Suri, H. Fenniri, B. Singh, Nanotechnology-based drug delivery systems, J. Occup. Med. Toxicol. (2007). doi:10.1186/1745-6673-2-16.

[383] C. Vitale-Brovarone, F. Baino, M. Miola, R. Mortera, B. Onida, E. Verné, Glass-ceramic scaffolds containing silica mesophases for bone grafting and drug delivery, J. Mater. Sci. Mater. Med. (2009). doi:10.1007/s10856-008-3635-7.

[384] I.I. Slowing, B.G. Trewyn, S. Giri, V.S.Y. Lin, Mesoporous silica nanoparticles for drug delivery and biosensing applications, Adv. Funct. Mater. (2007). doi:10.1002/adfm.200601191.

[385] M. Vallet-Regí, Revisiting ceramics for medical applications, Dalt. Trans. (2006). doi:10.1039/b610219k.

[386] A.Z. Wilczewska, K. Niemirowicz, K.H. Markiewicz, H. Car, Nanoparticles as drug delivery systems, Pharmacol. Reports. (2012). doi:10.1016/S1734-1140(12)70901-5.

[387] R. Bax, R. Bywater, G. Cornaglia, H. Goossens, P. Hunter, V. Isham, V. Jarlier, R. Jones, I. Phillips, D. Sahm, S. Senn, M. Struelens, D. Taylor, A. White, Surveillance of antimicrobial resistance — what, how and whither?, Clin. Microbiol. Infect. 7 (2001) 316–325. doi:10.1046/j.1198-743x.2001.00239.x.

[388] R. Labruère, A.J. Sona, E. Turos, Anti–methicillin-resistant staphylococcus aureus nanoantibiotics, Front. Pharmacol. (2019). doi:10.3389/fphar.2019.01121.

[389] P. Sepulveda, J.R. Jones, L.L. Hench, Characterization of melt-derived 45S5 and sol-gel-derived 58S bioactive glasses, J. Biomed. Mater. Res. 58 (2001) 734–740. doi:10.1002/jbm.10026.

[390] S.P. Chakraborty, S.K. Sahu, P. Pramanik, S. Roy, In vitro antimicrobial activity of nanoconjugated vancomycin against drug resistant Staphylococcus aureus, Int. J. Pharm. 436 (2012) 659–676. doi:10.1016/j.ijpharm.2012.07.033.

[391] Z. Gounani, M.A. Asadollahi, J.N. Pedersen, J. Lyngsø, J. Skov Pedersen, A. Arpanaei, R.L. Meyer, Mesoporous silica nanoparticles carrying multiple antibiotics provide enhanced synergistic effect and improved biocompatibility, Colloids Surfaces B Biointerfaces. (2019). doi:10.1016/j.colsurfb.2018.12.035.

[392] K. Madhumathi, T.S. Sampath Kumar, Regenerative potential and anti-bacterial activity of tetracycline loaded apatitic nanocarriers for the treatment of periodontitis, Biomed. Mater. 9 (2014) 035002. doi:10.1088/1748-6041/9/3/035002.

[393] S.P. Victor, T.S.S. Kumar, Tailoring calcium-deficient hydroxyapatite nanocarriers for enhanced release of antibiotics, J. Biomed. Nanotechnol. (2008). doi:10.1166/jbn.2008.019.

[394] H.M. Myers, H.J. Tochon-Danguy, C.A. Baud, IR absorption spectrophotometric analysis

of the complex formed by tetracycline and synthetic hydroxyapatite, Calcif. Tissue Int. (1983). doi:10.1007/BF02405117.

[395] Z. Gounani, M.A. Asadollahi, R.L. Meyer, A. Arpanaei, Loading of polymyxin B onto anionic mesoporous silica nanoparticles retains antibacterial activity and enhances biocompatibility, Int. J. Pharm. (2018). doi:10.1016/j.ijpharm.2017.12.039.

[396] S. Ghosh, V. Wu, S. Pernal, V. Uskoković, Self-Setting Calcium Phosphate Cements with Tunable Antibiotic Release Rates for Advanced Antimicrobial Applications, ACS Appl. Mater. Interfaces. (2016). doi:10.1021/acsami.6b01160.

[397] S. Dorozhkin, Self-Setting Calcium Orthophosphate Formulations, J. Funct. Biomater. (2013). doi:10.3390/jfb4040209.

[398] E. Breukink, B. de Kruijff, Lipid II as a target for antibiotics, Nat. Rev. Drug Discov. 5 (2006) 321–323. doi:10.1038/nrd2004.

[399] K. Hiramatsu, Vancomycin resistance in staphylococci, Drug Resist. Updat. (1998). doi:10.1016/S1368-7646(98)80029-0.

[400] K. Sieradzki, M.G. Pinho, A. Tomasz, Inactivated pbp4 in Highly Glycopeptide-resistant Laboratory Mutants of Staphylococcus aureus, J. Biol. Chem. 274 (1999) 18942–18946. doi:10.1074/jbc.274.27.18942.

[401] P.E. Reynolds, Structure, biochemistry and mechanism of action of glycopeptide antibiotics, Eur. J. Clin. Microbiol. Infect. Dis. 8 (1989) 943–950. doi:10.1007/BF01967563.

[402] C. Walsh, Molecular mechanisms that confer antibacterial drug resistance., Nature. 406 (2000) 775–781. doi:10.1038/35021219.

[403] M.E. Jones, M.R. Visser, M. Klootwijk, P. Heisig, J. Verhoef, F.J. Schmitz, Comparative activities of clinafloxacin, grepafloxacin, levofloxacin, moxifloxacin, ofloxacin, sparfloxacin, and trovafloxacin and nonquinolones linozelid, quinupristin-dalfopristin, gentamicin, and vancomycin against clinical isolates of ciprofloxacin-resistant and -susceptible Staphylococcus aureus strains., Antimicrob. Agents Chemother. 43 (1999) 421–3.

[404] R. Detsch, A.R. Boccaccini, The role of osteoclasts in bone tissue engineering, J. Tissue Eng. Regen. Med. 9 (2015) 1133–1149. doi:10.1002/term.1851.

[405] M. Zaidi, M. Pazianas, V. Shankar, B. Bax, C. Bax, P. Bevis, C. Stevens, C. Huang, D. Blake, B. Moonga, A. Et, Osteoclast function and its control, Exp. Physiol. 78 (1993) 721–739. doi:10.1113/expphysiol.1993.sp003721.

[406] N.A.P. van Gestel, G.H. Schuiringa, J.H.P.H. Hennissen, A.C.A. Delsing, K. Ito, B. van

Rietbergen, J.J. Arts, S. Hofmann, Resorption of the calcium phosphate layer on S53P4 bioactive glass by osteoclasts, J. Mater. Sci. Mater. Med. 30 (2019) 94. doi:10.1007/s10856-019-6295-x.

[407] S. Mistry, S. Burman, S. Roy, N.J. Maitra, R. Roy, A. Chanda, Biological analysis of an innovative biodegradable antibiotic eluting bioactive glass/gypsum composite bone cement for treating experimental chronic MRSA osteomyelitis, J. Pharm. Anal. (2021). doi:10.1016/j.jpha.2021.02.005.

[408] W. Stöber, A. Fink, E. Bohn, Controlled growth of monodisperse silica spheres in the micron size range, J. Colloid Interface Sci. (1968). doi:10.1016/0021-9797(68)90272-5.

[409] A.A.R. de Oliveira, D.A. de Souza, L.L.S. Dias, S.M. de Carvalho, H.S. Mansur, M. de Magalhães Pereira, Synthesis, characterization and cytocompatibility of spherical bioactive glass nanoparticles for potential hard tissue engineering applications, Biomed. Mater. 8 (2013) 025011. doi:10.1088/1748-6041/8/2/025011.

[410] S. Sadasivan, D.H. Rasmussen, F.P. Chen, R.K. Kannabiran, Preparation and characterization of ultrafine silica, Colloids Surfaces A Physicochem. Eng. Asp. (1998). doi:10.1016/S0927-7757(97)00148-9.

[411] S. Sadasivan, A.K. Dubey, Y. Li, D.H. Rasmussen, Alcoholic solvent effect on silica synthesis - NMR and DLS investigation, J. Sol-Gel Sci. Technol. (1998). doi:10.1023/A:1008659708390.

[412] Y. Huang, J.E. Pemberton, Synthesis of uniform, spherical sub-100nm silica particles using a conceptual modification of the classic LaMer model, Colloids Surfaces A Physicochem. Eng. Asp. (2010). doi:10.1016/j.colsurfa.2010.02.031.

[413] S. Lin, C. Ionescu, K.J. Pike, M.E. Smith, J.R. Jones, Nanostructure evolution and calcium distribution in sol–gel derived bioactive glass, J. Mater. Chem. 19 (2009) 1276. doi:10.1039/b814292k.

[414] B. Borak, J. Krzak, M. Ptak, W. Strek, A. Lukowiak, Spherical nanoparticles of europium-doped silica–calcia glass and glass-ceramic: Spectroscopic characterization, J. Mol. Struct. 1166 (2018) 48–53. doi:10.1016/J.MOLSTRUC.2018.04.019.

[415] I.A.M. Ibrahim, A.A.F. Zikry, M.A. Sharaf, A. Zikry, Preparation of spherical silica nanoparticles: Stober silica, 2010.

[416] K. Do Kim, H.T. Kim, Formation of silica nanoparticles by hydrolysis of TEOS using a mixed semi-batch/batch method, J. Sol-Gel Sci. Technol. (2002). doi:10.1023/A:1020217105290.

[417] I.A. Rahman, P. Vejayakumaran, C.S. Sipaut, J. Ismail, M.A. Bakar, R. Adnan, C.K. Chee, An optimized sol-gel synthesis of stable primary equivalent silica particles, Colloids

Surfaces A Physicochem. Eng. Asp. (2007). doi:10.1016/j.colsurfa.2006.08.001.

[418] L.L. Hench, Bioceramics: From Concept to Clinic, J. Am. Ceram. Soc. 74 (1991) 1487–1510. doi:10.1111/j.1151-2916.1991.tb07132.x.

[419] A.E. Clark, C.G. Pantano, L.L. Hench, Auger Spectroscopic Analysis of Bioglass Corrosion Films, J. Am. Ceram. Soc. 59 (1976) 37–39. doi:10.1111/j.1151-2916.1976.tb09382.x.

[420] M. Edén, The split network analysis for exploring composition–structure correlations in multi-component glasses: I. Rationalizing bioactivity-composition trends of bioglasses, J. Non. Cryst. Solids. 357 (2011) 1595–1602. doi:10.1016/j.jnoncrysol.2010.11.098.

[421] B. Lei, X. Chen, Y. Wang, N. Zhao, C. Du, L. Zhang, Acetic acid derived mesoporous bioactive glasses with an enhanced in vitro bioactivity, J. Non. Cryst. Solids. 355 (2009) 2583–2587. doi:10.1016/j.jnoncrysol.2009.09.014.

[422] B. Lei, X. Chen, Y. Wang, N. Zhao, C. Du, L. Fang, Fabrication, structure and biological properties of organic acid-derived sol–gel bioactive glasses, Biomed. Mater. 5 (2010) 054103. doi:10.1088/1748-6041/5/5/054103.

[423] P. Stoor, E. Söderling, J.I. Salonen, Antibacterial effects of a bioactive glass paste on oral microorganisms., Acta Odontol. Scand. 56 (1998) 161–165. doi:10.1080/000163598422901.

[424] N. Beales, Adaptation of Microorganisms to Cold Temperatures, Weak Acid Preservatives, Low pH, and Osmotic Stress: A Review, Compr. Rev. Food Sci. Food Saf. (2004). doi:10.1111/j.1541-4337.2004.tb00057.x.

[425] A.J. Varkey, A.F. Fort, Some optical properties of silver peroxide (AgO) and silver oxide (Ag2O) films produced by chemical-bath deposition, Sol. Energy Mater. Sol. Cells. (1993). doi:10.1016/0927-0248(93)90040-A.

[426] D.K. Bhui, H. Bar, P. Sarkar, G.P. Sahoo, S.P. De, A. Misra, Synthesis and UV-vis spectroscopic study of silver nanoparticles in aqueous SDS solution, J. Mol. Liq. (2009). doi:10.1016/j.molliq.2008.11.014.

[427] H.H. Lu, S.R. Pollack, P. Ducheyne, Temporal zeta potential variations of 45S5 bioactive glass immersed in an electrolyte solution, J. Biomed. Mater. Res. 51 (2000) 80–87. doi:10.1002/(SICI)1097-4636(200007)51:1<80::AID-JBM11>3.0.CO;2-6.

[428] P. Naruphontjirakul, A.E. Porter, J.R. Jones, In vitro osteogenesis by intracellular uptake of strontium containing bioactive glass nanoparticles, Acta Biomater. (2018). doi:10.1016/j.actbio.2017.11.008.

[429] P. Naruphontjirakul, O. Tsigkou, S. Li, A.E. Porter, J.R. Jones, Human mesenchymal stem cells differentiate into an osteogenic lineage in presence of strontium containing bioactive

glass nanoparticles, Acta Biomater. 90 (2019) 373–392. doi:10.1016/j.actbio.2019.03.038.

[430] N.A. Twine, L. Chen, C.N. Pang, M.R. Wilkins, M. Kassem, Identification of differentiation-stage specific markers that define the ex vivo osteoblastic phenotype, Bone. (2014). doi:10.1016/j.bone.2014.06.027.

[431] M.T. Tsai, W.J. Li, R.S. Tuan, W.H. Chang, Modulation of osteogenesis in human mesenchymal stem cells by specific pulsed electromagnetic field stimulation, J. Orthop. Res. (2009). doi:10.1002/jor.20862.

[432] J.B. Lian, G.S. Stein, Development of the osteoblast phenotype: molecular mechanisms mediating osteoblast growth and differentiation., Iowa Orthop. J. (1995).

[433] M.B. Keogh, F.J. O'Brien, J.S. Daly, A novel collagen scaffold supports human osteogenesis - Applications for bone tissue engineering, Cell Tissue Res. (2010). doi:10.1007/s00441-010-0939-y.

[434] B. Setzer, M. Bächle, M.C. Metzger, R.J. Kohal, The gene-expression and phenotypic response of hFOB 1.19 osteoblasts to surface-modified titanium and zirconia, Biomaterials. (2009). doi:10.1016/j.biomaterials.2008.10.054.

[435] M.H. Choi, W.C. Noh, J.W. Park, J.M. Lee, J.Y. Suh, Gene expression pattern during osteogenic differentiation of human periodontal ligament cells in vitro, J. Periodontal Implant Sci. (2011). doi:10.5051/jpis.2011.41.4.167.

[436] J. Kim, Protein adsorption on polymer particles, J. Biomed. Mater. Res. (2002).

[437] X. Huang, X. Teng, D. Chen, F. Tang, J. He, The effect of the shape of mesoporous silica nanoparticles on cellular uptake and cell function, Biomaterials. (2010). doi:10.1016/j.biomaterials.2009.09.060.

[438] M. Kafshgari, F. Harding, N. Voelcker, Insights into Cellular Uptake of Nanoparticles, Curr. Drug Deliv. (2015). doi:10.2174/1567201811666140821110631.

[439] F. Zhao, Y. Zhao, Y. Liu, X. Chang, C. Chen, Y. Zhao, Cellular uptake, intracellular trafficking, and cytotoxicity of nanomaterials, Small. (2011). doi:10.1002/smll.201100001.

[440] I.M. Adjei, B. Sharma, V. Labhasetwar, Nanoparticles: Cellular uptake and cytotoxicity, Adv. Exp. Med. Biol. (2014). doi:10.1007/978-94-017-8739-0_5.

[441] N. Oh, J.H. Park, Endocytosis and exocytosis of nanoparticles in mammalian cells, Int. J. Nanomedicine. (2014). doi:10.2147/IJN.S26592.

[442] J.L. Vivero-Escoto, I.I. Slowing, V.S.Y. Lin, B.G. Trewyn, Mesoporous silica nanoparticles for intracellular controlled drug delivery, Small. (2010). doi:10.1002/smll.200901789.

[443] Q. Gan, D. Dai, Y. Yuan, J. Qian, S. Sha, J. Shi, C. Liu, Effect of size on the cellular endocytosis and controlled release of mesoporous silica nanoparticles for intracellular delivery, Biomed. Microdevices. (2012). doi:10.1007/s10544-011-9604-9.

[444] S. Mayor, R.E. Pagano, Pathways of clathrin-independent endocytosis, Nat. Rev. Mol. Cell Biol. (2007). doi:10.1038/nrm2216.

[445] D.R. Radu, C.Y. Lai, K. Jeftinija, E.W. Rowe, S. Jeftinija, V.S.Y. Lin, A polyamidoamine dendrimer-capped mesoporous silica nanosphere-based gene transfection reagent, J. Am. Chem. Soc. (2004). doi:10.1021/ja046275m.

[446] F.R. Maxfield, T.E. McGraw, Endocytic recycling, Nat. Rev. Mol. Cell Biol. (2004). doi:10.1038/nrm1315.

[447] A. Salis, M. Fanti, L. Medda, V. Nairi, F. Cugia, M. Piludu, V. Sogos, M. Monduzzi, Mesoporous Silica Nanoparticles Functionalized with Hyaluronic Acid and Chitosan Biopolymers. Effect of Functionalization on Cell Internalization, ACS Biomater. Sci. Eng. (2016). doi:10.1021/acsbiomaterials.5b00502.

[448] I. Slowing, B.G. Trewyn, V.S.Y. Lin, Effect of surface functionalization of MCM-41-type mesoporous silica nanoparticles on the endocytosis by human cancer cells, J. Am. Chem. Soc. (2006). doi:10.1021/ja0645943.

[449] D. Huang, Y. Hung, B. Ko, S. Hsu, W. Chen, C. Chien, C. Tsai, C. Kuo, J. Kang, C. Yang, C. Mou, Y. Chen, Highly efficient cellular labeling of mesoporous nanoparticles in human mesenchymal stem cells: implication for stem cell tracking, FASEB J. (2005). doi:10.1096/fj.05-4288fje.

[450] Y.S. Lin, C.P. Tsai, H.Y. Huang, C.T. Kuo, Y. Hung, D.M. Huang, Y.C. Chen, C.Y. Mou, Well-ordered mesoporous silica nanoparticles as cell markers, Chem. Mater. (2005). doi:10.1021/cm051014c.

[451] B.D. Chithrani, A.A. Ghazani, W.C.W. Chan, Determining the size and shape dependence of gold nanoparticle uptake into mammalian cells, Nano Lett. (2006). doi:10.1021/nl052396o.

[452] B.D. Chithrani, W.C.W. Chan, Elucidating the mechanism of cellular uptake and removal of protein-coated gold nanoparticles of different sizes and shapes, Nano Lett. (2007). doi:10.1021/nl070363y.

[453] B.G. Trewyn, J.A. Nieweg, Y. Zhao, V.S.Y. Lin, Biocompatible mesoporous silica nanoparticles with different morphologies for animal cell membrane penetration, Chem. Eng. J. (2008). doi:10.1016/j.cej.2007.09.045.

[454] E. Sharifi, M. Azami, A.M. Kajbafzadeh, F. Moztarzadeh, R. Faridi-Majidi, A. Shamousi, R. Karimi, J. Ai, Preparation of a biomimetic composite scaffold from gelatin/collagen and

bioactive glass fibers for bone tissue engineering, Mater. Sci. Eng. C. 59 (2016) 533–541. doi:10.1016/j.msec.2015.09.037.

[455] M. Azami, S. Tavakol, A. Samadikuchaksaraei, M.S. Hashjin, N. Baheiraei, M. Kamali, M.R. Nourani, A porous hydroxyapatite/gelatin nanocomposite scaffold for bone tissue repair: In vitro and in vivo evaluation, J. Biomater. Sci. Polym. Ed. 23 (2012) 2353–2368. doi:10.1163/156856211X617713.

[456] M.T. Wolf, K.A. Daly, E.P. Brennan-Pierce, S.A. Johnson, C.A. Carruthers, A. D'Amore, S.P. Nagarkar, S.S. Velankar, S.F. Badylak, A hydrogel derived from decellularized dermal extracellular matrix, Biomaterials. 33 (2012) 7028–7038. doi:10.1016/j.biomaterials.2012.06.051.

[457] M.W. Tibbitt, K.S. Anseth, Hydrogels as extracellular matrix mimics for 3D cell culture, Biotechnol. Bioeng. 103 (2009) 655–663. doi:10.1002/bit.22361.

[458] S.F. Badylak, The extracellular matrix as a biologic scaffold material, Biomaterials. 28 (2007) 3587–3593. doi:10.1016/j.biomaterials.2007.04.043.

[459] S.F. Badylak, The extracellular matrix as a scaffold for tissue reconstruction, Semin. Cell Dev. Biol. 13 (2002) 377–383. doi:10.1016/S1084952102000940.

[460] D. Mohamad Yunos, O. Bretcanu, A.R. Boccaccini, Polymer-bioceramic composites for tissue engineering scaffolds, in: J. Mater. Sci., 2008: pp. 4433–4442. doi:10.1007/s10853-008-2552-y.

[461] A.R. Boccaccini, J.J. Blaker, Bioactive composite materials for tissue engineering scaffolds, Expert Rev. Med. Devices. 2 (2005) 303–317. doi:10.1586/17434440.2.3.303.

[462] M. Erol, W.J. Stark, D. Mohn, Z. Hong, Polymer/bioactive glass nanocomposites for biomedical applications: A review, Compos. Sci. Technol. 70 (2010) 1764–1776. doi:10.1016/J.COMPSCITECH.2010.06.002.

[463] J.A. Killion, S. Kehoe, L.M. Geever, D.M. Devine, E. Sheehan, D. Boyd, C.L. Higginbotham, Hydrogel/bioactive glass composites for bone regeneration applications: Synthesis and characterisation, Mater. Sci. Eng. C. 33 (2013) 4203–4212. doi:10.1016/J.MSEC.2013.06.013.

[464] S. Chen, A. Osaka, T. Ikoma, H. Morita, J. Li, M. Takeguchi, N. Hanagata, Fabrication, microstructure, and BMP-2 delivery of novel biodegradable and biocompatible silicate-collagen hybrid fibril sheets, J. Mater. Chem. 21 (2011) 10942–10948. doi:10.1039/c1jm10829h.

[465] G.S. Alvarez, C. Hélary, A.M. Mebert, X. Wang, T. Coradin, M.F. Desimone, Antibiotic-loaded silica nanoparticle-collagen composite hydrogels with prolonged antimicrobial activity for wound infection prevention, J. Mater. Chem. B. 2 (2014) 4660–4670.

doi:10.1039/c4tb00327f.

[466] M. Peter, N.S. Binulal, S. Soumya, S.V. Nair, T. Furuike, H. Tamura, R. Jayakumar, Nanocomposite scaffolds of bioactive glass ceramic nanoparticles disseminated chitosan matrix for tissue engineering applications, Carbohydr. Polym. 79 (2010) 284–289. doi:10.1016/J.CARBPOL.2009.08.001.

[467] C. Helary, I. Bataille, A. Abed, C. Illoul, A. Anglo, L. Louedec, D. Letourneur, A. Meddahi-Pellé, M.M. Giraud-Guille, Concentrated collagen hydrogels as dermal substitutes, Biomaterials. 31 (2010) 481–490. doi:10.1016/j.biomaterials.2009.09.073.

[468] H.K. Kleinman, D. Philp, M.P. Hoffman, Role of the extracellular matrix in morphogenesis, Curr. Opin. Biotechnol. 14 (2003) 526–532. doi:10.1016/j.copbio.2003.08.002.

[469] M.G. Patino, M.E. Neiders, S. Andreana, B. Noble, R.E. Cohen, Collagen as an implantable material in medicine and dentistry., J. Oral Implantol. 28 (2002) 220–225. doi:10.1563/1548-1336(2002)028<0220:CAAIMI>2.3.CO;2.

[470] L.J. Currie, J.R. Sharpe, R. Martin, The Use of Fibrin Glue in Skin Grafts and Tissue-Engineered Skin Replacements: A Review, Plast Reconstr Surg . 108 (2001) 1713–26.

[471] A.S. Mistry, A.G. Mikos, Tissue engineering strategies for bone regeneration, Adv. Biochem. Eng. Biotechnol. 94 (2005) 1–22. doi:10.1007/b99997.

[472] Y.Y. Wang, X. Chatzistavrou, D. Faulk, S. Badylak, L. Zheng, S. Papagerakis, L. Ge, H. Liu, P. Papagerakis, Biological and bactericidal properties of Ag-doped bioactive glass in a natural extracellular matrix hydrogel with potential application in dentistry, Eur. Cells Mater. 29 (2015) 342–355. doi:10.22203/eCM.v029a26.

[473] K. Esmaeili Pourfarhangi, S. Mashayekhan, S.G. Asl, Z. Hajebrahimi, Construction of scaffolds composed of acellular cardiac extracellular matrix for myocardial tissue engineering, Biologicals. 53 (2018) 10–18. doi:10.1016/j.biologicals.2018.03.005.

[474] H. Otsuka, Y. Nagasaki, K. Kataoka, PEGylated nanoparticles for biological and pharmaceutical applications, Adv. Drug Deliv. Rev. 55 (2003) 403–419. doi:10.1016/S0169-409X(02)00226-0.

[475] S.S. Yu, C.M. Lau, S.N. Thomas, W. Gray Jerome, D.J. Maron, J.H. Dickerson, J.A. Hubbell, T.D. Giorgio, Size- and charge-dependent non-specific uptake of PEGylated nanoparticles by macrophages, Int. J. Nanomedicine. 7 (2012) 799–813. doi:10.2147/IJN.S28531.

[476] R.R. Castillo, M. Vallet-Regí, Functional mesoporous silica nanocomposites: Biomedical applications and biosafety., Int. J. Mol. Sci. (2019). doi:10.3390/ijms20040929.

[477] R.R. Castillo, D. Hernández-Escobar, S. Gómez-Graña, M. Vallet-Regí, Reversible

Nanogate System for Mesoporous Silica Nanoparticles Based on Diels–Alder Adducts, Chem. - A Eur. J. (2018). doi:10.1002/chem.201706100.

[478] S.J. Mattingly, M.G. Otoole, K.T. James, G.J. Clark, M.H. Nantz, Magnetic nanoparticle-supported lipid bilayers for drug delivery, Langmuir. (2015). doi:10.1021/la504830z.